Copyright

by

Robert John Stover

2015

The Dissertation Committee for Robert John Stover Certifies that this is the approved version of the following dissertation:

Controlled Assembly of Biodegradable Gold Nanoclusters for In Vivo Imaging

Committee:

Keith P. Johnston, Supervisor

Konstantin Sokolov

Thomas Truskett

Donglei Fan

Brian Korgel

Controlled Assembly of Biodegradable Gold Nanoclusters for In Vivo Imaging

by

Robert John Stover, B.S.M.S.E.

Dissertation

Presented to the Faculty of the Graduate School of

The University of Texas at Austin

in Partial Fulfillment

of the Requirements

for the Degree of

Doctor of Philosophy

The University of Texas at Austin

December 2015

Dedication

To my parents, whose weekly phone calls helped keep me focused and calm.

To my brother, whose visits were always a much needed distraction.

To my friends, who kept me laughing through this all.

Acknowledgements

These past five years has brought about immense personal growth in many areas of my life and I am grateful to so many for their respective roles. Firstly, I must thank my advisor, Dr. Keith Johnston, whose unique style and intense scientific drive has shaped so much of my organizational and research abilities. My primary goal for graduate school of becoming a competent scientist and leader has been met and far exceeded thanks to his guidance. Next I must thank Dr. Konstantin Sokolov and Dr. Stanislav Emelianov for helping me to hone my collaboration skills as well as grow my biomedical engineering knowledge. Additionally, Dr. Thomas Truskett has served as an excellent role model and mentor. His willingness to lend a hand and put students first did not go unnoticed. I'd like to thank Dr. Donglei Fan for serving on my committee and judging so many of my TMI posters throughout the years. Thanks are also due to Dr. Brian Korgel for providing helpful feedback on my research and sharing his heli-skiing stories.

My time at UT has been shaped heavily by my lab-mates; who have resembled more of a family than co-workers since the beginning. I extend a great debt of gratitude to my primary mentor, Dr. Avinash Murthy, who spent so many hours teaching me the ways of this project and helped me grow so much as a young researcher. I would also like to thank Ehsan Moaseri who has been so instrumental in helping me finish this thesis and carry the project into the future. Next, I must thank all of my other lab-mates over the years who always made themselves available to lend a hand, share ideas, or de-stress over drinks after work. Particularly, to Will Hardin, Andrew Worthen, Bart Dear, Ameya Borwankar, Dan Slanac, and Amro Elhag; the times we've shared both in and out of lab are times that will not be forgotten. Special thanks goes out to my many undergraduates -

Bobby Schramm, Robin Nguyen, Golay Nie, Miguel Martinez, Gerard Isaac, Nathan Rebello, Joe Schroer, Negin Rahbar, and Sai Gourisankar - who have supported me and endured many frustrations and trials throughout these years. I could not have done this without their willingness to put forth great effort towards our goal. I also must extend significant gratitude to both the Sokolov and Emelianov groups – especially, Dr. Justina Tam, Dr. Pratixa Joshi, and Dr. Soon Joon Yoon – for all of their help on the biomedical side of the science and for letting me see my work come to fruition in cellular, animal, and photoacoustic imaging studies. Thanks also goes out to Dwight Romanovicz who spent countless hours helping me with TEM analysis and sharing stories of the great Austin mountain biking scene.

Lastly, I must thank my parents, brother, grandparents, aunts, uncles, and friends who have supported and prayed for me throughout these years. This has certainly not been a solo effort; and I'm proud to say we have finally achieved this goal!

Controlled Assembly of Biodegradable Gold Nanoclusters for In Vivo Imaging

Robert John Stover, Ph.D.

The University of Texas at Austin, 2015

Supervisor: Keith P. Johnston

Gold nanoparticles are of interest in biomedical imaging applications due to their inert nature and ability to exhibit surface plasmon resonance. These phenomena can result in high near-infrared extinction (NIR) due to asymmetry or close interparticle spacings within gold structures, making these materials ideal for photoacoustic imaging. Using this imaging modality, these materials allow for high contrast compared to the body's tissues which exhibit a transparent "window" between 700-1100 nm, making them perfect for early cancer detection. However many gold structures designed for this application fail to achieve high NIR-absorbance at the <5 nm sizes which are required for efficient kidney clearance. Therefore, we designed a system which assembles ~4 nm primary gold particles into closely-spaced clusters of controlled size using a biodegradable, weakly adsorbing polymer and balance of colloidal attractive and repulsive forces. Thus, when the polymer degrades in acidic environments – such as within cells – the residual charge on the primary particles leads to dissociation of the clusters back to renal-clearable constituents.

Since proteins in the blood and cells can increase the diameter of the primary particles above the 5 nm threshold, nanoparticle surfaces were designed to have a mixture of charged and zwitterionic molecules to limit protein interactions through buried charges

and increased particle hydration. Strongly-bound, zwitterionic thiol-containing ligands were also investigated to resist the intracellular exchange of biomolecules which could compromise the clearable nature of the particles. These decorated nanoparticles were then assembled into clusters through one of two methods which varied either gold and polymer concentrations through evaporation, or particle charge via electrolyte addition prior to quenching by dilution in DI water. Once assembled, clusters assembled with polymer showed dissociation behavior after incubation in pH 5 acidic solutions to mimic the cellular pH environment. In other cases, sintering of the gold nanoparticle clusters prevented such dissociation. This thesis demonstrates the ability to not only create biocompatible nanoparticle surfaces, but to establish control size control over nanocluster assemblies which are capable of being used as NIR contrast agents.

Table of Contents

List of Tables

List of Figures

Chapter 1: Introduction

Reversible gold nanoparticle assemblies which exhibit high-NIR extinction are of interest in biomedical imaging and therapy.[1-5] nanostructures as well as their ability to exhibit surface plasmon resonance (SPR)[6-7], has made these materials ideal candidates for use as in vivo contrast agents for detection of diseases such as cancer and atherosclerosis.[8-17] These materials exploit the near infrared (NIR) window of the body – a region between 700-1100 nm where the body's tissue absorbance is at a minimum (Figure 1.1).[18-19] The SPR effect arises from the collective oscillations of the outermost electrons and gives rise to a high absorption of light in the NIR region.[7] This allows the imaging of the nanomaterials with modalities such as photoacoustic (PA) measurements which detect thermal fluctuations from the nanoparticles as a result of NIR laser irradiation.[18] The increased contrast from the nanoparticles allows for greater imaging penetration depth than most standard medical techniques.[20-23] Additionally, irradiation with higher intensity NIR lasers can heat the materials enough to cause necrosis in surrounding tissues; a technique called photothermal therapy.[11, 24-25]

Shifts the SPR peak to longer wavelengths, termed a "red-shift", can occur due to changes in nanoparticle symmetry giving rise to formation of dipoles and higher-order multipoles in the material.[26-28] This effect has been widely observed for numerous gold shapes such as nanorods[27, 29], nanoshells[11, 13, 30], nanocages[31-32], nanostars[33], and nanorose[15-16]. However, with typical sizes > 30nm for high-NIR absorbance, these materials are well beyond the ~5.5 nm cutoff for efficient renal clearance.[34-37] If not cleared through the kidneys, significant liver accumulation has been observed and clearance kinetics significantly decrease.[38] Therefore materials used for in vivo imaging must be capable of dissociation to sub-5.5 nm sizes.

High-NIR absorbance has also been shown for nanoparticle aggregates as a result of close interparticle spacings and accumulation of dipolar "hot spots" between nanoparticles within the structures.[24, 26, 39-40] However to maintain a renally clearable size, nanoparticles must also prevent protein adsorption in the blood stream, as even a single protein can result in sizes too large for renal clearance. Additionally, high intracellular concentrations of strong-binding thiol molecules such as glutathione, GSH, can replace particle surface ligands leaving the particles susceptible to additional protein adsorption or aggregation.[41-42] Therefore novel methods are required to achieve a multitude of goals: 1) to design < 5 nm particle surfaces to prevent protein adsorption and resist GSH exchange; and 2) to assemble these nanoparticles into reversible, closely-spaced clusters (Figure 1.2).

1.1 NANOPARTICLE SURFACE DESIGN

The size of human serum albumin (HSA), the most common protein in serum, has an average diameter of ~ 8 nm.[43] Therefore, adsorption of even a single HAS protein onto a ~ 4 nm primary particle can render it incapable of efficient renal clearance, preventing its use as a biomedical agent. A significant amount of research has been done on assembling protein resistant layers on surfaces and nanoparticles.[34, 44-47] Neutral layers of PEG or other neutral ligands have widely been shown to prevent adsorption.48-49 Whitesides et al. even showed that a neutral surface composed of a 1:1 mixture of positive and negative surface charges showed high resistance to fibrinogen adsorption on gold surfaces.[50] Meanwhile polymeric zwitterionic molecules which contain both positive and negative charge, were also shown to prevent adsorption in an experiment nanoparticles.[44] Dynamic light scattering (DLS) analysis showed no size increase was

shown for neutral, zwitterionic-capped particles. Meanwhile, evidence of protein adsorption for charged particles, as well as those conjugated with PEG was present. Similar combinations of low electrostatic attraction and the formation of a steric hydration layer around the hydrophilic surfaces have subsequently been shown to prevent protein-nanoparticle interactions.[51]

While neutral surface coatings have generally been shown to reduce protein adsorption, the opposite is true for highly-charged single ligand surfaces. Gold nanoparticles capped with negatively-charged citrate or dihydrolipoic acid (DHLA) have widely been shown to attract significant amounts of protein.[34, 52-58] Size increases of ~10 nm were shown after incubation of citrate-capped nanoparticles, indicating adsorption of numerous proteins. Nanoparticle size has been shown to play a role in protein resistance as well.[59] Recently, 2 nm GSH-capped gold particles were shown to prevent adsorption in 10 % fetal bovine serum (FBS) as well as show highly efficient renal clearance despite carrying a negative surface charge.[36] Furthermore, ligand orientation has been shown to play an important role as Stellaci et al. engineered mixed neutral (octanethiol) and negatively charged (mercaptoundecanesulfonate) surfaces which prevented protein adsorption with a -35 mV zeta potential.[60] The interaction between distinct hydrophobic and hydrophilic regions on the particle surface resulting from the "striped" ligand pattern compared to a random orientation of ligands was attributed for the protein resistance.

There is a significant discrepancy in techniques and methods used to detect protein adsorption onto nanoparticles.[57, 61-66] Due to difficulties with protein scattering signals in techniques such as DLS, several studies incubate particles in dilute serum concentrations of 10% or less.[36, 60, 67] However, Yang et al. demonstrated that charged gold nanoparticles which appeared to resist protein interactions in 10% FBS, adsorbed a large number in 100% FBS.[44-45] Techniques, such as florescent microscopy[66], SPR

sensing[61-62], electrophoresis[63-64], or quartz crystal microbalance (QCM) analysis[65] can be used at such concentrations; however do not provide single-protein adsorption sensitivity. Rotello et al. recently demonstrated an analysis method using a combination of DLS and centrifugation to attempt to identify nanoparticles with even small quantities of adsorbed proteins through measuring the size and density changes expected with nanoparticle attachment.[68] This technique helped prove the protein resistance of HSA adsorption onto gold nanoparticles capped with zwitterions of varying hydrophobicity.

In addition to preventing protein adsorption, a significant challenge for designing clearable particles is intracellular ligand exchange.[42] Thiols are well known to bind more strongly to gold than any other functional group.[69-71] Biological thiols, such as GSH, have been shown to be capable of exchange onto nanoparticle surfaces at ~10 mM concentrations found inside cells, which could impact the effectiveness of a pre-designed protein resistant surface.[42, 72] Therefore using strongly-bound ligands which also resist proteins must be utilized. Additionally if these particles also allow their assembly into reversible, high-NIR clusters, these materials can be promising as clearable biomedical imaging contrast agents.

1.2 Colloidal Assembly of Nanoparticle Clusters

Assemblies of nanoparticles are often mediated through specific interactions with materials such as DNA, alkane-thiols, peptides, or polymers.[73-80] Typically, gold-binding functional groups on template materials act as tethers to bring two particles together. However significant amounts of template material remain after assembly preventing close interaprticle spacings and reducing the yield of particles within a cluster. Nanoparticle clusters have also been reported in vivo, within cells due to high ionic strength and

reduced volumes.[9, 81] Similar manipulation of particle debye length has been reported extensively in vitro through varying the pH and ionic strength of the solution.[82-91] Turkevich et al. demonstrated the tendency for 20 nm citrate-capped gold nanospheres to aggregate under increasing ionic strength. The size of the aggregates was shown to be dependent upon $NaClO^4$ concentration and time.[92] Cluster growth has also been controlled with addition of NaCl to 14 nm citrate and thioglycolic acid (TGA)-capped gold particles followed by removal of Na^+ ions through treatment with an ion exchange resin.[93]

Further control over nanoparticle aggregation has been shown through balancing the total colloidal interaction potentials as described in DLVO theory.[94] Specifically, the balance of long-range repulsive and short-range attraction has led to clusters of controlled size. An in situ procedure showed CdSe nanoparticles self-assembled into clusters limited by the build-up of negative charges within the clusters arising from citrate ligands on particle surfaces.[95] Similar behavior was seen for clusters made from premade primary particles. Pozzo et al. demonstrated size control through a balance of hydrophobic attraction between gold particles self-limited by increased steric repulsion from the addition of a high-molecular weight (MW) poly(ethylene glycol) (PEG).[96-97]

Self-assembly equilibrium procedures have proven especially effective in organic solvents[83, 98-100] due to lowered electrostatic repulsion as a result of the low dielectric constant, as is described by a free energy model.[101-102] Meanwhile aqueous systems tend to show smaller, less stable clusters due to the increased Debye lengths.[97] Still, ~100 nm protein nanoclusters were recently shown to form equilibrium assemblies in water with a pH around their isoelectric point and large vdW and depletion contributions from high concentrations of protein and non-specific crowder molecules.[103] The nanocluster sizes were predicted using a free energy model and the clusters were shown to revert back to

monomer upon dilution indicated a fully equilibrium process. Such reversible behavior has not been observed for inorganic metal nanoparticles, especially with short ligands. Reversible gold nanoparticle aggregates shown in literature are typically capped with high-MW ligands as the increased sterics reduces the vdW potential which can trap closely-spaced nanoparticles in their aggregate formation.[86, 89, 104-109] However Lim et al. has shown elevated temperature and time can overcome such barriers and allow reversibility for cysteine-capped gold nanoparticles at high pH.[85]

Partial dissociation has been observed in vitro and in vivo within macrophage cells from clusters assembled from ~ 4 nm lysine/citrate-capped gold nanospheres.[3] The clusters used solvent evaporation to increase attractive vdW and depletion forces to balance the electrostatic repulsion of the negatively-charged particles.[2] A biodegradable PLA(1k)-PEG(10k)-PLA(1k) polymer was used to quench the nanocluster growth and prevent heteroaggregation between clusters. Upon hydrolysis of the PLA anchoring groups, the residual surface charge repelled the primary particles back into solution, suggesting a quasi-equilibrium approach. This work was the basis for the studies presented in this thesis and chapter 3 will further build upon this concept.

For use as biomedical contast agents, small (30-80 nm) gold nanoclusters must also be capable of achieving high-NIR extinction; a product of close interparticle spacings, asymmetry, and density of particles.[24, 26, 39-40, 42, 110] Due to their small size and potential for incomplete coverage, citrate-capped particles are often used in high-NIR nanocluster assembly.[111-112] Lysine, a molecule used extensively throughout this theis, has been shown to promote particle aggregation through electrostatic attractions between particles which typically leads to significant absorption in the NIR.[113-115] However, most gold nanoparticle assemblies which achieve NIR produce clusters > 100 nm, well outside the optimal range to avoid the RES system.[93, 98, 115] This is typically due to the use of

large (15-20 nm) primary particles which require several nanoparticles to achieve high-NIR extinction, therefore increasing the cluster size. Few studies have produced the desired optical properties from clearable primary particle aggregates[116]; and even fewer with reversible properties.[3] Therefore this concept of assembling sub-5 nm gold nanoparticles into reversible, high-NIR absorbing clusters is further examined and extended in Chapters 3-5.

1.2 OBJECTIVES

Herein, this thesis details a novel set of methods for designing a high-NIR contrast agent material with the potential for efficient renal clearance. This is achieved first through the careful design of ~ 4 nm gold nanoparticle surfaces to prevent protein adsorption and resist exchange with intracellular thiols. This effect is shown through incubation of the particles in 100 % FBS and measured by DLS and centrifugation analysis. Next, these nanoparticles are assembled into closely-spaced nanoclusters through two different pathways. The first uses a balance of long-range electrostatic repulsion and short-range vdW and depletion attraction to control the cluster size and NIR absorbance properties. A second method utilizes pH manipulation to balance the electrostatic and vdW forces to bring the clusters into close contact. This system shows that by manipulating the particle charge, the citrate particles essentially self-assemble into clusters of controlled size based on a balance of electrostatic repulsion with vdW attraction. In both cases, the clusters are stabilized against reversibility with a biodegradable, weakly-adsorbing PLA(1k)-PEG(10k)-PLA(1k) polymer. These synthesis procedures are shown to be versatile and compatible with a variety of ligand combinations, including cysteine/citrate. Thiolated ligands of varying length are also

shown to impact the interparticle spacings and shape of the nanoclusters as detailed with UV-vis-NIR, transmission electron microscopy (TEM), and small-angle x-ray scattering (SAXS) studies. Lastly, dissociation of the cluster assemblies is demonstrated via UV-vis and DLS analysis upon hydrolysis of the PLA under cellular pH 5 conditions.

In chapter 2 of this dissertation, the design of protein-resistant nanoparticle surfaces will be detailed. Herein, we design charged ~5 nm Au nanospheres coated with binary mixed charge ligand monolayers that do not change in size upon incubation in pure fetal bovine serum (FBS) as measured by DLS. The mixed charge monolayers are comprised of anionic citrate ligands modified by place exchange with naturally-occurring amino acids: either cationic lysine or zwitterionic cysteine ligands. The zwitterionic tips of either the lysine or cysteine ligands interact weakly with the proteins and furthermore increase the distance between the "buried" charges closer to the Au surface and the interacting sites on the protein surface. To support the DLS analysis, further centrifugation studies are done, showing significantly less sediment for samples with less protein adsorption.

Chapter 3 discusses a quenched-equilibrium approach to assemble Au nanoclusters of controlled size by tuning the colloidal interactions with a polymeric stabilizer, PLA(1k)-b-PEG(10k)-b-PLA(1k). The nanoclusters form upon mixing a dispersion of ~5 nm Au nanospheres with a polymer solution followed by partial solvent evaporation. A weakly adsorbed polymer quenches the equilibrium nanocluster size and provides steric stabilization. The <100 nm nanocluster sizes are tuned by experimentally varying the vdW and depletion attraction via final Au nanoparticle concentration and the polymer/Au ratio, respectively, along with the charge on the initial Au nanoparticle surface. Upon biodegradation of the quencher, the nanoclusters reversibly dissociate to individual ~5 nm primary particles. Equilibrium cluster size is predicted semi-

quantitatively with a free energy model that balances short-ranged depletion and van der Waals attractions with longer-ranged electrostatic repulsion, as a function of the Au and polymer concentrations. The close spacings of the Au nanoparticles in the clusters produce strong NIR extinction.

A similar quenched-equilibrium assembly approach is utilized in chapter 4 for the assembly of the cysteine/citrate, protein-resistant nanoparticles detailed in chapter 2. However instead of varying vdW attraction through Au and polymer concentrations, the electrostatic repulsion is varied via pH and NaCl in addition to depletion attraction through solvent evaporation. Upon lowering the pH from 7 to 5 at a given salinity, the magnitude of the charge on the primary particles decreased, such that the weaker electrostatic repulsion increased the hydrodynamic diameter, and consequently, NIR extinction of the clusters. At a given pH, as the concentration of NaCl was increased, the NIR extinction decreased monotonically. Furthermore, the greater screening of the charges on the nanoclusters weakened the interactions with PLA(1k)-b-PEG(10k)-b-PLA(1k), and thus lowered the amount of adsorbed polymer on the nanocluster surface. The generalization of the concept of self-assembly of small NIR active nanoclusters to include a strongly bound thiol – capable of resisting GSH exchange - is important for these materials' use as biomedical contrast agents.

In chapter 5, evaporation is removed from the nanocluster process as controlled, electrostatically-driven assembly is shown. Small, 5 nm citrate-capped particles were assembled into branched nanochains with $CaCl_2$ and more spherical nanoparticle clusters with NaCl by tuning the colloidal interactions. The electrostatic repulsion and the interparticle bridging attraction between the cations and citrate ligands were varied by changing the concentration of either Na^+ or Ca^{2+} at pH 7 to form the nanoclusters at various times from 1 to 1800 s. For very dilute Ca^{2+} and thus very thick double layers

around the particles, strong interparticle bridging resulted in small branched chains with lengths as short as 20 nm and strong NIR extinction out to 1100 nm. Furthermore, the bridging produced very small interparticle spacings leading to partial fusion that further increased the NIR extinction.

Lastly, the structure of various nanoparticle clusters will be examined through TEM and SAXS analysis in appendix A. Nanoclusters made from primaries capped with lysine/citrate, cysteine/citrate, and GSH/citrate were studied. As each ligand differs in length and binding affinity for Au, the respective nanocluster structures for each system will be shown to be markedly distinct. Lysine/citrate is shown to grow into more linear chains, while cysteine/citrate are more spherical. GSH/Citrate clusters will show clear interparticle distances due to its long chain length. As a result, the NIR absorbance of the clusters decreases as the ligand length gets longer which is consistent with theory. My undergraduate Sai Gourisankar, who worked closely with me for four years, was responsible for authoring this work and it is published in its entirety in his honors thesis.

1.4 WORK CREDITS

The studies detailed in chapters 2-4 were done in close collaboration with Dr. Avinash Murthy. Experimental design, data collection, and data analysis was completed by both Dr. Murthy and I; however the writing of these chapters was done entirely by Dr. Murthy. These chapters are also published in his doctoral thesis.[117] Appendix A was authored by Sai Gourisankar, an undergraduate who worked closely with me over four years. Again, experimental design, data collection, and data analysis were a combination of both of our efforts, however this part of my thesis was written entirely by Gourisankar. This work is published in full in his honors thesis.[118]

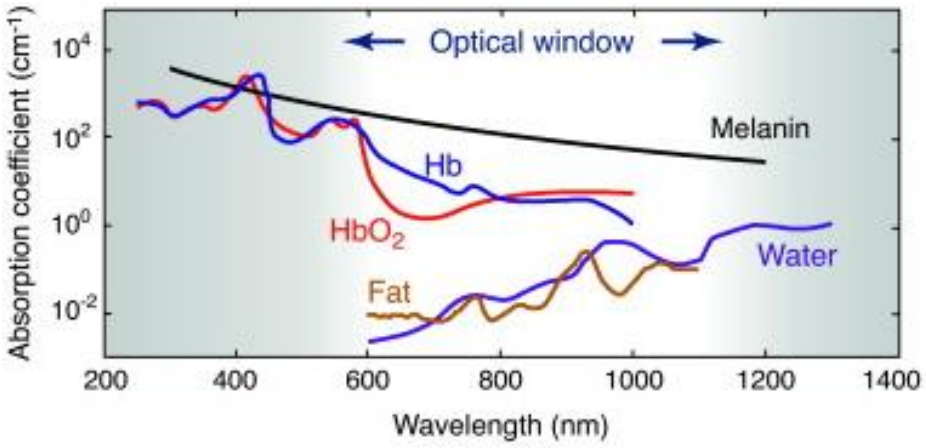

Figure 1.1[18]: Absorption spectra of various biological components showing the NIR optical window.

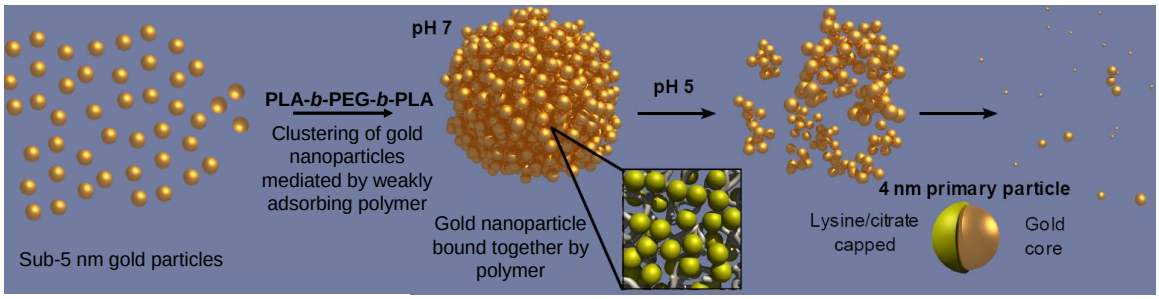

Figure 1.2[3]: Schematic illustrating the formation and partial dissociation of biodegradable gold nanoclusters.

1.5 REFERENCES

1. Guarise, C.; Pasquato, L.; Scrimin, P. Reversible Aggregation/Deaggregation of Gold Nanoparticles Induced by a Cleavable Dithiol Linker. Langmuir 2005, 21, 5537-5541.
2. Tam, J. M.; Murthy, A. K.; Ingram, D. R.; Nguyen, R.; Sokolov, K. V.; Johnston, K. P. Kinetic Assembly of Near-IR Active Gold Nanoclusters Using Weakly Adsorbing Polymers to Control the Size. Langmuir 2010, 26, 8988-8999.
3. Tam, J. M.; Tam, J. O.; Murthy, A.; Ingram, D. R.; Ma, L. L.; Travis, K.; Johnston, K. P.; Sokolov, K. V. Controlled Assembly of Biodegradable Plasmonic Nanoclusters for Near-Infrared Imaging and Therapeutic Applications. ACS Nano 2010, 4, 2178-2184.
4. Xi, C.; Marina, P. F.; Xia, H.; Wang, D. Directed self-assembly of gold nanoparticles into plasmonic chains. Soft Matter 2015, 11, 4562-4571.
5. Romo-Herrera, J. M.; Alvarez-Puebla, R. A.; Liz-Marzan, L. M. Controlled assembly of plasmonic colloidal nanoparticle clusters. Nanoscale 2011, 3, 1304-1315.
6. Huang, X.; Jain, P. K.; El-Sayed, I. H.; El-Sayed, M. A. Gold nanoparticles: interesting optical properties and recent applications in cancer diagnostics and therapy. 2007.
7. Willets, K. A.; Van Duyne, R. P. Localized surface plasmon resonance spectroscopy and sensing. Annu. Rev. Phys. Chem. 2007, 58, 267-297.
8. Larson, T. A.; Bankson, J.; Aaron, J.; Sokolov, K. Hybrid plasmonic magnetic nanoparticles as molecular specific agents for MRI/optical imaging and photothermal therapy of cancer cells. Nanotechnology 2007, 18.
9. Aaron, J.; Nitin, N.; Travis, K.; Kumar, S.; Collier, T.; Park, S. Y.; Jose-Yacaman, M.; Coghlan, L.; Follen, M.; Richards-Kortum, R.; Sokolov, K. Plasmon resonance coupling of metal nanoparticles for molecular imaging of carcinogenesis in vivo. Journal of Biomedical Optics 2007, 12.
10. Sokolov, K.; Follen, M.; Aaron, J.; Pavlova, I.; Malpica, A.; Lotan, R.; Richards-Kortum, R. Real-time vital optical imaging of precancer using anti-epidermal growth factor receptor antibodies conjugated to gold nanoparticles. Cancer Research 2003, 63, 1999-2004.
11. Hirsch, L. R.; Stafford, R. J.; Bankson, J. A.; Sershen, S. R.; Rivera, B.; Price, R. E.; Hazle, J. D.; Halas, N. J.; West, J. L. Nanoshell-mediated near-infrared thermal therapy of tumors under magnetic resonance guidance. Proceedings of the National Academy of Sciences 2003, 100, 13549-13554.
12. Kennedy, L. C.; Bickford, L. R.; Lewinski, N. A.; Coughlin, A. J.; Hu, Y.; Day, E. S.; West, J. L.; Drezek, R. A. A New Era for Cancer Treatment: Gold-Nanoparticle-Mediated Thermal Therapies. Small 2011, 7, 169-183.
13. Loo, C.; Lowery, A.; Halas, N.; West, J.; Drezek, R. Immunotargeted Nanoshells for Integrated Cancer Imaging and Therapy. Nano Letters 2005, 5, 709-711.

14. Copland, J. A.; Eghtedari, M.; Popov, V. L.; Kotov, N.; Mamedova, N.; Motamedi, M.; Oraevsky, A. A. Bioconjugated gold nanoparticles as a molecular based contrast agent: implications for imaging of deep tumors using optoacoustic tomography. Molecular Imaging & Biology 2004, 6, 341-349.
15. Ma, L. L.; Tam, J. O.; Willsey, B. W.; Rigdon, D.; Ramesh, R.; Sokolov, K.; Johnston, K. P. Selective Targeting of Antibody Conjugated Multifunctional Nanoclusters (Nanoroses) to Epidermal Growth Factor Receptors in Cancer Cells. Langmuir 2011, 27, 7681-7690.
16. Ma, L. L.; Feldman, M. D.; Tam, J. M.; Paranjape, A. S.; Cheruki, K. K.; Larson, T. A.; Tam, J. O.; Ingram, D. R.; Paramita, V.; Villard, J. W.; Jenkins, J. T.; Wang, T.; Clarke, G. D.; Asmis, R.; Sokolov, K.; Chandrasekar, B.; Milner, T. E.; Johnston, K. P. Small Multifunctional Nanoclusters (Nanoroses) for Targeted Cellular Imaging and Therapy. ACS Nano 2009, 3, 2686-2696.
17. Luke, G.; Yeager, D.; Emelianov, S. Biomedical Applications of Photoacoustic Imaging with Exogenous Contrast Agents. Ann Biomed Eng 2012, 40, 422-437.
18. Mallidi, S.; Luke, G. P.; Emelianov, S. Photoacoustic imaging in cancer detection, diagnosis, and treatment guidance. Trends in Biotechnology 2011, 29, 213-221.
19. Weissleder, R. A clearer vision for in vivo imaging. Nature Biotechnology 2001, 19, 316-317.
20. Yoon, S. J.; Mallidi, S.; Tam, J. M.; Tam, J. O.; Murthy, A.; Johnston, K. P.; Sokolov, K. V.; Emelianov, S. Y. Utility of biodegradable plasmonic nanoclusters in photoacoustic imaging. Optics Letters 2010, 35, 3751-3753.
21. Spirou, G. M.; Vitkin, I. A.; Wilson, B.; Whelan, W. M.; Henrichs, P. M.; Mehta, K.; Miller, T.; Yee, A.; Meador, J.; Oraevsky, A. A. In Development and testing of an optoacoustic imaging system for monitoring and guiding prostate cancer therapies, Biomedical Optics 2004, 2004; International Society for Optics and Photonics, pp 44-56.
22. Zhang, H. F.; Maslov, K.; Stoica, G.; Wang, L. V. Functional photoacoustic microscopy for high-resolution and noninvasive in vivo imaging. Nature Biotechnology 2006, 24, 848-851.
23. Larin, K. V.; Larina, I. V.; Esenaliev, R. O. Monitoring of tissue coagulation during thermotherapy using optoacoustic technique. Journal of Physics D: Applied Physics 2005, 38, 2645.
24. Khlebtsov, B.; Zharov, V.; Melnikov, A.; Tuchin, V.; Khlebtsov, N. Optical amplification of photothermal therapy with gold nanoparticles and nanoclusters. Nanotechnology 2006, 5167-5179.
25. Wang, S.; Chen, K. J.; Wu, T. H.; Wang, H.; Lin, W. Y.; Ohashi, M.; Chiou, P. Y.; Tseng, H. R. Photothermal effects of supramolecularly assembled gold nanoparticles for the targeted treatment of cancer cells. Angewandte Chemie International Edition 2010, 49, 3777-3781.
26. Halas, N. J.; Lal, S.; Chang, W.-S.; Link, S.; Nordlander, P. Plasmons in Strongly Coupled Metallic Nanostructures. Chemical Reviews 2011, 111, 3913-3961.

27. Link, S.; Mohamed, M. B.; El-Sayed, M. A. Simulation of the Optical Absorption Spectra of Gold Nanorods as a Function of Their Aspect Ratio and the Effect of the Medium Dielectric Constant. Journal of Physical Chemistry B 1999, 103, 3073-3077.
28. Murphy, C. J. S., T.K; Gole, A.M; Orendorff, C.J; Gao, J.; Gou, L.; Hunyadi, S.E; Li, T. Anisotropic Metal Nanoparticles: Synthesis, Assembly, and Optical Applications. Journal of Physical Chemistry B 2005, 109, 13857-13870.
29. Huang, X.; El-Sayed, I. H.; Qian, W.; El-Sayed, M. A. Cancer Cell Imaging and Photothermal Therapy in the Near-Infrared Region by Using Gold Nanorods. Journal of the American Chemical Society 2006, 128, 2115-2120.
30. Gobin, A. M.; Lee, M. H.; Halas, N. J.; James, W. D.; Drezek, R. A.; West, J. L. Near-Infrared Resonant Nanoshells for Combined Optical Imaging and Photothermal Cancer Therapy. Nano Letters 2007, 7, 1929-1934.
31. Chen, J.; Saeki, F.; Wiley, B. J.; Cang, H.; Cobb, M. J.; Li, Z. Y.; Au, L.; Zhang, H.; Kimmey, M. B.; Li, X.; Xia, Y. Gold Nanocages: Bioconjugation and Their Potential Use as Optical Imaging Contrast Agents. Nano Letters 2005, 5, 473-477.
32. Song, K. H.; Kim, C.; Cobley, C. M.; Xia, Y.; Wang, L. V. Near-Infrared Gold Nanocages as a New Class of Tracers for Photoacoustic Sentinel Lymph Node Mapping on a Rat Model. Nano Letters 2009, 9, 183-188.
33. Trigari, S.; Rindi, A.; Margheri, G.; Sottini, S.; Dellepiane, G.; Giorgetti, E. Synthesis and modelling of gold nanostars with tunable morphology and extinction spectrum. Journal of Materials Chemistry 2011, 21, 6531-6540.
34. Choi, H. S.; Liu, W.; Misra, P.; Tanaka, E.; Zimmer, J. P.; Ipe, B. I.; Bawendi, M. G.; Frangioni, J. V. Renal clearance of quantum dots. Nature Biotechnology 2007, 25, 1165-1170.
35. Yu, M.; Zheng, J. Clearance Pathways and Tumor Targeting of Imaging Nanoparticles. ACS Nano 2015.
36. Zhou, C.; Long, M.; Qin, Y.; Sun, X.; Zheng, J. Luminescent Gold Nanoparticles with Efficient Renal Clearance. Angewandte Chemie International Edition 2011, 50, 3168-3172.
37. Zhang, X.-D.; Luo, Z.; Chen, J.; Song, S.; Yuan, X.; Shen, X.; Wang, H.; Sun, Y.; Gao, K.; Zhang, L.; Fan, S.; Leong, D. T.; Guo, M.; Xie, J. Ultrasmall Glutathione-Protected Gold Nanoclusters as Next Generation Radiotherapy Sensitizers with High Tumor Uptake and High Renal Clearance. Scientific Reports 2015, 5, 8669.
38. Balasubramanian, S. K.; Jittiwat, J.; Manikandan, J.; Ong, C.-N.; Liya, E. Y.; Ong, W.-Y. Biodistribution of gold nanoparticles and gene expression changes in the liver and spleen after intravenous administration in rats. Biomaterials 2010, 31, 2034-2042.
39. Khlebtsov, N.; Dykman, L.; Krasnov, Y. M.; Mel'nikov, A. Light absorption by the clusters of colloidal gold and silver particles formed during slow and fast aggregation. Colloid Journal 2000, 62, 765-779.

40. Lassiter, J. B.; Aizpurua, J.; Hernandez, L. I.; Brandl, D. W.; Romero, I.; Lal, S.; Hafner, J. H.; Nordlander, P.; Halas, N. J. Close encounters between two nanoshells. Nano Letters 2008, 8, 1212-1218.
41. Hassan, S. S.; Rechnitz, G. Determination of glutathione and glutathione reductase with a silver sulfide membrane electrode. Analytical Chemistry 1982, 54, 1972-1976.
42. Hong, R.; Han, G.; Fernandez, J. M.; Kim, B.; Forbes, N. S.; Rotello, V. M. Gluathione-Mediated Delivery and Release Using Monolayer Protected Nanoparticle Carriers. Journal of the American Chemical Society 2006, 128, 1078-1079.
43. Lindman, S.; Lynch, I.; Thulin, E.; Nilsson, H.; Dawson, K. A.; Linse, S. Systematic investigation of the thermodynamics of HSA adsorption to N-iso-propylacrylamide/N-tert-butylacrylamide copolymer nanoparticles. Effects of particle size and hydrophobicity. Nano Letters 2007, 7, 914-920.
44. Yang, W.; Zhang, L.; Wang, S.; White, A. D.; Jiang, S. Functionalizable and ultra stable nanoparticles coated with zwitterionic poly(carboxybetaine) in undiluted blood serum. Biomaterials 2009, 30, 5617-5621.
45. Yang, W.; Xue, H.; Li, W.; Zhang, J.; Jiang, S. Pursuing "Zero" Protein Adsorption of Poly(carboxybetaine) from Undiluted Blood Serum and Plasma. Langmuir 2009, 25, 11911-11916.
46. Walkey, C. D.; Olsen, J. B.; Guo, H.; Emili, A.; Chan, W. C. W. Nanoparticle Size and Surface Chemistry Determine Serum Protein Adsorption and Macrophage Uptake. Journal of the American Chemical Society 2012, 134, 2139-2147.
47. Li, L.; Chen, S.; Zheng, J.; Ratner, B. D.; Jiang, S. Protein Adsorption on Oligo(ethylene glycol)-Terminated Alkanethiolate Self-Assembled Monolayers: The Molecular Basis for Nonfouling Behavior. Journal of Physical Chemistry B 2005, 109, 2934-2941.
48. Folkers, J. P.; Laibinis, P. E.; Whitesides, G. M. Self-assembled monolayers of alkanethiols on gold: comparisons of monolayers containing mixtures of short- and long-chain constituents with methyl and hydroxymethyl terminal groups. Langmuir 1992, 8, 1330-1341.
49. Liu, J.; Yu, M.; Ning, X.; Zhou, C.; Yang, S.; Zheng, J. PEGylation and Zwitterionization: Pros and Cons in the Renal Clearance and Tumor Targeting of Near- IR- Emitting Gold Nanoparticles. Angewandte Chemie 2013, 125, 12804-12808.
50. Holmlin, R. E.; Chen, X.; Chapman, R. G.; Takayama, S.; Whitesides, G. M. Zwitterionic SAMs that Resist Nonspecific Adsorption of Protein from Aqueous Buffer. Langmuir 2001, 17, 2841-2850.
51. Moyano, D. F.; Ray, M.; Rotello, V. M. Nanoparticle–protein interactions: Water is the key. MRS Bulletin 2014, 39, 1069-1073.

52. Mahmoudi, M.; Lynch, I.; Ejtehadi, M. R.; Monopoli, M. P.; Bombelli, F. B.; Laurent, S. Protein-Nanoparticle Interactions: Opportunities and Challenges. Chemical Reviews 2011, 111, 5610-5637.
53. Beurer, E.; Venkataraman, N. V.; Sommer, M.; Spencer, N. D. Protein and Nanoparticle Adsorption on Orthogonal, Charge-Density-Versus-Net-Charge Surface-Chemical Gradients. Langmuir 2012, 28, 3159-3166.
54. Brewer, S. H.; Glomm, W. R.; Johnson, M. C.; Knag, M. K.; Franzen, S. Probing BSA Binding to Citrate-Coated Gold Nanoparticles and Surfaces. Langmuir 2005, 21, 9303-9307.
55. Dobrovolskaia, M. A.; Patri, A. K.; Zheng, J.; Clogston, J. D.; Ayub, N.; Aggarwal, P.; Neun, B. W.; Hall, J. B.; McNeil, S. E. Interaction of colloidal gold nanoparticles with human blood: effects on particle size and analysis of plasma protein binding profiles. Nanomedicine 2009, 5, 106-117.
56. De Paoli Lacerda, S. H.; Park, J. J.; Meuse, C.; Pristinski, D.; Becker, M. L.; Karim, A.; Douglas, J. F. Interaction of Gold Nanoparticles with Common Human Blood Proteins. ACS Nano 2010, 4, 365-379.
57. Dominguez-Medina, S.; McDonough, S.; Swanglap, P.; Landes, C. F.; Link, S. In Situ Measurement of Bovine Serum Albumin Interaction with Gold Nanospheres. Langmuir 2012, 28, 9131-9139.
58. Casals, E.; Pfaller, T.; Duschl, A.; Oostingh, G. J.; Puntes, V. Time Evolution of the Nanoparticle Protein Corona. ACS Nano 2010, 4, 3623-3632.
59. Vinluan III, R. D.; Liu, J.; Zhou, C.; Yu, M.; Yang, S.; Kumar, A.; Sun, S.; Dean, A.; Sun, X.; Zheng, J. Glutathione-coated luminescent gold nanoparticles: a surface ligand for minimizing serum protein adsorption. ACS Appl. Mater. Interfaces 2014, 6, 11829-11833.
60. Verma, A.; Uzun, O.; Hu, Y.; Hu, Y.; Han, H.-S.; Watson, N.; Chen, S.; Irvine, D. J.; Stellacci, F. Surface-structure-regulated cell-membrane penetration by monolayer-protected nanoparticles. Nature Materials 2008, 7, 588-595.
61. Chen, S.; Yu, F.; Yu, Q.; He, Y.; Jiang, S. Strong Resistance of a Thin Crystalline Layer of Balanced Charged Groups to Protein Adsorption. Langmuir 2006, 22, 8186-8191.
62. Chen, S.; Zhen, J.; Li, L.; Jiang, S. Strong Resistance of Phosphorylcholine Self-Assembled Monolayers to Protein Adsorption: Insights into Nonfouling Properties of Zwitterionic Materials. Journal of the American Chemical Society 2005, 127, 14473-14478.
63. Yu, M.; Zhou, C.; Liu, J.; Hankins, J. D.; Zheng, J. Luminescent Gold Nanoparticles with pH-Dependent Membrane Adsorption. Journal of the American Chemical Society 2011, 133, 11014-11017.
64. Liu, X. S.; Huang, H. Y.; Jin, Q.; Ji, J. Mixed Charged Zwitterionic Self-Assembled Monolayers as a Facile Way to Stabilize Large Gold Nanoparticles. Langmuir 2011, 27, 5242-5251.
65. Kaufman, E. D.; Belyea, J.; Johnson, M. C.; Nicholson, Z. M.; Ricks, J. L.; Shah, P. K.; Bayless, M.; Pettersson, T.; Feldoto, Z.; Blomberg, E.; Claesson, P.;

Franzen, S. Probing Protein Adsorption onto Mercaptoundecanoic Acid Stabilized Gold Nanoparticles and Surfaces by Quartz Crystal Microbalance and Z-Potential Measurements. Langmuir 2007, 23, 6053-6062.
66. Röcker, C.; Pötzl, M.; Zhang, F.; Parak, W. J.; Nienhaus, G. U. A quantitative fluorescence study of protein monolayer formation on colloidal nanoparticles. Nature Nanotechnology 2009, 4, 577-580.
67. Jia, G.; Cao, Z.; Xue, H.; Xu, Y.; Jiang, S. Novel Zwitterionic-Polymer-Coated Silica Nanoparticles. Langmuir 2009, 25, 3196-3199.
68. Moyano, D. F.; Saha, K.; Prakash, G.; Yan, B.; Kong, H.; Yazdani, M.; Rotello, V. M. Fabrication of corona-free nanoparticles with tunable hydrophobicity. ACS Nano 2014, 8, 6748-6755.
69. Lin, S.-Y.; Tsai, Y.-T.; Chen, C.-C.; Lin, C.-M.; Chen, C.-h. Two-step functionalization of neutral and positively charged thiols onto citrate-stabilized Au nanoparticles. The Journal of Physical Chemistry B 2004, 108, 2134-2139.
70. Hill, H. D.; Millstone, J. E.; Banholzer, M. J.; Mirkin, C. A. The role radius of curvature plays in thiolated oligonucleotide loading on gold nanoparticles. ACS Nano 2009, 3, 418-424.
71. Templeton, A. C.; Wuelfing, W. P.; Murray, R. W. Monolayer-protected cluster molecules. Accounts of Chemical Research 2000, 33, 27-36.
72. Duncan, B.; Kim, C.; Rotello, V. M. Gold nanoparticle platforms as drug and biomacromolecule delivery systems. Journal of Controlled Release 2010, 148, 122-127.
73. Lu, Z.; Yin, Y. Colloidal nanoparticle clusters: functional materials by design. Chemical Society Reviews 2012, 41, 6874-6887.
74. Guerrini, L.; McKenzie, F.; Wark, A. W.; Faulds, K.; Graham, D. Tuning the interparticle distance in nanoparticle assemblies in suspension via DNA-triplex formation: correlation between plasmonic and surface-enhanced Raman scattering responses. Chemical Science 2012, 3, 2262-2269.
75. Srivastava, S.; Frankamp, B. L.; Rotello, V. M. Controlled Plasmon Resonance of Gold Nanoparticles Self-Assembled with PAMAM Dendrimers. Chemistry of Materials 2005, 17, 487-490.
76. Ofir, Y. S., B.; Rotello, V.M. Polymer and biopolymer mediated self-assembly of gold nanoparticles. Chemical Society Reviews 2008, 37, 1814-1825.
77. Pruneanu, S.; Olenic, L.; Farha Al-Said, S.; Borodi, G.; Houlton, A.; Horrocks, B. Template and template-free preparation of one-dimensional metallic nanostructures. Journal of Materials Science 2010, 45, 3151-3159.
78. Lubitz, I.; Kotlyar, A. G4-DNA-Coated Gold Nanoparticles: Synthesis and Assembly. Bioconjugate Chemistry 2011, 22, 2043-2047.
79. Grzelczak, M.; Vermant, J.; Furst, E. M.; Liz-Marzán, L. M. Directed Self-Assembly of Nanoparticles. ACS Nano 2010, 4, 3591-3605.
80. Zhao, Y.; Xu, L.; Liz-Marzán, L. M.; Kuang, H.; Ma, W.; Asenjo-García, A.; García de Abajo, F. J.; Kotov, N. A.; Wang, L.; Xu, C. Alternating plasmonic

nanoparticle heterochains made by polymerase chain reaction and their optical properties. The Journal of Physical Chemistry Letters 2013, 4, 641-647.
81. Aaron, J.; Travis, K.; Harrison, N.; Sokolov, K. Dynamic Imaging of Molecular Assemblies in Live Cells Based on Nanoparticle Plasmon Resonance Coupling. Nano Letters 2009, 9, 3612-3618.
82. Meyer, M.; Le Ru, E. C.; Etchegoin, P. G. Self-Limiting Aggregation Leads to Long-Lived Metastable Clusters in Colloidal Solutions. The Journal of Physical Chemistry B 2006, 110, 6040-6047.
83. Wang, X.; Li, G.; Chen, T.; Yang, M.; Zhang, Z.; Wu, T.; Chen, H. Polymer-Encapsulated Gold-Nanoparticle Dimers: Facile Preparation and Catalytical Application in Guided Growth of Dimeric ZnO-Nanowires. Nano Letters 2008, 8, 2643-2647.
84. Han, X.; Goebl, J.; Lu, Z.; Yin, Y. Role of Salt in the Spontaneous Assembly of Charged Gold Nanoparticles in Ethanol. Langmuir 2011, 27, 5282-5289.
85. Lim, I. I. S.; Ip, W.; Crew, E.; Njoki, P. N.; Mott, D.; Zhong, C.-J.; Pan, Y.; Zhou, S. Homocysteine-Mediated Reactivity and Assembly of Gold Nanoparticles. Langmuir 2007, 23, 826-833.
86. Sistach, S.; Rahme, K.; Pérignon, N.; Marty, J.-D.; Viguerie, N. L.-d.; Gauffre, F.; Mingotaud, C. Bolaamphiphile surfactants as nanoparticle stabilizers: application to reversible aggregation of gold nanoparticles. Chemistry of Materials 2008, 20, 1221-1223.
87. Liu, Y.; Han, X.; He, L.; Yin, Y. Thermoresponsive assembly of charged gold nanoparticles and their reversible tuning of plasmon coupling. Angewandte Chemie International Edition 2012, 51, 6373-6377.
88. Xia, H.; Su, G.; Wang, D. Size- Dependent Electrostatic Chain Growth of pH-Sensitive Hairy Nanoparticles. Angewandte Chemie International Edition 2013, 52, 3726-3730.
89. Ah, C. S.; Kim, W.-J.; Yun, W. S.; Joo, S.-W. Colorimetric quantitative sensing of alkali metal ions based on reversible assembly and disassembly of gold nanoparticles. Current Applied Physics 2013, 13, 1889-1893.
90. Li, N.; Yu, L.; Zou, J. Critical Coagulation Concentration–Based Salt Titration for Visual Quantification in Gold Nanoparticle–Based Colorimetric Biosensors. Journal of laboratory automation 2013, 2211068213498240.
91. Semyonov, S. A. A study of electrolytic coagulation of gold sols by the method of localized surface plasmon resonance spectroscopy. Colloid Journal 2013, 75, 421-426.
92. Enustun, B. V.; Turkevich, J. Coagulation of Colloidal Gold. Journal of the American Chemical Society 1963, 85, 3317-3328.
93. Zhang, H.; Wang, D. Controlling the Growth of Charged-Nanoparticle Chains through Interparticle Electrostatic Repulsion. Angewandte Chemie 2008, 120, 4048-4051.

94. Wang, T.; LaMontagne, D.; Lynch, J.; Zhuang, J.; Cao, Y. C. Colloidal superparticles from nanoparticle assembly. Chemical Society Reviews 2013, 42, 2804-2823.
95. Xia, Y. S.; Nguyen, T. D.; Yang, M.; Lee, B.; Santos, A.; Podsiadlo, P.; Tang, Z. Y.; Glotzer, S. C.; Kotov, N. A. Self-assembly of self-limiting monodisperse supraparticles from polydisperse nanoparticles. Nature Nanotechnology 2011, 6, 580-587.
96. Larson-Smith, K.; Pozzo, D. C. Competitive Adsorption of Thiolated Poly(ethylene glycol) and Alkane-Thiols on Gold Nanoparticles and Its Effect on Cluster Formation. Langmuir 2012, 28, 13157-13165.
97. Larson-Smith, K.; Pozzo, D. C. Scalable synthesis of self-assembling nanoparticle clusters based on controlled steric interactions. Soft Matter 2011, 7, 5339-5347.
98. Yang, M.; Chen, G.; Zhao, Y.; Silber, G.; Wang, Y.; Xing, S.; Han, Y.; Chen, H. Mechanistic investigation into the spontaneous linear assembly of gold nanospheres. Physical Chemistry Chemical Physics 2010, 12, 11850-11860.
99. Sedgwick, H.; Egelhaaf, S. U.; Poon, W. C. K. Clusters and gels in systems of sticky particles. Journal of Physics-Condensed Matter 2004, 16, S4913-S4922.
100. Buitenhuis, J.; Dhont, J. K. G.; Lekkerkerker, H. N. W. Static and Dynamic Light Scattering by Concentrated Colloidal Suspensions of Polydisperse Sterically Stabilized Boehmite Rods. Macromolecules 1994, 27, 7267-7277.
101. Groenewold, J.; Kegel, W. K. Colloidal cluster phases, gelation and nuclear matter. Journal of Physics-Condensed Matter 2004, 16, S4877-S4886.
102. Groenewold, J.; Kegel, W. K. Anomalously Large Equilibrium Clusters of Colloids. Journal of Physical Chemistry B 2001, 105, 11702-11709.
103. Johnston, K. P.; Maynard, J. A.; Truskett, T. M.; Borwankar, A. U.; Miller, M. A.; Wilson, B. K.; Dinin, A. K.; Khan, T. A.; Kaczorowski, K. J. Concentrated Dispersion of Equilibrium Protein Nanoclusters That Reversibly Dissociate Into Active Monomers. ACS Nano 2012, 6, 1357-1369.
104. Hiemenz, P. C.; Rajagopalan, R. Principles of Colloid and Surface Chemistry, revised and expanded; CRC press1997; Vol. 14.
105. Si, S.; Mandal, T. K. pH-controlled reversible assembly of peptide-functionalized gold nanoparticles. Langmuir 2007, 23, 190-195.
106. Nabika, H.; Oikawa, T.; Iwasaki, K.; Murakoshi, K.; Unoura, K. Dynamics of gold nanoparticle assembly and disassembly induced by pH oscillations. The Journal of Physical Chemistry C 2012, 116, 6153-6158.
107. Chen, Y.; Mao, C. pH- Induced Reversible Expansion/Contraction of Gold Nanoparticle Aggregates. Small 2008, 4, 2191-2194.
108. Tan, J.; Liu, R.; Wang, W.; Liu, W.; Tian, Y.; Wu, M.; Huang, Y. Controllable aggregation and reversible pH sensitivity of AuNPs regulated by carboxymethyl cellulose. Langmuir 2009, 26, 2093-2098.
109. Guo, Y. M., Y.; Xu, L.; Li, J.; Yang, W. Conformational Change Induced Reversible Assembly/Disassembly of Poly-L-lysine-Functionalized Gold Nanoparticles. Journal of Physical Chemistry C 2007, 111, 9172-9176.

110. Khlebtsov, B. N.; Khanadeyev, V. A.; Ye, J.; Mackowski, D. W.; Borghs, G.; Khlebtsov, N. G. Coupled plasmon resonances in monolayers of metal nanoparticles and nanoshells. Physical Review B 2008, 77, 035440.
111. Park, J.-W.; Shumaker-Parry, J. S. Strong Resistance of Citrate Anions on Metal Nanoparticles to Desorption under Thiol Functionalization. ACS Nano 2015, 9, 1665-1682.
112. Park, J.-W.; Shumaker-Parry, J. S. Structural study of citrate layers on gold nanoparticles: role of intermolecular interactions in stabilizing nanoparticles. Journal of the American Chemical Society 2014, 136, 1907-1921.
113. Horovitz, O.; Mocanu, A.; Tomoaia, G.; Bobos, L.; Dubert, D.; Daian, I.; Yusanis, T.; Tomoaia-Cotisel, M. Lysine Mediated Assembly of Gold Nanoparticles. Studia Universitatis Babes-Bolyai Chemia 2007, 52.
114. Zakaria, H. M.; Shah, A.; Konieczny, M.; Hoffmann, J. A.; Nijdam, A. J.; Reeves, M. Small molecule-and amino acid-induced aggregation of gold nanoparticles. Langmuir 2013, 29, 7661-7673.
115. Li, W.-C.; Lee, S.-W. The characteristics of lysine-mediated self-assembly of gold nanoparticles on the ITO glass. Current Applied Physics 2012, 12, 1361-1365.
116. Lee, J.; Zhou, H.; Lee, J. Small molecule induced self-assembly of Au nanoparticles. Journal of Materials Chemistry 2011, 21, 16935-16942.
117. Murthy, A. K. Surface design and controlled assembly of gold nanoparticles into biodegradable nanoclusters for biomedical imaging applications. Ph.D., University of Texas at Austin, 2013.
118. Gourisankar, S. Structure and Assembly of Gold Nanoclusters for Biomedical Imaging Applications. B.S., University of Texas at Austin, 2015.

Chapter 2: Charged Gold Nanoparticles with Essentially Zero Serum Protein Adsorption in Undiluted Fetal Bovine Serum[1]

The adsorption of even a single serum protein molecule on a gold nanosphere used in biomedical imaging may increase the size too much for renal clearance. Herein, we design charged ~5 nm Au nanospheres coated with binary mixed charge ligand monolayers that do not change in size upon incubation in pure fetal bovine serum (FBS). This lack of protein adsorption is unexpected given the Au surface is moderately charged. The mixed charge monolayers are comprised of anionic citrate ligands modified by place exchange with naturally-occurring amino acids: either cationic lysine or zwitterionic cysteine ligands. The zwitterionic tips of either the lysine or cysteine ligands interact weakly with the proteins and furthermore increase the distance between the "buried" charges closer to the Au surface and the interacting sites on the protein surface. The ~5 nm nanospheres were assembled into ~20 nm diameter nanoclusters with strong NIR absorbance (of interest in biomedical imaging and therapy) with a biodegradable polymer, PLA(1k)-*b*-PEG(10k)-*b*-PLA(1k). Upon biodegradation of the polymer in acidic solution, the nanoclusters dissociated into primary ~5 nm Au nanospheres, which also did not adsorb any detectable serum protein in undiluted FBS.

[1] Large parts of this chapter have been published as: Murthy, A.K.; Stover, R.J.; Hardin, W.G.; Schramm, R.; Nie, G.D.; Gourisankar, S.; Truskett, T.M.; Sokolov, K.V.; Johnston, K.P., Charged Gold Nanoparticles with Essentially Zero Serum Protein Adsorption in Undiluted Fetal Bovine Serum. *Journal of the American Chemical Society* **2013**, *135,* 7799-7802.

2.1 INTRODUCTION

For Au nanoparticles of interest in biomedical imaging, the hydrodynamic diameter (D_h) must be less than ~6 nm for efficient renal clearance.[1, 2] As these nanoparticles are exposed to blood, the adsorption of even a single protein molecule on their surface, particularly the highly prevalent serum albumin (D_h = ~ 7 nm),[3, 4] may increase the size too much for clearance. The adsorption of serum proteins on flat surfaces[5-9] and curved nanoparticles[10-14] coated with nonionic, zwitterionic, or charged ligands depends in a complex manner on the ligand orientation on the surface, charge, and hydrophobicity.[15-17] Remarkably, precisely defined experiments to study renal clearance indicated that protein adsorption from 10% fetal bovine serum (FBS) was fully prevented for neutral (PEG) or zwitterionic (cysteine) ligands, but was high for charged anionic and cationic ligands such as dihydrolipoic acid (DHLA) and cysteamine, respectively.[1] In numerous other studies, serum protein adsorption has been found to be relatively low on zwitterionic and nonionic surface coatings with zero net charge.[1, 7, 11, 13, 18-21] For example, zwitterionic peptide ligands on flat Au surfaces synthesized from equal amounts of lysine (q = +1) and glutamic acid (q = -1) were shown to adsorb minimal amounts (< 0.3 ng protein/cm^2) of the model serum proteins lysozyme and fibrinogen.[8] Similar low adsorption levels of these proteins were found for flat Au surfaces tailored with binary ligands with equal amounts of positive and negative charges.[5, 6] The close spacings between the positive and negative charges on single zwitterionic ligands favor hydration and essentially zero protein adsorption on nanoparticles, as measured by dynamic light scattering (DLS).[11, 22]

For Au nanoparticles coated with charged ligands, electrostatic interactions, as well as charge-dipole interactions and specific interactions with hydrogen bond donor and acceptor sites raise adsorption, relative to nonionic and zwitterionic ligands.[1, 5, 23, 24]

However, the roles of net charge and the topology of charge on the Au and protein surfaces on adsorption are not well understood. For nanoparticles coated with highly charged citrate, DHLA, or cysteamine ligands, adsorption of serum proteins has been found to increase the D_h significantly, on the order of 10 nm.[1, 25, 26] For highly anionic citrate-capped Au nanoparticles with zeta potentials (ζ) of ~-40 mV, the D_h grew from 30 to ~80 nm upon incubation in undiluted human plasma.[25] Interestingly, very small ~3 nm highly charged Au nanospheres coated with glutathione (GSH), with two negative and one positive charge at neutral pH, were shown to clear efficiently through the kidneys.[2] While very low adsorption is typically measured with techniques such as gel electrophoresis,[27, 28] surface plasmon resonance sensing,[6, 29] and quartz crystal microbalance analysis,[30] these techniques do not have the sensitivity to measure the adsorption at the single protein molecule level, as can be done by DLS[2, 10, 11, 22] or gel filtration chromatography.[1]

Although charged monolayers on nanoparticles composed of single ligands are not thought to resist protein adsorption,[1, 25, 26, 31] relatively little is known about the behavior for binary and multicomponent mixed charge monolayers. For binary zwitterionic mixtures with equal amounts of cationic and anionic ligands, adsorption is very low.[5, 6, 8, 29] However, mixed monolayers of charged ligands, such as peptides on Au composed of lysine and glutamic acid, bind significant amounts of proteins (> 50 ng/cm^2) such as fibrinogen and lysozyme when the lysine to glutamic acid ratio deviates from unity and the surface becomes charged.[8] Verma *et al.,* however, reported that Au nanospheres with ordered "stripes" of anionic mercaptoundecanesulfonate (MUS) and nonionic octanethiol (OT) adsorbed nearly zero serum protein upon incubation in 10% serum, as shown by a negligible change in D_h via DLS, despite a highly negative ζ of ~-35 mV.[10] Here, the inhibition of protein adsorption was attributed to the close proximities

(~5 Å) of hydrophobic and hydrophilic groups on the nanosphere surface.[10, 32] However, Yang *et al.* have demonstrated that Au nanoparticles and flat Au surfaces which do not adsorb protein in 10% human blood serum may adsorb significant amounts of protein in 100% serum.[7, 11] Novel concepts are required to determine if it is possible to form charged mixed monolayers for essentially zero protein adsorption, even in undiluted serum.

Herein, we design charged ~ 5 nm Au nanospheres that adsorb essentially zero protein from undiluted fetal bovine serum, as shown by a negligible increase in the D_h by dynamic light scattering. The charged surfaces were tailored with binary ligand monolayers composed of two naturally occurring, relatively hydrophilic ligands, citrate (q = -3) and either cationic lysine (q = +1) or zwitterionic cysteine (q = 0). The Au surface charge was tuned by place exchange of the citrate ligands with each amino acid, as characterized by the zeta potential and X-ray photoelectron spectroscopy (XPS). Relatively hydrophilic ligands were used to attempt to limit hydrophobic interactions that may increase adsorption.[12, 23, 33] For pure citrate or highly charged mixed charge monolayers with high citrate levels, the D_h increased ~3 nm or more with protein adsorption. However, the change in D_h was negligible for lower citrate fractions, even for a moderate ζ of -22 mV in undiluted fetal bovine serum. The zwitterionic tips of the lysine and cysteine ligands interact weakly with the protein and, furthermore, mitigate the interactions of the "buried" charges on the anchor groups at the Au surface. Upon assembly of the Au nanospheres into ~20 nm nanoclusters of closely spaced primary particles, following an earlier methodology,[34-36] they exhibited intense NIR extinction that is of interest in biomedical applications including photoacoustic imaging.[37] Upon biodegradation of PLA(1k)-*b*-PEG(10k)-*b*-PLA(1k) on the surface of the nanoclusters,

they dissociated into the original ~5 nm constituent nanospheres, which will now be shown to totally resist adsorption of serum proteins.

2.2 EXPERIMENTAL

2.2.1 Materials

$HAuCl_4 \cdot 3H_2O$ was purchased from MP Biomedicals LLC (Solon, OH), and $Na_3C_3H_5O(COO)_3 \cdot 2H_2O$ as well as $NaBH_4$ were obtained from Fisher Scientific (Fair Lawn, NJ). L-(+)-lysine and cysteine were acquired from Acros Chemicals (Morris Plains, NJ), and PLA(1k)-*b*-PEG(10k)-*b*-PLA(1k) was purchased from Sigma-Aldrich (St. Louis, MO). Fetal bovine serum was obtained from Hyclone (Logan, UT).

2.2.2 Synthesis of Citrate-Capped Primary Au Nanospheres

Citrate-coated gold nanoparticles were synthesized by adapting a method described previously.[34] Briefly, 3 L of deionized water was heated to ~97 °C. Aqueous solutions of 1% $HAuCl_4 \cdot 3H_2O$, 1% $Na_3C_3H_5O(COO)_3 \cdot 2H_2O$, and 0.075% $NaBH_4$ in 1% $Na_3C_3H_5O(COO)_3 \cdot 2H_2O$ were prepared, and 30 mL of each solution was added successively in 1 min intervals while the solution was vigorously stirred. The gold nanoparticle solution was allowed to cool to room temperature and then was centrifuged in 250 mL centrifuge tubes at 10000 rpm for 10 min at 4 °C in order to remove ~100 ml of the 3 L solution as large particles. The remaining supernatant (~0.02 mg Au/ml) was then passed through a tangential flow filtration (TFF) device (Krosflo Research II, Spectrum Labs, Rancho Domingo, CA) using a polystyrene filter with a pore size of 10 kDa and filter surface area of 1050 cm^2 in order to remove water and excess reaction reagents. The TFF process concentrated the gold solution to a concentration of ~1

mg/ml. 15 mL centrifugal filter devices with a 30000 Da MW cutoff (Ultracel YM-30, Millipore Co., Billerica, MA) were used to additionally concentrate gold particles by centrifuging the gold solution at 6000 rpm for 5 min to remove water through the filter. The concentration of the aqueous citrate-capped gold nanoparticle dispersion was then adjusted with DI water to 3.0 ± 0.1 mg/ml Au, as measured by FAAS.

2.2.3 Place exchange with lysine and cysteine ligands

The lysine place exchange of ligands was carried out by adding freshly prepared aqueous solutions of lysine (1% or 5% w/v) to dispersions of citrate-capped Au nanospheres at ambient temperature. The initial amount of citrate coated on the Au nanospheres was ~4% w/w citrate, measured by thermogravimetric analysis (TGA), as described below. Given an Au concentration of 3 mg/ml, measured by FAAS, the citrate concentration was thus ~0.12 mg/ml. For a 4.5/1 lysine/citrate feed ratio, 50 µl of freshly prepared 1% (w/v) lysine was added to 1.2 ml of a ~3 mg/ml citrate-capped gold nanoparticle dispersion to form nanospheres. Here the addition of the basic lysine ligand increased the pH of the citrate-capped Au nanoparticle dispersion to pH ~8.3. For a lysine/citrate feed ratio of 9/1, 20 µl of 50 mg/ml (5%) aqueous lysine was added to 1.2 ml of a ~3 mg/ml citrate-capped gold nanoparticle solution. Here the pH of the dispersion increased from pH ~7 to pH ~8.8 upon adding the basic lysine ligand. Place exchange reactions were also performed with cysteine ligands using a 1% (w/v) solution of cysteine. For the 0.3/1 cysteine/citrate ratio, 1.4 µl of aqueous cysteine was added to 0.6 ml of a ~3 mg/ml citrate-capped Au nanosphere dispersion, and for the 0.7/1 cysteine/citrate feed ratio, 3.2 µl of 1% cysteine was added to 0.6 ml of the citrate-capped Au nanosphere dispersion. In each ligand exchange reaction, the mixtures were stirred for

15 min at room temperature. Immediately after reaction, aliquots of the samples were diluted in DI water to a concentration of ~0.02-0.04 mg/ml and analyzed by dynamic light scattering (DLS) and zeta potential (ζ) analysis. The undiluted mixtures not used for DLS and ζ analysis were used to form nanoclusters as described below.

2.2.4 Nanosphere Characterization

After place exchange, nanospheres were analyzed by dynamic light scattering (DLS), ζ analysis, and thermogravimetric analysis (TGA), X-ray photoelectron spectroscopy (XPS) and UV-Vis-NIR spectroscopy. DLS measurements were taken at a scattering angle of 45° using an avalanche photodiode at ~25 °C. DLS sample concentrations were adjusted such that the measured count rate was between 100 and 300 kcps. Data were analyzed using a digital autocorrelator (Brookhaven BI-9000AT) and the CONTIN method. The Stokes-Einstein equation was then used in order to obtain a volume-weighted distribution of particle hydrodynamic diameters (D_h). For lysine/citrate nanospheres, the average of 3 separate samples is reported (as shown in Tables B.4-B.7), whereas for cysteine/citrate nanospheres, the average of 2 separate samples is reported (Tables B.4-B.7). As a control experiment, DLS was conducted on pure FBS without any added Au nanospheres. The average D_h of pure FBS was 8.6 ± 5.2 nm, as shown in Figure B.3. Here, the average DLS count rate was 39 ± 6 kcps, substantially lower than the average count rate with added nanospheres (1.4 lysine citrate) of 257 ± 2 kcps. Thus, the vast majority of scattering for DLS comes from Au nanospheres, and we conclude that the DLS D_h distributions primarily reflect the sizes of Au nanospheres. As a result, we do not separately consider the different refractive indices and absorbance of the proteins and nanoparticles in the calculation of DLS volume-weighted D_h distributions.

Additionally, for 1.4 lysine/citrate and 1.6 cysteine/citrate nanospheres, the extremely small (~3% by volume) portion of the size distribution ~10 nm in size (Tables B.8 and B.9) may be attributed to the above scattering from the free protein, as this size agrees with the D_h distribution of pure FBS (Figure B.3). Due to the fact that Au nanospheres scatter 6 times more intensely than free proteins (as shown by count rate measurements), the free proteins in FBS provide only a small perturbation in the overall size distributions in the 5 to 10 nm range. The dynamic light scattering technique is particularly effective for particles smaller than 10 nm where the adsorption of a single protein molecule produces a significant change in hydrodynamic diameter. Future studies would be warranted with larger particle diameters and with other experimental techniques to determine the role of Au particle diameter and curvature.

ζ analysis was performed using a Brookhaven ZetaPALS zeta potential analyzer, and the average and standard deviations of at least three measurements were reported. For lysine/citrate nanospheres, the average for 3 separate samples is reported in Table 3.1, whereas for cysteine/citrate nanospheres, the average of 2 separate samples is reported. Nanosphere samples were ultracentrifuged for 45 min at 45000 rpm in order to remove excess citrate and lysine ligands, and the resulting pellet was dried for XPS analysis. UV-vis-NIR extinction spectra were measured with a Varian Cary 3E spectrophotometer with a path length of 1 cm.

XPS was performed with a Kratos AXIS Ultra DLD spectrometer with a monochromatic Al X-ray source (Al α, 1.4866 eV). Elemental analysis was performed on the Au 4f, C 1s, N 1s, and O 1s regions with pass energies of 30 eV, 20 eV, 40 eV, and 20 eV, respectively. A 0.1 eV step and a 4 s dwell time was used in all cases. Charge compensation was not used due to the conductivity of the samples. Peak positions and

areas were calculated using a Gaussian + Lorentzian fit and a Shirley background correction.

2.2.5 Centrifugation to Support DLS Measurements

Centrifugation of mixed monolayer nanosphere samples was performed after incubating samples in either 100% FBS or DI water. In a typical experiment, 50 ul of 3 mg/ml Au nanosphere solution was incubated in 5 ml of either pure FBS or DI water for 4 h at 37 °C. Samples were then centrifuged at 10000 rpm for 15 min in an Eppendorf 5810R centrifuge in order to form a nanosphere pellet. The mass of Au in the pellet was then determined from FAAS in order to calculate the Au mass yield of each sample.

2.2.6 Nanocluster Formation

Immediately after 15 min of lysine place exchange, clusters of nanoparticles were formed with a procedure modified from our previous work.[34-36] An aqueous 120 mg/ml solution of PLA(1k)-b-PEG(10k)-PLA(1k) was initially prepared. The 3 mg/ml lysine/citrate capped gold nanoparticle dispersion was diluted to 0.5 mg/ml with deionized water. 250 µl of the PLA(1k)-b-PEG(10k)-b-PLA(1k) solution was then added to 3 ml of the nanosphere dispersion in 5 iterations of 50 µl each over 10 min under vigorous stirring. After 10 min, this mixture was placed in a 19 x 48 mm glass vial, and the vial was placed in a 40 °C water bath and stirred using a magnetic stirrer. Using a small tube inserted into the vial, dried air was blown gently over the sample. The combination of water bath and airflow kept the sample temperature at 25 ± 3 °C, and the sample was evaporated to 50% of its original volume over ~40 min. After sample evaporation, cluster formation was terminated by adding 30 ml of DI water to the sample.

The solution was then centrifuged at 10000 rpm for 10 min in order to separate unclustered and loosely-clustered particles from the dense gold nanoclusters.

2.2.7 Nanocluster Characterization

The morphology of nanoclusters was observed by transmission electron microscopy (TEM) performed on a FEI TECNAI G2 F20 X-TWIN TEM using a high-angle annular dark-field detector. Samples were prepared by dipping 200 mesh copper-coated carbon TEM grids (Electron Microscopy Sciences) into liquid nitrogen and then pipetting 5 µl of a dilute NC dispersion onto the grid. The grid was then dried using a VirTis AdVantage tray lyophilizer (VirTis, Gardiner, NY). Unless noted, the characterization techniques were the same as for the nanospheres. The scattering angle for DLS was 90°. Flame atomic absorption spectroscopy (FAAS) (GBC Scientific Equipment Pty Ltd., GBC 908AA) was used to determined Au concentrations of primary citrate-capped nanoparticles as well as gold nanoclusters. Measurements were conducted at 242.8 nm using an air-acetylene flame on samples diluted in aqua regia to between 1 ppm and 5 ppm of gold.

2.2.8 Nanocluster Dissociation and Characterization

After nanocluster formation, nanocluster dissociation was monitored by adding ~100 µl of ~1 mg/ml nanocluster dispersion to 2 mL of pH 5 HCl to degrade the polymer. Addition of the nanocluster dispersion did not change the pH of the HCl solution from pH 5. After incubation in pH 5 HCl for 48 h, nanoclusters dissociated to primary Au nanospheres, and these dissociated nanoclusters were characterized by UV-Vis-NIR spectroscopy and DLS. For DLS, the scattering angle was 45°.

2.2.9 Protein Adsorption Studies

Mixed monolayer-capped nanospheres, as well as dissociated nanoclusters, were incubated in 100% fetal bovine serum (FBS) at a concentration of ~0.03 mg/ml Au at 37 °C in a water bath for 4 h and subsequently characterized by DLS at a scattering angle of 45°.

2.3 Results and Discussion

In order to form the binary mixed charge monolayers on the surface of ~5 nm Au nanospheres, citrate-capped nanospheres were first synthesized and place exchange reactions were conducted with either lysine or cysteine ligands (schematically depicted in Figures 2.1a and 2.1b). In order to determine the final ligand ratio on the nanosphere surface, excess ligands were removed by ultracentrifugation, and XPS was conducted on the dried nanosphere pellet, as described in detail in the supplemental section. For lysine/citrate molar feed ratios from 4.5 to 9, place exchange led to final ligand ratios of 0.5 to 1.4 according to XPS (Table 2.1, Figure B.1). The initial D_h value of 4.3 ± 0.8 nm (Table 2.1) increased only slightly for both lysine/citrate ratios after place exchange (Table 2.1, Figure 2.1c). This result is expected given the very small difference in the size of these two ligands relative to the diameter of the Au core. The increase in the amount of lysine from lysine/citrate ratios of 0.5 to 1.4 raised the ζ to -28.9 ± 3.9 mV and -16.1 ± 2.9 mV, compared with a strongly negative value of -58.4 ± 5.3 mV for pure citrate (Table 2.1). The ratios of each of these zeta potentials relative to that of citrate were 49 and 28% in good agreement of estimated ratios of 56 and 22%, respectively, from the number of charges on the ligands and known ratio from XPS. (Table B.1, see Appendix B for calculations and for reproducibilities in D_h and ζ, Tables B.4-B.7) incubation. For the place exchange of citrate with zwitterionic cysteine, smaller feed ratios were used than

for lysine, given the stronger binding of the thiol group on cysteine to Au relative to the amino group on lysine. Again the increase in D_h was negligible (Table 2.1, Figure 2.1d). The final cysteine/citrate ligand ratios, as determined by XPS, were 1.0 and 1.6 for feed ratios of 0.3 and 0.7, respectively. (Table 2.1, Figure B.1), and the ζ values were -28.8 ± 3.2 mV to -21.6 ± 1.7 mV. The corresponding zeta potential ratios of 49 and 37% relative to pure citrate-coated nanospheres were in good agreement with the calculated ratios of 49 and 39%, respectively, from the stoichiometries *via* XPS (Table B.1).

The resistance of the charged mixed monolayer nanospheres to serum protein adsorption was evaluated in 100% fetal bovine serum (FBS). Here, even adsorption of a single 7 nm BSA or 14 nm immunoglobulin G molecule,[4] would produce a substantial change in D_h. The adsorption of one BSA molecule would correspond to ~ 0.1 μg/cm^2 BSA, for a 5 nm Au nanosphere. For highly charged nanospheres with single ligands, the D_h increased significantly, by 16 nm for citrate-capped nanospheres (Table 2.1, Figure 2.1c) and 13 nm for glutathione-capped nanospheres (Figure B.2). In control experiments with DLS reported in the supporting information, it was found that scattering from FBS solutions without added Au nanospheres was weak relative to the scattering by the Au nanospheres. For incubation in 100% FBS for lysine/citrate nanospheres with the lower ratio of 0.5, the D_h increased only modestly, by 3 nm as shown in Table 3.1. With a greater lysine/citrate ratio of 1.4 and ζ of only -16.1 mV, serum protein adsorption was completely inhibited, as the change in D_h was less than 1 nm, within experimental error (Table 2.1, Figure 2.1c). Similar behavior was observed in the case of the cysteine/citrate mixed monolayers. For the lower cysteine/citrate ratio of 1.0, D_h increased only 4 nm (Table 2.1). For a larger ratio of 1.6, however, protein adsorption was completely inhibited, as the nanosphere D_h change from 3.4 ± 2.5 nm to 3.4 ± 2.7 nm was within experimental error (Table 2.1, Figure 2.1d). Remarkably, not a single protein molecule

was adsorbed, despite the substantial nanosphere surface charge ($\zeta = 21.6 \pm 1.7$ mV). If protein molecules adsorb they may produce aggregation of Au nanospheres; however, our DLS distributions did not reveal any aggregates in the 100 nm-1000 nm size range (Tables B.8 and B.9).

To support the results by DLS, nanosphere sedimentation was measured in a centrifugal field. The Au yield by mass was measured in the pellet, after centrifugation for 15 min at 10000 rpm as described in the Experimental section. For Au nanospheres in deionized water, the yield was ~ 20% (Appendix B) in each case. For the 1.6 cysteine/citrate level a similar yield of 21% was observed in FBS consistent with the lack of protein adsorption. However, for the ratio of 1.0 where the D_h increased to 8.8 nm, the yield in the pellet increased to 39% indicating the centrifugation technique was also highly sensitive to protein adsorption. A similar trend was observed for lysine/citrate nanospheres (see Appendix B). Thus, the DLS and sedimentation techniques provide complimentary evidence that the protein adsorption was neglible for the Au nanospheres coated with either cysteine/citrate or lysine/citrate ligands at the higher ratios. To our knowledge, this study presents the first examples of moderately charged gold nanospheres coated with binary mixed charge ligands that completely prevent serum protein adsorption in undiluted serum. Furthermore, both ligands are naturally found in the body.

The significant level of protein adsorption on citrate and GSH-capped nanospheres can be partially attributed to overall electrostatic interactions between negatively charged nanosphere surfaces and positively-charged proteins, as well as local charges and hydrogen bonding sites on protein surfaces. Beurer *et al.*, for example, found that protein adsorption on surfaces with a charge gradient from positively-charged aminoundecanethiol to negatively-charged mercaptoundecanoic acid was correlated with

overall electrostatic attraction.[24] Here, negatively charged BSA and fibrinogen adsorbed mostly on the cationic quaternary ammonium section and positively-charged lysozyme adsorbed mainly on the anionic carboxylates.[24] The most prevalent protein in serum, BSA, with a pI of 4.7,[24] is negatively charged at neutral pH and thus the overall electrostatic interaction with anionic Au surfaces is repulsive. However, interactions must be considered between the charged ligands and local charges and hydrogen bonding sites on the protein surface. For example, local attraction or salt bridges between cationic lysine residues on BSA and citrate ligands on Au nanospheres contribute to adsorption.[31, 38] Thus, serum protein adsorption observed on citrate and GSH-capped nanospheres may be caused by overall electrostatic interactions with positively-charged proteins, as well as local electrostatic and hydrogen bonding interactions for both positively and negatively charged proteins.

Our observation *via* DLS of essentially zero serum protein adsorption on a moderately charged binary monolayer is unexpected, relative to previous studies with single ligand monolayers[1, 31, 38, 39] as well as mixed charge monolayers with substantial net charge.[24, 29] For the 1.4 lysine/citrate monolayers, the lack of protein adsorption suggests that the lysine screens the strong interactions of the trivalent citrate with the proteins, similar to the 1.6 cysteine/citrate monolayers. The overall electrostatic interaction between the net negative charge of the binary monolayer and positively charged serum proteins is attractive. The difference in length of the citrate ligand versus either lysine or cysteine, however, may be expected to play an important role in resisting protein adsorption. For example, the zwitterionic tips of lysine or cysteine will interact weakly with protein surfaces given the lack of net charge and strong hydration, as is known for other zwitterions.[5, 6, 29] Another important factor is that each of these amino acids is considerably longer than the citrate molecule, as shown in Figures 1a and 1b. The

amino acids in the monolayers thus provide steric hindrance by increasing the distance between the three carboxylates on citrate and the protein surface. Thus, the local "buried" charges in the ligand monolayers will interact more weakly with the local charges and hydrogen bonding sites on the protein surface. In addition, delocalization of the charge with the gold electrons for the two carboxylate anions on citrate and the protonated amine on lysine will further reduce the strength of the electrostatic interactions with the proteins.

Lysine and cysteine, as well as citrate, are all highly hydrophilic unlike hydrophobic ligands that interact with hydrophobic segments of serum proteins and facilitate adsorption of serum proteins.[33] For example, the hydrophilicity value is 3.0 for lysine, relative to 0.0 for glycine and -3.4 for highly hydrophobic tryptophan in the Hopp and Woods hydrophilicity index.[40] Cysteine is more hydrophobic than lysine (hydrophilicity value of -1.0[40]) but hydrophilic enough to resist protein adsorption when combined with citrate in our mixed monolayers. In summary, the tunability of the ligand ratio and thus surface charge for each of our mixed monolayers could be utilized to tailor the surfaces to resist protein adsorption even for moderate net charge.

Various techniques have been used to form nanoclusters with controlled properties from primary particles.[41-44] The 1.4 lysine/citrate nanospheres were assembled into nanoclusters upon solvent evaporation in the presence of a weakly adsorbing polymer, PLA-*b*-PEG-*b*-PLA, following a previously reported procedure, as discussed in the supplemental section.[34-36] The nanoclusters with a D_h of 21.7 ± 4.3 nm were composed of closely-spaced primary Au nanospheres (Figure 2.2), which shifted the extinction in the near infrared region (NIR) from 650 nm to 900 nm. Upon incubating the nanoclusters in pH 5 HCl for 24 h, the PLA(1k)-*b*-PEG(10k)-*b*-PLA(1k) on the surface was hydrolyzed, and consequently the nanoclusters dissociated to Au nanospheres with

the original nanosphere size, as seen in the UV-Vis-NIR spectrum (Figure 2.2c) as well as the DLS size distribution (Figure 2.2d). The dissociated nanoclusters did not adsorb serum proteins, as the D_h remained only 4.2 ± 2.6 nm upon incubation in 100% FBS (Figure 2.2d), a desired size for kidney clearance.

In this robust colloidal assembly approach,[34-36] the size of nanoclusters may be tuned as a function of the polymer and gold concentrations, chemical structure of the surface ligands, and the extent of solvent evaporation. The biodegradable polymer adsorbs on the surface of the nanoclusters and quenches the size *via* an equilibrium mechanism.[36] In the current study, we show for the first time that these clusters may be formed from Au particles with a large enough charge for nanocluster dissociation upon biodegradation of the polymer coating, but yet the surface charge is small enough to fully resist protein adsorption.

2.4 CONCLUSIONS

In conclusion, incubation of charged ~5 nm Au nanospheres with binary natural and relatively hydrophilic ligands in undiluted serum protein does not increase the hydrodynamic diameter according to dynamic light scattering, indicating essentially zero protein adsorption. A secondary conclusion is that the Au nanospheres may be assembled into NIR-active nanoclusters which biodegrade *in vitro* to primary Au nanospheres, again with essentially zero protein adsorption.

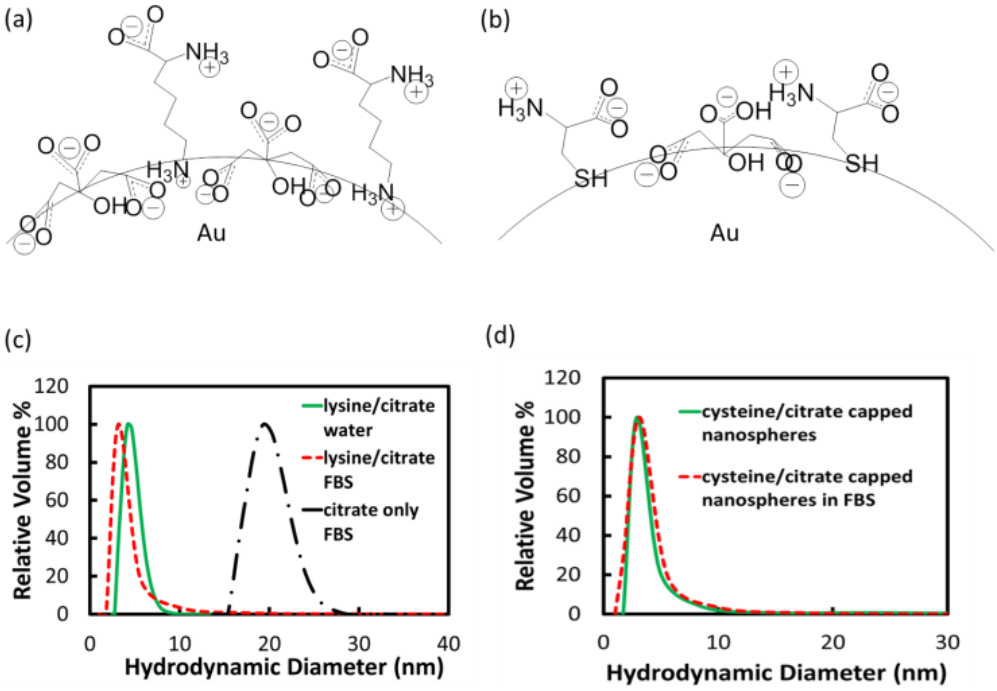

Figure 2.1: Schematics of nanosphere surfaces coated with (a) citrate and lysine, and (c) citrate and cysteine. DLS distributions in water (green curve) and FBS (red curve) for (c) 1.4 lysine/citrate nanospheres, and (d) 1.6 cysteine/citrate nanospheres. Black curve in (c) is DLS distribution of citrate only-capped nanospheres after FBS incubation.

Table 2.1: Properties of nanospheres capped with citrate or binary ligands before and after incubation in FBS.

Ligand(s)	Ligand Ratio (feed)	Ligand Ratio (XPS)	D_h (nm)	ζ (mV)	D_h in FBS (nm)
Citrate	n/a	n/a	4.3 ± 0.8	-58.4 ± 5.3	19.9 ± 2.1
Lysine/citrate	4.5	0.5	5.0 ± 1.2	-28.9 ± 3.9	7.7 ± 3.8
Lysine/citrate	9	1.4	4.6 ± 1.1	-16.1 ± 2.9	3.9 ± 2.1
Cysteine/ citrate	0.3	1.0	5.1 ± 3.9	-28.8 ± 3.2	8.8 ± 5.8
Cysteine/ citrate	0.7	1.6	3.4 ± 2.5	-21.6 ± 1.7	3.4 ± 2.7

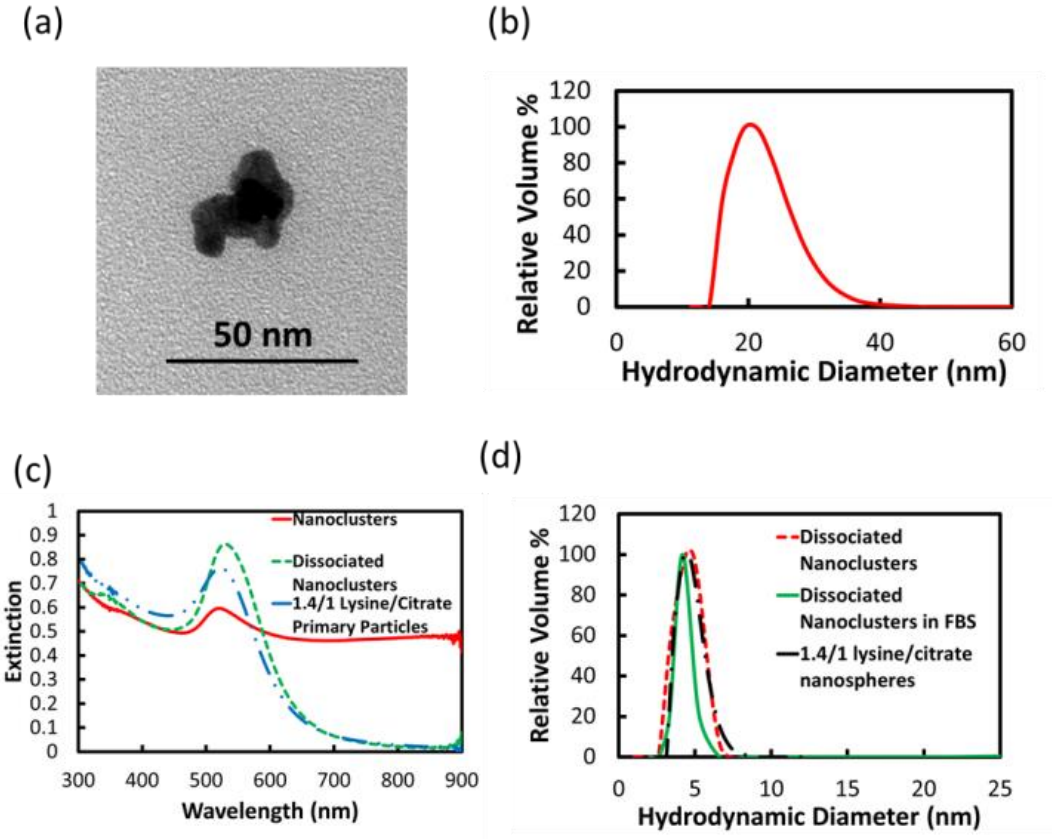

Figure 2.2: Lysine/citrate nanoclusters (a) TEM image, (b) DLS D_h distribution, and (c) UV-Vis-NIR extinction spectrum, with spectra of dissociated nanoclusters and nanospheres included, and (d) DLS D_h distributions of dissociated nanoclusters, dissociated nanoclusters in FBS, and lysine/citrate nanospheres.

2.5 REFERENCES

1. Choi, H. S.; Liu, W.; Misra, P.; Tanaka, E.; Zimmer, J. P.; Ipe, B. I.; Bawendi, M. G.; Frangioni, J. V. Renal Clearance of Quantum Dots. *Nat. Biotechnol.* **2007**, *25*, 1165-1170.

2. Zhou, C.; Long, M.; Qin, Y.; Sun, X.; Zheng, J. Luminescent Gold Nanoparticles with Efficient Renal Clearance. *Angew. Chem. Int. Ed.* **2011**, *50*, 3168-3172.

3. Tirumalai, R. S.; Chan, K. C.; Prieto, D. A.; Issaq, H. J.; Conrads, T. P.; Veenstra, T. D. Characterization of the Low Molecular Weight Human Serum Proteome. *Molecular & Cellular Proteomics* **2003**, *2*, 1096-1103.

4. Striemer, C. C.; Gaborski, T. R.; McGrath, J. L.; Fauchet, P. M. Charge- and Size-Based Separation of Macromolecules Using Ultrathin Silicon Membranes. *Nature* **2007**, *445*, 749-753.

5. Holmlin, R. E.; Chen, X.; Chapman, R. G.; Takayama, S.; Whitesides, G. M. Zwitterionic Sams That Resist Nonspecific Adsorption of Protein from Aqueous Buffer. *Langmuir* **2001**, *17*, 2841-2850.

6. Chen, S.; Yu, F.; Yu, Q.; He, Y.; Jiang, S. Strong Resistance of a Thin Crystalline Layer of Balanced Charged Groups to Protein Adsorption. *Langmuir* **2006**, *22*, 8186-8191.

7. Yang, W.; Xue, H.; Li, W.; Zhang, J.; Jiang, S. Pursuing "Zero" Protein Adsorption of Poly(Carboxybetaine) from Undiluted Blood Serum and Plasma. *Langmuir* **2009**, *25*, 11911-11916.

8. Chen, S.; Cao, Z.; Jiang, S. Ultra-Low Fouling Peptide Surfaces Derived from Natural Amino Acids. *Biomaterials* **2009**, *30*, 5893-5896.

9. Ostuni, E.; Chapman, R. G.; Holmlin, R. E.; Takayama, S.; Whitesides, G. M. A Survey of Structure-Property Relationships of Surfaces That Resist the Adsorption of Protein. *Langmuir* **2001**, *17*, 5605-5620.

10. Verma, A.; Uzun, O.; Hu, Y.; Hu, Y.; Han, H.-S.; Watson, N.; Chen, S.; Irvine, D. J.; Stellacci, F. Surface-Structure-Regulated Cell-Membrane Penetration by Monolayer-Protected Nanoparticles. *Nature Materials* **2008**, *7*, 588-595.

11. Yang, W.; Zhang, L.; Wang, S.; White, A. D.; Jiang, S. Functionalizable and Ultra Stable Nanoparticles Coated with Zwitterionic Poly(Carboxybetaine) in Undiluted Blood Serum. *Biomaterials* **2009**, *30*, 5617-5621.

12. Cedervall, T.; Lynch, I.; Lindman, S.; Berggard, T.; Thulin, E.; Nilsson, H.; Dawson, K. A.; Linse, S. Understanding the Nanoparticle-Protein Corona Using Methods to Quantify Exchange Rates and Affinities of Proteins for Nanoparticles. *Proceedings of the National Academy of Sciences* **2006**, *104*, 2050-2055.

13. Walkey, C. D.; Olsen, J. B.; Guo, H.; Emili, A.; Chan, W. C. W. Nanoparticle Size and Surface Chemistry Determine Serum Protein Adsorption and Macrophage Uptake. *Journal of the American Chemical Society* **2012**, *134*, 2139-2147.

14. Larson, T. A.; Joshi, P. P.; Sokolov, K. Preventing Protein Adsorption and Macrophage Uptake of Gold Nanoparticles Via a Hydrophobic Shield. *ACS Nano* **2012**, *6*, 9182-9190.

15. Chen, S.; Li, L.; Zhao, C.; Zheng, J. Surface Hydration: Principles and Applications toward Low-Fouling/Nonfouling Biomaterials. *Polymer* **2010**, *51*, 5283-5293.

16. Lundqvist, M.; Stigler, J.; Elia, G.; Lynch, I.; Cedervall, T.; Dawson, K. A. Nanoparticle Size and Surface Properties Determine the Protein Corona with Possible Implications for Biological Impacts. *Proceedings of the National Academy of Sciences* **2008**, *105*, 14265-14270.

17. Markarucha, A. J.; Todorova, N.; Yarovsky, I. Nanomaterials in Biological Environment: A Review of Computer Modelling Studies. *Eur. Biophys. J.* **2011**, *40*, 103-115.

18. Li, L.; Chen, S.; Zheng, J.; Ratner, B. D.; Jiang, S. Protein Adsorption on Oligo(Ethylene Glycol)-Terminated Alkanethiolate Self-Assembled Monolayers: The Molecular Basis for Nonfouling Behavior. *Journal of Physical Chemistry B* **2005**, *109*, 2934-2941.

19. Liu, W.; Choi, H. S.; Zimmer, J. P.; Tanaka, E.; Frangioni, J. V.; Bawendi, M. Compact Cysteine-Coated Cdse(Zncds) Quantum Dots for in Vivo Applications. *Journal of the American Chemical Society* **2007**, *129*, 14530-14531.

20. Ladd, J.; Zhang, Z.; Chen, S.; Hower, J. C.; Jiang, S. Zwitterionic Polymers Exhibiting High Resistance to Nonspecific Protein Adsorption from Human Serum and Plasma. *Biomacromolecules* **2008**, *9*, 1357-1361.

21. Estephan, Z. G.; Jaber, J. A.; Schlenoff, J. B. Zwitterion-Stabilized Silica Nanoparticles: Toward Nonstick Nano. *Langmuir* **2010**, *26*, 16884-16889.

22. Jia, G.; Cao, Z.; Xue, H.; Xu, Y.; Jiang, S. Novel Zwitterionic-Polymer-Coated Silica Nanoparticles. *Langmuir* **2009**, *25*, 3196-3199.

23. Mahmoudi, M.; Lynch, I.; Ejtehadi, M. R.; Monopoli, M. P.; Bombelli, F. B.; Laurent, S. Protein-Nanoparticle Interactions: Opportunities and Challenges. *Chemical Reviews* **2011**, *111*, 5610-5637.

24. Beurer, E.; Venkataraman, N. V.; Sommer, M.; Spencer, N. D. Protein and Nanoparticle Adsorption on Orthogonal, Charge-Density-Versus-Net-Charge Surface-Chemical Gradients. *Langmuir* **2012**, *28*, 3159-3166.

25. Dobrovolskaia, M. A.; Patri, A. K.; Zheng, J.; Clogston, J. D.; Ayub, N.; Aggarwal, P.; Neun, B. W.; Hall, J. B.; McNeil, S. E. Interaction of Colloidal Gold Nanoparticles with Human Blood: Effects on Particle Size and Analysis of Plasma Protein Binding Profiles. *Nanomedicine* **2009**, *5*, 106-117.

26. De Paoli Lacerda, S. H.; Park, J. J.; Meuse, C.; Pristinski, D.; Becker, M. L.; Karim, A.; Douglas, J. F. Interaction of Gold Nanoparticles with Common Human Blood Proteins. *ACS Nano* **2010**, *4*, 365-379.

27. Yu, M.; Zhou, C.; Liu, J.; Hankins, J. D.; Zheng, J. Luminescent Gold Nanoparticles with Ph-Dependent Membrane Adsorption. *Journal of the American Chemical Society* **2011**, *133*, 11014-11017.

28. Wei, H.; Insin, N.; Lee, J.; Han, H.-S.; Cordero, J. M.; Liu, W.; Bawendi, M. G. Compatct Zwitterion-Coated Iron Oxide Nanoparticles for Biological Applications. *Nano Letters* **2011**, *12*, 22-25.

29. Chen, S.; Zhen, J.; Li, L.; Jiang, S. Strong Resistance of Phosphorylcholine Self-Assembled Monolayers to Protein Adsorption: Insights into Nonfouling Properties of Zwitterionic Materials. *Journal of the American Chemical Society* **2005**, *127*, 14473-14478.

30. Kaufman, E. D.; Belyea, J.; Johnson, M. C.; Nicholson, Z. M.; Ricks, J. L.; Shah, P. K.; Bayless, M.; Pettersson, T.; Feldoto, Z.; Blomberg, E.*, et al.* Probing Protein Adsorption onto Mercaptoundecanoic Acid Stabilized Gold Nanoparticles and Surfaces by Quartz Crystal Microbalance and Z-Potential Measurements. *Langmuir* **2007**, *23*, 6053-6062.

31. Brewer, S. H.; Glomm, W. R.; Johnson, M. C.; Knag, M. K.; Franzen, S. Probing Bsa Binding to Citrate-Coated Gold Nanoparticles and Surfaces. *Langmuir* **2005**, *21*, 9303-9307.

32. Jackson, A. M.; Myerson, J. W.; Stellacci, F. Spontaneous Assembly of Subnanometre-Ordered Domains in the Ligand Shell of Monolayer-Protected Nanoparticles. *Nature Materials* **2004**, *3*, 330-336.

33. You, C.-C.; De, M.; Han, G.; Rotello, V. M. Tunable Inhibition and Denaturation of a-Chymotrypsin with Amino Acid-Functionalized Gold Nanoparticles. *Journal of the American Chemical Society* **2005**, *127*, 12873-12881.

34. Tam, J. M.; Murthy, A. K.; Ingram, D. R.; Nguyen, R.; Sokolov, K. V.; Johnston, K. P. Kinetic Assembly of near-Ir Active Gold Nanoclusters Using Weakly Adsorbing Polymers to Control the Size. *Langmuir* **2010**, *26*, 8988-8999.

35. Tam, J. M.; Tam, J. O.; Murthy, A.; Ingram, D. R.; Ma, L. L.; Travis, K.; Johnston, K. P.; Sokolov, K. V. Controlled Assembly of Biodegradable Plasmonic Nanoclusters for near-Infrared Imaging and Therapeutic Applications. *ACS Nano* **2010**, *4*, 2178-2184.

36. Murthy, A. K.; Stover, R. J.; Borwankar, A. U.; Nie, G. D.; Gourisankar, S.; Truskett, T. M.; Sokolov, K. V.; Johnston, K. P. Equilibrium Gold Nanoclusters Quenched with Biodegradable Polymers. *ACS Nano* **2013**, *7*, 239-251.

37. Yoon, S. J.; Mallidi, S.; Tam, J. M.; Tam, J. O.; Murthy, A.; Johnston, K. P.; Sokolov, K. V.; Emelianov, S. Y. Utility of Biodegradable Plasmonic Nanoclusters in Photoacoustic Imaging. *Opt. Lett.* **2010**, *35*, 3751-3753.

38. Dominguez-Medina, S.; McDonough, S.; Swanglap, P.; Landes, C. F.; Link, S. In Situ Measurement of Bovine Serum Albumin Interaction with Gold Nanospheres. *Langmuir* **2012**, *28*, 9131-9139.

39. Casals, E.; Pfaller, T.; Duschl, A.; Oostingh, G. J.; Puntes, V. Time Evolution of the Nanoparticle Protein Corona. *ACS Nano* **2010**, *4*, 3623-3632.

40. Hopp, T. P.; Woods, W. R. Prediction of Protein Antigenic Determinants from Amino Acid Sequences. *Proceedings of the National Academy of Sciences* **1981**, *78*, 3824-3828.

41. Zhuang, J.; Wu, H.; Yang, Y.; Cao, Y. C. Controlling Colloidal Superparticle Growth through Solvophobic Interactions. *Angew. Chem. Int. Ed.* **2008**, *47*, 2208-2212.

42. Ma, L. L.; Feldman, M. D.; Tam, J. M.; Paranjape, A. S.; Cheruki, K. K.; Larson, T. A.; Tam, J. O.; Ingram, D. R.; Paramita, V.; Villard, J. W.*, et al.* Small Multifunctional Nanoclusters (Nanoroses) for Targeted Cellular Imaging and Therapy. *ACS Nano* **2009**, *3*, 2686-2696.

43. Xia, Y. S.; Nguyen, T. D.; Yang, M.; Lee, B.; Santos, A.; Podsiadlo, P.; Tang, Z. Y.; Glotzer, S. C.; Kotov, N. A. Self-Assembly of Self-Limiting Monodisperse Supraparticles from Polydisperse Nanoparticles. *Nat. Nanotechnol.* **2011**, *6*, 580-587.

44. Lu, Z.; Yin, Y. Colloidal Nanoparticle Clusters: Functional Materials by Design. *Chem. Soc. Rev.* **2012**, *41*, 6874-6887.

Chapter 3: Equilibrium Gold Nanoclusters Quenched with Biodegradable Polymers[2]

Although sub-100 nm nanoclusters of metal nanoparticles are of interest in many fields including biomedical imaging, sensors and catalysis, it has been challenging to control their morphologies and chemical properties. Herein, a new concept is presented to assemble equilibrium Au nanoclusters of controlled size by tuning the colloidal interactions with a polymeric stabilizer, PLA(1k)-*b*-PEG(10k)-*b*-PLA(1k). The nanoclusters form upon mixing a dispersion of ~5 nm Au nanospheres with a polymer solution followed by partial solvent evaporation. A weakly adsorbed polymer quenches the equilibrium nanocluster size and provides steric stabilization. Nanocluster size is tuned from ~20 nm to ~40 nm by experimentally varying the final Au nanoparticle concentration and the polymer/Au ratio, along with the charge on the initial Au nanoparticle surface. Upon biodegradation of the quencher, the nanoclusters reversibly and fully dissociate to individual ~5 nm primary particles. Equilibrium cluster size is predicted semi-quantitatively with a free energy model that balances short-ranged depletion and van der Waals attractions with longer-ranged electrostatic repulsion, as a function of the Au and polymer concentrations. The close spacings of the Au nanoparticles in the clusters produce strong NIR extinction over a broad range of wavelengths from 650 to 900 nm, which is of practical interest in biomedical imaging.

[2] Large parts of this chapter have been published as: Murthy, A.K.; Stover, R.J.; Borwankar, A.U.; Nie, G.D.; Gourisankar, S.; Truskett, T.M.; Sokolov, K.V.; Johnston, K.P., Equilibrium Gold Nanoclusters Quenched with Biodegradable Polymers. *ACS Nano* **2013**, *7*(1), 239-251.

3.1 INTRODUCTION

Metal nanoclusters composed of primary nanoparticles are of interest in a wide array of applications such as biomedical imaging, catalysis, sensors, and electromagnetic imaging of subsurface reservoirs.[1-6] Structure-directing agents including polymers, dendrimers, proteins, or DNA are often used to template the orientation of the primary particles within the clusters.[7, 8] Typically, the amount of inactive templating agents in the product must be 50% or more to direct the assembly. Recently, sub-100 nm nanoclusters of ~5 nm Au primary charged nanoparticles with controlled size were assembled by adding small amounts of stabilizing polymers.[4, 5] Additionally, the "self-limiting" assembly of citrate-stabilized cadmium selenide (CdSe) nanoparticles into clusters was observed upon the addition of cadmium perchlorate and sodium selenosulfate precursors in water, as characterized by computer simulation.[6] Furthermore, "kinetically trapped" clusters of controlled size comprising poly(ethylene glycol) (PEG)-stabilized Au nanoparticles have been reported by balancing van der Waals attractive forces with the steric repulsion provided by the PEG layer, which is modulated by the addition of an alkanethiol to the Au nanoparticle surface.[9]

Although aggregates of nanoparticles may be formed by kinetic assembly, the growth often produces large, uncontrolled microparticle aggregates and/or gels upon varying colloidal interactions through pH, salinity,[10] and the addition of polymers to induce depletion attraction.[11] Given the uncertainty in control of the cluster size morphology *via* kinetic assembly, it would be desirable to devise a fundamental strategy to tune cluster architecture and size by equilibrium assembly. If this equilibrium assembly were fully reversible, the clusters may dissociate all the way to monomer upon changes in the solvent conditions.

The equilibrium assembly of nanoparticles into nanoclusters has been reported in organic solvents[12, 13] and more recently in aqueous environments.[6, 14] The size of clusters of poly(methylmethacrylate) (PMMA) spheres (~4-10 μm)[12] and Boehmite rods (~350-450 nm)[13] in organic solvents with low dielectric constants is governed by a balance of strong, short-ranged attraction and weak, longer-ranged electrostatic repulsion, as described with a free energy equilibrium model.[15] In aqueous solvents, nanoclusters of primary protein nanocolloids were found to be extremely small[16] and short-lived[17] given strong electrostatic repulsion between primary particles.[15] However, for slightly charged proteins near the isoelectric point, large (~100 nm), long-lived equilibrium clusters of ~10 nm protein molecules were formed.[14] Here, crowder molecules (depletants) were added to balance short-ranged depletion attraction between the protein particles against the long ranged electrostatic repulsion and thereby tune the cluster size.[14, 15] Upon dilution, these clusters reversibly dissociated to stable protein monomers.

To date, it is unknown whether equilibrium nanoclusters may be assembled from inorganic nanoparticles in aqueous media and whether they would reversibly dissociate back to individual nanoparticles. Partially dissociable Au nanoclusters, with sizes < 100 nm in diameter, were formed by mixing Au nanoparticle dispersions with small amounts (~20%) of solid polylactic acid (PLA) and PEG copolymer, PLA(1k)-*b*-PEG(10k)-*b*-PLA(1k). The shift in the surface plasmon resonance (SPR) to the near-infrared (NIR) indicated very close spacings between the Au nanoparticles, consistent with the low polymer loadings.[4, 5] The cluster formation was attributed to kinetic assembly upon screening the electrostatic repulsion between the primary particles by the weakly adsorbed polymer. Upon biodegradation of the polymer, the clusters underwent significant, but not full dissociation into ~5.5 nm Au primary particles, according to the measured change in the SPR.

Herein, we demonstrate the assembly of Au nanoclusters with tunable equilibrium sizes from ~20 nm to ~40 nm, whereby the equilibrium state is quenched by weak adsorption of a triblock copolymer, PLA(1k)-*b*-PEG(10k)-*b*-PLA(1k) stabilizer on the nanocluster surface. Furthermore, the nanoclusters reversibly dissociate completely to ~5 nm Au nanospheres upon biodegradation of the polymeric quencher, as shown in Figure 4.1. The magnitude of the charge of the mixed ligand monolayer on the Au surfaces was designed to be small enough to enable formation of nanoclusters in the presence of the copolymer, yet sufficiently large for nanocluster dissociation upon dilution after polymer biodegradation. The polymer is shown to induce depletion attraction between the Au spheres to supplement van der Waals attraction to drive assembly of the charged Au nanoparticles into nanoclusters. The equilibrium cluster size is predicted semi-quantitatively with a free energy model that balances short-ranged attraction with long-ranged electrostatic repulsion, as a function of the experimentally measured charges on both the primary Au particles and the nanoclusters. Remarkably, the same model describes both Au and protein[14] nanoclusters. The cluster size is tuned with the Au and polymer concentrations in a new process that utilized well-controlled mixing and partial solvent evaporation, as shown in Figure 3.1. Additionally, polymer adsorption to the Au nanocluster surface quenches the nanoclusters such that their size does not change upon dilution in deionized water. The close spacings of the Au nanoparticles in the clusters produce strong NIR extinction over a broad range in wavelength from 650 nm to 900 nm. This wavelength range, where blood is weakly absorbing,[18] is of interest in biomedical imaging including photoacoustic imaging,[19-21] photothermal therapy[22, 23] and combined imaging and therapy.[24-26] Furthermore, the nanoclusters are shown to dissociate completely to 5.5 nm Au nanoparticles, which would be small enough for kidney clearance.[27]

3.2 EXPERIMENTAL

3.2.1 Materials

$HAuCl_4 \cdot 3H_2O$ was obtained from MP Biomedicals LLC (Solon, OH) and $Na_3C_3H_5O(COO)_3 \cdot 2H_2O$ was acquired from Fisher Scientific (Fair Lawn, NJ). $NaBH_4$ was also obtained from Fisher Scientific. L-(+)-lysine was purchased from Acros Chemicals (Morris Plains, NJ), and PLA(1k)-*b*-PEG(10k)-*b*-PLA(1k) was obtained from Sigma-Aldrich (St. Louis, MO).

3.2.2 Synthesis of citrate-capped Au nanospheres and lysine ligand exchange

~ 4 nm citrate-capped Au nanospheres were formed by reduction of $HAuCl_4$ with $NaBH_4$ by scaling up an earlier method and purifying synthesized particles with tangential flow filtration, as described in Appendix C.[5] The synthesis resulted in ~25 mL of 3 mg/ml Au.

Lysine place exchange was conducted by adding 20 µl of freshly prepared aqueous solution of 5% w/v (50 mg/ml) lysine to 1.2 mL of the 3 mg/ml citrate-capped Au nanosphere dispersion. Here the pH of the solution increased from pH ~6 to pH ~8.8 upon addition of the basic lysine ligand. At pH 8.8, lysine has two positive charges and one negative charge.[58] After lysine addition, the mixture was stirred for 15 min at room temperature to enable place exchange. Immediately after this reaction, nanosphere samples were either ultracentrifuged for X-ray photoelectron spectroscopy (XPS) or thermogravimetric analysis (TGA), diluted for dynamic light scattering (DLS), UV-Visible-NIR (UV-Vis-NIR) spectroscopy, or zeta potential (ζ) analysis, or used to form nanoclusters.

3.2.3 Nanocluster Formation

Immediately after 15 min of lysine place exchange, Au nanospheres were used to form nanoclusters. An aqueous, 120 mg/ml solution of PLA(1k)-*b*-PEG(10k)-*b*-PLA(1k) was freshly prepared. In the base case, the lysine/citrate capped Au dispersion was diluted to 1 mg/ml from 3 mg/ml. 500 µl of the PLA(1k)-*b*-PEG(10k)-*b*-PLA(1k) solution was then added to 3 ml of 1 mg/ml lysine/citrate capped Au nanospheres in 5 iterations of 100 µl each over 10 min. The addition of polymer solution was done under vigorous stirring. After addition of the polymer solution, the resulting Au concentration was 0.9 mg/ml, and the polymer concentration was 17 mg/ml. This mixture was placed in a 19 x 48 mm glass vial, and the vial was placed in a 40 °C water bath and stirred using a magnetic stirrer. Dried air was blown gently over the sample *via* a small tube that was inserted a few cm into the vial. The combination of water bath and airflow kept the sample temperature at 25 ± 3 °C as the sample was evaporated to 50% of its original volume over ~40 min, resulting in final Au and polymer concentrations of 1.7 mg/ml and 36 mg/ml, respectively. These base-case samples were denoted 20-1.7 particles, designating to a polymer/Au ratio of 20/1 and a final Au concentration of 1.7 mg/ml (nomenclature adopted throughout). After sample evaporation, the cluster formation was terminated by adding 30 mL of DI water to dilute the Au. The solution was then centrifuged at 10000 rpm for 10 min in order to separate unclustered and loosely-bound particles from the ~30% (by mass) dense Au nanoclusters.

The nanocluster formation process described above was carried out at initial Au concentrations (after addition of polymer solution) from 0.5 to 2.0 mg/ml, and initial polymer concentrations of 9 mg/ml, 40 mg/ml, 8.5 mg/ml, and 42.5 mg/ml (after polymer

solution addition). Evaporation, centrifugation, and redispersion were carried out in a manner identical to 20-1.7 particles.

3.2.4 Characterization of primary Au nanospheres

After lysine place exchange, samples were diluted to ~0.04 mg/ml in DI water for DLS measurements, measurement of ζ potential, and UV-Vis-NIR spectroscopy measurements, without purification. DLS measurements were taken using a custom-built apparatus at a scattering angle of 45° using an avalanche photodiode at ~ 25°C.[59] Data were analyzed using a digital autocorrelator (Brookhaven BI-9000AT) and the CONTIN method. The Stokes-Einstein equation was used to obtain a volume-weighted distribution of hydrodynamic diameters (D_H). UV-Vis-NIR spectroscopy was performed using a Varian Cary 3E spectrophotometer with a 1 cm path length. UV-Vis-NIR extinction measurements were all conducted at a Au concentration of ~90 μg/ml. Extinction values at 800 nm were used to calculate extinction coefficients (ε_{800}) for nanospheres, as described in Appendix C. ζ analysis was conducted using a Brookhaven ZetaPlus zeta potential analyzer. Samples were diluted to ~0.02-0.04 mg/ml in 1 mM KCl at pH 7, and the average and standard deviations for 30 single-cycle measurements are reported. Due to the small size of the nanospheres (see Results), the Huckel model was used to relate the measured electrophoretic mobility to a ζ potential.[60]

For TGA and XPS analysis, nanosphere samples were ultracentrifuged for 45 min at 40000 rpm in order to remove excess citrate and lysine ligands, and the resulting pellet was dried. TGA was performed using a Mettler Toledo TGA/DSC 1 STAR^e system with a gas controller (GC 200) and a temperature set at 22°C (Julabo). TGA samples were initially heated to 100 °C and held at that temperature for 10 min to eliminate any

residual moisture remaining in the samples. The samples were subsequently heated to 900 °C at a heating rate of 20 °C/min, and the mass loss of organic content of the samples was determined.

XPS analysis was performed using a Kratos AXIS Ultra DLD spectrometer equipped with a monochromatic Al X-ray source (Al α, 1.4866 keV). High-resolution elemental analysis was performed on the Au 4f, C 1s, N 1s and O 1s regions with pass energies of 30 eV, 20 eV, 40 eV, and 20 eV, respectively. A 0.1 eV step and a 4 s dwell time was used in all cases. Charge compensation was not used because of the conductivity of each sample. Peak positions and areas were calculated using a Gaussian + Lorentzian fit and a Shirley background correction.

Au concentrations in nanosphere samples were determined using flame atomic absorption spectroscopy (FAAS) using a GBC FAAS analyzer (GBC Scientific Equipment Pty Ltd., GBC 908AA) with an air-acetylene flame and at a wavelength of 242.8 nm. Samples were diluted, without purification, in aqua regia to between 1 ppm and 5 ppm before analysis.

3.2.5 Nanocluster Characterization

Nanocluster morphologies were observed by transmission electron microscopy (TEM) performed on an FEI TECNAI G2 F20 X-TWIN TEM using a high-angle annular dark-field detector. Samples were prepared by dipping 200 mesh copper-coated carbon TEM grids (Electron Microscopy Sciences, Hatfield, PA) into liquid nitrogen and then pipetting 5 µl of a dilute nanocluster dispersion onto the grid. The grid was then dried using a VirTis AdVantage tray lyophilizer (VirTis, Gardiner, NY). Unless otherwise noted, DLS, UV-Vis-NIR spectroscopy, ζ analysis, and FAAS were performed

identically to nanosphere characterization. DLS was conducted on a Brookhaven ZetaPALS analyzer with a scattering angle of 90°. Due to nanocluster size (see Results), the Huckel model was also used to fit measured electrophoretic mobilities in ζ analysis.[60] TGA was conducted on nanoclusters after centrifugation without the ultracentrifugation necessary for nanospheres, using a Mettler-Toledo TGA/SDTA851e instrument.

3.2.6 Nanocluster Dissociation

Dissociation of 20-4.0 and 20-1.7 particles was performed *via* dilution in pH 5 HCl. Dissociation of 20-4.0 particles was monitored by adding ~200 µl of ~1.6 mg/ml nanocluster dispersion to 2 ml of pH 5 HCl, such that the Au concentration was ~160 µg/ml. For 20-1.7 particles, ~200 µl of a ~0.4 mg/ml nanocluster dispersion was added to 2 ml of pH 5 HCl, such that the Au concentration was ~60 µg/ml. Addition of the pH 7 nanocluster dispersion did not change the mixture pH from pH 5 in either case. Nanoclusters were analyzed *via* UV-Vis-NIR spectroscopy and DLS without further dilution at 6 h, 12 h, 24 h, and 48 h time points for 20-4.0 particles, and after 24 h for 20-1.7 particles. DLS was performed at a scattering angle of 45°, similar to the case for nanospheres.

3.3 RESULTS

3.3.1 Place Exchange of Citrate Ligands with Lysine to Design the Surface Charge

The properties of primary Au nanospheres before and after lysine ligand exchange are given in Table 3.1. The hydrodynamic diameter (DH) of nanospheres before ligand exchange was 4.3 ± 0.7 nm (Table 3.1, Table C.1a), and the extinction at 800 nm, with a

Au concentration of 90 μg/ml, was 0.04. As a result, the extinction coefficient at 800 nm (ε_{800}) was 0.44 cm^2/mg. (Table 3.1, Table C.1b). The ζ potential was -58.4 ± 5.3 mV (Table 4.1). The ligand coverage was determined to be 4% w/w by thermogravimetric analysis (TGA) (Table 4.1), which is similar to the theoretical weight percent of a citrate monolayer on a 4 nm Au nanoparticle (see Appendix C). The concentration of the citrate-capped Au particle dispersion was determined to be 3.0 ± 0.1 mg Au/ml by flame atomic absorption spectroscopy (FAAS).

After place exchange, the D_H of the lysine/citrate capped Au nanoparticles was 4.7 ± 0.8 nm (Table 3.1, Figure C.1a), relatively close to the initial value, indicating that the nanospheres did not aggregate. In addition, the extinction was 0.06 at 800 nm, and the ε_{800} value was similar to that of citrate-capped nanospheres at 0.67 cm^2/mg (Table 3.1, Figure C.1b). The slight red-shift of the peak of the extinction spectra on lysine/citrate nanospheres from 512 nm to 520 nm (Figure C.1b) may be attributed to the change in surface properties and thus local dielectric constants of the nanoparticles upon lysine displacement of citrate.[28] After place exchange, the magnitude of the ζ potential dropped significantly to -16.0 ± 6.6 mV (Table 3.1), indicating a substantial degree of replacement of negatively-charged citrate ligands with positively-charged lysine. The ligand weight percentage did not increase from 4% w/w, as may be expected given the similar molecular weights of lysine and citrate of 146 g/mol and 192 g/mol, respectively. The XPS spectrum revealed characteristics peaks at ~532 eV for O 1s, ~400 eV for N 1s, ~285 eV for C 1s, and peaks at 88 eV and 84 eV for Au 4f (Figure C.2a). The atomic ratio of nitrogen to oxygen was determined by integration of the O 1s peak (Figure C.2b) and the N 1s peak (Figure C.2c). Integration of the N 1s peak yielded a peak area of 2387, while integration of the O 1s peak yielded an area of 8574. Based on these peak

integrations, the nitrogen/oxygen atomic ratio was 0.28. From this value, the lysine/citrate ratio was calculated to be 1.4 (Table 3.1), as discussed in Appendix C.

The reduction in nanosphere surface charge after ligand exchange can be correlated to the XPS results of the composition of the mixed surface layer. TGA results on citrate-capped nanospheres (Table 4.1) indicate that approximately 196 citrate ligands are present per particles (Appendix C), which corresponds to 196 × 3 = 588 negative charges. Ligand exchange with lysine replaces 3 negative charges with 1 positive charge, such that the 114 lysine ligands and 82 citrate ligands present after ligand exchange (Appendix C), which corresponds to an equivalent of (82 × 3) – (114 × 1) = 132 negative charges. Thus, the surface charge magnitude after ligand exchange would be expected to be 132/588 = 22% of the original surface charge, which is in good agreement with the zeta potential values, which dropped to 28% of its original value after lysine ligand exchange. While the actual number of negative charges on the surface cannot be directly captured by ζ potential measurements, the amount of *relative* charge can be compared, as is done here.

3.3.2 Nanocluster Formation by Equilibrium Assembly of the Primary Au Nanoparticles

After ligand exchange, citrate/lysine capped primary nanoparticles were assembled into nanoclusters, as shown schematically in Figure 3.1. The morphologies of equilibrium nanoclusters formed *via* the pathways depicted in Figure 3.1 are shown in Figure 3.2, based on transmission electron microscopy (TEM), for the Au and polymer concentrations given in Table 3.2. Images of several 20-4.0 and 20-0.9 particles are shown in Figure C.5. These images show densely-packed primary Au nanoparticles within each nanocluster. Due to this dense Au packing and the polymer, it can be difficult

to discern the boundaries of individual nanospheres. These nanoclusters were purified by centrifugation and redispersed in DI water. Centrifugation removed unclustered primary nanospheres, excess polymer and ligands, and smaller and/or less closely-packed nanoclusters, yielding a substantial population of densely-packed nanoclusters (as seen by TEM). Nanocluster yields increased with Au concentration and polymer/Au ratio, reaching 61%, as both of these factors will be shown to drive equilibrium nanocluster formation.

The effects of increasing final Au concentration on the Au nanocluster hydrodynamic diameter and optical properties are shown in Figure 3.3 and Table 3.2. In the first set of experiments, the polymer/Au ratio was fixed at 20/1. As the final Au concentration is increased from 0.9 mg/ml to 1.7 mg/ml, the nanocluster D_H increased from 21.4 ± 4.4 nm to 29.4 ± 3.2 nm (Figure 3.3a, Table 3.2). The D_H increased to 40.1 ± 4.3 nm (Figure 3.3a, Table 3.2) as the final Au concentration was increased from 1.7 mg/ml to 4.0 mg/ml. Secondary populations of large aggregates were not observed in either volume-weighted D_H distributions or intensity-weighted D_H distributions, which are more sensitive to large aggregates (Figure C.8a). Nanocluster D_H distributions were highly reproducible, as shown for 20-0.9 and 20-4.0 particles in Figure C.10. Furthermore, analysis of TEM images of the nanoclusters (at least 20 clusters in several images analyzed) indicated reasonable agreement between the measured D_H and the nanocluster size measured with TEM (Table 3.2). For TEM analysis, it is somewhat challenging to discern the boundaries between individual nanoclusters at high surface coverages in the images, relative to simpler geometries such as spheres or rods.[4, 5] Thus, we intentionally used low surface coverage on the grids, and acquired multiple images of nanoclusters to conduct a sizing analysis. Histograms which present a detailed analysis of the TEM images for 20-0.9, 20-1.7, and 20-4.0 particles are shown in Figure C.6. An

increase in the final Au concentration from 0.9 mg/ml to 1.7 mg/ml also increased the extinction at 800 nm from 0.95 to 1.05, thus increasing the extinction coefficient ε_{800} from 10.6 cm^2/mg to 11.7 cm^2/mg (Figure 3.3b, Table 3.2). Further increase of the final Au concentration from 1.7 mg/ml to 4.0 mg/ml increased the nanocluster extinction at 800 nm and ε_{800} to 1.16 and 12.9 cm^2/mg (Figure 3.3b, Table 3.2), respectively. The nanocluster ζ potential increased in magnitude slightly from -12.3 ± 1.1 mV for 20-0.9 particles to -16.4 ± 3.6 mV for 20-1.7 particles (Table 4.2). For 20-4.0 particles, the nanocluster ζ potential decreased very slightly in magnitude to -13.2 ± 0.6 mV (Table 3.2).

For a final Au concentration of 1.7 mg/ml, the morphologies from TEM with increasing polymer/Au concentration, for samples 10-1.7, 20-1.7, and 50-1.7 particles are shown in Figure 3.4. In each case, densely packed Au nanoclusters are observed. The Au yields for 10-1.7, 20-1.7, and 50-1.7 particles were 26 ± 13%, 31 ± 12%, and 57 ± 18% by mass of Au, respectively, indicating that the increase in polymer concentration facilitated nanocluster formation.

The effect of polymer/Au ratio on nanocluster size and extinction are shown in Figure 3.5 and Table 3.2. As the polymer/Au ratio is increased from 10/1 to 20/1, the nanocluster D_H increases modestly from 24.0 ± 5.6 nm to 29.4 ± 3.2 nm (Figure 3.5a, Table 3.2), and increasing the polymer/Au ratio further to 50/1 increased the D_H to 38.4 ± 7.3 nm (Figure 3.5a, Table 3.2). Size analysis of TEM images of 10-1.7 and 50-1.7 particles (at least 20 particles in several images analyzed) revealed agreement between D_H distributions measured by dynamic light scattering (DLS) and the size measured by TEM analysis (Table 3.2). TEM histograms for 10-1.7 and 50-1.7 particles are shown in Figure C.7. NIR extinction increased with nanocluster D_H, as the extinction at 800 nm increased slightly from 1.01 to 1.05 as polymer/Au ratio was increased from 10/1 to 20/1

(Figure 3.5b). As a result, the ε_{800} increased from 11.2 cm^2/mg to 11.7 cm^2/mg (Figure 3.5b, Table 3.2). A further increase in polymer/Au ratio to 50/1 increased the extinction at 800 nm to 1.17 (Figure 4.5b) and increased ε_{800} to 13.0 cm^2/mg (Figure 3.5b, Table 3.2). The nanocluster ζ potential did not change significantly as the polymer/Au ratio was increased from 10/1 to 20/1, while the ζ potential decreased slightly in magnitude to -12.5 ± 1.2 mV for a polymer/Au ratio of 50/1 (Table 3.2). Large aggregates were not observed in any of these nanocluster samples, even in intensity-weighted D_H distributions (Figure C.8). TGA was conducted on 20-0.9, 20-1.7, and 20-4.0 particles. The organic content in the nanoclusters remained fairly constant (Table C.1) for 20-0.9 and 20-1.7 particles, but a decrease in organic content from 50% w/w to 31.8% w/w was observed as the nanocluster size increased.

In order to provide further evidence for equilibrium formation of nanoclusters, a control experiment was performed, in which 20-0.9 particles were synthesized with solvent evaporation over approximately 4.5 h, in contrast to only ~40 min for particles shown in Figures 3.4. Here, the extinction spectrum and D_H did not change with evaporation rate (Table C.9), supporting the concept of equilibrium rather than kinetically-controlled assembly.

3.3.3 Nanocluster Dissociation

Dissociation of 20-4.0 particles was monitored over 48 h in pH 5 HCl by DLS and UV-Vis-NIR spectroscopy. As the incubation time increased from 6 h to 48 h, the D_H decreased monotonically from 40.1 ± 4.3 nm to 5.0 ± 4.3 nm (Figure 3.6a, Table 3.3), and the extinction at 800 nm (for a Au concentration of 160 μg/ml) decreased from 1.85 to 1.00. As a result, ε_{800} decreased from 12.9 cm^2/mg to 6.3 cm^2/mg (Figure 3.6b, Table

3.3). After 48 h in pH 5 HCl, 20-4.0 nanoclusters dissociated nearly completely to monomer. The high standard deviation of the D_H distribution of dissociated nanoclusters indicates very small oligomers are still present, which is supported by the small (~3% by volume) peak in the size distribution centered around 20 nm as well as the difference between the dissociated nanocluster ε_{800} and the primary particle ε_{800} value of 0.67 cm^2/mg (Table 3.1). These differences are attributed to dimers, trimers, and undissociated nanoclusters that might still be present in solution and which contribute to the NIR extinction and scattering for DLS.[4] The variation of the natural logarithm of the number of particles per nanocluster *versus* time is shown in Figure 3.6c. The number of particles in a cluster n_c is determined by Equation C.6. The plot is quite linear with an R^2 value of ~0.98 (Figure 3.6c) indicating approximately first-order kinetics. The dissociation of 20-4.0 particles was also highly reproducible for two separate samples, as shown in the kinetics plots in Figure C.11. TEM analysis of dissociated 20-4.0 particles after 48 h incubation in pH 5 HCl showed similar results as those given by DLS, as the image showed small primary ~5 nm Au nanospheres (Figure C.12a).

The nanocluster dissociation was further investigated by also placing 20-1.7 particles into pH 5 HCl. Interestingly, after only 24 h of exposure to HCl, the D_H of 20-1.7 particles decreased all the way from 30.0 ± 3.3 nm to 4.0 ± 3.1 nm (Figure 3.7a), and the extinction at 800 nm (for an Au concentration of 60 ug/ml) dropped from 0.71 to 0.06 (Figure 3.7b). As a result, the ε_{800} dropped from 11.8 cm^2/mg to 1.0 cm^2/mg, which is reasonably close to the primary particle ε_{800} value of 0.67 cm^2/mg (Table 3.1). Here, only 0.4% of the particles by volume show a D_H above 5.5 nm, thus leading to the lower standard deviation in the DLS distribution as well as the lower ε_{800} relative to dissociated 20-4.0 particles. TEM analysis of dissociated 20-1.7 particles after 24 h in pH 5 HCl showed ~5 nm primary Au nanospheres, as shown in Figure C.12b.

3.4 DISCUSSION

3.4.1 Equilibrium Cluster Size Model

The equilibrium formation of nanoclusters of primary nanoparticles may be shown to be governed by a balance of short-ranged attractive forces with longer-ranged electrostatic repulsion[29, 30] as described with a free energy model.[12, 14-16, 31] An equilibrium nanocluster with a diameter D_c is depicted in Figure 3.8, along with primary nanoparticles with charge of magnitude q. A fraction of the counter-ions within the nanocluster dissociate and leave the cluster. As the total nanocluster charge grows with added monomer, eventually, the cluster reaches an equilibrium size when the electric field from the nanocluster repels addition of further monomer. Here, short-ranged attractive forces between individual nanoparticle monomers which favor cluster growth are mediated by longer-ranged electrostatic repulsion at the monomer-cluster levels.

The free energy model describes the assembly of nc primary particles into a cluster of radius R_c. [14, 15] Here, the magnitude of attractive interaction between two primary particles with C nearest neighbors is represented by a. The surface energy of the cluster is $4\pi R_c^2\gamma$, where the surface tension γ is approximated as $a/4\pi R^2$, where R is the radius of the primary particle. The attractive component of the free energy is then

$$F_A = -\frac{aCn_c}{2} + a\left(\frac{R_c}{R}\right)^2 \tag{3.1}$$

The repulsive component to cluster free energy is approximated by the expression for a uniform distribution of point charges within a sphere

$$F_R = \frac{3\lambda_b k_B T n_c^2 q^2}{5R_c} \tag{3.2}$$

where λ_b is the Bjerrum length

$$\lambda_b = \frac{e^2}{4\pi\epsilon_r\epsilon_0 k_B T} \tag{3.3}$$

Here, e is the elementary unit of charge, ϵr is the dielectric constant within the nanocluster, and ϵ_0 is the relative permittivity of free space.

The minimization of the free energy with respect to the cluster radius R_c yields the following expression for equilibrium cluster size:

$$n^* = \frac{5aR}{6\lambda_b k_B T q^2} \tag{3.4}$$

where n* is the equilibrium number of monomers per cluster. From Equation 4.4, the cluster size increases with the magnitude of attraction a between primary particles and decreases with the magnitude of charge q. More recently, this theory was extended to include the effect of the fractal dimension of the cluster, and was shown to capture the trends in the size of protein nanoclusters, by fitting ϵr and the number of dissociable ion sites per primary particle, σs (Appendix C), as adjustable parameters.[14]

The experimentally observed correlation between polymer concentration and nanocluster size led us to postulate that polymer-induced depletion attraction plays an important role in nanocluster formation. Upon addition of the weakly adsorbing triblock copolymer, an osmotic pressure gradient is produced from the exclusion of the polymer from the gap between Au particles. This pressure gradient creates an attractive force ("depletion attraction") between the Au nanoparticles. Depletion interactions, which have been carefully characterized in other related systems (see, e.g., Edwards and Bevan,[32] Piech and Walz,[33] and Kulkarni et al.[34]), are strongly dependent on polymer

concentration and the distance between Au particles.[35] We estimate the depletion potential using the Asakura-Oosawa potential,[36, 37] which can be written as:[35]

$$\frac{V_{dep}}{kT} = -\left(\frac{R_g}{R}\right)^{-3}\left(\frac{c_p}{c^*}\right)\left(\frac{R_g}{R}-\frac{H}{2R}\right)^2\left(\frac{3}{2}+\frac{R_g}{R}+\frac{H}{4R}\right) \quad (3.5)$$

where R_g is the radius of gyration of the polymer depletant, c_p is the polymer concentration, and c* is the overlap concentration where polymer chains begin to overlap, which is defined as:[35]

$$c^* = \frac{3M}{4\pi R_g^3 N_{av}} \quad (3.6)$$

where M is the molecular weight of the polymer, and N_{av} is Avogadro's number. Here, we assume that the polymer micelles may be approximated by a PEG chain with a hydrodynamic radius (R_h) equivalent to the radius of the micelle, which was measured to be 7 nm.[5] This assumption is reasonable since the triblock copolymer is mostly composed of PEG. The calculation of the molecular weight of the micelle from the hydrodynamic diameter is given in Appendix C.

3.4.2 Equilibrium Assembly of Au Nanoclusters

The assembly of ~5 nm Au nanoparticles into nanoclusters will now be described in terms of the colloidal forces shown schematically to Figure 3.8. The magnitude of the charge on primary particles was initially reduced by replacing some of the citrate ligands (charge of -3) with cationic lysine ligands (charge of +1) to create a mixed charge

monolayer.[38] The resulting reduction in the zeta potential magnitude from -58 mV to -16 mV will be shown to favor nanocluster formation below.

Equilibrium nanocluster diameters (D_c) predicted by the free energy model are shown to increase over a selected range of 20 to 40 nm with increasing c_{Au} and/or c_p in Figure 3.9.[14, 15] The theoretical model, despite its simplicity, semi-quantitatively predicts the experimental data. The parameters in the model, shown in Table C.2, are discussed in detail in the Appendix C. The total number of charges on the primary nanoparticles in water, 2.78, was determined from zeta potential measurements on lysine/citrate capped primary particles (Table 3.1) using Equation C.6. The charge on a Au nanoparticle within the nanoclusters q was determined by calculating the total number of charges per nanocluster from the measured zeta potentials using Equation C.6, as shown in Appendix C and the number of nanoparticles in a cluster from Equation C.7. We chose a local dielectric constant in the dense nanoclusters of 25, approximately capturing the expected loss with respect to bulk water, as described further in Appendix C. This value is the only adjustable parameter in the model. The interparticle distance in the model was assumed to be 1 nm, which is reasonable because of the high NIR extinction and dense morphologies observed within the nanoclusters. Additionally, the equilibrium model is not very sensitive to interparticle distance, as further discussed in Appendix C.

The rate of depletion-attraction-induced cluster assembly is assumed to be much faster than the rate of polymer adsorption on Au. This is a reasonable assumption given the very low affinity of the dominant PEG block for Au. While depletion attraction is the first effect of the polymer during nanocluster formation, the slower polymer adsorption quenches the final nanocluster size. Thus, we treat the nanocluster formation process, prior to polymer adsorption, as a pseudo-equilibrium process.

As the polymer concentration c_p increases, depletion attraction raises the overall attraction a in Eq. 3.4, consequently increasing the nanocluster size. This trend is shown in Table 3.2 and Figure 3.9 for a final Au concentration of 1.7 mg/ml. Note that the theory mildly underpredicts D_H for the highest polymer concentration (50-1.7). As the number of monomers in the cluster increases, the charge per cluster determined from the zeta potential increases. This experimental charge in the nanocluster, relative to the total charge expected based on the initial charge on each primary particle, was only 11.0% for the 10-1.7 cluster, indicating significant ion pairing. Furthermore, this ratio decreased monotonically from 11.0% to 4.3% (Table 3.4) as the cluster size increased with c_p. Additionally, an increase in final c_{Au} leads to a decrease in the charge per particle q, since fewer counterions are required to dissociate per volume to provide the same entropic gain, as shown in Equation C.11. As the charge decreases, the equilibrium nanocluster size increases, according to Equation 3.4. Thus, as the final c_{Au} is increased, D_c increases.

The combined effect of increased depletion attraction and reduction in charge is seen experimentally through the variance in final Au concentration while maintaining a constant polymer/Au ratio. As c_{Au} is increased from 0.9 mg/ml (20-0.9 particles) to 4.0 mg/ml (20-4.0 particles), the enhanced depletion attraction as well as the reduced Coulombic repulsion increase the D_c of the cluster. The decrease in q is shown in Table 3.4, as the charge retained in a nanocluster decreases monotonically from 10.0% to 4.3% (Table 3.4), due to entropic effects. Thus, the experimental nanocluster sizes are predicted semi-quantitatively by the theoretical model.

Nanocluster formation pathways are illustrated schematically in Figure 3.10. Here, open symbols represent the Au and polymer concentrations resulting from the mixing of polymer and Au nanoparticle solutions. Evaporation of water from these mixed solutions is shown by the solid lines with arrows, resulting in the final Au and c_p

represented by the solid symbols (Figure 3.10). During solvent evaporation, the increase in c_p increases the magnitude of polymer- induced depletion attraction between particles, as is shown by Equation 3.5. In addition, the increase in c_{Au} decreases the charge, as shown in Equation C.11. Both of these factors increase the cluster size.

3.4.3 Quenching of Nanocluster Size

After assembly of the Au nanospheres into nanoclusters, this quasi-equilibrium state is quenched by irreversible polymer adsorption. The hydrophobic nature of the PLA groups in the PLA-PEG-PLA triblock copolymer drives the polymer adsorption on the hydrophobic Au surface.[39] The rate of this polymer adsorption, however, is expected to be much slower than the rate of depletion attraction-induced equilibrium particle assembly. The weak driving force for adsorption reflects the large amount of hydrophilic PEG in the polymer which interacts only weakly with the hydrophobic Au surface.[39] If polymer adsorbed on individual Au spheres, which then formed clusters, the Au primary particle spacings would be too large for the intense NIR extinction observed in Figures 3b and 5b. Instead, the slow kinetics of polymer adsorption relative to rapid nanocluster formation, led to very closely spaced Au particles. Additionally, the adsorbed polymer provided steric stabilization on the nanoclusters surface. To harvest the nanoclusters, they were rapidly diluted in deionized water, as shown by the dashed lines in Figure 3.10. Here, the cluster size did not change. The high degree of dilution would lead to Au monomer particles according the equilibrium model (Figure 3.10). Instead, the irreversible polymer adsorption on the nanocluster surface maintained a "quenched" equilibrium cluster size. Furthermore, attraction between the highly ion paired Au primary particles within the cluster with low charge prevented nanocluster dissociation.

The polymer played a multifunctional role in: (1) driving the depletion attraction to assemble the primary Au particles into clusters, (2) providing steric stabilization of the clusters, and (3) quenching the nanoclusters with an equilibrium size. The clusters were fairly dilute and colloidally stable over weeks, so we did not calculate the interaction potential between the clusters.

The concept of quenched equilibrium Au nanoclusters presented in this work is substantially different from our previous Au nanocluster studies, which attributed nanocluster formation to a kinetic assembly mechanism.[5] In our previous work, a kinetic stability ratio was estimated based on the time required for a qualitative color change in the nanocluster dispersion by eye during formation.[5] This approach was not applicable to nanoclusters smaller than 50 nm where the color change was very rapid and heavily dependent upon the evaporation rate of the solvent. The previous work did not recognize the depletion force was sufficiently strong to produce equilibrium assembly (given the micelle concentration was unknown), and thus equilibrium assembly was not thought to be present.[5] Furthermore, the composition of the ligands on the surface was not measured, and the charge on the Au surface was not well-characterized, which limited the analysis of the formation mechanism.[4, 5] In most cases, all of the water was evaporated for form Au-polymer films which were later diluted to harvest the clusters. This two-step approach may involve complex cluster formation mechanisms. As a result, the present study represents a major and novel advance over previous work by demonstrating equilibrium nanocluster assembly and control over nanocluster size.

In an insightful related study, "self-limiting" clusters of CdSe primary particles have been observed in water, where cluster growth stopped upon reaching a balance between charge in the cluster and van der Waals attraction between particles.[6] Both nanocluster size and zeta potential measurements showed cluster growth followed by a

plateau as the self-limited cluster state was reached.[6] Building upon this "self-limiting" nanocluster concept, a novel aspect of the present work is that degradation of the polymer quencher allows for reversible cluster dissociation to recover ~5 nm monomers, which is critical for effective renal clearance. Moreover, the present study demonstrates the ability to tune nanocluster size by balancing effective colloidal interactions as well as the ability to semi-quantitatively predict this cluster size.

In the current study, we chose to form nanoclusters at a desired evaporation extent of only 50% and from primary Au nanospheres with a zeta potential of only -16 mV. If the zeta potential of the primary nanospheres were more negative, electrostatic repulsion would be too dominant, and the size would be too small, as shown in Equation 3.4. For example, for highly charged Au particles with only citrate ligands, the required evaporation extent was 85% to form nanoclusters, as would be evident in Figure 3.10. However at such high evaporation amounts, the particles form a viscous gel and it may become difficult to redisperse the clusters with the desired size and with low polydispersity.

For particular experimental pathways, other than those in Table 3.1 and Figure 3.10, we observed kinetic traps that prevented attainment of the sizes predicted by the equilibrium model. For example, adding polymer solution in one step, instead of iteratively, to the Au solution led to large nanoclusters with weak NIR extinction. Immediately after mixing the Au dispersion with the polymer solution, we observed a large increase in viscosity, which may have limited access to equilibrium configurations, leading to relatively large ~120 nm aggregates with weak NIR extinction (Table C.4). In addition, initial Au concentrations in excess of 6 mg/ml led to irreversible aggregation of nanoparticles even without adding any polymer, indicating insufficient electrostatic stabilization.

These quenched equilibrium Au nanoclusters are quite different from other clusters which are affected by dilution, such as protein nanoclusters[14] as well as clusters of cerium oxide[40] and iron oxide[41] nanoparticles and oppositely-charged diblock polymers. The size of kinetically "frozen" clusters of cerium oxide, from 100 nm to 500 nm in diameter, has been shown to change with dilution rate, with smaller clusters formed at faster dilution rates.[40] Equilibrium Au nanoclusters, if quenched by irreversible polymer adsorption, in contrast, do not change size after dilution.

4.4.4 Nanocluster Dissociation

For a Au dispersion without polymer present, depletion attraction between Au nanoparticles is not present and the equilibrium state was found to be individual charged primary particles (Figure 3.10). For polymer coated Au nanoclusters, dissociation was initiated by exposure to a pH 5 HCl environment, which accelerates the degradation rate of the PLA segments, relative to pH7.[42] As the polymeric quencher was gradually removed upon hydrolysis, the cluster size decreased continuously as charged Au primary particles left the nanocluster surface. After 48 h, enough polymer had degraded for the 20-4.0 nanoclusters to dissociate almost completely to monomer.

The plot of ln(n_c) *versus* time shown in Figure 3.6c indicates approximately first-order kinetics, as demonstrated in Equation 3.6:

$$\frac{dn_c}{dt} = -kn_c \tag{3.6}$$

Here, n_c is the number of particles in a cluster, given by Equation C.7, and k is the first-order rate constant. The linear fit to the data shown in Figure 3.6c reveals a k of ~0.12 hr^{-1}.

The dissociation of the smaller 20-1.7 nanoclusters was faster and more complete (Figure 3.7) relative to the larger 20-4.0 ones. For the smaller nanocluter size, less time is needed to degrade the smaller amount of polymeric quencher, for a fixed polymer/Au ratio. Additionally, there are fewer chances for dissociating nanoclusters to become trapped in metastable irreversible states involving even a small number dimers, trimers, and higher-order assemblies. The NIR extinction is significant for dimers and trimers at close spacing,[5] as seen in Figure 3.6 with 20-4.0 particles. The complete dissociation to charged Au monomer nanospheres supports the quenched equilibrium concept, whereby the polymer no longer influences the Au particles size after it is degraded. After PLA hydrolysis, the PEG central block did not have a tendency to adsorb strongly on Au,[39] and during dissociation the polymer concentration was too low to produce depletion attraction.

4.4.5 Nanocluster Spectral Properties

The surface plasmon resonance for Au nanoparticles is well known to shift to the NIR for various morphologies including nanoshells,[23, 24, 43, 44] nanocages,[45, 46] high aspect ratio nanorods,[47, 48] nanoflowers[49, 50] or nanostars.[51, 52] These particles with NIR extinction, however, often have diameters greater than 5.5 nm in diameter, which would be too large for efficient kidney clearance from the body.[27] Alternatively, the SPR has been experimentally demonstrated to shift towards the NIR for dimers and trimers of Au nanospheres,[43] and broad NIR extinction has been observed in larger clusters of Au

nanospheres.[4, 5] The amount of extinction broadening has been shown to be dependent on the interparticle spacing between constituent particles.[43] In the present work, intense NIR extinction is achieved *via* extremely close (less than a particle diameter[8, 53]) interparticle spacings within Au nanoclusters. As the polymer/Au ratio is increased, the corresponding increase in depletion attraction can potentially decrease the interparticle spacing, while simultaneously increasing nanocluster size. As a result, the amount of NIR extinction increases, as is shown in Figure 3.5b. In addition, as the final Au concentration was increased (along with the final polymer concentration), the charge per primary particle in a cluster was decreased, potentially decreasing the interparticle spacing and increasing nanocluster size. The resultant increase in cluster size and decrease in interparticle spacings creates broader extinction spectra and greater NIR extinction (Figure 3.3b).

The Au nanoclusters exhibited intense NIR extinction which is of interest in applications such as photoacoustic imaging[20] and photothermal therapy.[22, 23, 44] The fine control over nanocluster size demonstrated in this study from ~20 nm to ~40 nm is in an optimal range for cell uptake[54] and blood circulation.[55] In addition, the biodegradability of these nanoclusters into ~5 nm primary particles offers the possibility of clearance *via* the kidneys.[27] In future applications, the nanoclusters would potentially be targeted to cancer cells *via* biomarkers such as epidermal growth factor receptor (EGFR) and consequently undergo endosomal uptake.[56] Multiple studies have demonstrated that after intravascular (IV) administration in tumor animal models, injected nanoparticles accumulate mostly in the liver, spleen, and tumor.[57] Since nanoclusters have been shown to dissociate within acidic endosomal and lysosomal compartments,[4] we hypothesize that the nanoclusters in this work will dissociate completely to primary particles in the acidic endosomal/lysosomal cellular compartments, and that these particles will then be cleared from the body.

4.5 CONCLUSIONS

Equilibrium phenomena play a major role in governing the size of Au nanoclusters, which are quenched by irreversibly adsorbed polymer on the surface. Upon biodegradation of various amounts of the quencher, PLA(1k)-b-PEG(10k)-b-PLA(1k), the clusters reversibly become smaller and eventually dissociate completely to ~5 nm Au monomer nanospheres. Nanocluster size was tuned from ~20 nm to ~40 nm by varying the ratio of polymer/Au from 10/1 to 50/1 w/w, to vary the depletion attraction induced by the polymer, and also by varying the Au nanoparticle concentrations from 0.9 mg/ml to 4 mg/ml. The surface charge on primary Au nanospheres was modified by the addition of positively charged lysine to originally citrate-capped nanospheres to create a mixed charge monolayer on the Au nanosphere surface. The incremental mixing of the polymer solution with the initial Au dispersion, along with solvent evaporation to raise Au and polymer concentrations, provided exquisite regulation of the nanocluster size. The size was predicted semi-quantitatively with an equilibrium free energy model as a function of the Au concentration and the polymer/Au ratio. The free energy model describes the balance between long-ranged electrostatic repulsion between primary Au nanospheres with short-ranged van der Waals and depletion attractive interactions. The equilibrium size is quenched by an irreversibly adsorbed polymer layer on the nanocluster surface, and remains constant even after removal of excess polymer. The close spacings of primary nanospheres within the nanoclusters resulted in high NIR extinction for all sizes of nanoclusters explored in this work. Thus, a general concept has been demonstrated for forming quenched equilibrium nanoclusters with tunable sizes (and in this case NIR extinction), which reversibly dissociate upon biodegradation of the polymer quencher.

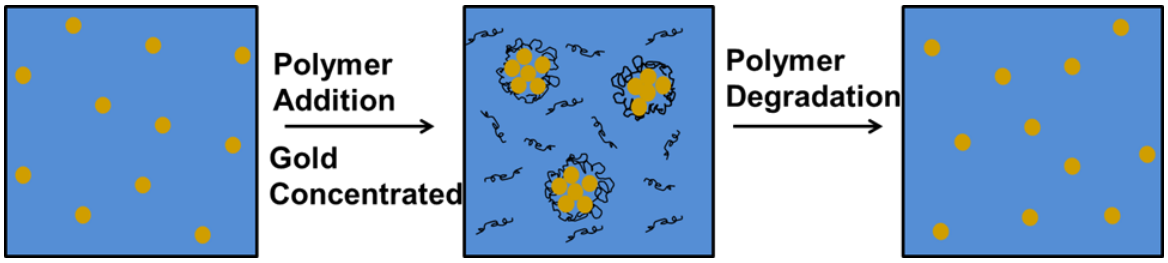

Figure 3.1: Schematic of quenched equilibrium nanocluster formation and dissociation process. A polymer solution is added to a Au nanoparticle dispersion, and the mixture is then concentrated through partial water evaporation in order to form Au nanoclusters. Polymer degradation upon hydrolysis results in the dissociation of nanoclusters back to primary charged Au nanospheres.

Table 3.1: Properties of nanospheres before and after place exchange

Sample	**D_H (nm)**	**ε_{800} (cm^2/mg)**	**Zeta Potential (mV)**	**Ligand % by weight (TGA)**	**Lysine/Citrate ratio (XPS)**
Citrate	4.3 ± 0.7	0.44	-58.4 ± 5.3	4%	n/a
Citrate/lysine	4.7 ± 0.8	0.67	-16.0 ± 6.6	4%	1.4

Table 3.2: Properties of nanoclusters. The final Au and polymer concentrations are after solvent evaporation but prior to dilution to harvest the nanoclusters. Sample names contain two numbers separated by a dash: final polymer/Au mass ratio and final Au concentration in mg/ml.

Sample	**Final Au Conc (mg/ml)**	**Final Polymer Conc (mg/ml)**	**D_H (nm)**	**TEM Diameter (nm)**	**ε_{800} (cm^2/mg)**	**Zeta Potential (mV)**	**Au Yield By Mass (%)**
20-0.9	0.9	18	21.4 ± 4.4	24.0 ± 6.2	10.6	-12.3 ± 1.1	17 ± 6
20-1.7	1.7	34	29.4 ± 3.2	31.1 ± 6.9	11.7	-16.4 ± 3.6	31 ± 12
20-4.0	4.0	80	40.1 ± 4.3	42.7 ± 9.4	12.9	-13.2 ± 0.6	61 ± 15
10-1.7	1.7	17	24.0 ± 5.6	21.0 ± 4.3	11.2	-16.7 ± 3.6	26 ± 13
50-1.7	1.7	85	38.4 ± 7.3	36.3 ± 5.6	13.0	-12.5 ± 1.2	57 ± 18

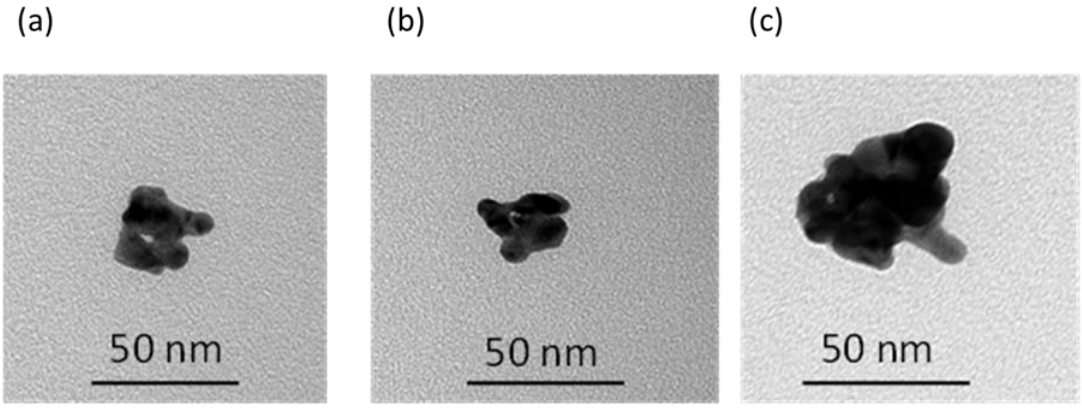

Figure 3.2: Representative TEM images of nanoclusters formed with a final Au concentration of (a) 0.9 mg/ml (20-0.9), (b) 1.7 mg/ml (20-1.7), and (c) 4.0 mg/ml (20-4.0). All samples had a final polymer/Au ratio of 20/1.

(a)

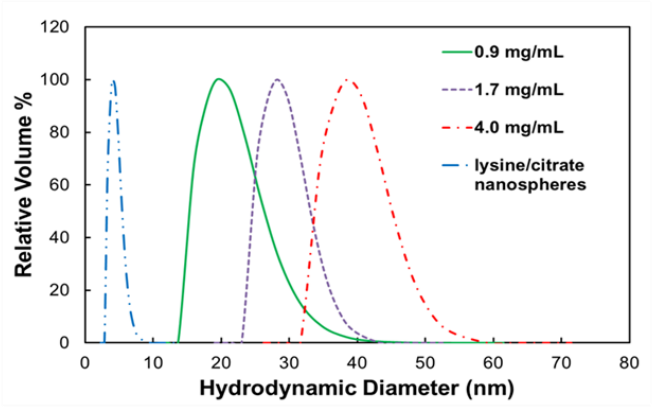

(b)

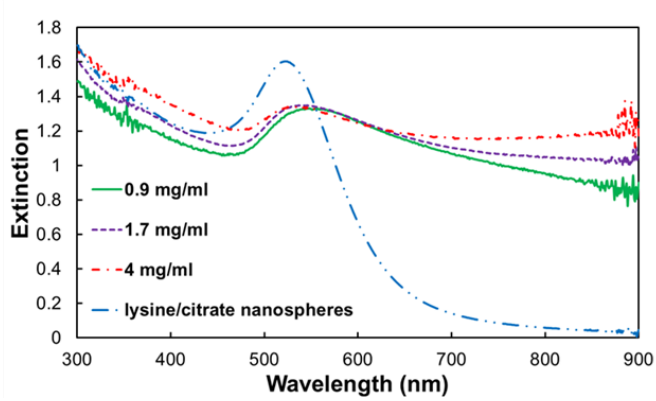

Figure 3.3: (a) DLS D_H distributions, and (b) UV-Vis-NIR extinction spectra of nanoclusters formed with 0.9 mg/ml (20-0.9), 1.7 mg/ml (20-1.7), and 4 mg/ml (20-4.0) final Au concentrations. UV-Vis-NIR spectra were taken at a Au concentration of ~90 µg/ml. All samples had a polymer/Au ratio of 20/1.

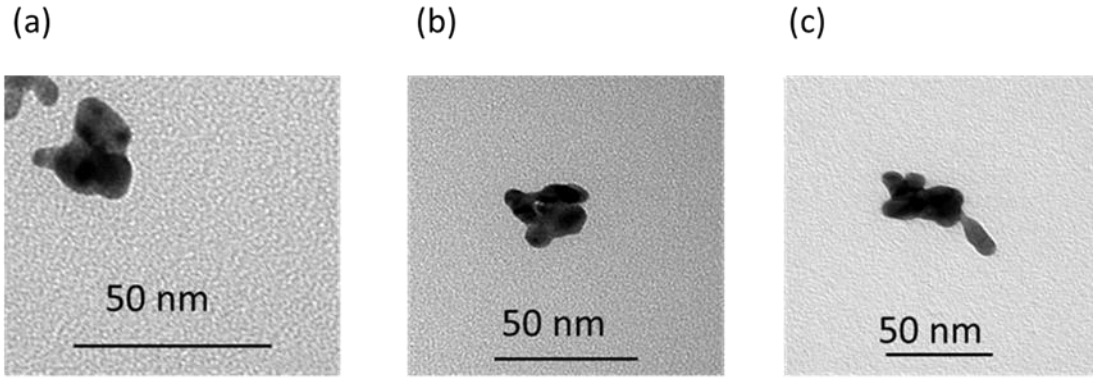

Figure 3.4: Representative TEM images of nanoclusters formed with a final Au concentration of 1.7 mg/ml and polymer/Au ratio of (a) 10/1 (10-1.7), (b) 20/1 (20-1.7), and (c) 50/1 (50-1.7).

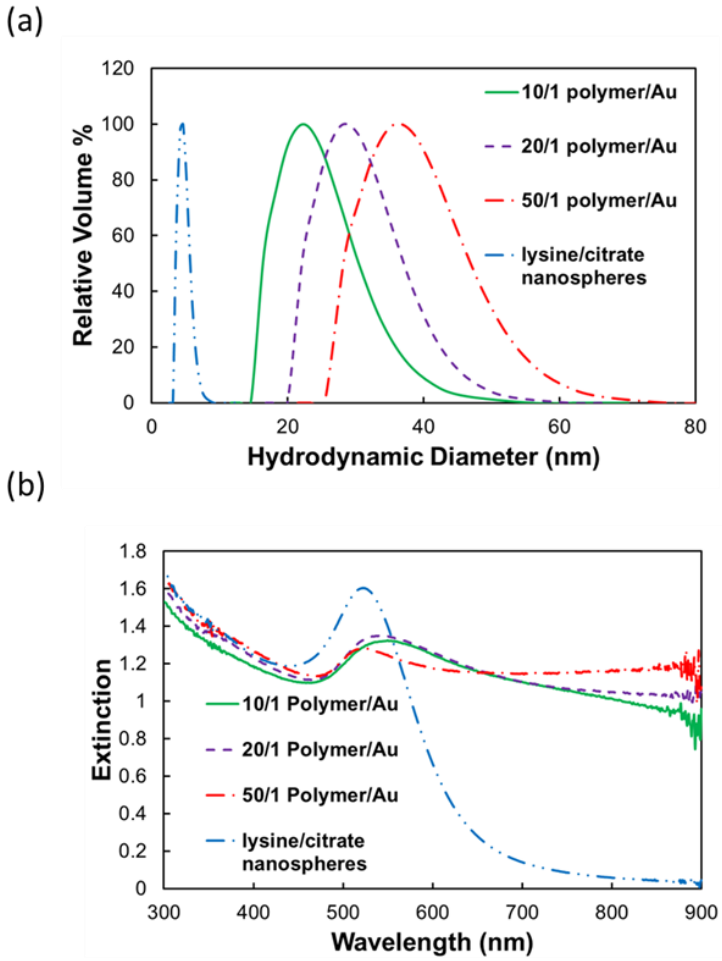

Figure 3.5: (a) DLS D_H distributions, and (b) UV-Vis-NIR extinction spectra of nanoclusters formed with polymer/Au ratios of 10/1 (10-1.7), 20/1 (20-1.7) and 50/1 (50-1.7). UV-Vis-NIR spectra were taken at a Au concentration of ~90 µg/ml. All samples had final Au concentrations of 1.7 mg/ml.

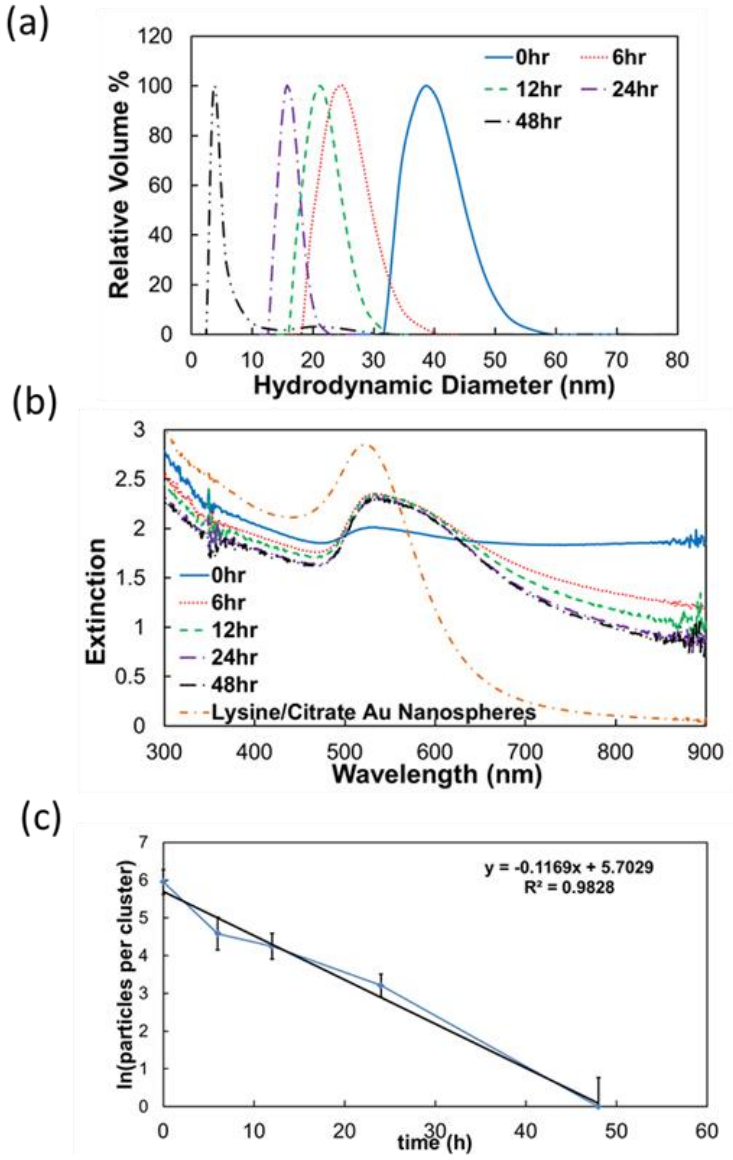

Figure 3.6: (a) DLS D_H distributions (b) UV-Vis-NIR extinction spectra, and (c) kinetics of dissociation of nanoclusters with a polymer/Au ratio of 20/1 and Au concentration of 4.0 mg/ml (20-4.0 particles) at various times after being exposed to a pH 5 HCl environment. UV-Vis-NIR spectra were taken at a Au concentration of ~160 μg/ml. Error bars in (c) correspond to the calculated standard deviation taken from D_H distributions measured by DLS.

Table 3.3: DLS sizes and extinction coefficients of nanoclusters at various dissociation time points.

Incubation Time (h)	**D_H (nm)**	**ε_{800} (cm^2/mg)**
0	40.1 ± 4.3	12.9
6	25.2 ± 3.6	8.4
12	22.7 ± 2.6	7.4
24	16.1 ± 1.6	6.4
48	5.0 ± 4.3	6.3

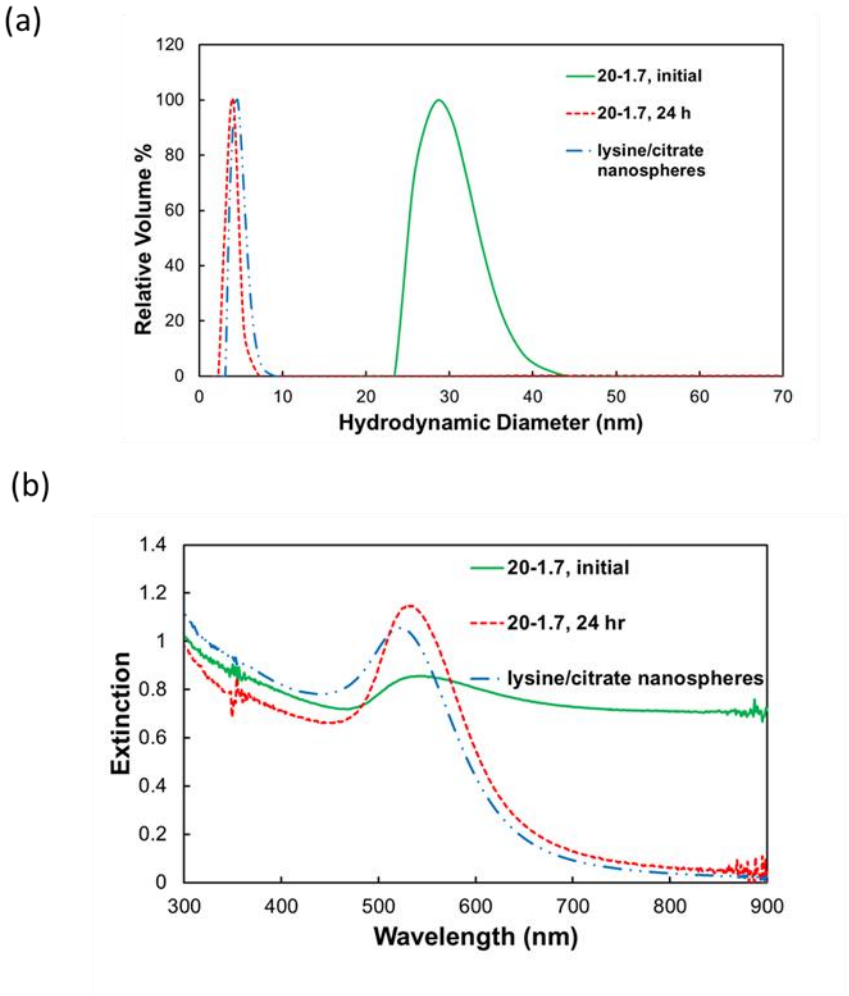

Figure 3.7: (a) DLS D_H distributions and (b) UV-Vis-NIR extinction spectra for nanoclusters with a polymer/Au ratio of 20/1 and a final Au concentration of 1.7 mg/ml (20-1.7 particles) before and after being exposed to a pH 5 HCl environment for 24 h. D_H distributions and UV-Vis-NIR spectra of lysine/citrate capped nanospheres are also included for reference. UV-Vis-NIR spectra were taken at a Au concentration of ~60 μg/ml.

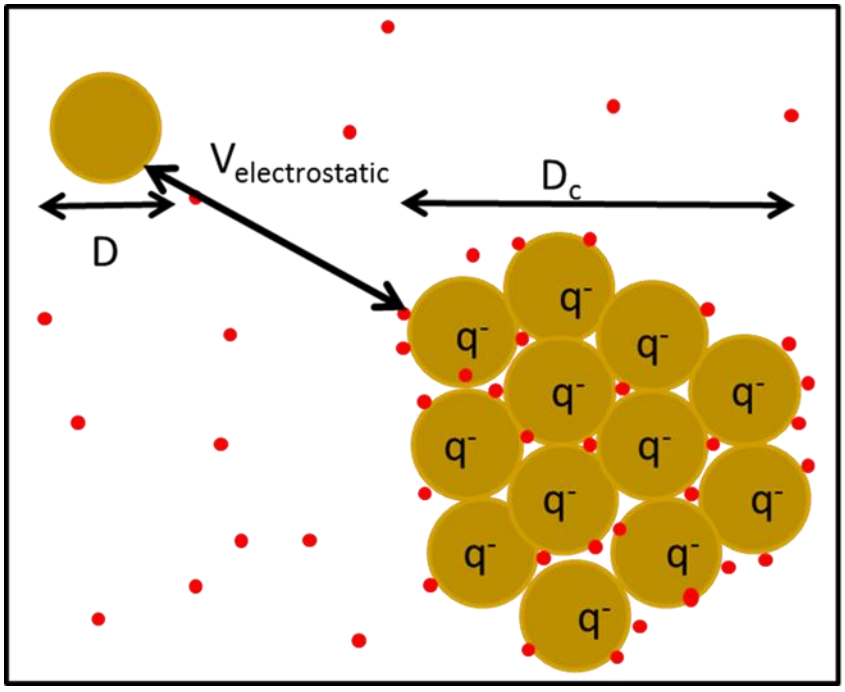

Figure 3.8: Equilibrium nanocluster with diameter D_c composed of primary particles (of diameter D) each with ion pairs and a negative charge of magnitude q. The highly charged monomer coated with ligands (negligible ion pairing) on the top left is repelled by the charged nanocluster ($V_{electrostatic}$). Bound and free counterions are represented by red dots.

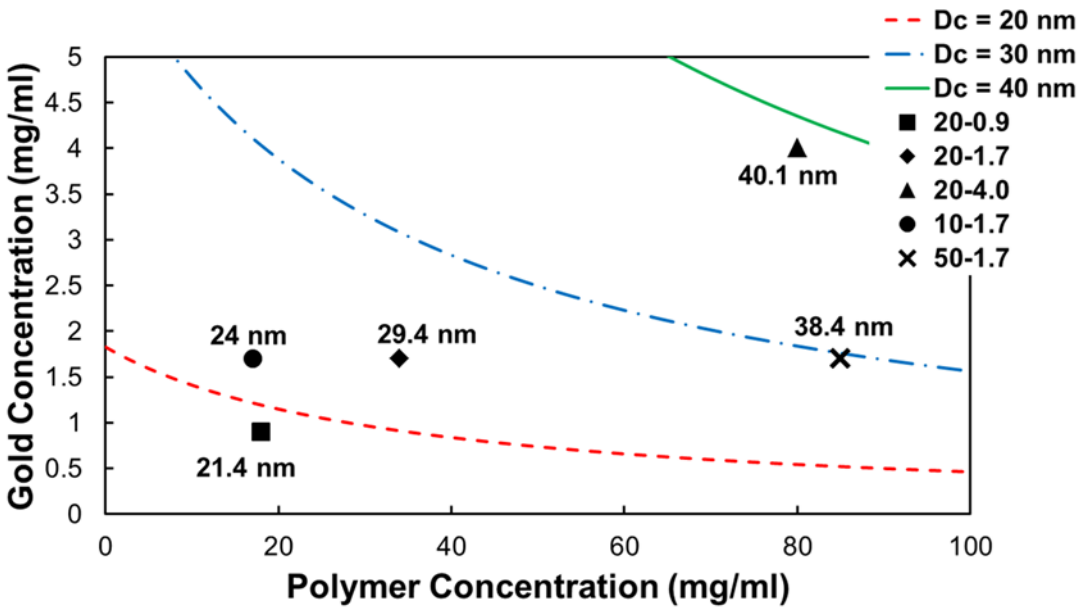

Figure 3.9: Cluster-size contours for various values of polymer and Au concentration, based on the equilibrium free energy model discussed in the text. Hydrodynamic diameters (DLS) shown by points are in reasonable agreement with the model.

Table 3.4: Zeta potentials and charges per cluster (experimental, based on zeta potential and aggregation number) compared with calculated charge if all monomers stayed fully charged upon cluster formation

Sample	**Zeta Potential (mV)**	**Negative Charges per Cluster**	**Negative Charges per Cluster Calc.**	**% Charge Retained**
20-0.9	-12.3 ± 1.1	15.1	157	10.0%
20-1.7	-16.4 ± 3.6	33.0	407	8.1%
20-4.0	-13.2 ± 0.6	44.2	1033	4.3%
10-1.7	-16.7 ± 3.6	24.4	221	11.0%
50-1.7	-12.5 ± 1.2	38.8	907	4.3%

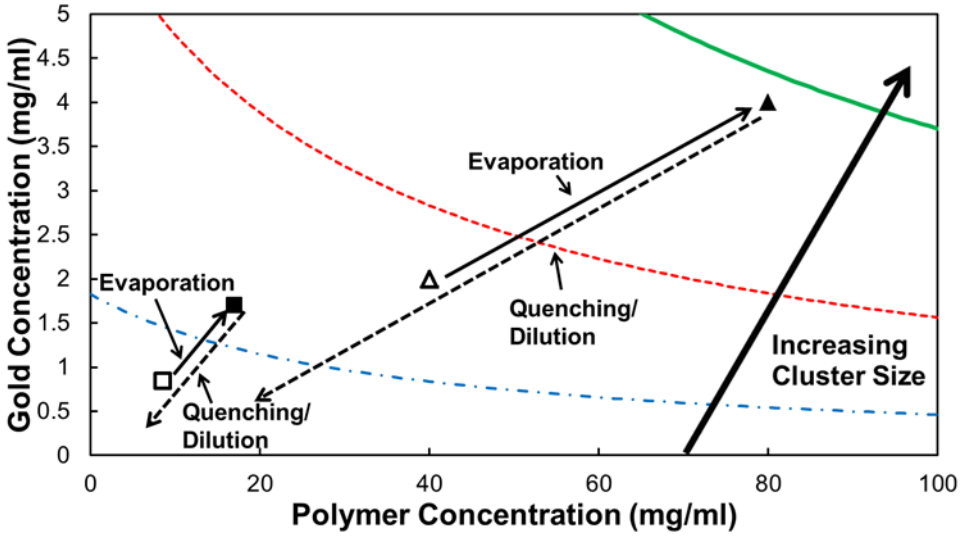

Figure 3.10: Schematic of equilibrium nanocluster formation process followed by polymer quenching. Curves of constant cluster diameter (D_c) as a function of polymer and Au concentrations are shown as countours predicted from the equilibrium free energy model discussed in the text and parameters in Table C.2. Open symbols represent concentrations upon mixing of polymer and Au nanoparticle solutions, and filled symbols represent Au and polymer concentrations after evaporation of 50% of the solvent. Solid lines represent the evaporation process, and dashed lines represent the dilution of the quenched clusters, during which nanocluster size is constant (*i.e.*, quenched due to polymer adsorption). Process lines are presented for 20-4.0 (triangles) and 10-1.7 particles (squares).

3.6 REFERENCES

1. Boal, A. K.; Ilhan, F.; DeRouchey, J. E.; Thurn-Albrecht, T.; Russell, T. P.; Rotello, V. M. Self-Assembly of Nanoparticles into Structured Spherical and Network Aggregates. *Nature* **2000**, *404*, 746-748.

2. Shenhar, R.; Norsten, T. B.; Rotello, V. M. Polymer-Mediated Nanoparticle Assembly: Structural Control and Applications. *Adv. Mater.* **2005**, *17*, 657-669.

3. Ma, L. L.; Feldman, M. D.; Tam, J. M.; Paranjape, A. S.; Cheruki, K. K.; Larson, T. A.; Tam, J. O.; Ingram, D. R.; Paramita, V.; Villard, J. W.*, et al.* Small Multifunctional Nanoclusters (Nanoroses) for Targeted Cellular Imaging and Therapy. *ACS Nano* **2009**, *3*, 2686-2696.

4. Tam, J. M.; Tam, J. O.; Murthy, A.; Ingram, D. R.; Ma, L. L.; Travis, K.; Johnston, K. P.; Sokolov, K. V. Controlled Assembly of Biodegradable Plasmonic Nanoclusters for Near-Infrared Imaging and Therapeutic Applications. *ACS Nano* **2010**, *4*, 2178-2184.

5. Tam, J. M.; Murthy, A. K.; Ingram, D. R.; Nguyen, R.; Sokolov, K. V.; Johnston, K. P. Kinetic Assembly of Near-IR Active Gold Nanoclusters Using Weakly Adsorbing Polymers to Control the Size. *Langmuir* **2010**, *26*, 8988-8999.

6. Xia, Y. S.; Nguyen, T. D.; Yang, M.; Lee, B.; Santos, A.; Podsiadlo, P.; Tang, Z. Y.; Glotzer, S. C.; Kotov, N. A. Self-Assembly of Self-Limiting Monodisperse Supraparticles from Polydisperse Nanoparticles. *Nat. Nanotechnol.* **2011**, *6*, 580-587.

7. Ofir, Y.; Samanta, B.; Rotello, V. M. Polymer and Biopolymer Mediated Self-Assembly of Gold Nanoparticles. *Chem. Soc. Rev.* **2008**, *37*, 1814-1825.

8. Srivastava, S.; Frankamp, B. L.; Rotello, V. M. Controlled Plasmon Resonance of Gold Nanoparticles Self-Assembled with PAMAM Dendrimers. *Chem. Mater.* **2005**, *17*, 487-490.

9. Larson-Smith, K.; Pozzo, D. C. Scalable Synthesis of Self-Assembling Nanoparticle Clusters Based on Controlled Steric Interactions. *Soft Matter* **2011**, *7*, 5339-5347.

10. Wilcoxon, J. P.; Martin, J. E.; Schaefer, D. W. Aggregation in Colloidal Gold. *Phys. Rev. A* **1989**, *39*, 2675-2688.

11. Lu, P. J.; Zaccarelli, E.; Ciulla, F.; Scholfield, A. B.; Sciortino, F.; Weitz, D. A. Gelation of Particles with Short-Range Attraction. *Nature* **2008**, *453*, 499-504.

12. Sedgwick, H.; Egelhaaf, S. U.; Poon, W. C. K. Clusters and Gels in Systems of Sticky Particles. *J. Phys.-Condes. Matter* **2004**, *16*, S4913-S4922.

13. Buitenhuis, J.; Dhont, J. K. G.; Lekkerkerker, H. N. W. Static and Dynamic Light Scattering by Concentrated Colloidal Suspensions of Polydisperse Sterically Stabilized Boehmite Rods. *Macromolecules* **1994**, *27*, 7267-7277.

14. Johnston, K. P.; Maynard, J. A.; Truskett, T. M.; Borwankar, A. U.; Miller, M. A.; Wilson, B. K.; Dinin, A. K.; Khan, T. A.; Kaczorowski, K. J. Concentrated Dispersion of Equilibrium Protein Nanoclusters That Reversibly Dissociate into Active Monomers. *ACS Nano* **2012**, *6*, 1357-1369.

15. Groenewold, J.; Kegel, W. K. Anomalously Large Equilibrium Clusters of Colloids. *J. Phys. Chem. B* **2001**, *105*, 11702-11709.

16. Stradner, A.; Sedgwick, H.; Cardinaux, F.; Poon, W. C. K.; Egelhaaf, S. U.; Schurtenberger, P. Equilibrium Cluster Formation in Concentrated Protein Solutions and Colloids. *Nature* **2004**, *432*, 492-495.

17. Porcar, L.; Falus, P.; Chen, W.-R.; Faraone, A.; Fratini, E.; Hong, K.; Baglioni, P.; Liu, Y. Formation of the Dynamic Clusters in Concentrated Lysozyme Protein Solutions. *J. Phys. Chem. Lett.* **2010**, *1*, 126-129.

18. Weissleder, R. A Clearer Vision for *in Vivo* Imaging. *Nat. Biotechnol.* **2001**, *19*, 316-317.

19. Mallidi, S.; Larson, T.; Aaron, J.; Sokolov, K.; Emelianov, S. Molecular Specific Optoacoustic Imaging with Plasmonic Nanoparticles. *Opt. Express* **2007**, *15*, 6583-6588.

20. Mallidi, S.; Larson, T.; Tam, J.; Joshi, P. P.; Karplouk, A.; Sokolov, K.; Emelianov, S. Multiwavelength Photoacoustic Imaging and Plasmon Resonance Coupling of Gold Nanoparticles for Selective Detection of Cancer. *Nano Lett.* **2009**, *9*, 2825-2831.

21. Agarwal, A.; Huang, S. W.; O'Donnell, M.; Day, K. C.; Day, M.; Ashkenazi, S. Targeted Gold Nanorod Contrast Agent for Prostate Cancer Detection by Photoacoustic Imaging. *J. Appl. Phys.* **2007**, *102*, 0647011-0647014.

22. Khlebtsov, B.; Zharov, V.; Melnikov, A.; Tuchin, V.; Khlebtsov, N. Optical Amplification of Photothermal Therapy with Gold Nanoparticles and Nanoclusters. *Nanotechnology* **2006**, *17*, 5167-5179.

23. Hirsch, L. R.; Stafford, R. J.; Bankson, J. A.; Sershen, S. R.; Rivera, B.; Price, R. E.; Hazle, J. D.; Halas, N. J.; West, J. L. Nanoshell-Mediated Near-Infrared Thermal Therapy of Tumors under Magnetic Resonance Guidance. *Proc. Natl. Acad. Sci.* **2003**, *100*, 13549-13554.

24. Loo, C.; Lowery, A.; Halas, N.; West, J.; Drezek, R. Immunotargeted Nanoshells for Integrated Cancer Imaging and Therapy. *Nano Lett.* **2005**, *5*, 709-711.

25. Larson, T. A.; Bankson, J.; Aaron, J.; Sokolov, K. Hybrid Plasmonic Magnetic Nanoparticles as Molecular Specific Agents for MRI/Optical Imaging and Photothermal Therapy of Cancer Cells. *Nanotechnology* **2007**, *18*.

26. von Maltzahn, G.; Park, J.-H.; Agrawal, A.; Bandaru, N. K.; Das, S. K.; Sailor, M. J.; Bhatia, S. N. Computationally Guided Photothermal Tumor Therapy Using Long-Circulating Gold Nanorod Antennas. *Cancer Res.* **2009**, *69*, 3892-3900.

27. Choi, H. S.; Liu, W.; Misra, P.; Tanaka, E.; Zimmer, J. P.; Ipe, B. I.; Bawendi, M. G.; Frangioni, J. V. Renal Clearance of Quantum Dots. *Nat. Biotechnol.* **2007**, *25*, 1165-1170.

28. Gavrilenko, V. I., *Optics of Nanomaterials*. Pan Stanford Publishing: Singapore, 2011; p 63-66.

29. Zhang, C.; Pansare, V. J.; Prud'homme, R. K.; Priestley, R. D. Flash Nanoprecipitation of Polystyrene Nanoparticles. *Soft Matter* **2012**, *8*, 86-93.

30. Cheng, C.; Wen, Y.; Xu, X.; Gu, H. Tunable Synthesis of Carboxyl-Functionalized Magnetite Nanocrystal Clusters with Uniform Size. *J. Mater. Chem.* **2009**, *19*, 8782-8788.

31. Zaccarelli, E. Colloidal Gels: Equilibrium and Non-Equilibrium Routes. *J. Phys.-Condes. Matter* **2007**, *19*, 1-50.

32. Edwards, T. D.; Bevan, M. A. Polymer Mediated Depletion Attraction and Interfacial Colloidal Phase Behavior. *Macromolecules* **2012**, *45*, 585-594.

33. Piech, M.; Walz, J. Y. Direct Measurement of Depletion and Structural Forces in Polydisperse, Charged Systems. *J. Colloid Interface Sci.* **2002**, *253*, 117-129.

34. Kulkarni, A. M.; Chatterjee, A. P.; Schweizer, K. S.; Zukoski, C. F. Depletion Interactions in the Protein Limit: Effects of Polymer Density Fluctuations. *Phys. Rev. Lett.* **1999**, *83*, 4554-4557.

35. Lekkerkerker, H. N. W.; Tuinier, R., *Colloids and the Depletion Interaction*. Springer: New York, 2011; Vol. 833, p 12-15.

36. Asakura, S.; Oosawa, F. On Interaction between 2 Bodies Immersed in a Solution of Macromolecules. *J. Chem. Phys.* **1954**, *22*, 1255-1256.

37. Asakura, S.; Oosawa, F. Interaction between Particles Suspended in Solutions of Macromolecules. *J. Polym. Sci.* **1958**, *33*, 183-192.

38. Chen, S.; Yu, F.; Yu, Q.; He, Y.; Jiang, S. Strong Resistance of a Thin Crystalline Layer of Balanced Charged Groups to Protein Adsorption. *Langmuir* **2006**, *22*, 8186-8191.

39. Sakai, T.; Alexandridis, P. Mechanism of Gold Metal Ion Reduction, Nanoparticle Growth and Size Control in Aqueous Amphiphilic Block Copolymer Solutions at Ambient Conditions. *J. Phys. Chem. B* **2005**, *109*, 7766-7777.

40. Fresnais, J.; Lavelle, C.; Berret, J.-F. Nanoparticle Aggregation Controlled by Desalting Kinetics. *J. Phys. Chem. C* **2009**, *113*, 16371-16379.

41. Berret, J.-F. Stoichiometry of Electrostatic Complexes Determined by Light Scattering. *Macromolecules* **2007**, *40*, 4260-4266.

42. Ivanova, T.; Panaiotov, I.; Proust, J. E.; Benoit, J. P.; Verger, R. Hydrolysis Kinetics of Poly(D,L-Lactide) Monolayers Spread on Basic or Acidic Aqueous Subphases. *Colloids and Surfaces B: Biointerfaces* **1997**, *8*, 217-225.

43. Halas, N. J.; Lal, S.; Chang, W.-S.; Link, S.; Nordlander, P. Plasmons in Strongly Coupled Metallic Nanostructures. *Chem. Rev.* **2011**, *111*, 3913-3961.

44. Gobin, A. M.; Lee, M. H.; Halas, N. J.; James, W. D.; Drezek, R. A.; West, J. L. Near-Infrared Resonant Nanoshells for Combined Optical Imaging and Photothermal Cancer Therapy. *Nano Lett.* **2007**, *7*, 1929-1934.

45. Chen, J.; Saeki, F.; Wiley, B. J.; Cang, H.; Cobb, M. J.; Li, Z. Y.; Au, L.; Zhang, H.; Kimmey, M. B.; Li, X.*, et al.* Gold Nanocages: Bioconjugation and Their Potential Use as Optical Imaging Contrast Agents. *Nano Lett.* **2005**, *5*, 473-477.

46. Song, K. H.; Kim, C.; Cobley, C. M.; Xia, Y.; Wang, L. V. Near-Infrared Gold Nanocages as a New Class of Tracers for Photoacoustic Sentinel Lymph Node Mapping on a Rat Model. *Nano Lett.* **2009**, *9*, 183-188.

47. Huang, X.; El-Sayed, I. H.; Qian, W.; El-Sayed, M. A. Cancer Cell Imaging and Photothermal Therapy in the Near-Infrared Region by Using Gold Nanorods. *J. Am. Chem. Soc.* **2006**, *128*, 2115-2120.

48. Link, S.; Mohamed, M. B.; El-Sayed, M. A. Simulation of the Optical Absorption Spectra of Gold Nanorods as a Function of Their Aspect Ratio and the Effect of the Medium Dielectric Constant. *J. Phys. Chem. B* **1999**, *103*, 3073-3077.

49. Wang, W.; Yang, X.; Cui, H. Growth Mechanism of Flowerlike Gold Nanostructures: Surface Plasmon Resonance (SPR) and Resonance Rayleigh Scattering (RRS) Approaches to Growth Monitoring. *J. Phys. Chem. C* **2008**, *112*, 16348-16353.

50. Wang, Z.; Zhang, J.; Ekman, J. M.; Kenis, P. J. A.; Lu, Y. DNA-Mediated Control of Metal Nanoparticle Shape: One-Pot Synthesis and Cellular Uptake of Highly Stable and Functional Gold Nanoflowers. *Nano Lett.* **2010**, *10*, 1886-1891.

51. Nehl, C. L.; Liao, H.; Hafner, J. H. Optical Properties of Star-Shaped Gold Nanoparticles. *Nano Letters* **2006**, *6*, 683-688.

52. Trigari, S.; Rindi, A.; Margheri, G.; Sottini, S.; Dellepiane, G.; Giorgetti, E. Synthesis and Modelling of Gold Nanostars with Tunable Morphology and Extinction Spectrum. *J. Mater. Chem.* **2011**, *21*, 6531-6540.

53. Rechberger, W.; Hohenau, A.; Leitner, A.; Krenn, J. R.; Lamprecht, B.; Aussenegg, F. R. Optical Properties of Two Interacting Gold Nanoparticles. *Opt. Commun.* **2003**, *220*, 137-141.

54. Chithrani, B. D.; Ghazani, A. A.; Chan, W. C. W. Determining the Size and Shape Dependence of Gold Nanoparticle Uptake into Mammalian Cells. *Nano Lett.* **2006**, *6*, 662-668.

55. Kooi, M. E.; Cappendijk, V. C.; Cleutjens, K. B. J. M.; Kessels, A. G. H.; Kitslaar, P. J. E. H. M.; Borgers, M.; Frederik, P. M.; Daemen, M. J. A. P.; van Engelshoven, J. M. A. Accumulation of Ultrasmall Superparamagnetic Particles of Iron Oxide in Human Atherosclerotic Plaques Can Be Detected by *in Vivo* Magnetic Resonance Imaging. *Circulation* **2003**, *107*, 2453-2458.

56. Aaron, J.; Travis, K.; Harrison, N.; Sokolov, K. Dynamic Imaging of Molecular Assemblies in Live Cells Based on Nanoparticle Plasmon Resonance Coupling. *Nano Lett.* **2009**, *9*, 3612-3618.

57. Khlebtsov, N.; Dykman, L. Biodistribution and Toxicity of Engineered Gold Nanoparticles: A Review of *in Vitro* and *in Vivo* Studies. *Chem. Soc. Rev.* **2011**, *40*, 1647-1671.

58. Xu, L.; Guo, Y.; Xie, R.; Zhuang, J.; Yang, W.; Li, T. Three-Dimensional Assembly of Au Nanoparticles Using Dipeptides. *Nanotechnology* **2002**, *13*, 725-728.

59. Ryoo, W.; Webber, S. E.; Johnston, K. P. Water-in-Carbon Dioxide Microemulsions with Methylated Branched Hydrocarbon Surfactants. *Ind. Eng. Chem. Res.* **2003**, *42*, 6348-6358.

60. Hiemenz, P. C.; Rajagopalan, R., *Principles of Colloid and Surface Chemistry*. 3 ed.; Taylor & Francis: New York, 1997; p 546-556.

Chapter 4: Quenched Assembly of NIR Active Gold Nanoclusters Capped with Strongly Bound Ligands by Tuning Particle Charge via pH and Salinity[3]

Gold nanospheres coated with a binary monolayer of bound citrate and cysteine ligands were assembled into nanoclusters, in which the size and NIR extinction were tuned by varying the pH and concentration of added NaCl. During full evaporation of an aqueous dispersion of 4.5 ± 1.8 nm Au primary particles, the nanoclusters were formed and quenched by the triblock copolymer polylactic acid (PLA)(1k)-b-polyethylene glycol (PEG)(10k)-b-PLA(1k), which also provided steric stabilization. The short-ranged depletion and van der Waals attractive forces were balanced against longer ranged electrostatic repulsion, to tune the nanocluster diameter and NIR extinction. Upon lowering the pH from 7 to 5 at a given salinity, the magnitude of the charge on the primary particles decreased, such that the weaker electrostatic repulsion increased the hydrodynamic diameter, and consequently, NIR extinction of the clusters. At a given pH, as the concentration of NaCl was increased, the NIR extinction decreased monotonically. Furthermore, the greater screening of the charges on the nanoclusters weakened the interactions with PLA(1k)-b-PEG(10k)-b-PLA(1k), and thus lowered the amount of adsorbed polymer on the nanocluster surface. The generalization of the concept of self-assembly of small NIR active nanoclusters to include a strongly bound thiol and the manipulation of the morphologies and NIR extinction by variation of pH and salinity is not only of fundamental interest, but is also important for optical biomedical imaging and therapy.

---

[3] Large parts of this chapter have been published as: Stover, R.J.; Murthy, Nie, G.D.; Gourisankar, S.; Dear, B.J.; Truskett, T.M.; Sokolov, K.V.; Johnston, K.P., Quenched Assembly of NIR Active Gold Nanoclusters Capped with Strongly Bound Ligands by Tuning Particle Charge via pH and Salinity. *Journal of Physical Chemistry C* **2014**, *118, 14291-14298.*.

4.1 INTRODUCTION

Gold nanoparticles which absorb light strongly in the near-infrared (NIR) wavelength region from 700-1100 nm, where blood and tissue absorb weakly,[1] are of great utility in biomedical imaging modalities such as photoacoustic imaging.[2-7] Strong NIR extinction is often produced from nanoclusters of closely-spaced primary gold spheres, which can be assembled *in vivo*[8, 9] or *in vitro*.[10-12] Here, the close spacings of individual nanoparticles within the clusters produce dipoles, quadrupoles, and higher-order multipoles that shift the surface plasmon resonance (SPR) to the NIR region.[13] Gold nanoparticles have been assembled with organic templates such as polymers, proteins, and DNA.[14] The interparticle spacing may be controlled in order to tune the NIR extinction properties of the assemblies.[15] In most cases, substantial amounts of inactive templating agent were required which may limit the spectral properties or functionality of the active material by affecting, for example, the spacing between gold plasmonic nanoparticles. Primary nanoparticles may be assembled into clusters of controlled sizes with small amounts of structure-directing agents by properly balancing the relevant colloidal forces.[16, 10, 11, 17, 18, 12, 19] Clusters of nanoparticles have also been formed during synthesis of primary particles from precursors in both organic[20] and aqueous solvents in the presence of various stabilizers.[21-23] In these cases, the kinetics of primary particle formation must be synchronized properly relative to the kinetics of nucleation and growth of the primary particles into clusters to prevent excessive growth and precipitation. The reversibility of nanoclusters to dissociate back into individual primary particles has received relatively little attention. In many cases, bridges between particles formed from soluble precursors will fuse the clusters together permanently.[21]

A highly versatile synthetic concept has been presented to assemble pre-synthesized primary particles into clusters by tuning equilibrium and non-equilibrium

colloidal interactions, even for small amounts of stabilizers.[16, 10, 11, 17, 18, 12] For example, primary iron oxide particles (~ 6 nm in diameter) have been assembled into clusters of ~100 nm to ~500 nm by controlling solvophobic interactions between oleic acid ligands on the primary particles and the ethylene glycol solvent.[16] Additionally, poly(ethylene glycol) (PEG)-capped gold nanoparticles have been assembled into clusters by modulating interparticle steric repulsions via an alkanethiol addition in water.[17] Recently, our group has developed a "quenched equilibrium" assembly method to assemble small (~4 nm) gold nanoparticles into clusters of controlled size and intense NIR extinction which reversibly dissociate to monomer.[10-12] The nanocluster diameter was predicted semi-quantitatively with a free-energy equilibrium model whereby attractive, short-ranged van der Waals and depletion interactions were balanced against repulsive, longer-ranged electrostatic interactions. Nanoclusters were "quenched" at a metastable equilibrium size by the adsorption of a biodegradable triblock copolymer, PLA(1k)-*b*-PEG(10k)-*b*-PLA(1k), to the gold surface. At the minimum free energy, the equilibrium number of particles n^* in a nanocluster for primary particles each with charge q is:[24, 25, 12]

$$n^* = \frac{5aR}{6\lambda_b kTq^2} \tag{4.1}$$

where a is the attractive short-ranged interaction between particles (in kT units) , R is the primary particle radius (in nm), and λ_b is the Bjerrum length (in nm).[12] Previously, this model has been used to predict the size of equilibrium Au nanoclusters semi-quantitatively, whereby short-ranged van der Waals and depletion interactions were tuned by varying Au and polymer concentrations, respectively.[12]

The clusters, moreover, reversibly dissociated to monomer upon degradation of the polymeric quencher.[10-12]

While recent studies[10, 12] provided insight into the mechanism of formation of reversible gold nanoclusters with high NIR extinction, the weak binding of the lysine ligands on the Au surfaces may have limited the nanocluster stability. In the protonated form, the amine group in lysine is known to bind very weakly to Au,[26] although it forms ion pairs with citrate ligands on Au surfaces.[27] A weakly bound ligand may be displaced *in vivo* or in cells by free thiols such as glutathione (GSH), as has been observed in related systems.[28, 29] To overcome this stability limitation, many strongly bound ligands, for example, thiolated or zwitterionic molecules may be investigated. Although nanoclusters with NIR absorbance have been formed with PEG-SH, the size was not reported.[10]

Recently, we reported ~4 nm Au primary particles capped with a binary monolayer of cysteine and citrate ligands at a ratio of 1.6/1 that do not adsorb any protein when incubated in fetal bovine serum, despite a moderate surface charge (zeta potential of -22 mV).[19] We hypothesize that the zwitterionic tips on the cysteine facilitate the weak protein adsorption by shielding the protein from the buried carboxylate charged groups of citrate. However, it remains unknown whether nanoclusters could be formed from these primary particles. Furthermore, the effect of the charge of the primary particle on the nanocluster morphology has received little attention, and the roles of pH and salinity have not been investigated.[12, 19]

Herein, we extend the concept of colloidal assembly of quenched nanoclusters to the case of primary Au nanospheres capped with a mixed monolayer containing a zwitterionic strongly bound thiol ligand, cysteine, along with citrate. Furthermore, the nanocluster size and UV-vis-NIR extinction are shown to be tunable by varying the pH and/or the concentration of added NaCl, which modulate the particle charge and degree of polymer adsorption. The compositions of the mixed ligand

monolayers on the surface of primary gold nanoparticles are controlled *via* a place exchange reaction of anionic citrate ligands with zwitterionic cysteine ligands (see Figure 4.1). A dispersion of cysteine/citrate-capped Au nanospheres was assembled into nanoclusters upon mixing with an aqueous solution of the triblock copolymer PLA(1k)-*b*-PEG(10k)-*b*-PLA(1k) and subsequent complete evaporation of the solvent.[12] The nanocluster size and NIR extinction are shown to increase with a decrease in surface charge (electrostatic repulsion) upon lowering the pH. At a given pH, an increase in salinity is used to vary the NIR extinction. Furthermore, the Debye screening weakens the interactions between the Au surfaces and the copolymer, resulting in a decrease in polymer content in the nanoclusters. The ability to further tailor the morphology and NIR properties of Au nanoclusters with the variables of pH and salinity, and to advance the understanding of the kinetic and equilibrium aspects of the self-assembly mechanism is not only of scientific interest, but of practical interest for optical biomedical imaging and therapy.

4.2 EXPERIMENTAL

4.2.1 Materials

$HAuCl_4 \cdot 3H_2O$ was purchased from MP Biomedicals LLC (Solon, OH). $Na_3C_3H_5O(COO)_3 \cdot 2H_2O$, $NaBH_4$ from Fisher Scientific (Fair Lawn, NJ), and L-cysteine from Acros Chemicals (Morris Plains, NJ). PLA(1k)-*b*-PEG(10k)-*b*-PLA(1k) was acquired from Sigma-Aldrich (St. Louis, MO). Phosphate-buffered saline (PBS) was purchased from Gibco (Grand Island, NY).

4.2.2 Synthesis of citrate-capped Au nanospheres and cysteine ligand exchange

The ~4 nm citrate-capped Au nanospheres were synthesized by the $NaBH_4$ reduction of $HAuCl_4$ and purified by tangential flow filtration, in an identical method to previous studies.[12] Cysteine place exchange was conducted according to a previously described method.[19] Briefly, a solution of 1% (w/v) cysteine in deionized water was freshly prepared. In a typical experiment, 3.2 µl of this solution was added to 0.6 ml of a 3 mg/ml citrate-capped Au nanosphere dispersion, and the mixture was stirred at room temperature for 15 min. To test exchange stability, a single nanosphere sample was reacted for 24 hours at room temperature as well. Immediately after the 15 minute reactions, nanospheres were either used for nanocluster formation or diluted for characterization.

4.2.3 Nanosphere Characterization

Following cysteine ligand exchange, nanosphere samples were either diluted to a concentration of ~0.04 mg/ml Au in DI water for dynamic light scattering (DLS) or UV-Visible-NIR (UV-Vis-NIR) analysis, or diluted to ~0.04 mg/ml Au in 1 mM KCl for zeta potential analysis. DLS measurements were taken on these diluted samples using a Brookhaven ZetaPALS analyzer with a scattering angle of 90° as reported previously.[12, 19] Each sample was filtered through a 200 nm polyethersulfone filter prior to testing. The data were analyzed using the CONTIN method (Brookhaven DLS software version 3.34), and the Stokes-Einstein equation was used to obtain intensity-weighted distribution of hydrodynamic diameters. The data were fit using a 32-channel auto-slope analysis option on each sample without specifying a minimum or maximum bound. UV-Vis-NIR spectroscopy of diluted nanocluster samples was obtained using a Varian Cary 60 spectrophotometer with a path length of 1 cm. Unless otherwise

noted, the extinction was normalized as unity at the peak wavelength longer than 500 nm. Unless specified otherwise, zeta potential measurements were performed using a Brookhaven ZetaPALS analyzer with an applied electric field of 5 V/cm, in which 10 runs of 30-cycle measurements were taken. In a few samples, zeta potentials taken of the 24 hour cysteine place exchanged nanospheres were obtained using a ZetaPlus analyzer in high precision mode of 30 single-cycle measurements under an applied electric field of 15 V/cm. The average and standard deviations of these measurements are reported. Due to the nanocluster size (see Results), the Hückel model was used to relate the measured electrophoretic mobility to a zeta potential.[30] Au dispersion concentrations were determined by flame atomic absorption spectroscopy (FAAS), utilizing a GBC 908AA analyzer (GBC Scientific Equipment Pty Ltd.) with an air/acetylene flame at a wavelength of 242.8 nm. Citrate ligand weight percents were measured on an OI Analytical 1030 TOC analyzer run in wet oxidation mode with 20 wt % sodium persulfate (Acros Chemical; Morris Plains, NJ). A sample of citrate-capped Au nanoparticles was diluted in DI water to ~4 ppm Au and run in non-purgeable organic carbon (NPOC) mode with a reaction time of 3 minutes.

4.2.4 Nanocluster Formation

Immediately after the completion of the cysteine place exchange reaction, cysteine/citrate-capped Au nanospheres were used to synthesize nanoclusters in a manner adapted from a previously reported method.[12] A 30 mg/ml solution of PLA(1k)-*b*-PEG(10k)-*b*-PLA(1k) was freshly prepared, with salt concentrations ranging from 0 mM to 100 mM. 250 µl of a 30 mg/ml polymer solution was added to 0.5 ml of 3 mg/ml cysteine/citrate capped nanospheres under vigorous stirring in order to achieve a 5/1

polymer/Au ratio. The polymer-gold mixture was then adjusted to the desired pH, as measured by a Mettler Toledo InLab Micro pH probe, using either 0.1 M HCl or 0.1 M NaOH and added to a 15 mm x 45 mm glass vial, which was placed in a 40 °C water bath and stirred vigorously. Dried air was subsequently blown over the sample through a small tube inserted into the vial at a flow rate of approximately 26 L/min. In all cases, the aqueous solvent was fully evaporated, which typically took ~35 min to form a film. After solvent evaporation, the nanoclusters were dispersed by adding 30 ml of deionized water to the sample. The resulting solution was then centrifuged in a 50 ml polystyrene centrifuge tube at 9700 rpm for 10 min, resulting in ~1 ml of a lower colloidal phase of densely-packed nanoclusters, which was collected. An upper colloidal phase (~ 29 ml) of monomer Au and highly fractal smaller aggregates was discarded. A light meniscus was observed between the dense lower phase and the upper phase.

4.2.5 Nanocluster Characterization

Nanocluster morphology was assessed by transmission electron microscopy (TEM), which was performed on an FEI TECNAI G2 F20 X-TWIN TEM using a high-angle annular dark-field detector. Samples were prepared by first dipping a 200 mesh copper-coated carbon type-A TEM grid (Electron Microscopy Sciences, Hatfield, PA) into liquid nitrogen. A 3 μL drop of dilute nanocluster dispersion was then pipetted onto the grid, which was then subsequently dried using a VirTis Advantage tray lyophilizer (VirTis, Gardiner, NY). DLS, UV-Vis-NIR, and zeta potential measurements were performed on the nanoclusters in an identical manner to the primary nanospheres at the same mg/mL concentration of Au. The total carbon weight percent was measured using the same OI Analytical 1030 TOC analyzer used for citrate analysis above. The

weight percent of carbon was then derived from the concentration of CO_2 detected, in ppm, for samples with a known Au concentration by UV-visible measurements at 400 nm..

4.3 Results and Discussion

4.3.1 Synthesis of Cysteine/Citrate Nanospheres

The cysteine/citrate-capped nanospheres used in this study were synthesized identically to nanospheres reported in a previous study.[19] The UV-Vis-NIR spectra and DLS D_h distribution of these nanospheres (Figure D.1) at ~pH 7 were determined to be essentially the same as those in the previous study[19] Also, the zeta potential of the nanospheres at pH 7 and a concentration of 1 mM KCl, was -22.5 ± 0.6 mV, similar to the earlier value of -21.6 ± 1.7 mV.[19] With 25 mM acetic acid buffer at pH 7 a similar value of -22.3 ± 2.3mV was measured. The zeta potentials were not measured at a salinity of 100 mM NaCl at pH 7 as the primary particles underwent aggregation. Moreover, in order to verify the degree of the cysteine ligand exchange with time, the zeta potential of the primary particles in 1 mM KCl was measured after 24 h of exchange. Here, the zeta potential after 24 h was -19.6 ± 2.4 mV, similar to the zeta potential of -22.5 ± 0.6 mV after 15 min. Thus, we conclude that the cysteine ligand exchange reaction reached a steady state equilibrium value after ~15 min. On the basis of these measurements and expected electrostatic screening with added salt, the changes in pH and salinity in this study are sufficient to manipulate the nanoparticle surface charge.

4.3.2 Effect of pH on Nanocluster formation

For pH values of 5 and 7, the nanocluster properties were determined either without added salt or with initial salinities of 17 or 33 mM (Table 4.1). Each sample is referred to by the notation of "pH-initial salinity", i.e. 7-17 for pH 7, and 17mM initial NaCl after polymer addition. The TEMs indicated a high polydispersity in the cluster size as shown in Figure 4.2b and 4.2c, where sizes were on the order of ~20 to ~100 nm. Given the high polydispersity, DLS intensity-weighted size distributions are reported throughout this paper and it was not attempted to determine volume distributions. It is however important to recognize that the mean size would be much smaller for the volume distribution. For samples made with no added NaCl, the hydrodynamic diameter of the clusters in the range of 40 to 250 nm shifted to smaller sizes with a pH increase from 5 to 7 (Figure 4.2a). This size decrease is consistent with the free energy model (Eq. 4.1), as the charged ligands on the gold surface become more deprotonated, which increases the magnitude of the charge. Thus the resulting stronger electrostatic repulsion between primary particles would limit growth of clusters as observed. In this self-limited growth model (Eq. 4.1) , as the overall charge in the cluster increases with each added primary particle, the cluster will eventually repel the addition of another charged particle. At pH 7 with larger charges on the primary particles, this condition will be realized at a smaller cluster size as observed.

The increase in the magnitude of charge from pH 5 to 7 may be shown to influence the decrease in the NIR extinction in two ways. Without added NaCl, the extinction ratio A_{800}/A_{525} was observed to decrease from 0.825 to 0.728. For a given spacing between primary particles, the extinction ratio is known to decrease with a decrease in the nanocluster size, as the SPR will become less polarized for a smaller cluster diameter.[10, 12] Also, the greater electrostatic repulsion has the potential to increase

the spacing between Au primary particles, which would also contribute to a decrease in A_{800}/A_{525}. Each of these trends with pH was also observed for 17 mM initial salinity. Here, the size distribution shifted to smaller sizes at pH 7. Furthermore, the extinction ratio dropped from 0.635 to 0.501, and for 33 mM NaCl, from 0.619 to 0.419. One exception to this behavior was the unusually high amount at 100-250 nm for the 33 mM initial salinity.

The total organic carbon (TOC) was measured for pH values of 5 and 7, at each salinity. For citrate-capped particles alone, the weight % carbon was determined to be 9.68 ± 0.46 %. As shown in table 4.1 for samples 5-0 and 7-0, the weight % of carbon on the nanoclusters decreased slightly from 26.9 ± 0.6 % to 24.3 ± 0.5 %, respectively. For the other two salinities the changes in TOC were even smaller. The weight % of the mixed citrate/cysteine monolayer is the same for all samples, as each nanocluster was composed of one type of primary nanoparticle. Thus, the changes in weight % C will only reflect changes in the weight % of adsorbed polymer. Since the pH had little effect on the C weight % at a given salinity, it also did not influence the polymer adsorption.

4.3.3 Effect of salt at constant pH

At each pH, the nanoclusters were assembled with the addition of 30 mg/mL polymer solutions containing 0 mM, 17 mM, or 33 mM NaCl. As the salinity increased, the TOC results indicate a decrease in weight % C and thus polymer adsorption. For the triblock PLA-*b*-PEG-*b*-PLA copolymer, the addition of NaCl will raise the chemical potential of the polymer in water due to desolvation of PEG,[31-33] which alone would enhance the driving force for polymer adsorption. However, salt also screens the charges on bound ligands and thus weakens the charge-dipole interactions and hydrogen bonding

with the polymer, which disfavors polymer adsorption. Therefore, the decrease in polymer adsorption indicates the charge screening is the dominant effect. In contrast, the polymer adsorption did not change much with an increase in pH at a given salinity despite the greater magnitude of the Au surface charge. Thus, some compensating effect was present such as the interaction of H^+, OH^-, Na^+ and Cl^- ions with the Au surfaces and ether oxygens in the PEG blocks.

As the NaCl concentration increases the electrostatic repulsion between primary particles decreases, which would be expected to shift the nanocluster size distribution to large sizes according to Eq. 4.1. In all but a single case this behavior was observed at each pH except for sample 7-17 which showed a modest gain in the smallest part of the distribution. With greater attraction between the primary particles, the primary particles could potentially become spaced more closely together, which would increase the NIR extinction. Instead, the opposite behavior was observed whereby the NIR extinction decreased with salinity. Perhaps the steric effects of the citrate and cysteine ligands limited the minimum spacing between the primary particles. Another possibility is that the NIR extinction is also influenced by the kinetics of assembly, which may influence the fractal dimensions.[34] In this scenario, the clusters may form more rapidly at higher salt concentrations due to the weaker electrostatic repulsion. Thus, the more strongly interacting nanoparticles will have less time to explore the interior of growing clusters and will have a smaller driving force to relax to form more dense aggregates. The behavior would be more indicative of diffusion limited cluster aggregation, resulting in looser, more fractal aggregates which would inherently yield lower NIR extinction. However any changes in the fractal dimension were not discernible in the TEM images.

Similar effects of salt were seen at pH 5 as observed at pH 7 for the polymer adsorption, size distribution and the NIR extinction ratio. The average size distributions

of the clusters shifted slight toward larger particles, as expected with the greater screening of electrostatic repulsion. Again, the extinction ratio decreased, as well as the polymer adsorption.

4.3.4 Comparison to Nanoclusters Made with Lysine/Citrate Nanospheres

The cysteine/citrate capped primary Au nanospheres used in this study have been previously shown to completely resist protein adsorption in undiluted fetal bovine serum.[19] Interestingly, however, in the present study these primary nanospheres were found to aggregate and settle immediately after incubation in both 1x phosphate buffered saline (PBS) or 150 mM NaCl at a gold concentration of ~0.04 mg/ml (data not shown), which is approximately the same salinity as FBS. Here charge screening weakens the electrostatic repulsion. The stability in FBS but not in NaCl nor PBS may be attributed to a potential "depletion stabilization" mechanism, whereby the proteins present in FBS impart stability to the primary nanospheres through creating a stabilizing osmotic pressure gradient without physically adsorbing to the nanosphere surfaces.[35] This mechanism has been previously proposed for the stabilization of Au nanoparticles in solutions of high salinity with PEG as well as iron oxide nanoparticles in fetal calf serum (FCS)-supplemented cellular growth media.[36, 37]

The use of zwitterionic cysteine instead of cationic lysine as a ligand along with citrate in the mixed monolayer-capped primary nanospheres also significantly affected the nanocluster formation process. The addition of zwitterionic cysteine reduced the charge on the primary particle to -21.6 ± 1.7 mV compared to-16.1 ± 2.9 mV with the addition of cationic lysine,[12, 19] resulting in a higher q value in Eq. 4.1 for cysteine/citrate capped nanospheres. Thus, in order to obtain similar nanocluster sizes and morphologies,

the attraction *a* had to be increased to overcome the excess repulsion. Thus, higher evaporation extents (~100% vs 50%) were used to achieve nanoclusters with the closely packed Au nanospheres necessary for intense NIR extinction. Moreover, the use of salt and pH modulation in the formation of cysteine/citrate nanoclusters allowed for lower polymer/Au ratios (5/1 compared with 20/1 for lysine/citrate), as a lower polymer/Au was required in order to achieve a similar level of quenching.

4.4 CONCLUSIONS

The concept of the colloidal assembly of gold nanoclusters quenched with a polymer stabilizer[10-12, 19] has been generalized to include primary particles capped with a strongly binding zwitterionic thiol, cysteine, to form a binary monolayer with citrate. Furthermore, the solution pH and salt concentration have been utilized as new variables to tune the particle size, NIR extinction and degree of polymer adsorption by manipulating the colloidal interactions, particularly the Au surface charge on the primary nanospheres. At each salinity (0 to 33 mM), the hydrodynamic diameter and NIR extinction increased as the solution pH was decreased from 7 to 5, consistent with weaker electrostatic repulsion, as would be expected from the equilibrium free energy model. Furthermore, at a given pH, the size distribution shifted to larger clusters with salt addition, again as may be expected with weakened electrostatic repulsion. Therefore, the free energy model may be used to provide a unified understanding of the size data in this study over a wide range of conditions in pH and salinity. Finally, the polymer adsorption decreased as the screening of the charges on the Au surfaces with salt weakened the interactions with the polar groups on PLA(1k)-*b*-PEG(10k)-*b*-PLA(1k). The ability to further tailor the morphology and NIR properties of Au nanoclusters with the variables of

pH and salinity, resulting from the emerging understanding of the kinetic and equilibrium aspects of the self-assembly mechanism in the current and previous studies[11, 17, 22, 12, 19], will be highly beneficial for practical application to optical biomedical imaging and therapy.

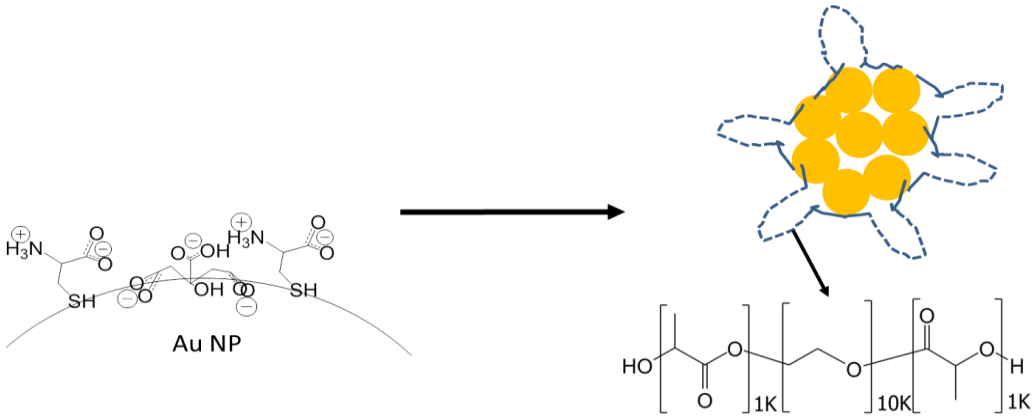

Figure 4.1: Schematic of nanoclusters assembled from cysteine/citrate capped Au nanospheres and stabilized with PLA(1k)-*b*-PEG(10k)-*b*-PLA(1k). The nanoclusters are formed upon mixing Au dispersions with polymer solutions, in some cases containing NaCl, and then full evaporation of the solvent. The dashed lines for the adsorbed polymers on the clusters represent PEG loops and the solid lines the PLA end groups.

Table 4.1: Effects of solution pH and salinity on intensity weighted hydrodynamic diameter size distribution, UV-Vis-NIR extinction ratios, and weight percent of organic carbon on the nanoclusters

pH-[NaCl]	Initial NaCl Conc. (mM)	DLS Intensity Weighted Size Distributions (nm) (Cumulative Size %)	A_{800}/A_{525}	Weight % Organic Carbon (from TOC)
5-0	0	5-40 (23%) 40-100 (25%) 100-250 (52%)	0.825	26.9 ± 0.6
5-17	17	5-40 (18%) 40-100 (22%) 100-250 (60%)	0.635	20.7 ± 0.9
5-33	33	5-40 (12%) 40-100 (19%) 100-250 (69%)	0.619	17.9 ± 0.7
7-0	0	5-40 (9%) 40-100 (62%) 100-250 (29%)	0.728	24.3 ± 0.5
7-17	17	5-40 (20%) 40-100 (52%) 100-250 (28%)	0.501	20.2 ± 0.5
7-33	33	5-40 (20%) 40-100 (4%) 100-250 (76%)	0.419	19.4 ± 0.3

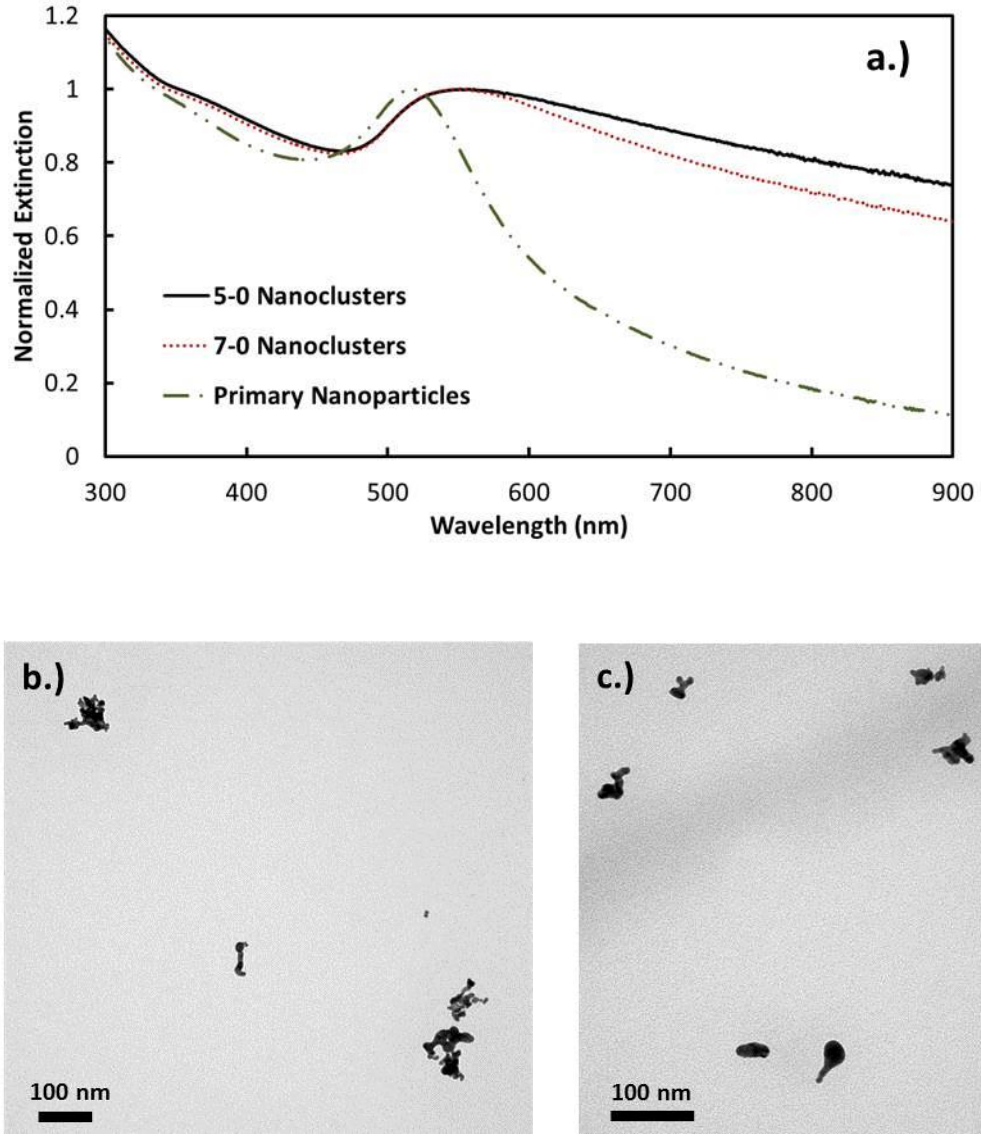

Figure 4.2: (a) UV-Vis-NIR extinction spectra, and TEM images for nanoclusters made with 0 mM NaCl at (b) pH 5 and (c) pH 7

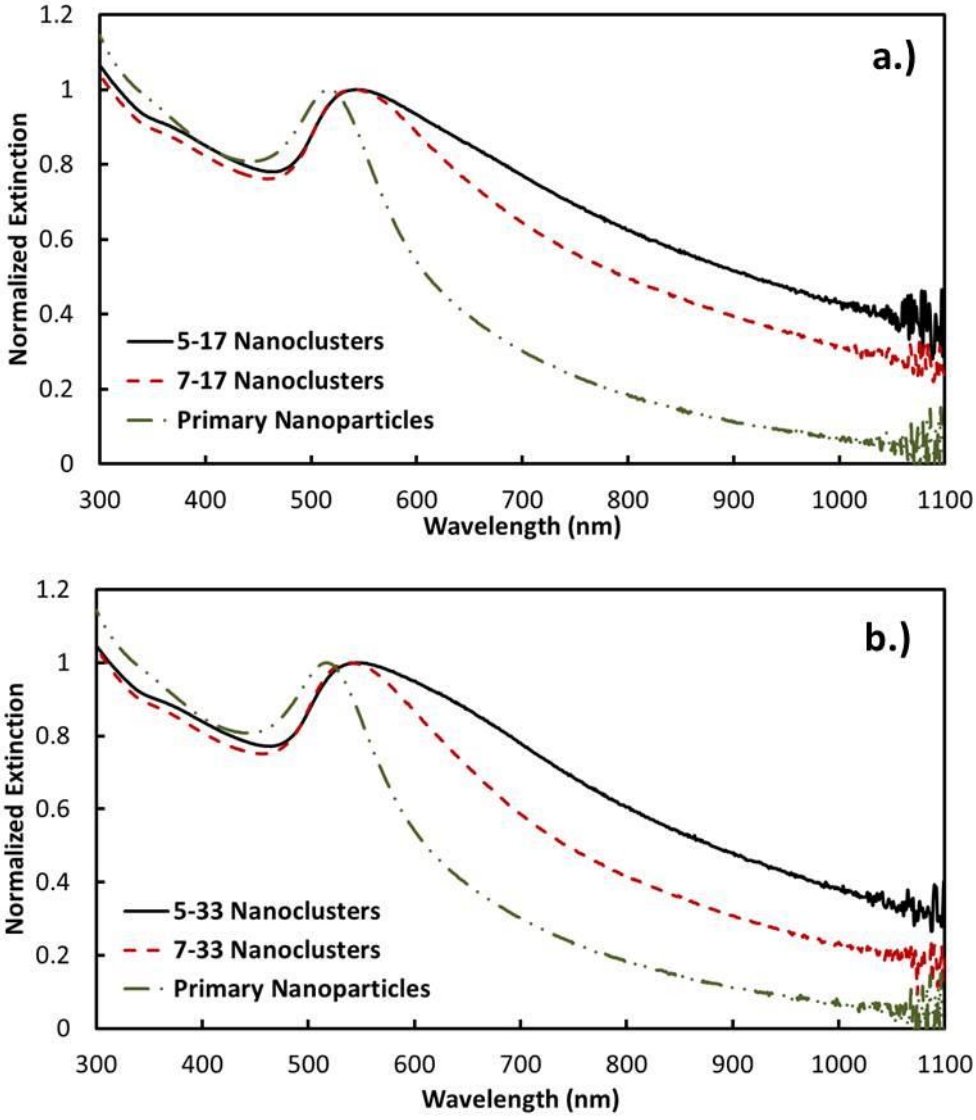

Figure 4.3: UV-Vis-NIR extinction spectra of nanoclusters made with (a) 17 mM and (b) 33 mM initial NaCl concentrations at pH 5 and 7. The syntax "5-17" denotes pH 5 and 17 mM NaCl.

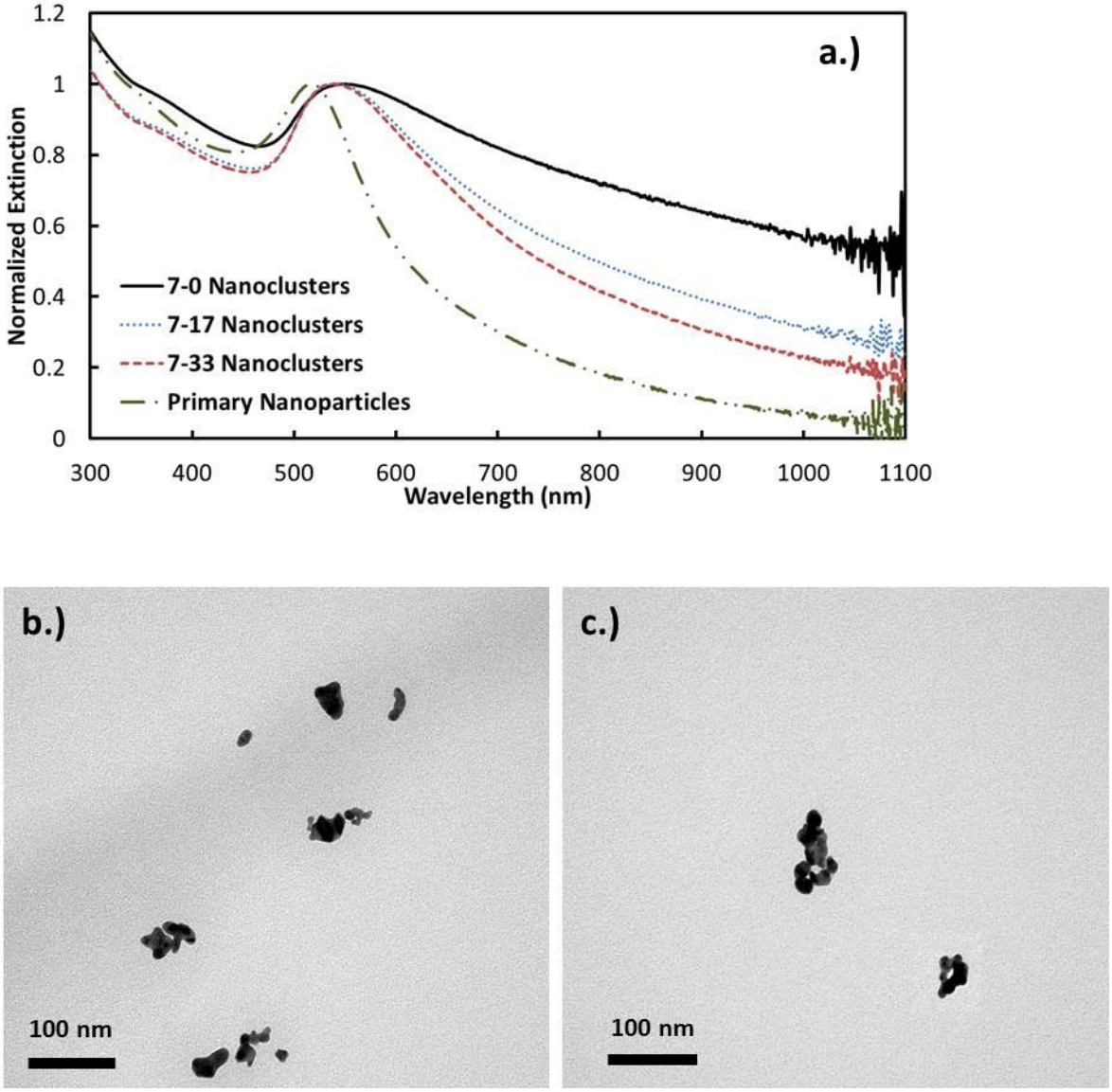

Figure 4.4: (a) UV-Vis-NIR extinction and TEM Images of clusters made at pH 7 and (b) 0 mM and (c) 17 mM initial NaCl concentrations, respectively

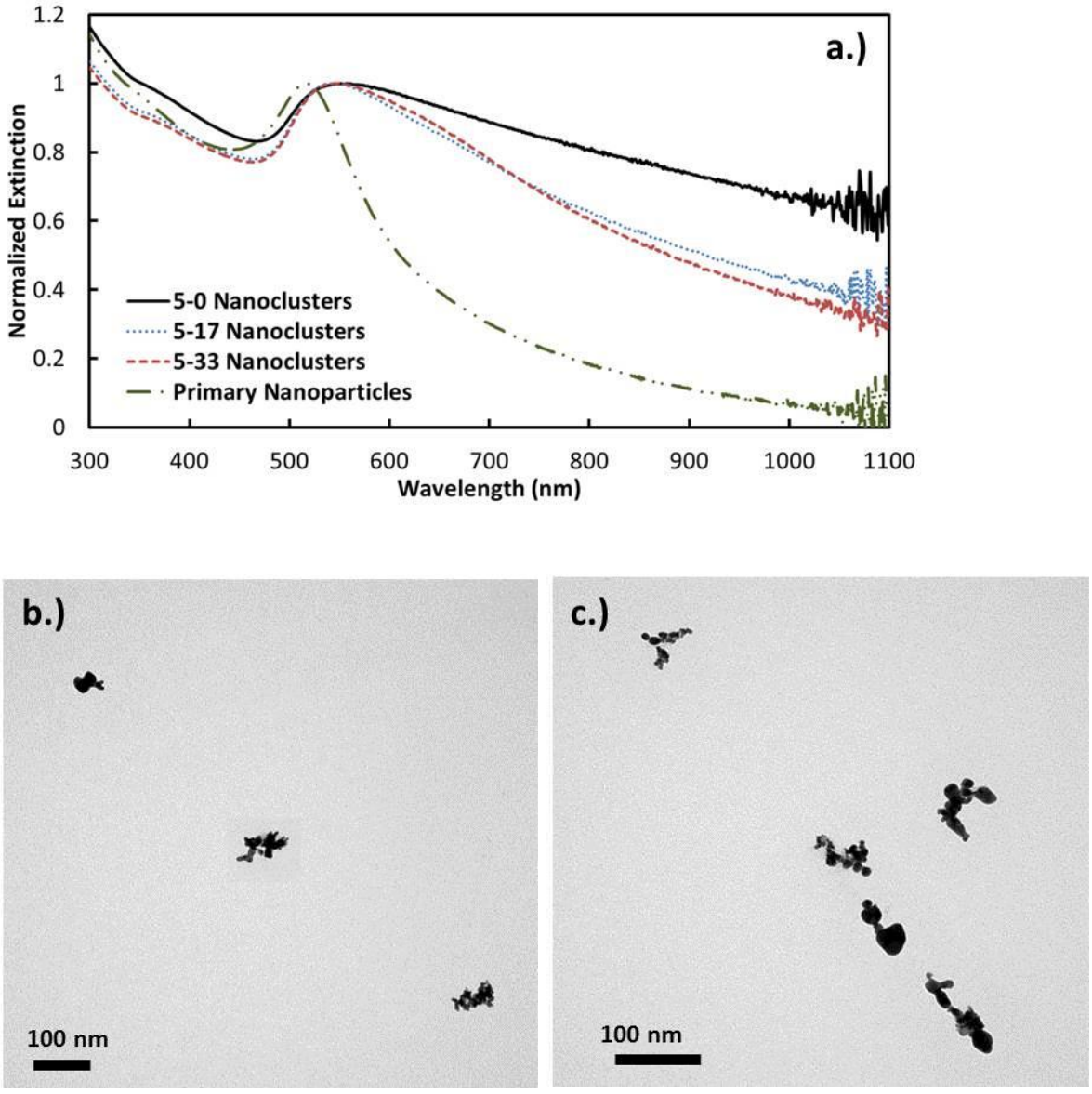

Figure 4.5: (a) UV-Vis-NIR extinction and TEM Images of clusters made at (b) 0 mM and (c) 33 mM initial NaCl concentrations, respectively at pH 5.

4.5 REFERENCES

1. Weissleder, R. A clearer vision for in vivo imaging. Nat Biotech 2001, 19, 316-317.
2. Barbosa, S.; Agrawal, A.; Rodríguez-Lorenzo, L.; Pastoriza-Santos, I.; Alvarez-Puebla, R. n. A.; Kornowski, A.; Weller, H.; Liz-Marzán, L. M. Tuning Size and Sensing Properties in Colloidal Gold Nanostars. Langmuir 2010, 26, 14943-14950.
3. Dreaden, E. C.; Alkilany, A. M.; Huang, X.; Murphy, C. J.; El-Sayed, M. A. The golden age: gold nanoparticles for biomedicine. Chemical Society Reviews 2012, 41, 2740-2779.
4. Agarwal, A.; Huang, S. W.; O'Donnell, M.; Day, K. C.; Day, M.; Ashkenazi, S. Targeted gold nanorod contrast agent for prostate cancer detection by photoacoustic imaging. Journal of Applied Physics 2007, 102, 0647011-0647014.
5. Mallidi, S.; Larson, T.; Tam, J.; Joshi, P. P.; Karplouk, A.; Sokolov, K.; Emelianov, S. Multiwavelength Photoacoustic Imaging and Plasmon Resonance Coupling of Gold Nanoparticles for Selective Detection of Cancer. Nano Letters 2009, 9, 2825-2831.
6. Song, K. H.; Kim, C.; Cobley, C. M.; Xia, Y.; Wang, L. V. Near-Infrared Gold Nanocages as a New Class of Tracers for Photoacoustic Sentinel Lymph Node Mapping on a Rat Model. Nano Letters 2009, 9, 183-188.
7. Yoon, S. J.; Mallidi, S.; Tam, J. M.; Tam, J. O.; Murthy, A.; Johnston, K. P.; Sokolov, K. V.; Emelianov, S. Y. Utility of biodegradable plasmonic nanoclusters in photoacoustic imaging. Optics Letters 2010, 35, 3751-3753.
8. Aaron, J.; Nitin, N.; Travis, K.; Kumar, S.; Collier, T.; Park, S. Y.; José-Yacamán, M.; Coghlan, L.; Follen, M.; Richards-Kortum, R.; Sokolov, K. Plasmon resonance coupling of metal nanoparticles for molecular imaging of carcinogenesis in vivo. BIOMEDO 2007, 12, 034007-034007-11.
9. Aaron, J.; Travis, K.; Harrison, N.; Sokolov, K. Dynamic Imaging of Molecular Assemblies in Live Cells Based on Nanoparticle Plasmon Resonance Coupling. Nano Letters 2009, 9, 3612-3618.
10. Tam, J. M.; Murthy, A. K.; Ingram, D. R.; Nguyen, R.; Sokolov, K. V.; Johnston, K. P. Kinetic Assembly of Near-IR Active Gold Nanoclusters Using Weakly Adsorbing Polymers to Control the Size. Langmuir 2010, 26, 8988-8999.
11. Tam, J. M.; Tam, J. O.; Murthy, A.; Ingram, D. R.; Ma, L. L.; Travis, K.; Johnston, K. P.; Sokolov, K. V. Controlled Assembly of Biodegradable Plasmonic Nanoclusters for Near-Infrared Imaging and Therapeutic Applications. ACS Nano 2010, 4, 2178-2184.

12. Murthy, A. K.; Stover, R. J.; Borwankar, A. U.; Nie, G. D.; Gourisankar, S.; Truskett, T. M.; Sokolov, K. V.; Johnston, K. P. Equilibrium Gold Nanoclusters Quenched with Biodegradable Polymers. ACS Nano 2013, 7, 239-251.

13. Halas, N. J.; Lal, S.; Chang, W.-S.; Link, S.; Nordlander, P. Plasmons in Strongly Coupled Metallic Nanostructures. Chemical Reviews 2011, 111, 3913-3961.

14. Ofir, Y.; Samanta, B.; Rotello, V. M. Polymer and biopolymer mediated self-assembly of gold nanoparticles. Chemical Society Reviews 2008, 37, 1814-1825.

15. Frankamp, B. L.; Boal, A. K.; Rotello, V. M. Controlled Interparticle Spacing through Self-Assembly of Au Nanoparticles and Poly(amidoamine) Dendrimers. Journal of the American Chemical Society 2002, 124, 15146-15147.

16. Zhuang, J.; Wu, H.; Yang, Y.; Cao, Y. C. Controlling Colloidal Superparticle Growth Through Solvophobic Interactions. Angewandte Chemie International Edition 2008, 47, 2208-2212.

17. Larson-Smith, K.; Pozzo, D. C. Scalable synthesis of self-assembling nanoparticle clusters based on controlled steric interactions. Soft Matter 2011, 7, 5339-5347.

18. Lu, Z.; Yin, Y. Colloidal nanoparticle clusters: functional materials by design. Chemical Society Reviews 2012, 41, 6874-6887.

19. Murthy, A. K.; Stover, R. J.; Hardin, W. G.; Schramm, R.; Nie, G. D.; Gourisankar, S.; Truskett, T. M.; Sokolov, K. V.; Johnston, K. P. Charged Gold Nanoparticles with Essentially Zero Serum Protein Adsorption in Undiluted Fetal Bovine Serum. Journal of the American Chemical Society 2013, 135, 7799-7802.

20. Ge, J.; Hu, Y.; Biasini, M.; Beyermann, W. P.; Yin, Y. Superparamagnetic Magnetite Colloidal Nanocrystal Clusters. Angewandte Chemie International Edition 2007, 46, 4342-4345.

21. Ma, L. L.; Feldman, M. D.; Tam, J. M.; Paranjape, A. S.; Cheruki, K. K.; Larson, T. A.; Tam, J. O.; Ingram, D. R.; Paramita, V.; Villard, J. W.; Jenkins, J. T.; Wang, T.; Clarke, G. D.; Asmis, R.; Sokolov, K.; Chandrasekar, B.; Milner, T. E.; Johnston, K. P. Small Multifunctional Nanoclusters (Nanoroses) for Targeted Cellular Imaging and Therapy. ACS Nano 2009, 3, 2686-2696.

22. Xia, Y. S.; Nguyen, T. D.; Yang, M.; Lee, B.; Santos, A.; Podsiadlo, P.; Tang, Z. Y.; Glotzer, S. C.; Kotov, N. A. Self-assembly of self-limiting monodisperse supraparticles from polydisperse nanoparticles. Nature Nanotechnology 2011, 6, 580-587.

23. Ma, L. L.; Borwankar, A. U.; Willsey, B. W.; Yoon, K. Y.; Tam, J. O.; Sokolov, K. V.; Feldman, M. D.; Milner, T. E.; Johnston, K. P. Growth of textured thin Au coatings on iron oxide nanoparticles with near infrared absorbance. Nanotechnology 2013, 24, 025606.

24. Johnston, K. P.; Maynard, J. A.; Truskett, T. M.; Borwankar, A. U.; Miller, M. A.; Wilson, B. K.; Dinin, A. K.; Khan, T. A.; Kaczorowski, K. J. Concentrated Dispersion of Equilibrium Protein Nanoclusters That Reversibly Dissociate Into Active Monomers. ACS Nano 2012, 6, 1357-1369.

25. Groenewold, J.; Kegel, W. K. Anomalously Large Equilibrium Clusters of Colloids. Journal of Physical Chemistry B 2001, 105, 11702-11709.

26. Joshi, H.; Shirude, P. S.; Bansal, V.; Ganesh, K. N.; Sastry, M. Isothermal Titration Calorimetry Studies on the Binding of Amino Acids to Gold Nanoparticles. Journal of Physical Chemistry B 2004, 108, 11535-11540.

27. Kondoh, H.; Kodama, C.; Sumida, H.; Nozoye, H. Molecular processes of adsorption and desorption of alkanethiol monolayers on Au(1 1 1). Journal of Chemical Physics 1999, 111, 1175-1184.

28. Chompoosor, A.; Han, G.; Rotello, V. M. Charge Dependent of Ligand Release and Monolayer Stability of Gold Nanoparticles by Biogenic Thiols. Bioconjugate Chemistry 2008, 19, 1342-1345.

29. Hong, R.; Han, G.; Fernandez, J. M.; Kim, B.; Forbes, N. S.; Rotello, V. M. Gluathione-Mediated Delivery and Release Using Monolayer Protected Nanoparticle Carriers. Journal of the American Chemical Society 2006, 128, 1078-1079.

30. Hiemenz, P. C.; Rajagopalan, R. Principles of Colloid and Surface Chemistry; 3 ed.; Taylor & Francis: New York, 1997. p 546-556.

31. Alexandridis, P.; Holzwarth, J. F. Differential Scanning Calorimetry Investigation of the Effect of Salts on Aqueous Solution Properties of an Amphiphilic Block Copolymer (Poloxamer). Langmuir 1997, 13, 6074-6082.

32. Su, Y.-L.; Wei, X.-F.; Liu, H.-Z. Effect of sodium chloride on association behavior of poly(ethylene oxide)-poly(propylene oxide)-poly(ethylene oxide) block copolymer in aqueous solutions. Journal of Colloid and Interface Science 2003, 264, 526-531.

33. Tadros, T. F.; Vincent, B. Influence of Temperature and Electrolytes on the Adsorption of Poly(ethylene oxide)-Poly(propylene oxide) Block Copolymer on Polystyrene Latex and on the Stability of the Polymer-Coated Particles. Journal of Physical Chemistry 1980, 84, 1575-1580.

34. Weitz, D. A.; Huang, J. S.; Lin, M. Y.; Sung, J. Limits of the Fractal Dimension for Irreversible Kinetic Aggregation of Gold Colloids. Physical Review Letters 1985, 54, 1416-1419.

35. Lekkerkerker, H. N. W.; Tuinier, R. Colloids and the Depletion Interaction; Springer: New York, 2011; Vol. 833. p 12-15.

36. Petri-Fink, A.; Steitz, B.; Finka, A.; Salaklang, J.; Hofmann, H. Effect of cell media on polymer coated superparamagnetic iron oxide nanoparticles (SPIONs): Colloidal stability, cytotoxicity, and cellular uptake studies. European Journal of Pharmaceutics and Biopharmaceutics 2008, 68, 129-137.

37. Zhang, X.; Servos, M. R.; Liu, J. Ultrahigh Nanoparticle Stability against Salt, pH, and Solvent with Retained Surface Accessibility via Depletion Stabilization. Journal of the American Chemical Society 2012, 134, 9910-9913.

Chapter 5: Formation of Small Gold Nanoparticle Chains with High-NIR Extinction Through Bridging with Calcium Ions[4]

Citrate capped Au nanoparticles (5 nm) were assembled into branched nanochains with $CaCl_2$ and more spherical nanoparticle clusters with NaCl by tuning the colloidal interactions. The electrostatic repulsion and the interparticle bridging attraction between the cations and citrate ligands were varied by changing the concentration of either Na+ or Ca^{2+} at pH 7 to form the nanoclusters at various times from 1 to 1800 s. For very dilute Ca^{2+} and thus very thick double layers around the particles, strong interparticle bridging resulted in small branched chains with lengths as short as 20 nm and strong NIR extinction out to 1100 nm. Furthermore, the bridging produced very small interparticle spacings leading to partial fusion that further increased the NIR extinction. The ability to design the size and shape of nanoparticle clusters, as well as the interparticle spacing by tuning bridging and electrostatic interactions, may be expected to be quite general and of broad applicability in materials synthesis.

[4] Large parts of this chapter have been submitted as: Stover, R.J.; Moaseri, E.; Gourisankar, S.; Iqbal, M.; Rahbar, N.K.; Changalvaie, B.; Truskett, T.M.; Johnston, K.P., Formation of Small Gold Nanoparticle Chains with High NIR Extinction through Bridging with Calcium Ions. *Lanmguir*, submitted.

5.1 INTRODUCTION

Nanoparticle clusters (nanoclusters, supraparticles) may be assembled from primary metal and semiconductor nanospheres by tuning the colloidal interactions. The morphology may be controlled from 1-D chains to 3-D spherical aggregates by an emerging understanding of how to balance the interparticle electrostatic and steric repulsion against the van der Waals (vdW) attraction, dipolar interactions, hydrophobic interactions, hydrogen bonding between ligands on the surface, and bridging interactions of these ligands with ions.[1-5] "Pearl-necklace" aggregates of closely spaced CdTe primary particles have been formed upon removal of thioglycolic acid (TGA) ligands from the surface to decrease electrostatic repulsion.[6] In this case, the permanent dipoles on the semiconductor nanocrystals provided an anisotropic force to guide linear assembly as has been described by Monte Carlo computer simulation.[7] For citrate stabilized Au nanoparticles (NPs), the formation of large dipoles on the NPs, upon partial replacement of citrate with 2-mercaptoethanol, was utilized to synthesize long branched chains.8 Zhang and Wang presented a model for the formation of 1-D chains based on a stronger net electric field and thus greater electrostatic repulsion of a particle at the side of a chain relative to the chain end.[9] They also were able to control the chain size by varying the electrostatic repulsion relative to the vdW attraction and dipolar interactions arising from the surface ligands. Enustun and Turkevich hypothesized that 1-D chains may be formed under slow coagulation (days to months) at low ionic strengths to maintain a thick double layer, when the total interaction potential was relatively small.[10] The low potential was obtained either with a low coverage of ionic citrate ligands on the surface, or low pH to decrease the charge of the ligands on the surface. Similarly, long branched chains composed of 10 nm citrate coated Au NPs in ethanol/water mixtures were formed by adding less than 1 mM NaCl to reduce the electrostatic repulsion.[11]

One of the simplest methods to investigate the mechanism and rate of NP assembly is to control the electrostatic repulsion with inorganic electrolytes in water to vary the Debye length, as described by DLVO theory.[10, 12-14] A key factor that governs the rate of aggregation of Au NPs is specific binding or bridging of carboxylate ligands on the surfaces with added monovalent cations.[13, 15-16] These bridging interactions become much stronger for divalent ions[12, 17] For example, Ca^{2+}, Cu^{2+} and Fe^{2+} have been used to chelate Ag and Au particles stabilized by lipoic acid, to form multilayer 3D close-packed structures.[18] Au NPs were also assembled into monodisperse spherical clusters (>100 nm) by bridging carboxylate anions with Zn^{2+} and Cd^{2+} with close packed order.[16] If this bridging attraction could be properly modulated against electrostatic repulsion and vdW attraction, it might be possible to control the properties of 1-D nanoclusters as well as 3-D nanoclusters.

To date, relatively few studies have reported colloidal assembly of Au and Ag NP clusters smaller than 70 nm from pre-synthesized sub-10 nm primary particles; although these small clusters are of great interest in many applications including biomedical imaging and therapy[19-20], sensors[4], catalysis[21], and conductors for electronics[22]. In the field of biomedical imaging and therapy, NPs smaller than 70 nm are often favored, as they have slower uptake by the reticuloendothelial system (RES) and also undergo more rapid endocytosis in cancer cells.[23]

For nanoclusters with very closely-spaced primary particles, the extinction spectra of the surface plasmon resonance shifts into the NIR region from 700-1100 nm, where blood and tissue are relatively transparent.[4, 20, 24-25] The red shift increases as the spacings between the primary particles decreases and the aggregation number increases given changes in the instantaneous dipoles and multipoles of the oscillating electrons.26-30 In order to shift the SPR to 1000 nm, the edge-to-edge spacing should be < ~10 % of the

particle diameter.[31] For example, Au NPs stabilized by a very short ligand, homocysteine, exhibit SPR bands shifts to 800 nm for aggregates of 30 nm Au particles, but only to 650 nm for 11 nm particles.[32] Thus, it appears to be a major challenge to shift the SPR to 1000 nm for sub-10 nm NPs.

A potential strategy to assemble Au NP clusters with high NIR extinction would be to design incomplete, non-uniform coverage of ligands on the particle surfaces to allow very close interparticle spacings on the order of <0.5 nm. Limited surface coverage has been used to achieve such small spacings for "pearl necklaces" that they could be converted to nanowires.[6] Similarly, 14 nm citrate-capped gold NPs adsorbed at an oil-in-water interface fused to form wires over 7 days, whereby the NIR extinction increased out to 1000 nm.[33] Furthermore, small Au nanoclusters with close spacings and strong NIR extinction were produced by exchanging citrate ligands with very weekly bound lysine molecules to weaken electrostatic repulsion.[34] For citrate ligands on Au NPs, an edge-to-edge spacing of 1.28 nm has been observed, which is only somewhat smaller than twice the estimated thickness of 0.7 to 1 nm for a citrate layer on Au.[35] Given that broad NIR extinction out to 1100 nm is observed for ~70 nm Au nanoclusters comprised of very small 5 nm primary particles coated with citrate ligands, it would appear that the spacings between primary particles must be less than 1.28 nm.[36-39] Moderate NIR extinction out to 1000 nm was observed for 5 nm citrate-capped gold NPs assembled into mostly linear aggregates after covalent modification with N-ethyl-N-(dimethylaminopropyl) carbodiimide (EDC).[36] However, high-resolution TEM (HR-TEM) indicated that the 70-100 nm aggregates underwent partial fusion from Ostwald ripening. In a related study, partial fusion between closely spaced NPs led to strong NIR shifts upon removal of citrate stabilizers from gold NP surfaces, although the particle size was not controlled.40 Based on these advances, a remaining challenge would be to utilize

interparticle attractive interactions with incomplete ligand coverage on the surface to achieve very closely spaced primary particles in nanoclusters to achieve strong NIR extinction for small nanoclusters with controlled shape.

Herein, we tune the assembly of 5 nm citrate-capped Au primary nanospheres to form either 1-D or 3-D NP clusters simply by adding monovalent or divalent cations to manipulate the colloidal interactions. Our hypothesis is that utilization of bridging attraction between cations and the citrate ligands, in addition to vdW and dipolar attraction, offers an additional degree of freedom to better tune the cluster size, shape and interparticle spacing. The electrostatic repulsion and the interparticle bridging attraction are varied simply by changing the concentration of either Na^+ or Ca^{2+} at pH 7. A mechanism is presented to describe the change from 3-D NP clusters observed with Na^+ to branched nanochains with Ca^{2+} by varying the range and strength of the electrostatic interactions relative to the bridging interaction. To form nanochains, thick double layers will be used at low Ca^{2+} concentrations to achieve selective growth on the chain ends relative to the sides, in the presence of the strong short-ranged bridging interaction. The effect of cation charge and concentration on the spacing between the primary particles within the nanocluster is analyzed from TEM micrographs and the red shift in the SPR. Partial fusion of the primary particles was observed for Ca^{2+} as a consequence of small interparticle spacings resulting from the strong interparticle bridging attraction. During approach of the NPs, the diffusion of citrate molecules on the surface or citrate desorption[11] could allow for close interparticle spacings in the clusters, given that Park et al. reported citrate coverages of only ~45 % on gold NP surfaces.[35] We demonstrate that close spacings and partial fusion may be used to achieve strong NIR extinction out to 1100 nm in short nanochains with lengths from 20 to 50 nm. In order to harvest the

growing nanoparticles at short times, they were quenched simply by dilution to lower the ion concentration; they were stable for 20 days.

5.2 METHODS AND MATERIALS

Tetrachloroauric acid ($HAuCl_4 \cdot 3H_2O$) and L-Lysine were purchased from Acros Chemicals (Morris Plains, NJ). Sodium borohydride ($NaBH_4$), sodium citrate ($Na_3C_6H_5O_7 \cdot 2H_2O$), calcium chloride ($CaCl_2$), sodium chloride (NaCl), hydrochloric acid (HCl), and sodium hydroxide (NaOH) from Fisher Chemical (Fair Lawn, NJ), PLA(1k)-PEG(10k)-PLA(1k) from Sigma Aldrich (St. Louis, MO), Proteinase K enzyme from MP Biomedicals (Solon, OH) and phosphate-buffered saline (PBS) from Gibco (Grand Island, NY).

5.2.1 Synthesis of primary citrate-capped nanospheres and addition or removal of citrate

Citrate-capped ~4 nm primary nanospheres were synthesized via a previously reported procedure.[37, 41] First, 30mL of a 25.4 mM $HAuCl_4 \cdot 3H_2O$ solution was added to 3 L of DI water at 95 °C under vigorous stirring. Next, 30 mL of a 34.0 mM $Na_3C_6H_5O_7 \cdot 2H_2O$ solution was added to the boiling solution. Approximately one minute later, as the solution darkened, a solution containing 30 mL of 34.0 mM $Na_3C_6H_5O_7 \cdot 2H_2O$ and a 19.8 mM $NaBH_4$ was added which resulted in a bright red color. The solution was then cooled in an ice bath before centrifugation at 14,000 rcf for 10 min to remove large aggregates. The supernatant was then concentrated and purified using a combination of tangential flow filtration (TFF) to a final volume of ~200 mL. Then filter centrifugation was carried out at a speed of 6000 rpm for 5 min to yield a final volume of

the solution of ~10 mL. Finally, approximately 20 mL of DI water was added to achieve a final Au concentration of ~3 mg/mL and final Na-Citrate concentration of 0.3 mM.

To lower the amount of excess citrate ions in the solution and on the Au surfaces for certain experiments, 2 mL of a 3 mg/mL Au solutions were diluted with 5 ml of DI water, placed into a 30 kDa filter centrifuge tube and spun at 6,000 rpm for 5 minutes to a final volume of ~0.5 mL. Once finished, an additional 6.5 mL of fresh DI water was added and the sample was centrifuged a second time. This procedure was repeated two more times. This low citrate level sample was then diluted to 0.3 mg/mL Au for nanocluster formation.

In some circumstances, a 100/1 molar excess of sodium citrate was added to the as-prepared gold nanoparticles at 0.3 mg/mL Au. In this case, the concentration of Na-Citrate in the system was raised from ~0.03 mM to 3 mM. However the excess Na-Citrate was added directly to the reaction mixture containing DI and electrolytes during cluster formation. No prior incubation of the particles with the excess Na-Citrate took place prior to cluster formation.

5.2.2 Characterization of nanospheres

Nanospheres were diluted to ~0.3 mg/mL Au and filtered through a 200 nm polyethersulfone (PES) syringe filter prior to dynamic light scattering (DLS), zeta potential, and UV-vis-NIR measurements. As reported previously,[37-38] hydrodynamic size distributions were measured on a Brookhaven ZetaPALS instrument using a 90° detection angle using a non-negatively constrained least squares multiple pass (NNLS) method and an auto-fit slope analysis option. Sizes less than 3 nm were ignored in the reported distributions on the basis of TEM micrographs, which indicated no particles that

small (Figure E.1). It is well-known that DLS models may yield unphysically small peaks for gold particles.[42] Intensity weighted DLS distributions are given for several samples in the supplemental section. For systems with small absorbance at the laser wavelength (650 nm), we also report volume distributions. For systems with high absorption at 650 nm, the conversion from the intensity distribution to the volume distribution would require Mie theory analysis, beyond the scope of this study. Thus, for systems with an absorbance ratio, $A_{1000/525}$, greater than 0.1, we report the minimum value of the larger NNLS Intensity-weighted peak. The larger peaks were ignored as very small fractions of large particles create intense scattering. This protocol was found to yield diameters that were in agreement with the TEM number average diameters as shown in Table E.7.

The zeta potentials were measured using the Brookhaven ZetaPALS instrument in the ZetaPALS mode. The gold concentration of the measured samples was 0.015 mg/mL at pH 7 and at various ionic strengths of NaCl and $CaCl_2$. Here the concentration was very dilute to minimize particle aggregation prior to measurement. A minimum of five runs were performed for each sample with 10 cycles with an average applied electric field of ~ 9 V/cm. All values reported assume the Hückel model. UV-vis-NIR spectroscopy was obtained with a Varian Cary 60 spectrophotometer with a sample path length of 1 cm. Extinction peaks were normalized to 1 for clarity of comparison. Most extinction results are reported as ratios of the absorbance at 1000 nm relative to 525 nm, termed $A_{1000/525}$, throughout this study.

Thermogravimetric analysis (TGA) measurements were made with a Mettler Toledo TGA/DSC 1 STAR. Samples were dried under desiccated air. The final sample was heated from 25 °C to 900 °C at a rate of 10 °C/min under nitrogen flow.

Gold concentrations were determined through flame atomic absorption spectroscopy (FAAS) using a GBC 908AA analyzer (GBC Scientific Equipment Pty Ltd.) with an air/acetylene flame at a wavelength of 242.8 nm. Samples were prepared by dissolving a known volume of nanospheres in an Aqua Regia (3:1 $HCl:HNO_3$, v/v) solution before exposing them to the flame. The absorbance data were then related to a set of Au standards of known mass to determine the sample concentration.

5.2.3 Nanocluster Formation

Varying amounts of 5 % NaCl or 0.5 % $CaCl_2$ were added to DI water prior to Au NP addition for a final volume of 1 mL. Then, 1 mL of the 0.3 mg/mL citrate-nanoparticle solution was added to a final Au concentration of 0.15 mg/mL. The electrolyte concentrations reported throughout the paper are the concentrations after both solutions were mixed. At differing time points, 200 μL of the resulting solution was removed and diluted to 0.025 mg/mL Au in 1 mL of DI water to reduce the concentration of electrolyte and Au to effectively quench the reaction by increasing the electrostatic repulsion and reducing the rate of interparticle collisions.

5.2.4 Nanocluster Characterization

Immediately after cluster dilution, nanocluster samples underwent DLS and UV-vis-NIR measurements. Certain samples also underwent zeta potential and TEM after both DLS and UV-vis-NIR were complete. . Given the samples were already dilute, only samples for TEM were diluted further to a final concentration of ~ 5 x 10^{-4} mg/mL Au prior to measurement. TEM samples were prepared by placing a 5 μL drop of a given sample onto a 200-mesh carbon Type-A grid (Ted Pella, Redding, CA). The majority of

the drop was then wicked off to form a thin liquid film on the grid which was then immersed in liquid nitrogen and lyophilized overnight at -40 °C using a VirTis AdVantage tray lyophilizer (VirTis, Gardiner, NY). The samples were then examined using an FEI TECNAI G2 F20 X-TWIN TEM with a high-angle annular dark-field detector.

5.3 RESULTS AND DISCUSSION

5.3.1 Characterization of primary citrate coated Au Nanospheres

For the citrate-capped gold NPs synthesized by reduction of $HAuCl_4$ with $NaBH_4$[43] (labelled "as prepared" in Table 5.1) UV-vis-NIR extinction, TEM core diameters, and zeta potential measurements agreed closely with previous studies (Table 5.1).[37, 44] Additionally, the polydispersity (std. deviation), 5.0 ± 0.7 nm, was very low for the TEM number average distribution measured from sizing 100 NPs (Figure E.1). A similar size was observed for particles incubated in 3 mM Na-Citrate, which is an excess of 100x compared to the as-prepared citrate particles which contained ~ 0.03 mM total Na-Citrate in the solution. For the 100x citrate particles, ζ decreased from -45.3 with a standard deviation of ± 1.7 mV to -53.0 ± 3.5 mV, indicating additional citrate binding directly to the Au surface, or H-bonding to other citrate moieties through dangling carboxylates.35 For a third "low citrate" type of particle, which was produced by washing the as-prepared particles 3x times with DI water via filter centrifugation, ζ decreased in magnitude to -34.4 ± 2.2 mV and the organic content according to TGA dropped to 3.3 wt. %. This decrease in stabilizing ligand led to moderate growth of the initial primary particles to 6.5 ± 1.9 nm via TEM analysis given a small population of dimers (Figure E.1c), yet the size remained stable for weeks at room temperature.

5.3.2 Interaction potentials for mono- and divalent electrolytes

To provide a basis for describing the colloidal assembly, we begin by examining the total interaction potential Vtot which is a sum of the vdW, bridging, and electrostatic potentials, all shown in Figure 5.2.[14] To understand the role of these particular terms, we did not include the unknown dipolar attraction and steric repulsion. The vdW potential can be expressed

$$V_{vdW} = -\frac{A}{6}\left[\frac{2a^2}{H(4a+H)} + \frac{2a^2}{(2a+H)^2} + \ln\left(\frac{H(4a+H)}{(2a+H)^2}\right)\right] \quad (1)$$

where A is the Hamaker constant, H is the surface to surface separation distance, and a is the particle radius. The electrostatic potential may be expressed for symmetric and asymmetric electrolytes for surface potentials $\Psi 0 < 25$ mV as[14, 45]

$$V_{electrostatic} = 4\pi\varepsilon_r\varepsilon_0 a^2\Psi_0^2 \exp(-\kappa H)/(H + 2a) \quad (2)$$

where εr is the relative dielectric of the solvent, ε_0 is the dielectric constant in vacuum, and κ is the inverse Debye length given by

$$\kappa = \sqrt{\frac{1000*e^2*N_A*}{\varepsilon_r\varepsilon_0 k_b T}} * (2I)^{1/2} \quad (3)$$

where N_A is Avagadro's number, and I is the ionic strength. Previous studies have shown mono- and divalent cations undergo bridging attraction with citrate ligands on Au

NP surfaces, which may be treated as linearly proportional to the free energy of cation dissociation[15-17] as follows

$$V_{bridging} = -f\Delta G_d \quad (4)$$

where f is a proportionality constant, taken to be 1.2, as established for monovalent cations with citrate by Wang et al.[15] The dissociation energy, ΔG_d for a cation from a citrate ligands is related to the equilibrium dissociation constant, K_d through

$$\Delta G_d = -RT\ln(K_d) \quad (5)$$

The electrostatic energy is shown for the -34 mV particles at a low ionic strength of 0.22 mM for $CaCl_2$ and 75 mM for NaCl, whereby the surface potential was approximated by ζ. For the widely used electrolyte concentrations used in this paper, the surface potentials were chosen as -10 and -20 for mV to reflect ζs in Table 5.2 and the unknown cation adsorption in the Stern layer. Furthermore, V_{elec}/kT is stronger and much longer ranged for Ca^{2+} versus Na^+ as a consequence of the 114 fold lower I and consequently much longer κ^{-1} as shown in Table 5.2. It is instructive to examine the various contributions to V_{tot} at a separation distance of closest approach between two fully citrate-capped NPs of 1.4 nm. This distance is based on the measured 0.7 nm length of a citrate molecule on a gold surface.[35] While V_{elec}/kT of the -34 mV particles is 2.4 without added electrolyte, it drops to below 1 in the presence of NaCl and $CaCl_2$ due to the lower surface potential (ζ) and increased ionic strength.

The attractive interaction energy between the particles is the sum of the vdW and bridging interaction potentials. The dissociation constants for Na^+- and Ca^{2+}-

citrate complexes have been measured as 0.2 M and 0.0007 M, respectively, indicating a significantly stronger binding affinity of the divalent cation.[46] The corresponding ΔG_d values were $6.6x10^{-21}$ and $3.0x10^{-20}$ J. As shown, in Fig. 1b, the $V_{bridging}$ was ~ 4.5x higher for Ca^{2+} than for Na^{+}, which will be shown below to have a large effect on the aggregation behavior. For the distance between two citrate-capped gold NPs of 1.4 nm, the vdW attraction is much smaller than the bridging interaction for both Na^{+} and Ca^{2+}. The variation in the total interaction energy with electrolyte concentration will be discussed below for each of the cations as a function of cation concentration.

5.3.3 Effect of $CaCl_2$ and NaCl on the Debye length and zeta potential of the primary particles

Before describing the particle growth to form the Au NP clusters, we first examine the effect of each electrolyte on ζ at a very low Au concentration of 0.015 mg/ml where growth was minimal. Both the as prepared (-45 mV) and low citrate (-35 mV) particles were characterized for key electrolyte concentrations used throughout this study (Table 5.1). These concentrations were based on known critical coagulation concentrations (CCC) of citrate-capped metal NPs of ~50-100 mM for NaCl and ~2.1-2.5 mM for $CaCl_2$.[17, 47] For dilute 0.08 mM and 0.22 mM $CaCl_2$, the Debye lengths were very large, 17.3 and 11.3 nm, respectively. For the much larger NaCl concentrations of 50 and 75 mM, the Debye lengths were much smaller, only 1.37 and 1.12 nm, respectively, as a consequence of the much larger ionic strengths.

The ζ values of the as prepared and -34 mV primary particles dropped significantly with the added electrolytes in Table 5.2. With only 0.08 mM $CaCl_2$, ζ were -20.9 ± 3.3 and -29.6 ± 0.9 mV for -34 mV and -45 mV particles, respectively. For 0.22 Ca^{2+} ζ dropped to -16.4 ± 1.5 and -23.0 ± 1.8 mV indicating greater Debye screening and

greater adsorption in the Stern layer. For NaCl as seen for $CaCl_2$, more negative ζ values were observed for the as prepared -45 mV particles at the lower NaCl concentration.

5.3.4 Effect of NaCl on NP aggregation

To further establish electrolyte concentrations for nanocluster formation, we first identified the critical coagulation at the diffusion controlled limit. Here, the Smoluchowski half-life is 1.6 ms for 5 nm spheres at a concentration of 0.3 mg/mL Au. Immediate aggregation was observed visually for our system at ~ 100 mM NaCl as the colloids grew to 75 nm within the shortest time measured, 1 s, and precipitated within 3 s (Figure E.2). This concentration was essentially the CCC where the stability ratio became unity, given the loss of electrostatic repulsion, and gain in bridging attraction. This value for a 5 nm particle is consistent with the trend previously reported values of 48 mM for 60 nm and 122 mM for 30 nm Ag spheres.[17, 47]

The NP clusters in this study were formed at a gold concentration of 0.15 mg/mL with NaCl concentrations from 25 to 100 mM. For the lowest NaCl concentration, the hydrodynamic diameters, D_H, grew to only 15 nm and 18 nm over 1800 s, for -45 mV and -34 mV citrate particles, respectively (Table S2). The small growth was not enough to create any significant changes in the SPR for either sample as $A_{1000/525}$ ratios remained <0.1. Notable size increases were observed as the concentration was doubled to 50 mM as shown for the -34 mV primary particles in Figure 5.3a. The NP cluster sizes grew to over 100 nm within 30 seconds and continued to steadily increase up to 300 s. Here, $A_{1000/525}$ values increased moderately to ~0.4 for the 465 nm aggregates with the color of the solution becoming reddish purple (Table E.4). Much higher NIR absorbance was observed for 75 mM NaCl as shown in the spectra at 1 and 30 s in Figure 5.3b for the -34

mV primary particle systems. With a NP cluster size of 50 nm $A_{1000/525}$ reached ~0.6 within 2 seconds. At 10 s, $A_{1000/525}$ rose to over 1.0, with a notable color change to purple, as D_H grew to 108 nm. At even greater times, there was little further change in the $A_{1000/525}$, but the D_H grew to 498 nm within one minute.

Strong SPR shifts into the NIR region of the electromagnetic spectrum are observed in a variety of gold NP clusters due to the overlap of hybridized plasmon modes.[48] The shifts are related to the interparticle spacings (<10% of the particle diameter), the nanocluster size, which governs the number of interparticle contacts, and the anisotropy in cluster shape.[26, 28, 31, 48-50] As the size increases, the larger number of contacts, "hot spots", between primary particles, where the electromagnetic fields are enhanced, produces a greater red shift. With a generalized multiparticle Mie solution and the T-matrix method, the shift in the SPR resonance for linear NP chains, 2D and 3D NP clusters was calculated as a function of the particle separation relative to the diameter, H/2a. For the smallest H/2a of 0.025, the peak maximum shifted to ~ 700 nm for a 4-mer chain and 800 nm for a 32-mer chain for 40 nm particles. In our case, this ratio would correspond to an H of only 0.125 nm. At the same ratio of 0.025, similar shifts were seen for 20 and 40 nm 1-D chains and 3-D clusters.[50] This distance is an order of magnitude below the value of 1.38 nm for the spacing between two particles coated with a monolayer of citrate. Thus, the relatively low NIR extinction for the small NP clusters produced with NaCl suggests that the vdW attraction and weak bridging were insufficient to produce interparticle spacings well below 1 nm. Eventually for extremely large clusters with a large number of contacts, the red shift was enough to give an $A_{1000/525}$ of 1.0. A similar result has been reported previously for 14 nm Au NP citrated clusters assembled with NaCl.[9] In contrast, small red shifts were observed for a more strongly binding ligand, thioglycolic acid (TGA), cysteine, and glutathione, as has been observed

for a number of ligands other than citrate.[9, 51-53] Therefore, it appears that the relatively high $A_{1000/525}$ for citrate may indicate it is somewhat mobile on the surface or leaves open Au patches that my approach each other more closely than 1.38 nm.

While similar growth rates were observed for the -45 mV relative to the -34 mV primary citrate particles, the sizes and NIR absorbance of the samples were consistently less. For instance, at 30 s and 75 mM NaCl, the cluster D_H for the -34 mV sample already reached 369 nm, as was also the case for the -45 mV particles (Table2). Figure 5.3b compares the UV-vis-NIR absorbance curves for the two types of primary particles at 1 s and 30 s. In both cases, a lower $A_{1000/525}$ ratio is observed for the -45 mV particle sample, consistent with smaller number of "hot spots" or electric field enhancement for the smaller NP clusters (Table S2).[26, 37-39] Furthermore, TEM images of the -34 mV, 75 mM NaCl samples after 2 s show closely-spaced distinct primary particles within the clusters (Figure 5.3c and Table S6-Row 12). However, at high resolution, a very small degree of partial fusion was evident as shown in Table E.6- Row 13. By 30 s, fusion was extensive as shown in Figure 5.3d and Table E.6-Row 14. Interestingly, for only 50 mM NaCl at 120 s, minimal fusion and weak NIR absorbance were observed, indicating greater separations with the stronger electrostatic repulsion.

5.3.5 Effect of $CaCl_2$ on NP aggregation

The concentrations were chosen for the experiments with Ca^{2+} by first determining the CCC. Through visual confirmation, a $CaCl_2$ concentration of ~1.5 mM induced immediate aggregation for 0.15 mg/mL Au, characteristic of the CCC. This was similar to the reported value of 2.1 mM CCC for $CaCl_2$ for 30 and 60 nm Ag spheres, and was ~100 fold smaller than for NaCl.[17, 47] From theory, the calculated CCCs for the

Darjaguin approximation in the limit as $\Psi_0 \rightarrow \infty$ are ~100 fold smaller for a 2:1 than at 1:1 electrolyte.[54] Therefore, $CaCl_2$ may be used to form NP clusters at much lower ionic strengths, whereby the longer Debye lengths may potentially be utilized to influence the morphology.

Notably different morphology and NIR absorbance were observed for NP clusters made in the presence of much more dilute divalent Ca^{2+} relative to Na^+ for the -34 mV particles. Figure 5.4 shows the absorbance spectra and TEM for growth of clusters made from -34 mV citrate primary particles in the presence of 0.22 mM $CaCl_2$ over 60 s. In addition, the $A_{1000/525}$ ratio and D_H are given in Figure 5.5a to 7200 s. The $A_{1000/525}$ ratio rose quickly to 0.6 within 10 s and then increased to 1.1 at 60 s with an upward sloping curve suggesting the first part of a second, broad peak in the NIR around 1000 nm. TEM images at the different time intervals show growth of what appear to be NP dimers into elongated, branched, 1-D chains over 60 s (Figure 5.4b-d). At 10 s, a large number of dimers are present along with larger aggregates, with a TEM number average size of 16.2 ± 8.8 nm (Table E.7-Row 1). After 30 s, the chains were elongated with an average length of 24.3 ± 14.3 nm and the formation of branches became visible. Remarkably, the $A_{1000/525}$ was already 1.0, despite the very small size of the branched nanochain. By 60 s, the chains grew longer and more branched with a greater polydispersity and an average length of 30.5 ± 17.2 nm as shown in Figure 5.4d and Table E.7-Row 3. The particles underwent fusion as shown by the HR-TEM image in the inset of Figure 5.4d and in Figure S3, as discussed in detail below. Here, the NIR absorbance was much greater than with NaCl for the small NP clusters. This difference may be attributed to the strong bridging between Ca^{2+} and the citrate ligands that produced closer interparticle spacing and fusion between primary particles, relative to NaCl.

These distinctly asymmetric geometries have a high aspect ratio as seen for nanorods. The high degree of anisotropy may explain the beginning of a secondary peak in the UV-vis-NIR absorbance spectra in Figure 5.4a. However due to the polydispersity in shape and degrees of fusion at the particle interfaces, the peak is quite broad as opposed to the narrow secondary, longitudinal peaks characteristic of many well-defined nanorods.[55]

Beyond 60 s, the branched nanochain structures displayed steady growth up to ~ 100 nm within 1800 s (Figure 5.5a). A decrease in the non-normalized UV-vis-NIR absorbance of the sample indicated that the additional growth resulted in slight precipitation from either a formation of a small population of much larger aggregates present in the solution, or the aggregation of pre-formed clusters in solution (Figure E.2). However, samples made within 300 s were stable for over 20 days at room temperature as characterized by UV-vis-NIR absorbance and D_H in Table E.3.

In contrast with the results for 0.22 mM $CaCl_2$, much smaller particles were formed for the -34 mV Au with only 0.08 mM $CaCl_2$. With the more negative ζ of -20.9 ± 3.3 mV, only a moderate size increase to 14 nm was observed within the first 300 s, with very little change in NIR absorbance. With the greater electrostatic repulsion and weaker bridging attraction with the lower Ca^{2+} concentration, the NP clusters did not grow significantly or undergo extensive fusion even up to 1800s (Table E.6-Rows 1-2). Thus, it appears that a higher driving force for aggregation with 0.22 mM $CaCl_2$ is needed for produce the small spacings and subsequent fusion that give the highest NIR absorbance.

For the more charged -45 mV primary particles (Figure 5.5b and e) , the results will now be shown to be similar to those observed at -34 mV in nearly all respects, but with less growth at small times and significantly weaker NIR absorbance. Minimal

growth was again observed with 0.08 mM $CaCl_2$. The clusters only grew to 16 nm aggregates with an $A_{1000/525}$ of 0.1 in 60 s. However, once again, as the concentration of Ca^{2+} was increased to 0.22 mM, the greater electrostatic screening and bridging attraction resulted in a significantly higher NIR absorbance, even for very small branched chains. After 1 s, the size grew to 20 nm with an $A_{1000/525}$ of 0.5 and further to 33 nm and an $A_{1000/525}$ of 0.7 by 60 s. Interestingly, the D_H values were similar for the -45 and -34 mV primary particle aggregates at the same conditions up to 180 s. After this, the less charged cluster aggregates grew more rapidly. At 1800 s, the D_H was 86 nm with an $A_{1000/525}$ of 1.1 for the -34 mV primary particles, and 57 nm with an $A_{1000/525}$ of 0.9 for the -45 mV ones. For an even higher $CaCl_2$ concentration of 0.5 mM, the rate of nanocluster growth increased significantly as the cluster D_H rose to 229 nm by 300 s; and the solution aggregated out of solution by 600 s. Despite the lower degree of growth and NIR for the more charged -45 mV samples with greater electrostatic repulsion, branched-chain morphologies were observed in both cases as shown in Figure 5.5e and Table S6-Row 9.

To rule out any potential changes in morphology from halide ion complexation with Au, and etching, clusters were made using 0.22 mM $Ca(NO_3)_2$ to determine if the linear, fused behavior was truly a result of Ca^{2+} bridging or Cl^- etching.[56] Despite an average 10 nm higher cluster D_H for the nitrate salt, NIR extinction and linear branched-chain morphology was present for both samples, as seen in Figure E.4. Thus, it is unlikely that Cl^- etching played a significant role in the linear growth or fusion.

While chains were formed for the -45 mV and -34 mV primary particles, clusters were not formed with 3 mM Na-citrate for the -53 mV primary particles within 600 s. After 3600 s, the solution remained red and dimer and trimers were formed with D_H of 17 nm (Table E.2). When the concentration of $CaCl_2$ was increased to 1.5 mM, the particles grew to 48 nm within 3600 s, but only with an $A_{1000/525}$ of 0.19 (Figure 5.5c). The

morphology of the resulting clusters resembled the spherical aggregates observed in the presence of NaCl, with notable interparticle spacings (Figure 5.5f). In the presence of excess citrate ions, bilayers can form on Au particle surfaces through H-bonding.[35] Despite the high concentration of bridging Ca^{2+} cations, the -53 mV initial particle charge and steric repulsion from multi-layers of citrate on the NP surface resulted in a more spherical geometry as opposed to the branched-chains formed at lower citrate concentrations. NIR $A_{1000/525}$ values above 1.0 were not achieved for clusters made from these particles until the D_H was over 100 nm in the case of 2.1 mM $CaCl_2$ concentrations. As seen for NaCl, larger numbers of hot-spots are required to raise the NIR absorbance for these particles, relative to the case of the -45 mV and -34 mV primary particles , as a consequence of larger interparticle spacings.[26, 48]

The chains appear to be partially fused, as is even more apparent in high resolution TEM shown in the inset of Fig. 5.3d. Figure E.3 shows HR-TEM images for both $CaCl_2$ chains and NaCl aggregates showing similar 0.24-0.26 nm lattice spacings for clusters made from both electrolytes, close to the 0.24 nm spacings characteristic of the (111) plane for Au.[57] The self-assembly of Au nanocrystals into 2-D nanowire arrays was investigated for dodecanethiol coated Ag nanocrystals.[58] Nanowire arrays were only formed, as monitored on a TEM grid, upon decreasing the dodecanethiol surface coverage to allow the particles to approach each other to within 0.5 nm. At this short spacing metallic bonding drives adhesion.[45] For higher dodecanethiol coverages where the spacing was 1.6 nm, still less than the closest expected spacing of 3 nm, that is twice the length of dodecanethiol adsorbed on a flat silver surface, wires were not formed. Similarly, upon partial removal of TGA ligands, “pearl necklaces” closely-spaced CdTe NPs fused into a single nanowire crystal, with a similar diameter as the primary particles. For dialyzed 17 nm citrate Au NPs, the degree of fusion was tuned by the amount of time

to remove the citrate ligands.[40] The fusion was thought to occur only for "reactive collisions" that shared the same crystallographic planes at the interface. For citrate ligands, the much smaller spacing of 1.4 nm[35] compared to 3 nm for dodecanethiol would favor close approach. However, for the higher citrate coverage with a higher ζ of – 53 mV and possibly multilayers, the particles were separated sufficiently to prevent partial fusion. Given that the degree of fusion is very sensitive to the particle spacing, the results in Figure 5a and b indicate the stronger attraction for 0.22 mM $CaCl^2$ for either the -34 or -45 mV particles provided close enough particle spacings on the order of 0.5 nm that lead to adhesion.

Linear 1-D assemblies were observed primarily in the presence of Ca^{2+} cations for the -45 mV and -34 mV primary citrate NPs, but not for NaCl or the -53 MV primary NPs. The formation of linear chains has been widely attributed to dipole-dipole interactions, for example in the case of CdTe semiconductor NPs with a permanent dipole.[6] For Au particles where the conductive cores do not have a permanent dipole moment, the dipole moment may be generated from inhomogeneities in the surface ligands, for example, for mixtures of a charged and uncharged ligands such as citrate and 2-mecaptothanol.[49] For Au NPs capped with TGA, the Au-S bonds were thought to produce dipoles that led to 1-D growth. Alternatively, the oriented interactions between glutamic acid dipoles on Au NPs surfaces oriented the particles into linear chains. In our case, dipole moments may be produced by inhomogeneities of the citrate ligands on the particle surfaces. In a study with FTIR and X-ray photoelectron spectroscopy, hydrogen bonds between citrate molecules led to the formation of citrate networks on the surface, when the citrate coverage was 45%.[35] In our case, these inhomogenities may be further enhanced by intraparticle bridging of citrate with the Ca^{2+} ions.[17, 47] For the higher citrate

coverage for the -53 mV particles, the lack of 1-D chain formation may suggest the dipole moment decreased as the citrate became more uniform on the surface.

Zhang et al. demonstrate the length of nanochains could be controlled via the addition of NaCl to modulate electrostatic repulsion relative to the vdW and dipolar attraction between primary particles.[9] When the electrostatic repulsion was at least 2 fold greater than the vdW force, chains were formed, given weaker electrostatic repulsion at the chain ends than the sides. In contrast, when electrostatic repulsion was weaker than the vdW attraction, addition of particles was no longer selective toward chain ends and 3-D assemblies are formed. Following this model, as a particle approaches a growing chain, we assume that the balance between electrostatic repulsion and vdW attraction would favor the chain ends for Ca^{2+} since $V_{elect} > V_{vdW}$ for the values shown in Figure 5.2. At particle separations greater than ~3 nm the bridging interaction is weak. The much lower concentration of Ca^{2+} to form clusters relative to Na^{+} led to thicker double layers and greater electrostatic repulsion, conditions needed to direct 1-D growth as observed.

This model may be modified to include the role of the bridging attraction that becomes very strong at very close separations (Fig. 5.2b) Our results indicate that despite the large strength of this bridging attraction, the greater electrostatic repulsion at chain ends for thick double layers with Ca^{2+} favored chains relative to Na^{+} (Fig. 5.2a) where 3-D clusters are formed. Thus the potential at larger separations before bridging becomes strong appears to guide the direction of approach of the primary particles. Thus, a 1-D cluster is formed by strong electrostatic repulsion from the very thick double layer, weak vdW attraction, and the strong bridging attraction at very short range, in the presence of the attraction between the dipoles on the particles. These forces may be manipulated by changing the cation concentration and valence to influence the double layer thickness and the bridging attraction to control the nanocluster morphology. Furthermore, the

interparticle Ca^{2+} bridging attraction provided a strong attractive driving force to overcome the strong electrostatic repulsion, despite the very low Ca^{2+} concentration. Therefore both attraction and repulsion were relatively strong, yet the balance between could be tuned with the Ca^{2+} concentration in order to control the cluster morphology.

Whereas short Na^{+} 1-D chains have been formed slowly in time frames from days to months in deionized water[10], we were able to form them rapidly given sufficient bridging attraction with Ca^{2+}, when properly balanced against long ranged electrostatic repulsion with relatively dilute Ca^{2+}.

The impact of the morphological changes for the various classes of NP clusters on the NIR absorbance is summarized in Figure 5.6 and Table 5.3. As shown in Figure 5.6, the NIR absorbance increased as the primary particle charge was reduced, but it changed very little as the D_H increased from 25 to 40 nm. For ~25 nm clusters, the $A_{1000/525}$ was 0.65 for -45 mV primary NPs and 1.10 for -34 mV NPs. Similarly, for ~40 nm nanoclusters, the $A_{1000/525}$ decreased with the primary NP charge from 1.10 (-34 mV), to 0.75 (-45 mV), and finally to 0.10 (-53 mV). Given the very small particles spacings <0.5 nm along with the fusion, it was not possible to discern the difference in particle spacings for the -34 and -45 mV cases by TEM (Figure 5.5d,e and Table E.6-Rows 1-9). However, as the electrostatic repulsion increases, expected larger spacings between primary particles and a decrease in fusion would result in weaker NIR absorbance, as observed.

Another way to relate the spectra to morphology is to determine what D_H is needed to produce a given $A_{1000/525}$ as a function of the primary particle charge and electrolyte type (Table 5.3). At $A_{1000/525}$ of 0.6, a D_H below 70 nm could be achieved for three of the four conditions. At each $A_{1000/525}$, the strong bridging attraction from Ca_{2+} compared to Na_{+}, resulted in a much smaller D_H. This difference in D_H is accentuated as

the $A_{1000/525}$ increases. For an $A_{1000/525}$ of 0.9, D_H for clusters made with $CaCl_2$ were 21 nm and 41 nm for -34 mV and -45 mV primary NPs, respectively, whereas much greater values were required for those formed with NaCl. It was not possible to achieve an $A_{1000/525}$ of 1.0 with the more charged -45 mV particles, whereas it could be attained for a D_H of only 33 nm with the -34 mV case with $CaCl_2$. These differences emphasize the strong correlation between interparticle spacings and fusion with the NIR extinction. The small interparticle spacings and asymmetry in shape with fusion for the branched nanochains produce high NIR absorbance with much fewer hot spots and much smaller D_H values than for the more spherical, loosely-packed NaCl aggregates in Figure 5.3c and in a previous study[9]. Even when fusion occurred for the NaCl clusters, a more rounded, spherical geometry led to high NIR only with large sizes, as seen in Figure 5.3.

5.4 CONCLUSIONS

The size and morphology of NP clusters of small 5 nm citrate coated Au primary particles was controlled by tuning the electrostatic repulsion and bridging attraction in the presence of vdW and dipolar attraction. In the case of Ca^{2+}, strong interparticle bridging with citrate anions produced branched nanochains in < 60 s with closely spaced and partially fused primary particles, resulting in a broad NIR extinction peak out to 1100 nm. This level of NIR extinction is highly unusual for such small nanochains with lengths as short as 20 nm. The branched nanochains were formed by strong electrostatic repulsion with a very thick double layer to favor growth on the chain ends instead of the sides, relative to weaker vdW forces.[9] At very close spacings on the order of 1.4 nm or less, the particles were bound to the cluster by strong short-ranged bridging attraction in addition to vdW attraction. In contrast, spherical nanoclusters were formed with NaCl often with

distinct spacings between the primary particles and minimal fusion according to TEM. For Na^+, much higher ionic strengths were needed to screen the electrostatic repulsion, and the bridging driving force was much weaker. Consequently, thinner double layers and weaker electrostatic repulsion no longer favored anisotropic particle growth to chains. For Ca^{2+}, intraparticle bridging of citrate may have produced dipoles on the particle surfaces that are known to favor anisotropy. In each case, the growth of the nanoclusters was quenched simply by dilution to lower the ionic strength to increase the electrostatic repulsion and weaken the interparticle bridging. The resulting particles were stable over 20 days. For the desired nanocluster size less than 50 nm, the small 5 nm primary particles provided a larger number of "hot spots" for electrical field enhancement resulting in larger NIR shifts relative to the much more commonly studied particles larger than 10 nm. The ability to design the size and shape of NP clusters, as well as the interparticle spacing, by tuning bridging and electrostatic interactions may be expected to be quite general and of broad applicability in materials synthesis.

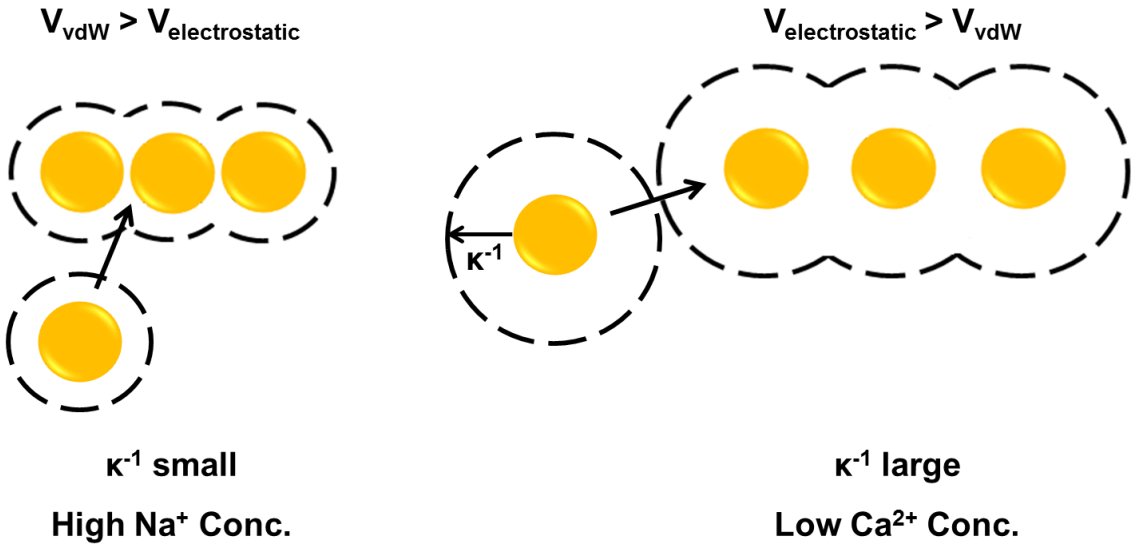

Figure 5.1: Schematic showing the assembly of gold NPs into spherical and linear chain morphologies. Shorter-ranged Debye lengths occur in the presence of the high Na^+ concentrations leading to a greater influence of the vdW potential and non-selective particle addition to the cluster. For the low Ca^{2+} concentrations, longer-ranged Debye lengths occur leading to stronger electrostatic potentials between neighboring particles resulting in selective addition of new NPs to the chain ends.

Table 5.1: Characteristics of primary Au particles with various citrate concentrations

	As Prepared	**100x Citrate**	**Low Citrate**
$A_{1000/525}$	0.02	0.01	0.03
TEM Volume Avg (nm)	5.0 ± 0.7	5.0 ± 1.4	6.5 ± 1.9
Zeta Potential (mV)	-45.3 ± 1.7	-53.0 ± 3.5	-34.4 ± 2.2
Organic Content (wt %)	4.8 ± 0.3	Not Measured	3.3 ± 0.2

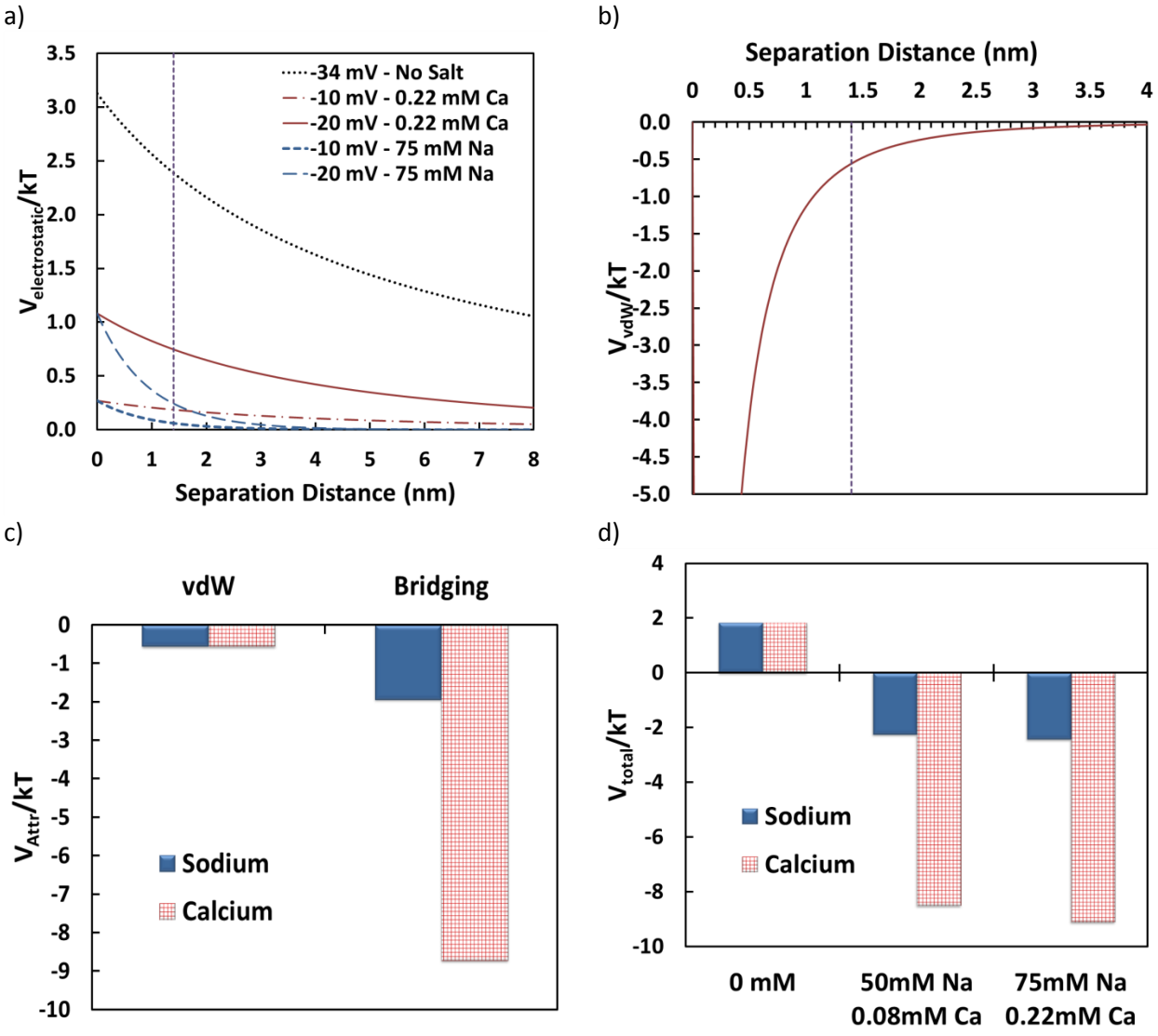

Figure 5.2: a.) Electrostatic potential for 5 nm primary citrate particles for various surface potentials and varying NaCl and $CaCl_2$ concentrations b) van der Waals potential. vdW and bridging attraction potentials (c) and total interaction potential (d) versus NaCl and $CaCl_2$ concentration for a separation distance of 1.4 nm. The separation distance for two particles coated with citrate ligands is ~ 1.4 nm.

Table 5.2: Debye length and primary particle zeta potential (0.015 mg/ml Au) and properties of the clusters formed at 30 and 300 s after electrolyte addition to 0.15 mg/mL Au at pH 7 for two types of primary particles

				t_1 = 30 s			t_2 = 300 s		
Primary Particle	**Salt Conc. (mM)**	**κ^{-1} (nm)**	**Primary Au ζ (mV)**	**D_H (nm)**	**$A_{1000/525}$**	**Cluster ζ (mV)**	**D_H (nm)**	**$A_{1000/525}$**	**Cluster ζ (mV)**
-34 mV	0.08 $CaCl_2$	17.32	-20.9 ± 3.3	7.2	0.02	-19.6 ± 1.1	9.9	0.06	-30.7 ± 1.9
	0.22 $CaCl_2$	11.34	-16.4 ± 1.5	22.4	1.00	-31.8 ± 1.8	48.2	1.15	-26.8 ± 2.9
	50 NaCl	1.37	-24.0 ± 6.1	16.4	0.02	-36.0 ± 3.1	465	0.37	-46.9 ± 0.8
	75 NaCl	1.12	-16.8 ± 5.8	369	1.00	-27.6 ± 1.8	Aggr	Aggr	Aggr
-45 mV	0.08 $CaCl_2$	17.32	-29.6 ± 0.9	7.7	0.03	-29.0 ± 1.6	15.6	0.10	-33.2 ± 1.5
	0.22 $CaCl_2$	11.34	-23.0 ± 1.8	25.0	0.60	-31.8 ± 1.3	49.5	0.84	-23.9 ± 4.0
	50 NaCl	1.37	-29.9 ± 2.1	26	0.01	-40.4 ± 1.9	180	0.28	-43.4 ± 0.6
	75 NaCl	1.12	-21.1 ± 0.8	243	0.82	-36.0 ± 2.9	Aggr	Aggr	Aggr

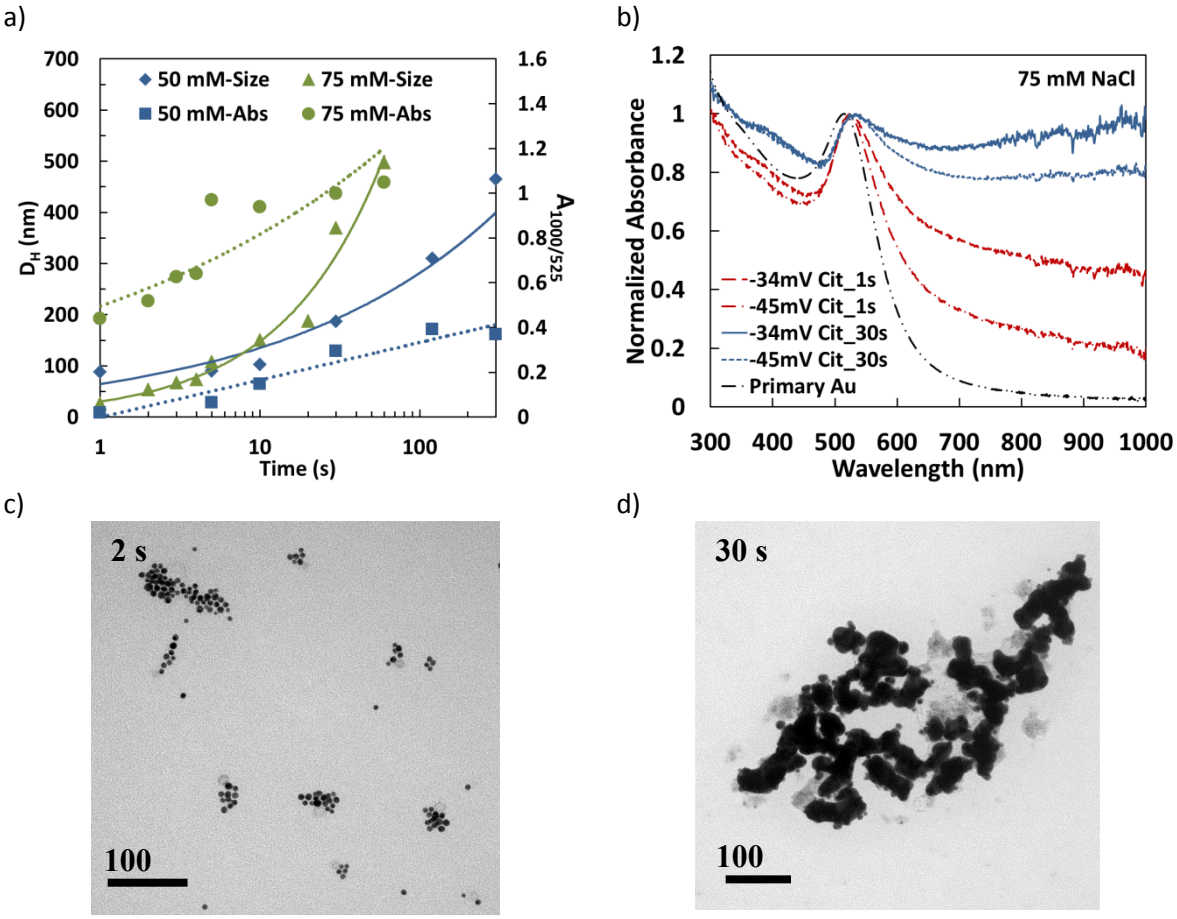

Figure 5.3: a.) Nanocluster D_H (DLS) and $A_{1000/525}$ ratio vs time for -34 mV primary particles for 50 and 75 mM NaCl. UV-vis-NIR extinction curves are shown in b) for 75 mM NaCl for reaction times of 1 and 30 s. TEM image of clusters made with 75 mM NaCl after 2 s (c) and 30 s(d).

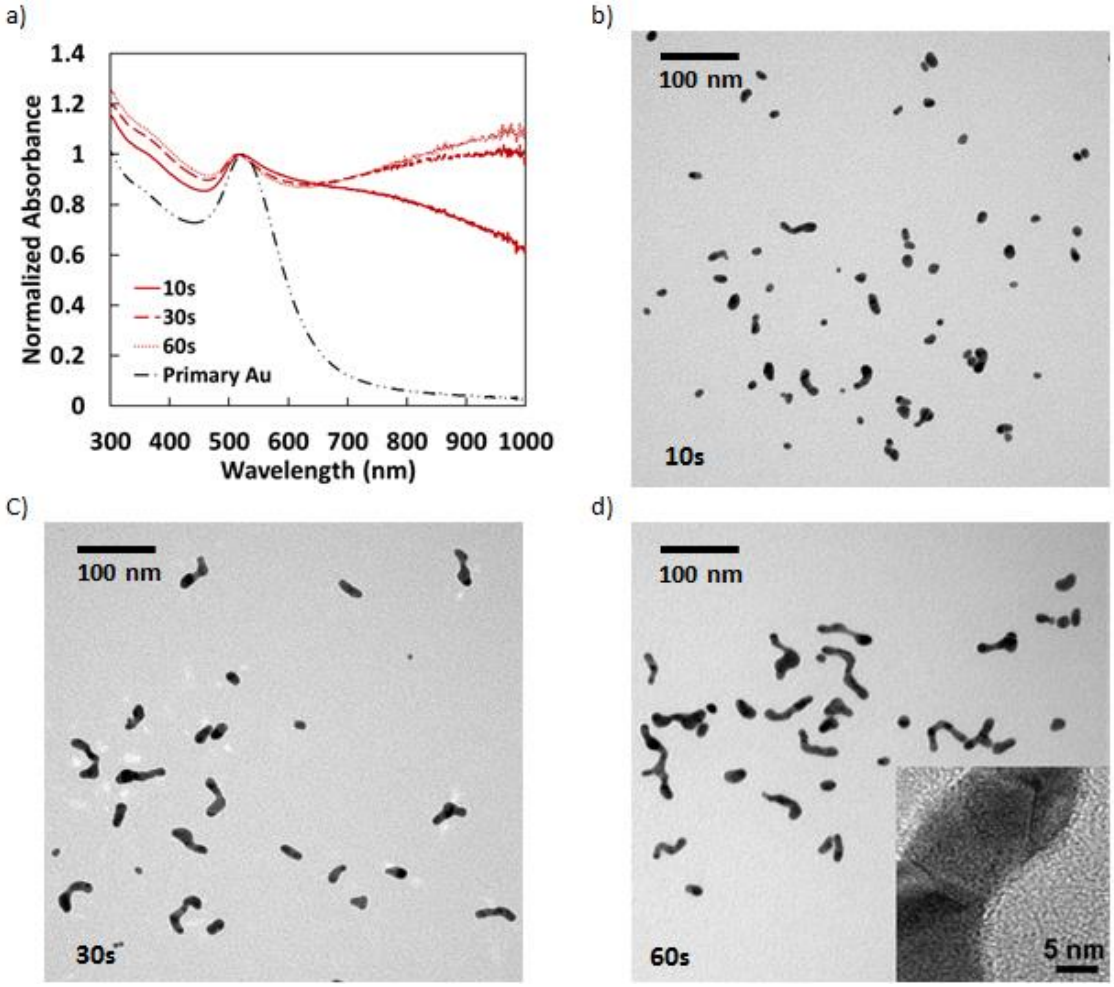

Figure 5.4: Absorbance versus time for -34 mV initial particles and 0.22 mM $CaCl_2$. b-d. TEM images. HR-TEM showing fusion of aggregates is shown in the inset in d.

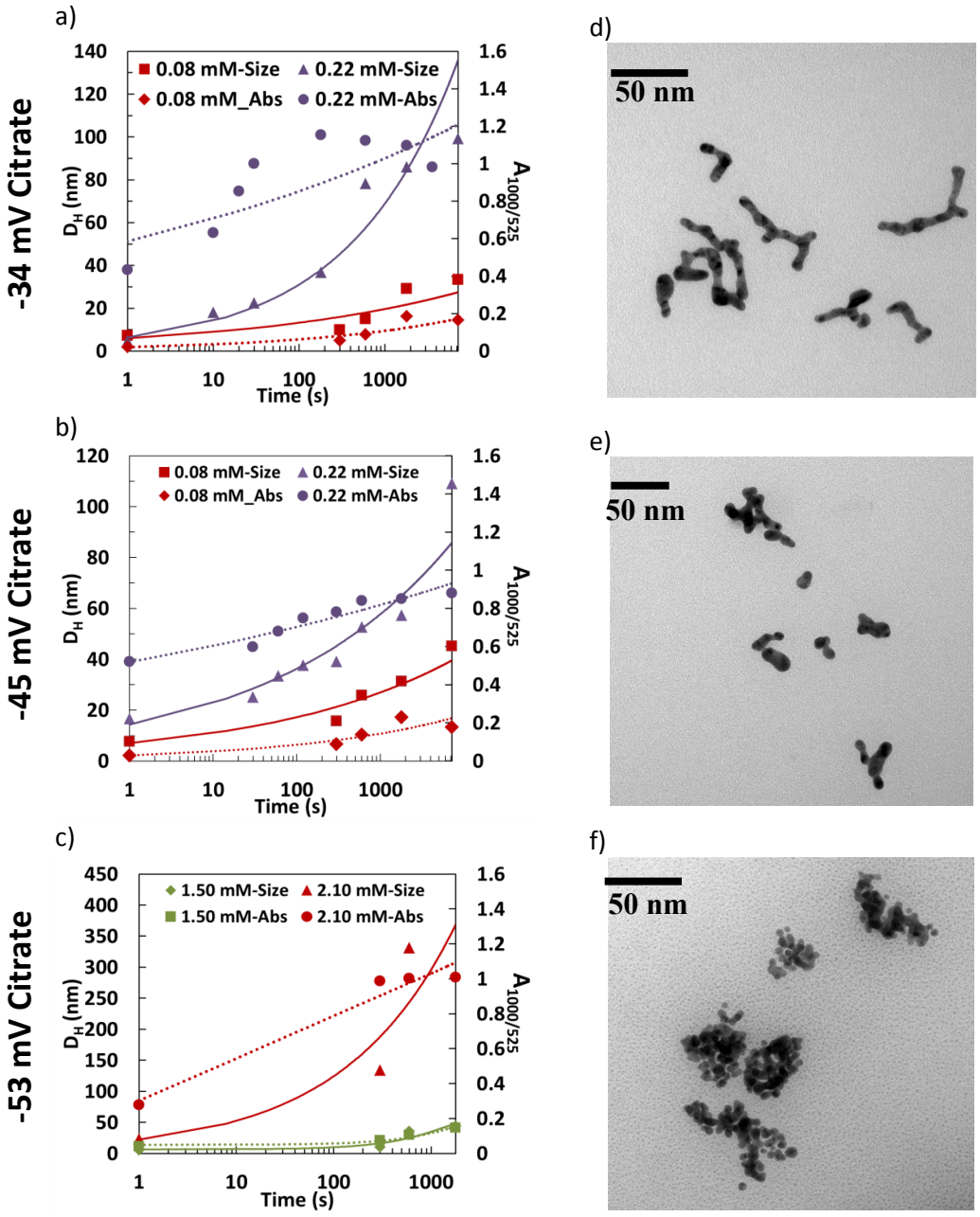

Figure 5.5: (a-c) Effect of $CaCl_2$ concentration and initial particle zeta potential on UV-vis-NIR absorbance and D_H of nanoclusters vs. time. TEM images of an ~40 nm representative sample are shown for: d) -34 mV primary particles and 0.22 mM $CaCl_2$ at 120 s, e) -45 mV primary particles and 0.22 mM $CaCl_2$ at 120 s, and f) -53 mV primary particles and 1.5 mM $CaCl_2$ at 3600 s.

a)

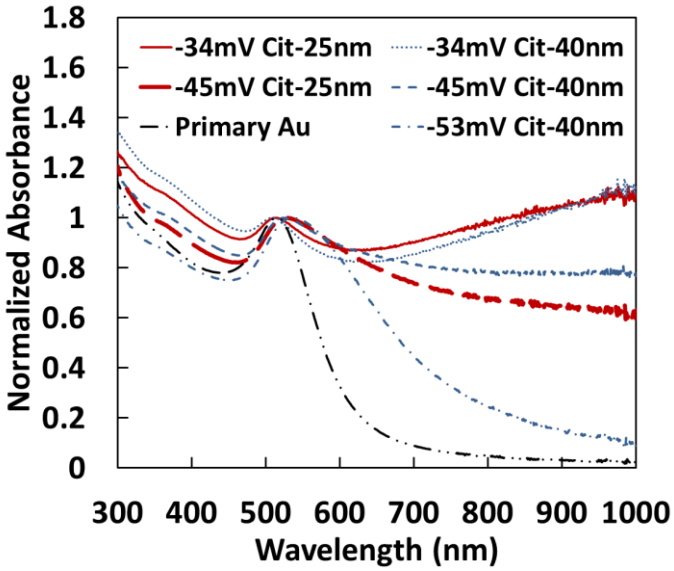

Figure 5.6: a) Normalized absorbance for 25 and 40 nm clusters formed with various types of primary particles

Table 5.3: D_H values and reaction times for clusters made with either -34 or -45 mV primary particles and electrolytes to achieve a given $A_{1000/525}$ ratio.

		$A_{1000/525}$					
Primary Particle	**Salt Conc. (mM)**	**0.6**		**0.8**		**1.0**	
		Time (s)	**D_H (nm)**	**Time (s)**	**D_H (nm)**	**Time (s)**	**D_H (nm)**
-34 mV	**0.22 mM $CaCl_2$**	10	18.0	20	21.0	30	32.7
	75 mM NaCl	3	66.7	5	108	30	369
-45 mV	**0.22 mM $CaCl_2$**	30	25.0	300	41.0	--	--
	75 mM NaCl	5	141	20	172	--	--

5.5 REFERENCES

1. Hill, L. J.; Pinna, N.; Char, K.; Pyun, J. Colloidal polymers from inorganic nanoparticle monomers. Prog. Polym. Sci. 2015, 40, 85-120.
2. Klinkova, A.; Choueiri, R. M.; Kumacheva, E. Self-assembled plasmonic nanostructures. Chem. Soc. Rev. 2014, 43, 3976-3991.
3. Lu, Z.; Yin, Y. Colloidal nanoparticle clusters: functional materials by design. Chem. Soc. Rev. 2012, 41, 6874-6887.
4. Romo-Herrera, J. M.; Alvarez-Puebla, R. A.; Liz-Marzan, L. M. Controlled assembly of plasmonic colloidal nanoparticle clusters. Nanoscale 2011, 3, 1304-1315.
5. Wang, T.; LaMontagne, D.; Lynch, J.; Zhuang, J.; Cao, Y. C. Colloidal superparticles from nanoparticle assembly. Chem. Soc. Rev. 2013, 42, 2804-2823.
6. Tang, Z.; Kotov, N. A.; Giersig, M. Spontaneous organization of single CdTe nanoparticles into luminescent nanowires. Science 2002, 297, 237-240.
7. Sinyagin, A. Y.; Belov, A.; Tang, Z.; Kotov, N. A. Monte Carlo computer simulation of chain formation from nanoparticles. The Journal of Physical Chemistry B 2006, 110, 7500-7507.
8. Li, M.; Johnson, S.; Guo, H.; Dujardin, E.; Mann, S. A Generalized Mechanism for Ligand- Induced Dipolar Assembly of Plasmonic Gold Nanoparticle Chain Networks. Adv. Funct. Mater. 2011, 21, 851-859.
9. Zhang, H.; Wang, D. Controlling the Growth of Charged-Nanoparticle Chains through Interparticle Electrostatic Repulsion. Angew. Chem. 2008, 120, 4048-4051.
10. Enustun, B. V.; Turkevich, J. Coagulation of Colloidal Gold. J. Am. Chem. Soc. 1963, 85, 3317-3328.
11. Han, X.; Goebl, J.; Lu, Z.; Yin, Y. Role of Salt in the Spontaneous Assembly of Charged Gold Nanoparticles in Ethanol. Langmuir 2011, 27, 5282-5289.
12. Burns, C.; Spendel, W.; Puckett, S.; Pacey, G. Solution ionic strength effect on gold nanoparticle solution color transition. Talanta 2006, 69, 873-876.
13. Elimelech, M.; Gregory, J.; Jia, X. Particle deposition and aggregation: measurement, modelling and simulation; Butterworth-Heinemann2013.
14. Hiemenz, P. C.; Rajagopalan, R. Principles of Colloid and Surface Chemistry, revised and expanded; CRC press1997; Vol. 14.
15. Wang, D.; Tejerina, B.; Lagzi, I.; Kowalczyk, B.; Grzybowski, B. A. Bridging interactions and selective nanoparticle aggregation mediated by monovalent cations. ACS Nano 2010, 5, 530-536.

16. Yao, Q.; Luo, Z.; Yuan, X.; Yu, Y.; Zhang, C.; Xie, J.; Lee, J. Y. Assembly of nanoions via electrostatic interactions: ion-like behavior of charged noble metal nanoclusters. Scientific Reports 2014, 4.

17. Huynh, K. A.; Chen, K. L. Aggregation kinetics of citrate and polyvinylpyrrolidone coated silver nanoparticles in monovalent and divalent electrolyte solutions. Environ. Sci. Technol. 2011, 45, 5564-5571.

18. Berchmans, S.; Thomas, P. J.; Rao, C. Novel effects of metal ion chelation on the properties of lipoic acid-capped Ag and Au nanoparticles. The Journal of Physical Chemistry B 2002, 106, 4647-4651.

19. Sokolov, K.; Stover, R.; Joshi, P.; Yoon, S. J.; Murthy, A.; Emelianov, S.; Johnston, K. In Biodegradable Plasmonic Nanoparticles: Overcoming Clinical Translation Barriers, Optical Molecular Probes, Imaging and Drug Delivery, 2015; Optical Society of America, p OM3D. 4.

20. Yoon, S. J.; Mallidi, S.; Tam, J. M.; Tam, J. O.; Murthy, A.; Johnston, K. P.; Sokolov, K. V.; Emelianov, S. Y. Utility of biodegradable plasmonic nanoclusters in photoacoustic imaging. Opt. Lett. 2010, 35, 3751-3753.

21. Hashmi, A. S. K. Gold-catalyzed organic reactions. Chem. Rev. 2007, 107, 3180-3211.

22. Huang, D.; Liao, F.; Molesa, S.; Redinger, D.; Subramanian, V. Plastic-compatible low resistance printable gold nanoparticle conductors for flexible electronics. J. Electrochem. Soc. 2003, 150, G412-G417.

23. Chithrani, B. D.; Stewart, J.; Allen, C.; Jaffray, D. A. Intracellular uptake, transport, and processing of nanostructures in cancer cells. Nanomed. Nanotechnol. Biol. Med. 2009, 5, 118-127.

24. Mallidi, S.; Larson, T.; Tam, J.; Joshi, P. P.; Karplouk, A.; Sokolov, K.; Emelianov, S. Multiwavelength Photoacoustic Imaging and Plasmon Resonance Coupling of Gold Nanoparticles for Selective Detection of Cancer. Nano Lett. 2009, 9, 2825-2831.

25. Weissleder, R. A clearer vision for in vivo imaging. Nat. Biotechnol. 2001, 19, 316-317.

26. Khlebtsov, B.; Zharov, V.; Melnikov, A.; Tuchin, V.; Khlebtsov, N. Optical amplification of photothermal therapy with gold nanoparticles and nanoclusters. Nanotechnology 2006, 5167-5179.

27. Khlebtsov, N.; Dykman, L.; Krasnov, Y. M.; Mel'nikov, A. Light absorption by the clusters of colloidal gold and silver particles formed during slow and fast aggregation. Colloid J. 2000, 62, 765-779.

28. Lassiter, J. B.; Aizpurua, J.; Hernandez, L. I.; Brandl, D. W.; Romero, I.; Lal, S.; Hafner, J. H.; Nordlander, P.; Halas, N. J. Close encounters between two nanoshells. Nano Lett. 2008, 8, 1212-1218.

29. Polavarapu, L.; Perez-Juste, J.; Xu, Q.-H.; Liz-Marzan, L. M. Optical sensing of biological, chemical and ionic species through aggregation of plasmonic nanoparticles. Journal of Materials Chemistry C 2014, 2, 7460-7476.

30. Srivastava, S.; Frankamp, B. L.; Rotello, V. M. Controlled Plasmon Resonance of Gold Nanoparticles Self-Assembled with PAMAM Dendrimers. Chem. Mater. 2005, 17, 487-490.

31. Khlebtsov, B. N.; Khanadeyev, V. A.; Ye, J.; Mackowski, D. W.; Borghs, G.; Khlebtsov, N. G. Coupled plasmon resonances in monolayers of metal nanoparticles and nanoshells. Physical Review B 2008, 77, 035440.

32. Lim, I. I. S.; Ip, W.; Crew, E.; Njoki, P. N.; Mott, D.; Zhong, C.-J.; Pan, Y.; Zhou, S. Homocysteine-Mediated Reactivity and Assembly of Gold Nanoparticles. Langmuir 2007, 23, 826-833.

33. Wang, M.-H.; Li, Y.-J.; Xie, Z.-X.; Liu, C.; Yeung, E. S. Fabrication of large-scale one-dimensional Au nanochain and nanowire networks by interfacial self-assembly. Mater. Chem. Phys. 2010, 119, 153-157.

34. Polavarapu, L.; Xu, Q.-H. A single-step synthesis of gold nanochains using an amino acid as a capping agent and characterization of their optical properties. Nanotechnology 2008, 19, 075601.

35. Park, J.-W.; Shumaker-Parry, J. S. Structural study of citrate layers on gold nanoparticles: role of intermolecular interactions in stabilizing nanoparticles. J. Am. Chem. Soc. 2014, 136, 1907-1921.

36. Lee, J.; Zhou, H.; Lee, J. Small molecule induced self-assembly of Au nanoparticles. J. Mater. Chem. 2011, 21, 16935-16942.

37. Murthy, A. K.; Stover, R. J.; Borwankar, A. U.; Nie, G. D.; Gourisankar, S.; Truskett, T. M.; Sokolov, K. V.; Johnston, K. P. Equilibrium Gold Nanoclusters Quenched with Biodegradable Polymers. ACS Nano 2013, 7, 239-251.

38. Stover, R. J.; Murthy, A. K.; Nie, G. D.; Gourisankar, S.; Dear, B. J.; Truskett, T. M.; Sokolov, K. V.; Johnston, K. P. Quenched Assembly of NIR-Active Gold Nanoclusters Capped with Strongly Bound Ligands by Tuning Particle Charge via pH and Salinity. The Journal of Physical Chemistry C 2014, 118, 14291-14298.

39. Tam, J. M.; Murthy, A. K.; Ingram, D. R.; Nguyen, R.; Sokolov, K. V.; Johnston, K. P. Kinetic Assembly of Near-IR Active Gold Nanoclusters Using Weakly Adsorbing Polymers to Control the Size. Langmuir 2010, 26, 8988-8999.

40. Dutta, A.; Das, S.; Paul, A.; Chattopadhyay, A. Kinetics of reaction of gold nanoparticles following partial removal of stabilizers. J. Nanopart. Res. 2015, 17, 1-13.

41. Grabar, K. C.; Allison, K. J.; Baker, B. E.; Bright, R. M.; Brown, K. R.; Freeman, R. G.; Fox, A. P.; Keating, C. D.; Musick, M. D.; Natan, M. J. Two-Dimensional Arrays of Colloidal Gold Particles: A Flexible Approach to Macroscopic Metal Surfaces. Langmuir 1996, 12, 2353-2361.

42. Khlebtsov, B. N.; Khlebtsov, N. G. On the measurement of gold nanoparticle sizes by the dynamic light scattering method. Colloid J. 2011, 73, 118-127.

43. Grabar, K. C.; Freeman, R. G.; Hommer, M. B.; Natan, M. J. Preparation and Characterization of Au Colloid Monolayers. Anal. Chem. 1995, 67, 735-743.

44. Murthy, A. K.; Stover, R. J.; Hardin, W. G.; Schramm, R.; Nie, G. D.; Gourisankar, S.; Truskett, T. M.; Sokolov, K. V.; Johnston, K. P. Charged Gold Nanoparticles with Essentially Zero Serum Protein Adsorption in Undiluted Fetal Bovine Serum. J. Am. Chem. Soc. 2013, 135, 7799-7802.

45. Israelachvili, J. N. Intermolecular and Surface Forces; 3 ed.; Elsevier: New York, 2011.

46. Walser, M. Dissociation constants for complexes of citrate with sodium, potassium, calcium, and magnesium ions. The Journal of Physical Chemistry 1961, 65, 159-161.

47. Baalousha, M.; Nur, Y.; Römer, I.; Tejamaya, M.; Lead, J. R. Effect of monovalent and divalent cations, anions and fulvic acid on aggregation of citrate-coated silver nanoparticles. Sci. Total Environ. 2013, 454–455, 119-131.

48. Halas, N. J.; Lal, S.; Chang, W.-S.; Link, S.; Nordlander, P. Plasmons in Strongly Coupled Metallic Nanostructures. Chem. Rev. 2011, 111, 3913-3961.

49. Lin, S.; Li, M.; Dujardin, E.; Girard, C.; Mann, S. One- Dimensional Plasmon Coupling by Facile Self- Assembly of Gold Nanoparticles into Branched Chain Networks. Adv. Mater. 2005, 17, 2553-2559.

50. Esteban, R.; Taylor, R. W.; Baumberg, J. J.; Aizpurua, J. How chain plasmons govern the optical response in strongly interacting self-assembled metallic clusters of nanoparticles. Langmuir 2012, 28, 8881-8890.

51. Zhang, H.; Fung, K.-H.; Hartmann, J. r.; Chan, C.; Wang, D. Controlled chainlike agglomeration of charged gold nanoparticles via a deliberate interaction balance. The Journal of Physical Chemistry C 2008, 112, 16830-16839.

52. Mandal, S.; Gole, A.; Lala, N.; Gonnade, R.; Ganvir, V.; Sastry, M. Studies on the reversible aggregation of cysteine-capped colloidal silver particles interconnected via hydrogen bonds. Langmuir 2001, 17, 6262-6268.

53. Fu, R.; Li, J.; Yang, W. Aggregation of glutathione-functionalized Au nanoparticles induced by Ni2+ ions. J. Nanopart. Res. 2012, 14, 1-8.

54. Hsu, J.-P.; Kuo, Y.-C. The critical coagulation concentration of counterions: Spherical particles in asymmetric electrolyte solutions. J. Colloid Interface Sci. 1997, 185, 530-537.

55. Pérez-Juste, J.; Pastoriza-Santos, I.; Liz-Marzán, L. M.; Mulvaney, P. Gold nanorods: synthesis, characterization and applications. Coord. Chem. Rev. 2005, 249, 1870-1901.

56. Kedia, A.; Kumar, P. S. Halide ion induced tuning and self-organization of gold nanostars. Rsc Advances 2014, 4, 4782-4790.

57. Wang, Y.; Liang, W.; Geng, C. Coalescence behavior of gold nanoparticles. Nanoscale research letters 2009, 4, 684-688.

58. Korgel, B. A.; Fitzmaurice, D. Self- assembly of silver nanocrystals into two-dimensional nanowire arrays. Adv. Mater. 1998, 10, 661-665.

Chapter 6: Conclusions and Recommendations

6.1 CONCLUSIONS

6.1.1 Design of Gold Nanosphere Surfaces to Resist Protein Adsorption

In chapter 2, the design of ~ 5 nm gold nanoparticle surfaces with a binary mixed-charge ligand system was detailed The charged surfaces were composed of two naturally occurring, relatively hydrophilic ligands, citrate and either cationic lysine or zwitterionic, thiol-containing cysteine. The Au surface charge was tuned by place exchange of the citrate ligands with each amino acid, as characterized by the zeta potential and XPS. Relatively hydrophilic ligands were used to attempt to limit hydrophobic interactions that may increase adsorption. For pure citrate or highly charged mixed charge monolayers with high citrate levels, the hydrodynamic diameter increased ~3 nm or more with protein adsorption. However, the change in size was negligible for lower citrate fractions, even for a moderate charge of -22 mV in undiluted FBS. The zwitterionic tips of the lysine and cysteine ligands interact weakly with the protein and, furthermore, mitigate the interactions of the "buried" charges on the anchor groups at the Au surface. The extension of this concept to include the thiolated cysteine molecule could possible prevent intracellular GSH exchange and protect the protein resistant properties. Regardless, this result shows a platform which could be adapted to even stronger-bound ligands in the future.

6.1.2 Reversible Assembly of high-NIR Nanoparticle Clusters

The assembly of lysine/citrate particles was detailed in chapter 3. Herein, it was shown that equilibrium phenomena play a major role in governing the size of Au

nanoclusters, which are quenched by irreversibly adsorbed polymer on the surface. Sub-100 nm nanocluster sizes were tuned by varying the ratio of polymer/Au and evaporation extent to manipulate the depletion attraction induced by the polymer. The Au nanoparticle concentration was also varied to alter the magnitude of vdW attraction during assembly. The size was predicted semi-quantitatively with an equilibrium free energy model as a function of the Au concentration and the polymer/Au ratio. The free energy model describes the balance between long-ranged electrostatic repulsion between primary Au nanospheres with short-ranged vdW and depletion attractive interactions. The equilibrium size is quenched by an irreversibly adsorbed polymer layer on the nanocluster surface, and remains constant even after removal of excess polymer. The close spacings of primary nanospheres within the nanoclusters resulted in high NIR extinction for all sizes of nanoclusters explored in this work, which showed partial dissociation upon biodegradation of the polymer quencher.

This concept was extended to cysteine/citrate nanoparticles in chapter 4. However with Au and polymer concentrations held constant, the solution pH and salt concentration were utilized as new variables to tune the particle size, NIR extinction, and degree of polymer adsorption by manipulating the the Au surface charge on the primary nanospheres. At each salinity (0−33 mM NaCl), the hydrodynamic diameter and NIR extinction increased as the solution pH was decreased from 7 to 5, consistent with weaker electrostatic repulsion, as would be expected from the equilibrium free energy model described in chapter 3. Furthermore, at a given pH, the size distribution shifted to larger clusters with salt addition, again as may be expected with weakened electrostatic repulsion. Finally, the polymer adsorption decreased as the screening of the charges on the Au surfaces with salt weakened the interactions with the polar groups on PLA(1K)-b-PEG(10K)-b-PLA(1K), therefore allowing close interparticle spacings and high-NIR

extinction from the strongly-bound nanoparticle system, which provides a promising avenue for in vivo application of such nanoclusters.

A novel nanocluster assembly method was proposed in chapter 5 as depletion attraction was no longer considered. Instead, the size and morphology of NP clusters of small 5 nm citrate coated Au primary particles was controlled by tuning the electrostatic repulsion and bridging attraction in the presence of vdW and dipolar attraction. In the case of Ca^{2+}, strong interparticle bridging with citrate anions produced branched nanochains in < 60 s with closely spaced and partially fused primary particles, resulting in a broad NIR extinction peak out to 1100 nm. This level of NIR extinction is highly unusual for such small nanochains with lengths as short as 20 nm. The branched nanochains were formed by strong electrostatic repulsion with a very thick double layer to favor growth on the chain ends instead of the sides, relative to weaker vdW forces. At very close spacings on the order of 1.4 nm or less, the particles were bound to the cluster by strong short-ranged bridging attraction in addition to vdW attraction. In contrast, spherical nanoclusters were formed with NaCl often with distinct spacings between the primary particles and minimal fusion according to TEM. For Na^{+}, much higher ionic strengths were needed to screen the electrostatic repulsion, and the bridging driving force was much weaker. Consequently, thinner double layers and weaker electrostatic repulsion no longer favored anisotropic particle growth to chains. For Ca^{2+}, intraparticle bridging of citrate may have produced dipoles on the particle surfaces that are known to favor anisotropy. In each case, the growth of the nanoclusters was quenched simply by dilution to lower the ionic strength to increase the electrostatic repulsion and weaken the interparticle bridging. For the desired nanocluster size less than 50 nm, the small 5 nm primary particles provided a larger number of "hot spots" for electrical field enhancement resulting in larger NIR shifts relative to the much more commonly studied particles larger

than 10 nm. Additionally, exposed gold surfaces were shown to be responsible for the high NIR extinction as NIR was unobtainable in the presence of excess citrate which passivated the remaining Au surface, which could help explain the overall lower NIR absorbance seen for cysteine/citrate nanoclusters in chapter 4.

6.1.3 Structure of Reversible Gold Nanoclusters

Small angle x-ray scattering (SAXS) analysis was carried out on the nanoclusters designed through methods described in chapter 5. The results were unable to be completed to publication quality at the time of this thesis, and were therefore partially discussed in the honors thesis of my four-year undergraduate partner, Sai Gourisankar.1 Relevant sections of that thesis are reproduced in Appendix A.

Nanoclusters were assembled from lysine/citrate, cysteine/citrate, and GSH/citrate nanoparticles. However high polydispersity limited the resolution of the SAXS measurements; although rough estimates of fractal dimension and interparticle spacings were still available. TEM analysis helped support the conclusion that lysine/citrate nanoclusters were mostly linear in shape with a relatively low fractal dimension. This behavior is indicative of DLA which is observed for rapid aggregation of particles with a high aggregation driving force.[2] More spherical structures were seen for the thiolated ligand systems as clear interparticle spacings were also observed. This was likely due to increased particle charge and steric stabilization imparted by the more strongly-bound ligands which can prevent direct interparticle surface interactions.3 Decreases in NIR for the thiolated systems was also observed and consistent with theory as closer-interparticle spacings and more fractal structures have been shown to increase NIR extinction.[4-6]

Lastly, high-resolution TEM images suggested physical necking was present for lysine/citrate nanoclusters. It is unclear if this behavior is a result of electron-induced

sintering or if it occurred in solution. However halide ion complexation has been shown to cause Ostwald ripening of gold nanoparticles.[7-8] Therefore further experiments were done to assemble nanoclustesr without HCl and shown to still produce high-NIR absorbing nanoclusters; although further TEM studies should be done to definitively rule out interparticle sintering behavior.

6.1.4 Animal Clearance and Tumor Targeting Studies

Though not specifically detailed in this thesis, several mouse studies to determine nanocluster clearance as well as targeting and imaging efficiency were carried out on materials synthesized during this work. Lysine/citrate nanoclusters were shown to accumulate in the liver with 70 % of the injected dose (ID), with ~35 % being cleared over four months. This was hypothesized to be due to either aggregation of the clusters within the cells, or unexpected poor exocytosis properties of the clusters from within liver sinusoidal cells.[9-10]

In a separate study, lysine/citrate nanoclusters targeted to EGFR-positive tumor mouse models. Anti-EGFR antibodies were conjugated to the lysine/citrate nanoclusters and shown to accumulate in significant amounts after 24 hours. Photoacoustic imaging showed specific targeting of the clusters to the EGFR-(+) tumor as opposed to the EGFR-(-) control tumor.[11] All animal study data has been published in the dissertations of Dr. Justina Tam, Dr. Soon Joon Yoon and Dr. Pratixa Joshi.[9-10, 12]

6.2 Future Research Outlook

6.2.1 Gold Nanoparticle Design

Several studies have shown that single thiols can be displaced by the high concentrations of GSH within cells. However di- or other multi-thiols have shown to be much more difficult to remove.[13] Studies have also established syntheses of zwitterionic di- or multi-thiols as well which have proven protein resistance on tests with quantum dots.[14] Therefore it would be advantageous to extend the mixed-charge ligand concept present in chapter 2 to include these more strongly-bound ligands. After place exchange of the thiols onto ~5 nm citrate nanoparticles, incubation in 10 mM GSH followed by FBS incubation would determine if these surfaces can withstand the challenging environment of the body. To be certain, renal clearance studies using mouse models would be optimus as biological systems are incredibly difficult to mimic in vitro.

As a secondary idea, 2 nm GSH-capped gold particles have already been shown to exhibit efficient renal clearance.[15-16] Therefore it would be worthwhile to establish a synthesis for 2 nm Au particles either with GSH or another favorable ligand. A secondary ligand shouldn't be a concern as GSH-exchange within cells appears to be favorable for such small particles.

6.2.2 Reversible, High-NIR Absorbing Nanocluster Assembly

An obvious next step following design of strongly-bound ligand surfaces is to assemble them into high-NIR clusters. However, as is shown in Appendix A, the ability to get close particle spacings from thiolated nanoparticle surfaces is challenging due to immobility of thiolated ligands unlike the more weakly-bound citrate to allow for direct gold surface interactions.[3] Therefore it will likely be necessary to moderate the ligand ratio of thiol/citrate in order to remove enough electrostatic repulsion for cluster

aggregation, but not add too much steric stabilization to prevent close interparticle spacings. If carefully controlled, clusters with adequate NIR should be possible. Additionally, the addition of small steric repulsion could enable fuller nanocluster dissociation as the vdW potential is weakened. Partial ligand exchange with strongly-bound ligands should also be considered due to the need for free Au surface to allow antibody conjugation required if these materials are to be used in their desired application.

A secondary consideration arises when considering the addition of zwitterions onto the particle surfaces. These ligands have proven to prevent protein adsorption through creation of a hydration layer as a result of the increasingly hydrophilic nature of surface. This hydrophilicity could present opposition to the hydrophobic PLA group on the currently used biodegradable polymer quenching agent, which preferentially adsorbs onto the more hydrophobic gold surface. Stability of the nanocluster could be dramatically reduced without this polymer. Therefore it may be necessary to explore other, more hydrophilic biodegradable polymers which would bind strongly to a hydrophilic surface.

Lastly, cluster assembly using 2 nm primary gold particles should be attempted. At their small size, gold particles do not exhibit a distinct SPR peak,[16] and it is unknown if assemblies of such small particles can yield significant NIR. However it is has been shown in literature and this thesis that for bigger Au particles, large aggregates can produce high-NIR shifts.[17] Therefore it is conceivable that such clusters of such small primary nanoparticles could become effective photoacoustic contrast agents.

6.3 REFERENCES

1. Gourisankar, S. Structure and Assembly of Gold Nanoclusters for Biomedical Imaging Applications. B.S., University of Texas at Austin, 2015.
2. Weitz, D. A.; Huang, J. S.; Lin, M. Y.; Sung, J. Limits of the Fractal Dimension for Irreversible Kinetic Aggregation of Gold Colloids. Physical Review Letters 1985, 54, 1416-1419.
3. Park, J.-W.; Shumaker-Parry, J. S. Strong Resistance of Citrate Anions on Metal Nanoparticles to Desorption under Thiol Functionalization. ACS Nano 2015, 9, 1665-1682.
4. Khlebtsov, N. G. T-matrix method in plasmonics: An overview. Journal of Quantitative Spectroscopy and Radiative Transfer 2013, 123, 184-217.
5. Khlebtsov, B. N.; Khanadeyev, V. A.; Ye, J.; Mackowski, D. W.; Borghs, G.; Khlebtsov, N. G. Coupled plasmon resonances in monolayers of metal nanoparticles and nanoshells. Physical Review B 2008, 77, 035440.
6. Khlebtsov, B.; Zharov, V.; Melnikov, A.; Tuchin, V.; Khlebtsov, N. Optical amplification of photothermal therapy with gold nanoparticles and nanoclusters. Nanotechnology 2006, 5167-5179.
7. Senapati, D.; Singh, A. K.; Khan, S. A.; Senapati, T.; Ray, P. C. Probing real time gold nanostar formation process using two-photon scattering spectroscopy. Chemical Physics Letters 2011, 504, 46-51.
8. Moiraghi, R.; Douglas-Gallardo, O.; Coronado, E.; Macagno, V.; Pérez, M. Gold nucleation inhibition by halide ions: a basis for a seed-mediated approach. Rsc Advances 2015, 5, 19329-19336.
9. Tam, J. O. Interactions of composite gold nanoparticles with cells and tissue: implications in clinical translation for cancer imaging and therapy. Ph.D., University of Texas at Austin, 2012.
10. Joshi, P. Near-IR Plasmonic Contrast Agents for Molecular Imaging, Cells Tracking and Clinical Translation. Ph.D., University of Texas at Austin, 2014.
11. Sokolov, K.; Stover, R.; Joshi, P.; Yoon, S. J.; Murthy, A.; Emelianov, S.; Johnston, K. In Biodegradable Plasmonic Nanoparticles: Overcoming Clinical Translation Barriers, Optical Molecular Probes, Imaging and Drug Delivery, 2015; Optical Society of America, p OM3D. 4.
12. Yoon, S. J. Photoacoustic Imaging using Nanoclsuters. Ph.D., University of Texas at Austin, 2014.
13. Zhan, N.; Palui, G.; Safi, M.; Ji, X.; Mattoussi, H. Multidentate Zwitterionic Ligands Provide Compact and Highly Biocompatible Quantum Dots. Journal of the American Chemical Society 2013, 135, 13786-13795.

14. Sun, M., Hoffman, D., Sundaresan, G., Yang, L., Lamichhane, N., Zweit, J. Synthesis and characterization of intrinsically radiolabeled quantum dots for bimodal detection. American Journal of Nuclear Medicine and Molecular Imaging 2012, 2, 122-135.

15. Zhang, X.-D.; Luo, Z.; Chen, J.; Song, S.; Yuan, X.; Shen, X.; Wang, H.; Sun, Y.; Gao, K.; Zhang, L.; Fan, S.; Leong, D. T.; Guo, M.; Xie, J. Ultrasmall Glutathione-Protected Gold Nanoclusters as Next Generation Radiotherapy Sensitizers with High Tumor Uptake and High Renal Clearance. Scientific Reports 2015, 5, 8669.

16. Zhou, C.; Long, M.; Qin, Y.; Sun, X.; Zheng, J. Luminescent Gold Nanoparticles with Efficient Renal Clearance. Angewandte Chemie International Edition 2011, 50, 3168-3172.

17. Lassiter, J. B.; Aizpurua, J.; Hernandez, L. I.; Brandl, D. W.; Romero, I.; Lal, S.; Hafner, J. H.; Nordlander, P.; Halas, N. J. Close encounters between two nanoshells. Nano Letters 2008, 8, 1212-1218.

Appendix A: Structure of Small, near-Infrared Active Gold Nanoclusters for Biomedical Imaging Applications [5]

A.1 INTRODUCTION

Spherical gold nanoparticles appear red and exhibit an absorption maximum at ~525 nm wavelength of light. Theory developed by Gustav Mie in the early 20th century explained why these sub-wavelength-sized objects show unique optical properties.[1, 2] Nonspherical nanostructures of gold such as nanoshells[3, 4] or nanorods[5, 6] undergo a red-shift to the near-infrared (NIR) region of light, 600-1100 nm, due to a surface plasmon resonance (SPR).[2, 7, 8, 9, 10] The collective oscillation of surface conduction electrons interact across particle surfaces and red-shift the optical absorbance. The figure below provides a schematic of the interaction between the incident electric field from incoming radiation and two gold nanospheres' interacting electron clouds.

The plasmon resonance depends on ratio between the surface-surface distance between the particles and the diameter of the spheres, d/D. Closer spacings, and a smaller d/D ratio, increases the SPR and produces greater red-shift of the extinction.[2] Several studies indicate that the ratio of the surface-to-surface distance between particles and the diameter of the particle, d/D, must be close to 0.1 for effective SPR and red-shifted extinction into the NIR.[2, 11, 12, 13, 14] If the nanoparticles are coated by surface ligands, this implies that the length of the ligand protruding from the surface plays an important role in governing NIR extinction. In larger aggregates of many nanospheres, the SPR also

[5] Large parts of this chapter were were written by Sai Gourisankar, B.S.E. and submitted as part of his requirements for his undergraduate Honors Thesis: Gourisankar, S. Structure and Assembly of Gold Nanoclusters for Biomedical Imaging Applications. B.S. Honors Thesis, *University of Texas at Austin*, **2015**.

depends on the number of particles, N, in the ensemble. The SPR can be modeled as N interactions of dipoles; the red-shift and breadth of the NIR extinction increases with N.[2] The SPR effect can be described as the coupling or resonance of two neighboring dipoles.[2] A higher-energy resonance, the transverse surface plasmon resonance (TSPR), occurs when the electric field aligns perpendicularly to the dipole moments.[2, 8] A lower-energy resonance, the longitudinal SPR (LSPR), occurs when the field interacts parallel to the dipole moments. Typically, the TSPR absorbs radiation at ~520 nm wavelength for gold nanospheres, while the wavelength of LSPR extinction can be anywhere in the NIR, depending on the length and aspect ratio of the elongated structure, for example a nanochain or nanorod.[5, 6, 8] Hybridization of these modes with multipolar interactions can cause further spectral shifts.[2]

We assembled highly asymmetric ~45 nm diameter gold nanoclusters of many ~ 5 nm diameter primary nanospheres that display high NIR extinction. The nanoclusters were assembled using a previously reported procedure11 from primary ~5 nm gold nanospheres coated with three different amino acid ligands: lysine, cysteine, and glutathione. Varying amounts of a triblock copolymer, PLA(1K)-PEG(10K)-PLA(1K), were added to the system to modulate steric repulsion and depletion-attraction forces between primary nanospheres. The results and discussion examine the morphology of nanoclusters produced and their impact on the SPR and NIR extinction. The broad NIR extinction seen in some of the nanoclusters is attributed to data indicating a small d/D ratio as well as the unique, fractal or chain-like morphology able to support the broad

LSPR mode. A mechanism is presented to explain the morphology seen, and design recommendations are given.

A.2 EXPERIMENTAL AND METHODOLOGY

A.2.1 Materials:

Sodium citrate ($Na_3C_3H_5O(COO)_3 \bullet 2H_2O$) and sodium borohydrate ($NaBH_4$) were obtained from Fisher Scientific (Fair Lawn, NJ). $HAuCl_4 \bullet 3H_2O$ was purchased from MP Biomedicals LLC (Solon, OH). L-(+)-Lysine, Glutathione, and L-(+)-Cysteine were purchased from Acros Chemicals (Morris Plains, NJ). PLA(1K)-PEG(10K)-PLA(1K) was purchased from Sigma-Aldrich (St. Louis, MO).

A.2.2 Synthesis of 5 nm Citrate-Capped Gold Nanospheres:

As described in Murthy et al.,[11] citrate capped gold nanospheres were synthesized by reducing $HAuCl_4$ with $NaBH_4$ and purifying by tangential flow filtration, resulting in ~20 mL of 3 mg/mL aqueous gold solution.

A.2.3 Place Exchange Reaction with Lysine, Citrate, or Glutathione:

A solution of 3 mg/mL citrate-capped gold was reacted with: i) 9/1 mol:mol ratio of lysine:citrate at room temperature for 12 hours to produce lysine/citrate capped 5 nm nanospheres; ii) 0.7/1 mol:mol ratio of cysteine:citrate at room temperature for 12 hours to produce cysteine/citrate capped 5 nm nanospheres; and iii) 5/1 mol:mol ratio of glutathione/citrate for 12 hours to produce glutathione/citrate capped gold nanospheres. The three different ligands used in this study are shown below at protonation states at pH 5.

A.2.4 Nanocluster Formation:

PLA(1K)-PEG(10K)-PLA(1K) was dissolved in water to form a 30 mg/mL solution and titrated with 10 M NaOH to pH 7. Various mass/mass ratios of polymer/gold were added each ligand's 3 mg/mL solution of ligand-exchanged 5 nm primary nanospheres. The solution was then titrated quickly (within a few minutes) to either pH 5 with 0.1 M HCl. "Mixing" Method: Nanocluster solutions made at 0.1/1 polymer/Au were immediately diluted with the 30 mg/mL polymer solution to reach a 10.1/1 polymer/Au final ratio and a 0.3 mg/mL gold concentration. Nanocluster solutions made with a 1/1 polymer/Au ratio were immediately diluted with deionized water to reach a 1/1 polymer Au final ratio and a 0.3 mg/mL gold concentration. "Evaporation" Method: Nanocluster solutions made with a 5/1 polymer/Au ratio were placed, stirring, under a continuous air stream at 40OC to evaporate 50% of the solvent for the pH 5 lysine/citrate particles, and 100% of the solvent for all other samples. After evaporation, the nanocluster solution was diluted with deionized water to reach 0.3 mg/mL gold concentration.
All samples were filtered through a 100nm poly(vinylidene difluoride) filter.

A.2.5 Small-Angle X-Ray Scattering (SAXS):

50 μL of each sample was loaded in a quartz 0.1 mm cuvette and shipped to the Center for Functional Nanomaterials at Brookhaven National Labs, Brookhaven, NY. SAXS was run on a Bruker Nanostar U rotating copper anode instrument at a wavelength of 1.54 Å for one hour. Analysis was carried out using IgorPro software. SAXS can quantify the network-like nature of a nanocluster – how many chains branch off from a core – by providing a mass fractal dimension. The mass fractal dimension characterizes aggregate morphology in which the structure possesses self-similarity; i.e. under

increasing magnification the structure continues to look similar.[15] Mathematically, if m is the mass of the nanocluster and r the radius, df is the fractal dimension (1< df <3) as given by the following expression.[16]

$$m(r) \propto r^{d_f} \quad \text{(A.1)}$$

A fractal dimension close to 3.0 implies spherical morphology while a fractal dimension close to 1.0 indicates rod-like morphology. By SAXS, a fractal structure will display the following relationship between intensity I of scattered radiation and angle of scattering.[16]

$$I(Q) \propto q^{-d_f} \quad \text{(A.2)}$$

Here, q is the scattering vector and is defined in terms of the scattering angle θ as:

$$q = \frac{4\pi}{\lambda}\sin(2\theta)\ [=]\mathrm{nm}^{-1} \quad \text{(A.3)}$$

If d_s represents the diameter of the primary nanosphere and dc the diameter of the cluster, the relationship remains valid only between ds-1< q < dc-1. At q > d_s-1, the scattering curve enters the so-called "Porod" regime, where for smooth spheres, the following relationship holds:

$$I(Q) \propto q^{-4} \quad \text{(A.4)}$$

The slope of -4 indicates the presence of distinct, smooth spherical surfaces in the nanostructure, far enough apart from each other to avoid interaction.

A.2.6 Dynamic Light Scattering (DLS):

Approximately 50 μL of each sample in 1 mL of DI H2O was loaded into a transparent quartz cuvette and characterized using a Brookhaven ZetaPALS analyzer with a scattering angle of 90OC and a laser wavelength of 660 nm. The data were analyzed

using the Non-Negative-Least-Squares (NNLS) method (Brookhaven DLS software version 3.34) and the correlation function fit using a 32-channel autoslope analysis.

A.2.7 UV-Vis-NIR Spectroscopy:

UV-Vis-NIR spectroscopy of approximately 50 μL of each sample in 1 mL of DI H2O was loaded into a quartz cuvette and analyzed with a Varian Cary 60 spectrophotometer with a path length of 1 cm. Extinction was normalized using the peak wavelength at 525 nm.

A.2.8 Transmission Electron Microscopy (TEM):

Images were taken on a 80 kV FEI Tecnai Transmission Electron Microscope using copper-coated carbon grids. 3 μL of sample was dropped on the grid, wicked with a KimWipe, and dipped in liquid nitrogen to maintain 3-D structural integrity. The grids were dried using a VirTis AdVantage tray lyophilizer (VirTis, Gardiner, NY). All structural data was analyzed from many TEM images containing a total of 100 different particles. Diameters of asymmetric shapes were quantified using the largest dimension. From TEM images, the "circularity" of a particle can be measured. Circularity is defined below, in which Dmaximum refers to the longest dimension measured on a TEM image. A circularity of 1 indicates a perfect circle and a circularity of 0 a perfectly slender rod.[17] We note that circularity should only be considered for relative measurements and not as an absolute metric of geometry. Circularity of nanoclusters were obtained from structures larger than 6 nm only, to avoid counting primary Au nanospheres.

$$\text{Circularity} = \frac{4 * \text{Area of Nanocluster}}{\pi D^2_{\text{maximum}}} \tag{A.5}$$

A.2.9 Hi-resolution TEM (AC-TEM):

Images were taken at the Center for Functional Materials, Brookhaven National Laboratory, Brookhaven, NY on a JEOL 2100F TEM at 200 kV.

A.3 Results and Discussion

TEM images indicate that the choice of surface ligand influences the shape and internal structure of a nanocluster. The images below show representative examples of nanoclusters built from lysine/citrate, cysteine/citrate, and glutathione/citrate primary nanospheres. We can visually detect distinct primary nanospheres in the glutathione nanocluster (Fig. A.3E) but less so in the cysteine and lysine nanoclusters. Qualitatively, the interparticle spacing between primary nanospheres is higher for the glutathione (Fig. A.2E) and cysteine (Fig. A.3C) nanoclusters than for the lysine nanoclusters (Fig. A.3B, D, F). Both the glutathione (Fig. A.3E) and cysteine (Fig. A.3C) nanoclusters appear more compact in shape, (see insets in figure), compared to the branched or chain-like lysine nanoclusters (Fig. A.3B, D, F).

Table A.1 quantifies that the nanoclusters assembled have similar volume-average diameters of ~45 nm. The circularities of cysteine and glutathione nanoclusters are higher than those for lysine, quantifying the shape difference seen in the TEM images. DLS measurements support the polydispersity seen in the TEM images; note that the intensity-weighted distribution overestimates the proportion of larger particles by a factor of $(\text{diameter})^6$ and should only be considered as a general indication of the size range present.

The UV-VIs-NIR spectra below show a broad extinction in the NIR for lysine nanoclusters, but little red-shift for cysteine and even less for glutathione. All nanoclusters display a prominent peak at ~525 nm resulting from the TSPR mode; the spectrum of primary 5 nm gold nanospheres is shown for comparison. Cysteine and glutathione nanoclusters produced less NIR extinction as shown by the decrease in the extinction ratio A_{1000}/A_{525} of absorbance at 1000 nm to that at 525 nm: cysteine nanoclusters, with 0.380, and glutathione nanoclusters, with 0.025, were much lower than the extinction ratios of lysine nanoclusters (A_{1000}/A_{525} = 1.05, 0.904, and 0.732).

Although SPR and NIR extinction depends on particle size, these extinction differences can be attributed to nanocluster structural properties – interparticle spacing and morphology – because TEM and DLS analysis demonstrated that the nanoclusters considered had similar sizes. SAXS analysis provides structural information and supports qualitative morphology analysis given by TEM data with regards to two key parameters, the interparticle spacing effect and the shape of the structure.

The interparticle spacing d/D ratio must be small for the SPR red-shift. Theoretically, it is suggested that d/D must be close to 10% for the SPR.[13] Experimental data support that theory: Lazarides et al. did not see an SPR shift until a d/D of 8%, for 13 nm DNA-linked gold nanospheres separated by 1.1 nm.[14] Lee at al. saw broad NIR extinction between 700 and 1300 nm for a quadrumer of gold nanospheres with a d/D of 1.3%.[17] Liz-Marzan did not see any red-shift of extinction between 600-900 nm for d/D greater than 7.5% of dimers of gold 20 nm nanospheres.[9] Previous simulation studies confirmed and extended these results: Estaban et al. simulated the extinction of 40 nm gold nanospheres with a d/D of 2.5% that showed an SPR shift out to 800 nm.[18] Lin et al. showed that a d/D of 15% for chains of 13 nm gold nanospheres did not show any NIR extinction until the chain size increased dramatically, beyond 1000 nm in length.[19]

The scattering supports nanocluster formation, seen by DLS and TEM analysis, for lysine and cysteine by the rising intensity at low q in the SAXS profiles in Fig. A.5. However, scattering from assemblies of glutathione-coated nanospheres does not show evidence of dense, highly-interacting nanospheres within a nanocluster: the scattering profile almost exactly matches the scattering from 5 nm primary Au nanospheres. The large molecular dimension (0.94 nm) of the glutathione molecule prevents assembly into dense nanoclusters with small spacings. The expected thickness of two organic shells of glutathione molecules coating 5 nm nanospheres, 1.9 nm, is much greater than the 0.5 nm spacing needed (10% of the nanosphere diameter) for SPR of 5 nm nanospheres. UV-Vis-NIR analysis supports the conclusion that glutathione is too long to produce the SPR red-shift: the extinction ratio of 0.025 is close to that of primary nanospheres, 0. 014 (Table A.1 and Fig. A.4). TEM images from Fig. A.3E (and inset) display qualitatively larger spacings between glutathione nanospheres in an assembled nanocluster.

The scattering for cysteine nanoclusters could indicate poorly-interacting 5 nm nanospheres spaced farther within a nanocluster. The small shoulder at q~1.6 nm-1 for cysteine indicates the presence of structures able to be distinguished as primary nanospheres; this analysis supports TEM qualitative conclusions about the greater spacing observed within cysteine nanoclusters. The lack of that feature for lysine nanoclusters could imply that the lysine nanospheres are in closer contact with a much smaller interparticle spacings, agreeing with the observations noted from the TEM images in Fig. A.3B, D, and F.

High-resolution TEM images support the conclusion that lysine nanospheres are in close contact within a nanocluster. Fig. A.6 shows primary gold nanospheres along with one section of a lysine nanocluster. The lattice lines overlap neighboring nanospheres in the nanocluster, indicating that the gold surfaces are touching each other.

The interparticle spacing d therefore remains <10% of the particle diameter D, supporting the broad NIR extinction seen for lysine nanoclusters in Fig. A.4.

The morphology of a nanocluster also contributes to its optical properties. Broad NIR extinction results from the longitudinal SPR mode, a resonance of surface plasmons parallel to the long axis of an asymmetric structure and parallel to the incoming radiation.[8] This LSPR mode needs asymmetry, and can be seen dramatically in very asymmetric structures such as nanorods and nanochains.[5, 6, 9] Chain-like structures have broad NIR extinction because that longitudinal SPR shift is maximized: the electric field can align with the long axis.[14] Many have shown, by simulation and experiment, that longer chains resonate at higher wavelengths (greater red-shift and lower energies), while shorter chains resonate at lower wavelengths (smaller red-shift and higher energies). Estaban et al. used computer modeling of the electrodynamic equations to show that increasing chain length from 2 to 16 40 nm gold nanospheres increased red-shift from 700 to 800 nm.[20] Chains of several hundred nanometers formed from 15 nm citrate-capped gold nanospheres had broad NIR extinction across the 600-1100 nm optical window as the growth increased.[21] Herrmann et al. experimentally produced chains of 60 nm gold nanospheres with constant spacings and found that the NIR extinction broadened as the chains grew.[22] Arnold et al. simulated increasing NIR extinction for longer chains of metal nanospheres.[23]

Some of the most asymmetric structures include diffusion-limited-aggregates (DLA), "stringy," "branched" or "tree-like" nanoclusters; these have shown some NIR extinction in previous simulation and experiment. Nanoclusters with fractal dimensions between 1.8 and 2.0, composed of 15 nm gold nanospheres spaced by 1 nm, had broad extinction between 500 and 650 nm by simulation studies.[13] The NIR extinction of fractal clusters has been described by the resonance of chains within the structure.[14, 20, 22] A

longitudinal SPR shift across the entire NIR 600-1100 nm optical window has been attributed to a polydispersity of fractal clusters, containing a mixture of both long chains and short chains.[14]

A similar effect of polydispersity can be observed in our system. SAXS analysis quantifies the morphological differences observed in the TEM images in Fig. A.3 by the fractal dimension (Table A.1). The fractal dimensions for all the nanoclusters support a diffusion-limited aggregation (DLA) growth model.16 We note that the fractal dimensions by SAXS analysis are between 1.2 and 1.8; given the polydisperity observed by DLS and TEM analysis, these numbers can be considered similar with an error in fractal dimension of about 0.3. The cartoon below displays TEM projections of simulated diffusion-limited 3D aggregates at various fractal dimensions. The fractal dimensions calculated of lysine nanoclusters (1.2, 1.5, 1.8) quantitatively support the qualitative conclusion from the TEM pictures in Fig. A.3, quantitative TEM circularity analysis in Table A.1 that lysine nanospheres form branched, chain-like highly asymmetric nanostructures. The polydispersity of structures with low fractal dimensions give asymmetry to support the LSPR mode across the entire NIR window from 600 to 1100 nm.

The mechanism leading lysine nanospheres to assemble into elongated, chain-like structures could be attributed to dipole-dipole attractions between nanospheres. Dipolar interactions stemming from non-uniform surface coverage by ligands have been shown before to assemble gold nanoparticles into linear networks and chain-like aggregates.[24, 25, 26, 27, 28, 29] The binding affinity of the lysine molecule's amine group to gold surfaces remains in question; exchange with citrate-capped primary gold nanospheres probably leads to non-uniform surface coverage of the lysine. The resulting dipole formed between the highly charged citrate and the zwitterionic lysine on opposite sides of the nanosphere

could influence network-like growth of asymmetric structures. We could still consider this model diffusion-limited, because the nanosphere surfaces are not fully covered with a repulsive ligand that influences a reaction-limited process.

A.4 CONCLUSION

Gold nanospheres of 5 nm in diameter have been assembled into high-NIR ~45 nm nanostructures in the presence of lysine. The asymmetry of the lysine nanospheres forming fractal nanoclusters with contacting gold surfaces contributes to the strong NIR extinction across the 600-1100 nm optical window, present even at the small size of ~ 45 nm. The molecular dimension of the glutathione ligand precluded any SPR shift because the interparticle spacing remained greater than 10% of the nanosphere diameter. The lysine nanoclusters merit further investigation because of their uniquely high NIR extinction for particles as small as ~ 45 nm: they could be useful for biological uptake in tumor cells and therefore as contrast agents for imaging modalities.

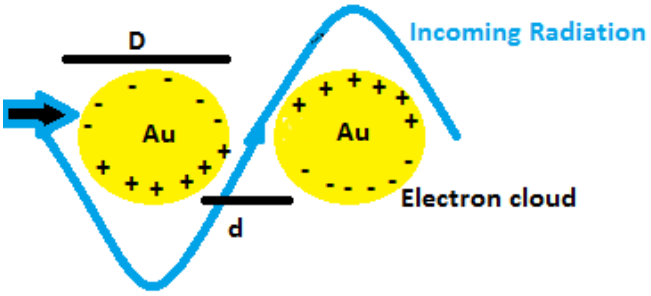

Figure A.1: Gold nanoparticles in close contact exhibit surface plasmon resonance due to coherently oscillating electron clouds.

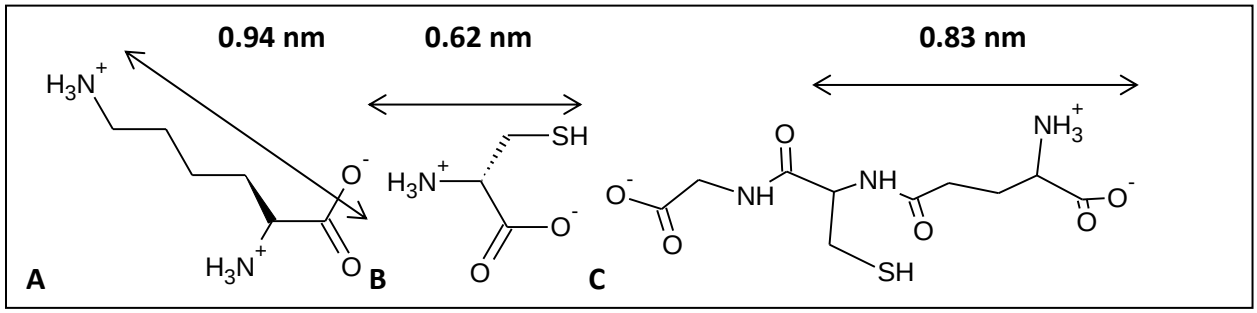

Figure A.2: Ligands used in this study to exchange with citrate on the primary gold nanosphere surface and reduce electrostatic repulsion: A) Lysine, B) Cysteine; C) Glutathione. All are shown with appropriate charge at pH 5 assembly conditions. molecular dimension from point of Au surface attachment, at thiol (-SH) or amine (NH_x) bond. Internuclear lengths were calculated using the ACD/3D visualization program, which uses a proprietary 3D energy optimization algorithm based on CHARMM parametrization.[30]

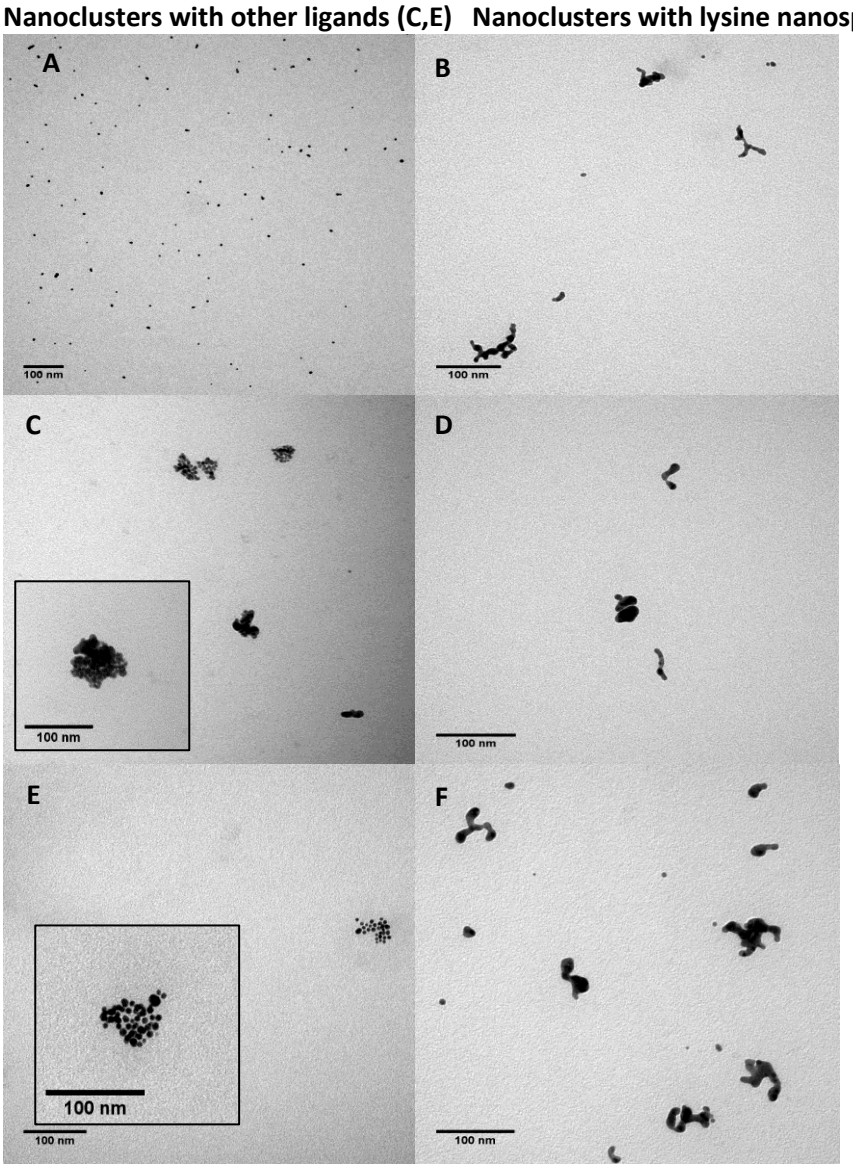

Figure A.3: Moving left to right, TEM images of (A) 5 nm Au nanospheres; (B) lysine/citrate nanoclusters assembled at pH 5 at 5/1 polymer/Au; (C) cysteine/citrate nanoclusters at pH 5 at 5/1 polymer/Au; (D) lysine/citrate nanoclusters at pH 5 at 1/1 polymer/Au; (E) glutathione/citrate nanoclusters at pH 5 at 5/1 polymer/Au; and (F) lysine/citrate nanoclusters at pH 5 at 0.1/1 polymer/Au, quenched in 10/1 polymer/Au.

Table A.1: Properties of Nanoclusters: intensity-weighted hydrodynamic diameter size distribution, TEM volume-average diameter, TEM-obtained Circularity, UV-vis-NIR extinction ratio A_{1000}/A_{525} of extinction at 1000nm to that at 525nm, and fractal dimension obtained from SAXS. TEM average diameters and circularities were calculated based on 100 measurements taken at different TEM grid locations.

Nanocluster			**DLS intensity weighted size distribution (cumulative, %)**				**TEM vol. avg. diameter (nm)**	**Circularity**	**A_{1000}/A_{525}**	**Fractal Dimension**
TEM Label	**Primary Nano-sphere**	**Polymer /Au**	**3 -10 nm**	**10 - 50 nm**	**50 - 100 nm**	**100 - 200 nm**				
A	5nm Au	--	100%	0%	0%	0%	5.4 ± 1.7	1	0.014	Spherical; Porod Slope= -4.0
F	Lysine	0.1/1: quench with 10/1	6.2%	11%	34%	49%	41 ± 27	0.6	0.732	1.8
D	Lysine	1/1: quench with 0/1	18%	16%	62%	4%	41 ± 22	0.5	0.904	1.2
B	Lysine	5/1	0%	5.2%	16%	79%	47 ± 32	0.5	1.05	1.5
C	Cysteine	5/1	7.2%	18%	70%	4%	51 ± 31	0.7	0.380	1.9
E	Glutath-ione	5/1	11%	54%	6.1 %	28%	44 ± 29	0.7	0.025	Spherical; Porod Slope= -4.0

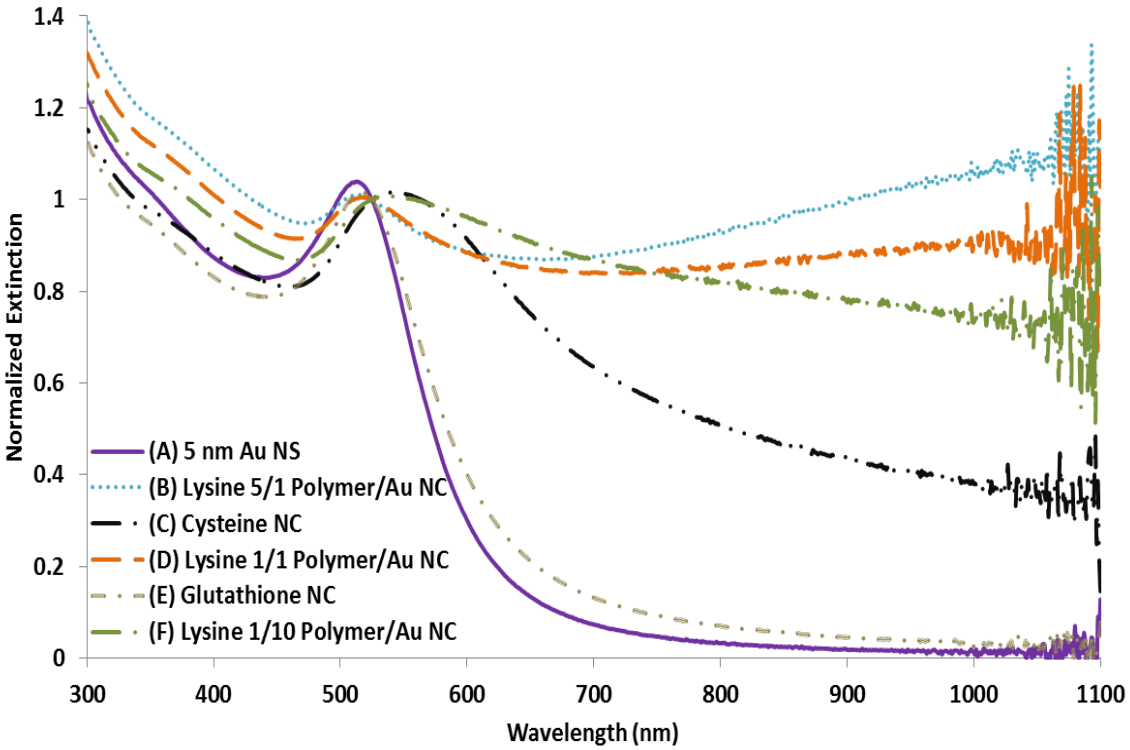

Figure A.4: The UV-vis-NIR spectra of (A) 5 nm Au nanospheres; (B) lysine/citrate nanoclusters assembled at pH 5 at 5/1 polymer/Au; (C) cysteine/citrate nanoclusters at pH 5 at 5/1 polymer/Au; (D) lysine/citrate nanoclusters at pH 5 at 1/1 polymer/Au; (E) glutathione/citrate nanoclusters at pH 5 at 5/1 polymer/Au; and (F) lysine/citrate nanoclusters at pH 5 at 0.1/1 polymer/Au, quenched in 10/1 polymer/Au.

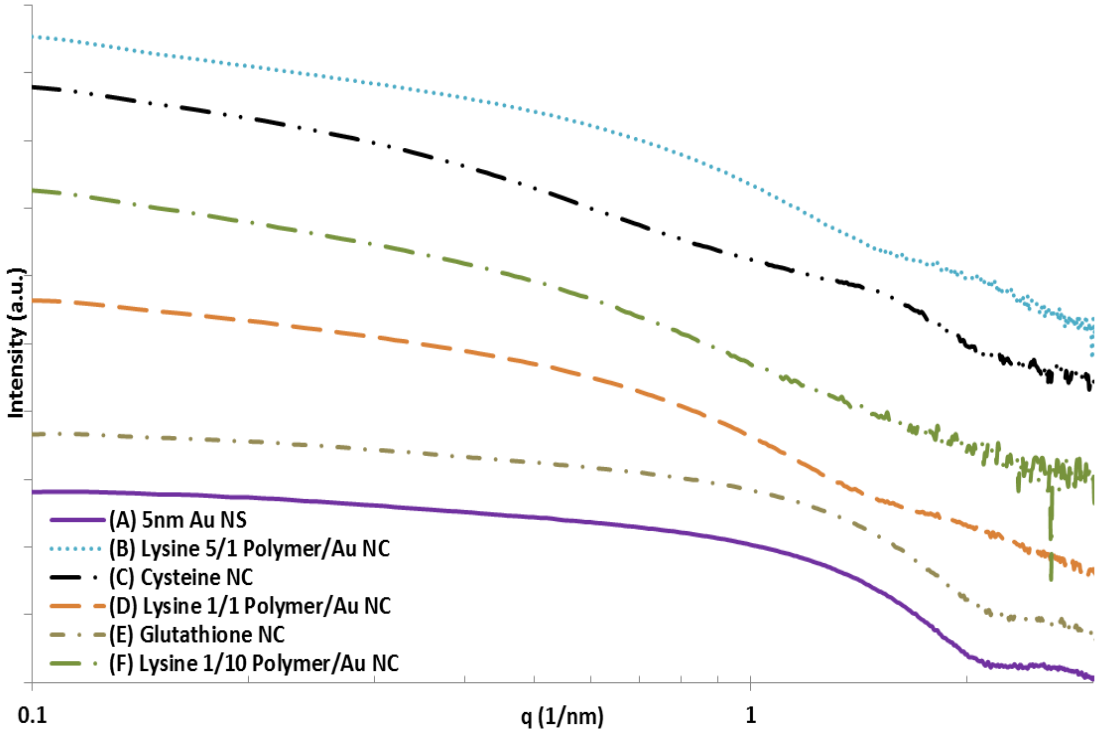

Figure A.5: The SAXS curves of (A) 5 nm Au nanospheres; (B) lysine/citrate nanoclusters assembled at pH 5 at 5/1 polymer/Au; (C) cysteine/citrate nanoclusters at pH 5 at 5/1 polymer/Au; (D) lysine/citrate nanoclusters at pH 5 at 1/1 polymer/Au; (E) glutathione/citrate nanoclusters at pH 5 at 5/1 polymer/Au; and (F) lysine/citrate nanoclusters at pH 5 at 0.1/1 polymer/Au, quenched in 10/1 polymer/Au. Curves are offset only for clarity, and intensity is plotted on a log scale.

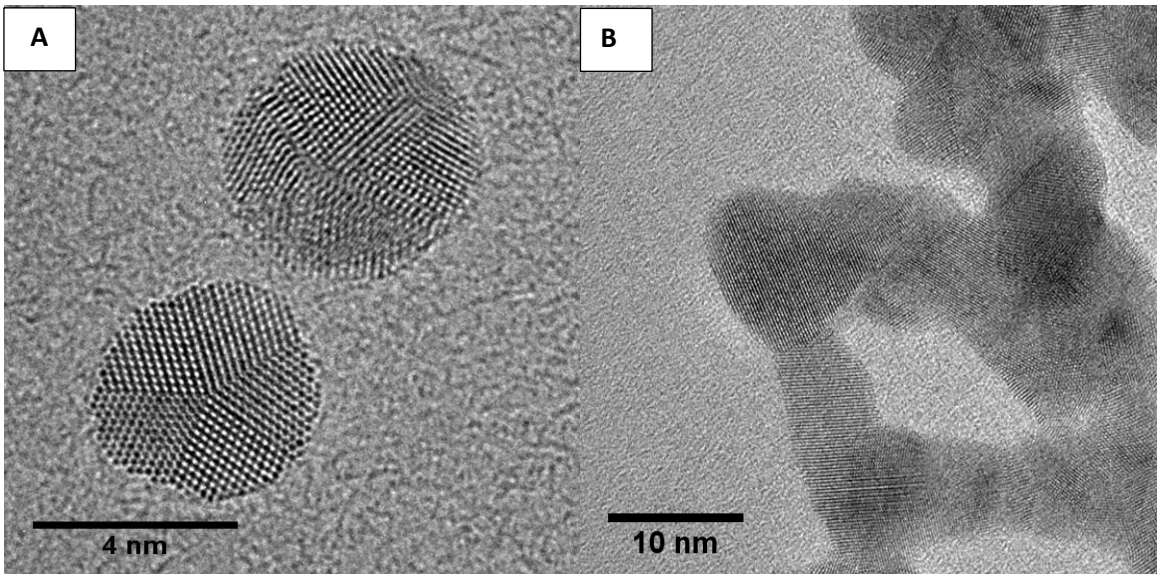

Figure A.6: High-resolution TEM images of (A) primary 5 nm Au nanospheres; and (B) lysine/citrate nanoclusters at pH 6 at 1/1 polymer/Au.

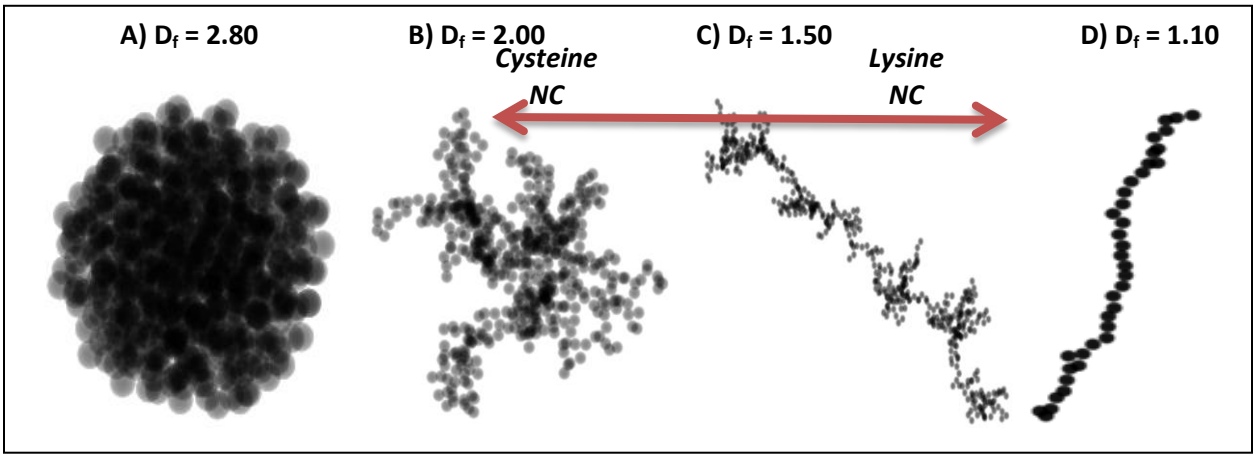

Figure A.7: Schematic of sample fractal dimensions and simulated diffusion-limited aggregates: (A): D_f = 2.80; (B): D_f = 2.00; (C): D_f = 1.50; (D) D_f = 1.10. The red arrow displays the range of fractal dimension of our nanoclusters. TEM 1D representation of images generated with 500 monomers by DLA/TEM Software.[18]

A.6 REFERENCES:

1. Horvath, H. Gustav Mie and the scattering and absorption of light by particles: Historic developments and basics. *Journal of Quantitative Spectroscopy and Radiative Transfer* 2009**, 110**, 787-799.
2. Halas, N. J.; Lal, S.; Chang, W.-S.; Link, S.; Nordlander, P. Plasmons in Strongly Coupled Metallic Nanostructures. *Chemical Reviews* 2011**, 111**, 3913-3961.
3. Hirsch, L. R.; Stafford, R. J.; Bankson, J. A.; Sershen, S. R.; Rivera, B.; Price, R. E.; Hazle, J. D.; Halas, N. J.; West, J. L. Nanoshell-mediated near-infrared thermal therapy of tumors under magnetic resonance guidance. *Proceedings of the National Academy of Sciences* 2003**, 100**, 13549-13554.
4. Loo, C.; Lowery, A.; Halas, N.; West, J.; Drezek, R. Immunotargeted Nanoshells for Integrated Cancer Imaging and Therapy. *Nano Letters* 2005**, 5**, 709-711.
5. Fang, Y.; Chang, W.-S.; Willingham, B.; Swanglap, P.; Dominguez-Medina, S.; Link, S. Plasmon emission quantum yield of single gold nanorods as a function of aspect ratio. *ACS Nano* 2012**, 6**, 7177-7184.
6. Jain, P. K.; Lee, K. S.; El-Sayed, I. H.; El-Sayed, M. A. Calculated Absorption and Scattering Properties of Gold Nanoparticles of Different Size, Shape, and Composition: Applications in Biological Imaging and Biomedicine. *The Journal of Physical Chemistry B* 2006**, 110**, 7238-7248.
7. Ghosh, S. K.; Pal, T. Interparticle Coupling Effect on the Surface Plasmon Resonance of Gold Nanoparticles: From Theory to Applications. *Chemical Reviews* 2007**, 107**, 4797-4862.
8. Norman, T.; Grant, C.; Zhang, J. Optical and dynamic properties of gold metal nanomaterials: From isolated nanoparticles to assemblies. *Nanoparticle Assemblies and Superstructures. Boca Raton, FL: CRC Press/Taylor & Francis* 2006**,** 193-206.
9. Liz-Marzán, L. M. Tailoring surface plasmons through the morphology and assembly of metal nanoparticles. *Langmuir* 2006**, 22**, 32-41.
10. Bohren, C. F.; Huffman, D. R. *Absorption and scattering of light by small particles*; John Wiley & Sons2008.
11. Murthy, A. K.; Stover, R. J.; Borwankar, A. U.; Nie, G. D.; Gourisankar, S.; Truskett, T. M.; Sokolov, K. V.; Johnston, K. P. Equilibrium Gold Nanoclusters Quenched with Biodegradable Polymers. *ACS Nano* 2013**, 7**, 239-251.
12. Tam, J. M.; Murthy, A. K.; Ingram, D. R.; Nguyen, R.; Sokolov, K. V.; Johnston, K. P. Kinetic Assembly of Near-IR Active Gold Nanoclusters Using Weakly Adsorbing Polymers to Control the Size. *Langmuir* 2010**, 26**, 8988-8999.

13. Khlebtsov, B.; Zharov, V.; Melnikov, A.; Tuchin, V.; Khlebtsov, N. Optical amplification of photothermal therapy with gold nanoparticles and nanoclusters. *Nanotechnology* 2006**,** 5167-5179.

14. Lazarides, A. A.; Schatz, G. C. DNA-Linked Metal Nanosphere Materials: Structural Basis for the Optical Properties. *Journal of Physical Chemistry B* 2000**,** **104**, 460-467.

15. Martin, J. E.; Hurd, A. Scattering from fractals. *Journal of applied Crystallography* 1987**,** **20**, 61-78.

16. Hiemenz, P. C.; Rajagopalan, R. *Principles of Colloid and Surface Chemistry, revised and expanded*; CRC press1997; Vol. 14.

17. Lee, Y.-J.; Schade, N. B.; Sun, L.; Fan, J. A.; Bae, D. R.; Mariscal, M. M.; Lee, G.; Capasso, F.; Sacanna, S.; Manoharan, V. N. Ultrasmooth, highly spherical monocrystalline gold particles for precision plasmonics. *ACS Nano* 2013**,** **7**, 11064-11070.

18. Wozniak, M.; Onofri, F.; Barbosa, S.; Yon, J.; Mroczka, J. Comparison of methods to derive morphological parameters of multi-fractal samples of particle aggregates from TEM images. *Journal of Aerosol Science* 2012**,** **47**, 12-26.

19. Lin, S.; Li, M.; Dujardin, E.; Girard, C.; Mann, S. One-Dimensional Plasmon Coupling by Facile Self-Assembly of Gold Nanoparticles into Branched Chain Networks. *Advanced Materials* 2005**,** **17**, 2553-2559.

20. Esteban, R.; Taylor, R. W.; Baumberg, J. J.; Aizpurua, J. How chain plasmons govern the optical response in strongly interacting self-assembled metallic clusters of nanoparticles. *Langmuir* 2012**,** **28**, 8881-8890.

21. Wang, M.-H.; Li, Y.-J.; Xie, Z.-X.; Liu, C.; Yeung, E. S. Fabrication of large-scale one-dimensional Au nanochain and nanowire networks by interfacial self-assembly. *Materials Chemistry and Physics* 2010**,** **119**, 153-157.

22. Herrmann, L.; Valev, V.; Aizpurua, J.; Baumberg, J. J. Self-sifting of chain plasmons: the complex optics of Au nanoparticle clusters. *Optics Express* 2013**,** **21**, 32377-32385.

23. Arnold, M. D.; Blaber, M. G.; Ford, M. J.; Harris, N. Universal scaling of local plasmons in chains of metal spheres. *Optics Express* 2010**,** **18**, 7528-7542.

24. Kitching, H.; Shiers, M. J.; Kenyon, A. J.; Parkin, I. P. Self-assembly of metallic nanoparticles into one dimensional arrays. *Journal of Materials Chemistry A* 2013**,** **1**, 6985-6999.

25. Murugadoss, A.; Chattopadhyay, A. Surface area controlled differential catalytic activities of one-dimensional chain-like arrays of gold nanoparticles. *The Journal of Physical Chemistry C* 2008**,** **112**, 11265-11271.

26. Zhang, H.; Fung, K.-H.; Hartmann, J. r.; Chan, C.; Wang, D. Controlled chainlike agglomeration of charged gold nanoparticles via a deliberate interaction balance. *The Journal of Physical Chemistry C* 2008**, 112**, 16830-16839.

27. Fernandes, R.; Li, M.; Dujardin, E.; Mann, S.; Kanaras, A. G. Ligand-mediated self-assembly of polymer-enveloped gold nanoparticle chains and networks. *Chemical Communications* 2010**, 46**, 7602-7604.

28. Polavarapu, L.; Xu, Q.-H. A single-step synthesis of gold nanochains using an amino acid as a capping agent and characterization of their optical properties. *Nanotechnology* 2008**, 19**, 075601.

29. Hill, L. J.; Pinna, N.; Char, K.; Pyun, J. Colloidal polymers from inorganic nanoparticle monomers. *Progress in Polymer Science* 2015**, 40**, 85-120.

30. Karplus, M. CHARMM: A program for macromolecular energy, minimization, and dynamics calculations. *J Comput Chem* 1983**, 4**, 187217.

Appendix B: Charged Gold Nanoparticles with Essentially Zero Serum Protein Adsorption in Undiluted Fetal Bovine Serum

B.1 Determination of Lysine/Citrate and Cysteine/Citrate Ratios by XPS

The lysine/citrate ratios on the surface of Au nanospheres with lysine/citrate feed ratios of 4.5/1 and 9/1 were determined from the integration of the N 1s and O 1s peaks in the XPS spectrum. Lysine contains 2 N and 2 O atoms, while citrate has 7 O and 0 N atoms. As a result, we set up the following system of simultaneous equations:

$$2y_L = y_N \tag{B.1}$$

$$2y_L + 7y_C = y_O \tag{B.2}$$

Here, y_L is the molar fraction of lysine, y_N is the molar fraction of nitrogen, y_c is the molar fraction of citrate, and y_O is the molar fraction of oxygen. For the nanospheres synthesized with a feed ratio of 4.5/1, integration of the N 1s and O 1s spectra yielded an average N/O ratio of 0.12, and thus a lysine/citrate ratio of 0.5. From the integration of the N 1s and O 1s spectra shown in Figure 3.2, we get an average N/O ratio of 0.28, and thus a lysine/citrate ratio of 1.4.

The cysteine/citrate ratios on the surface of the Au nanospheres synthesized with cysteine/citrate feed ratios of 0.3/1 and 0.7/1 were determined from the integration of the N 1s and O 1s peaks in the XPS spectrum, in a manner similar to that of lysine/citrate nanospheres. Cysteine contains 1 N and 2 O atoms, while citrate has 7 O and 0 N atoms. Thus, Equations B.1 and B.2 become:

$$y_{cys} = y_N \tag{B.3}$$

$$2y_{cys} + 7y_{cit} = y_O \quad \text{(B.4)}$$

Here, y_{cys} is the molar fraction of cysteine, and y_{cit} is the molar fraction of citrate. For a cysteine/citrate feed ratio of 0.3/1, integration of the N 1s and O 1s spectra yielded an average N/O ratio of 0.11, corresponding to a cysteine/citrate ratio of 1.0. For the 0.7/1 cysteine/citrate feed ratio, the average N/O ratio was 0.15, corresponding to a cysteine/citrate ratio of 1.6. In both cases, the ratios of N and O to Au were not quantified, due to the fact that the X-ray beam in XPS does not uniformly penetrate the entire Au sphere.[4]

B.2 Correlation of XPS and Zeta Potential Results

The reduction in nanosphere zeta potential after ligand exchange can be correlated to the XPS results on the mixed charge monolayers, as shown in Table B.1. Approximately 196 citrate ligands are present on the surface of the citrate-capped nanospheres,[3] which corresponds to 196 × 3 = 588 negative charges. Ligand exchange with lysine replaces 3 negative charges with one positive charge, and ligand exchange with cysteine replaces 3 negative charges with a net neutral charge. Thus, for the lysine/citrate nanospheres, the number of charges N on the nanosphere was determined by:

$$N = 3x\text{-}y \quad \text{(B.5)}$$

where x is the number of citrate ligands and y is the number of lysine ligands. For the cysteine/citrate monolayers, the number of charges N is determined by:

$$N = 3x \tag{B.6}$$

The calculated values of N is then compared to the value of 588 for citrate-capped nanospheres, in order to determine the percentage of negative charge retained on the nanosphere for each mixed charge monolayer. This number compares exceptionally well with the percentage of negative charge retained as determined by zeta potential measurements, as shown in Table B.1.

B.3 DESCRIPTION OF PREVIOUS CELLULAR STUDIES

Solid gold nanoparticles have been shown to aggregate within cellular endosomes.[5,6] In a previous study, however, we have demonstrated the cellular dissociation of ~80 nm nanoclusters within J477A murine macrophage cells.[2] Hyperspectral imaging indicated that over a period of 168 h, the scattering spectra shifted significantly out of the NIR region. Moreover, TEM analysis of cells indicated that dissociation of nanoclusters occurred, as ~80 nm nanoclusters which were visible in TEM images after 24 h, but only sub 5 nm Au nanoparticles were visible in cells after 168 h of incubation. As a result, this previous study provided proof of dissociation of nanoclusters within macrophage cells.

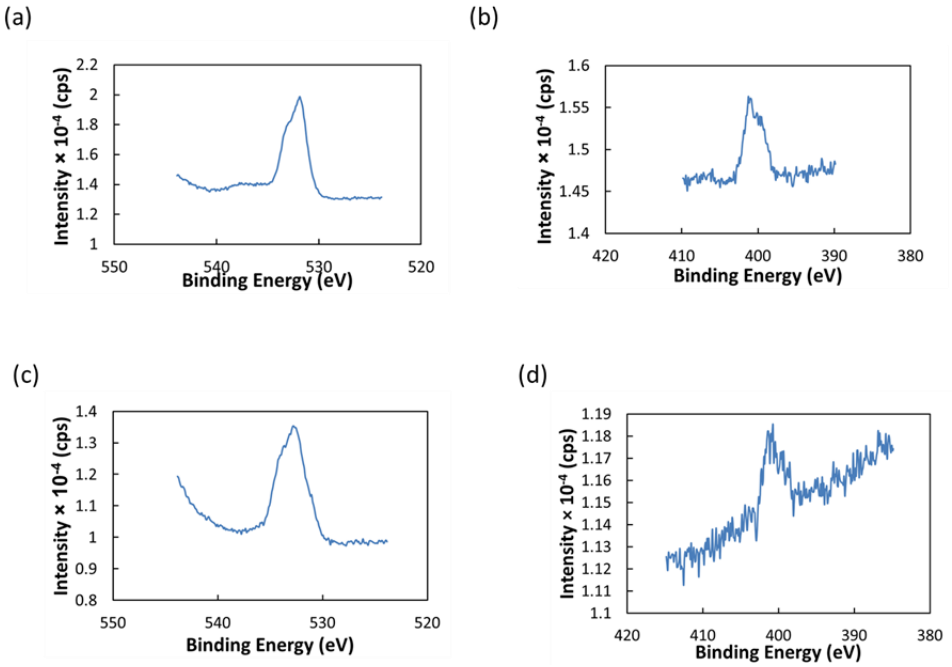

Figure B.1 XPS spectra of (a) O 1s for 1.4/1 lysine/citrate nanospheres, (b) N 1s for lysine/citrate, (c) O 1s for 1.6/1 cysteine/citrate nanospheres, and (d) N 1s for 1.6/1 cysteine/citrate nanospheres.

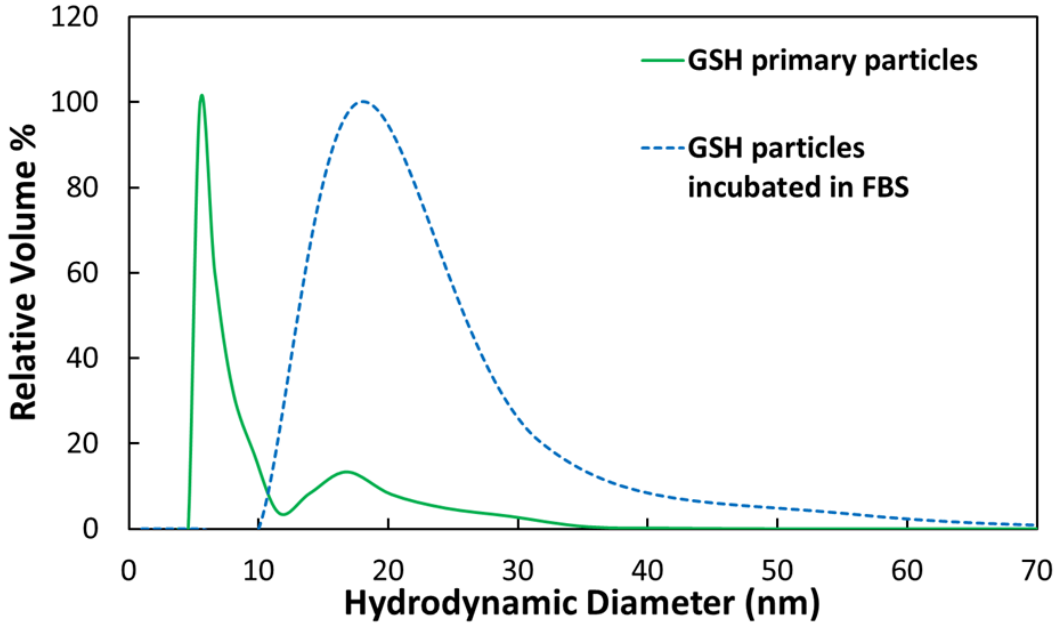

Figure B.2 DLS size distributions of GSH-capped nanospheres before (solid green curve) and after (dashed blue curve) incubation in 100% FBS for 4 h at 37 °C.

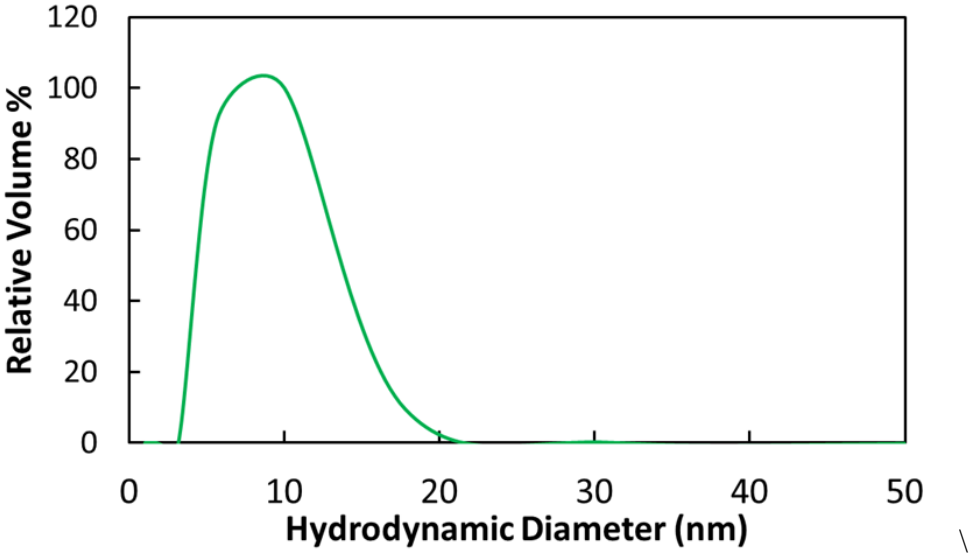

Figure B.3 DLS distribution of pure FBS.

(a)

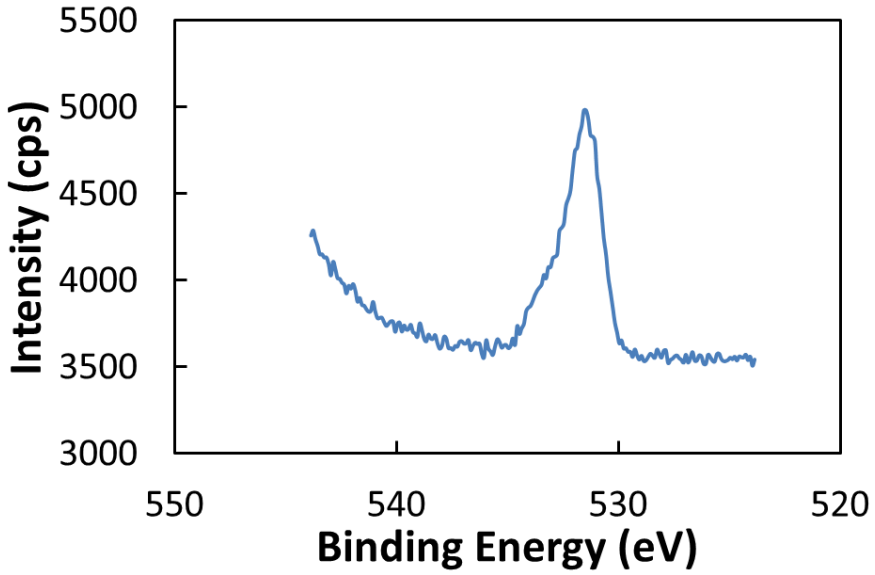

(b)

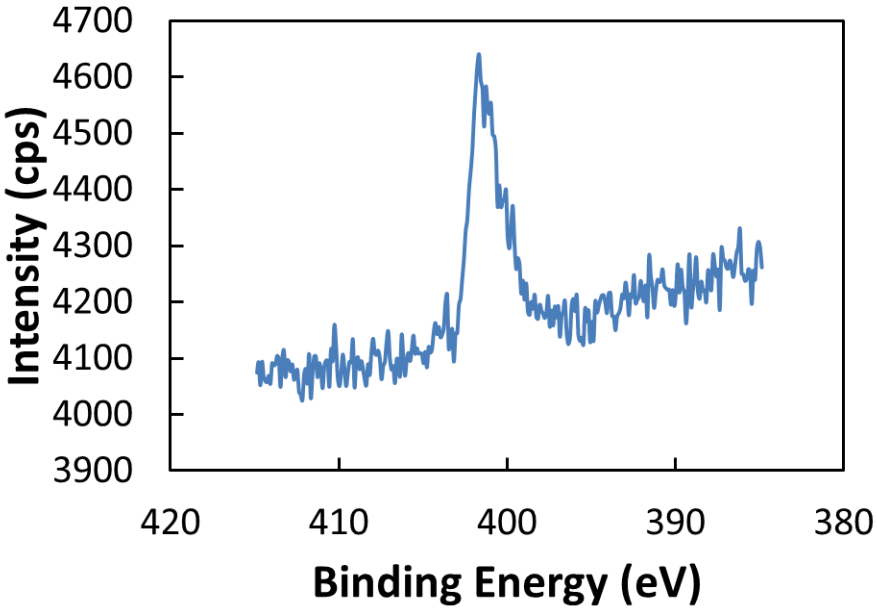

Figure B.4 (a) O 1s and (b) N 1s XPS spectra for nanospheres synthesized with a lysine/citrate feed ratio of 4.5/1.

(a)

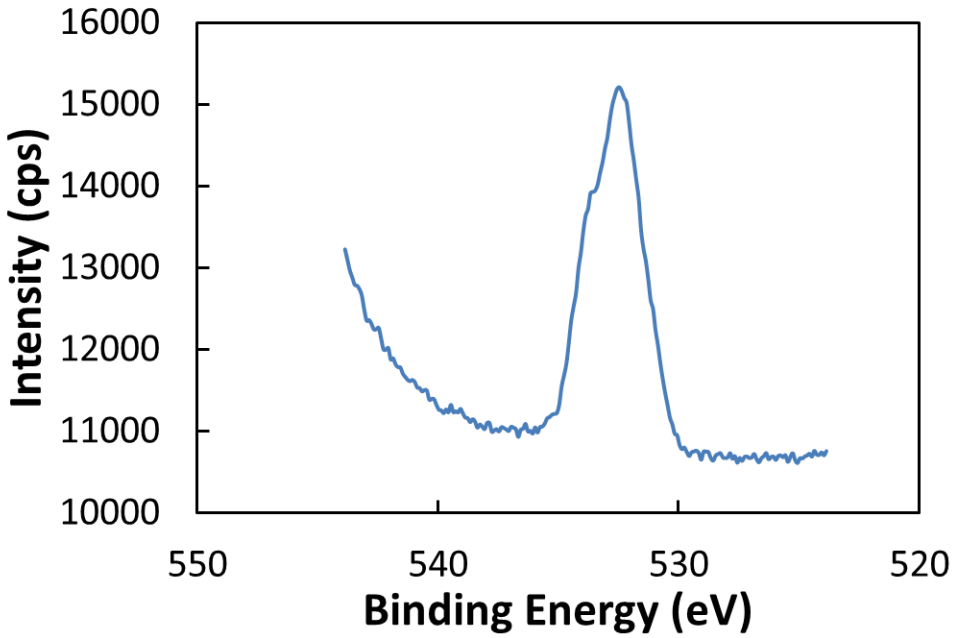

(b)

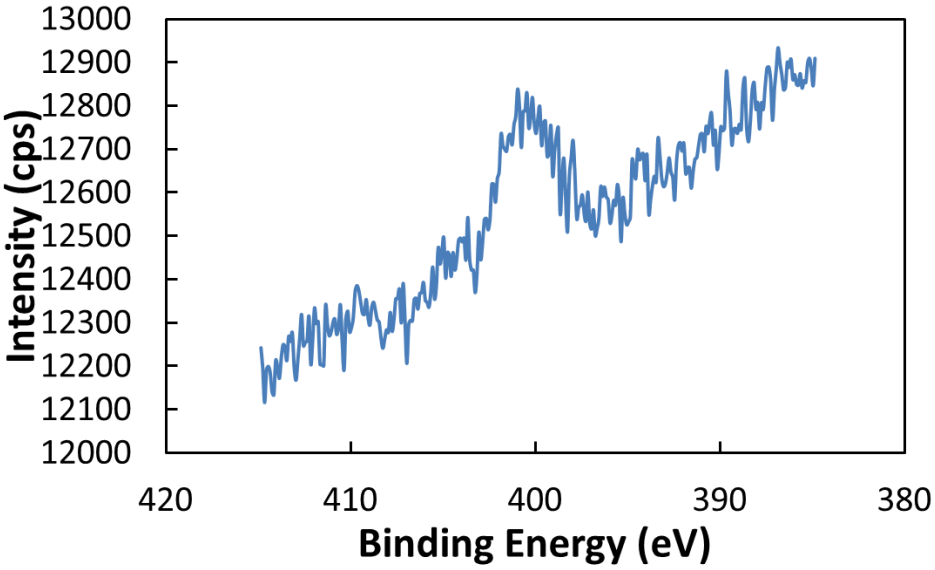

Figure B.5 (a) O 1s and (b) N 1s XPS spectra for nanospheres synthesized with a cysteine/citrate feed ratio of 0.3/1.

(a)

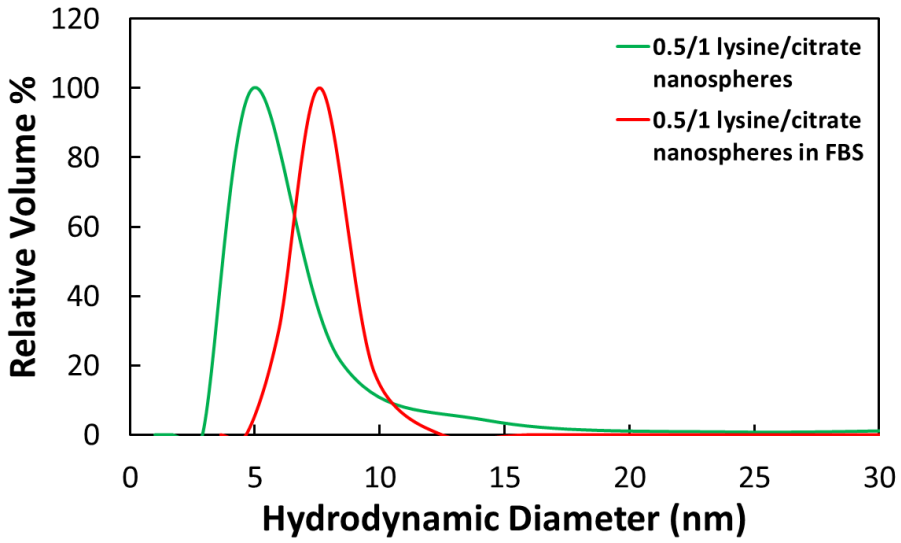

(b)

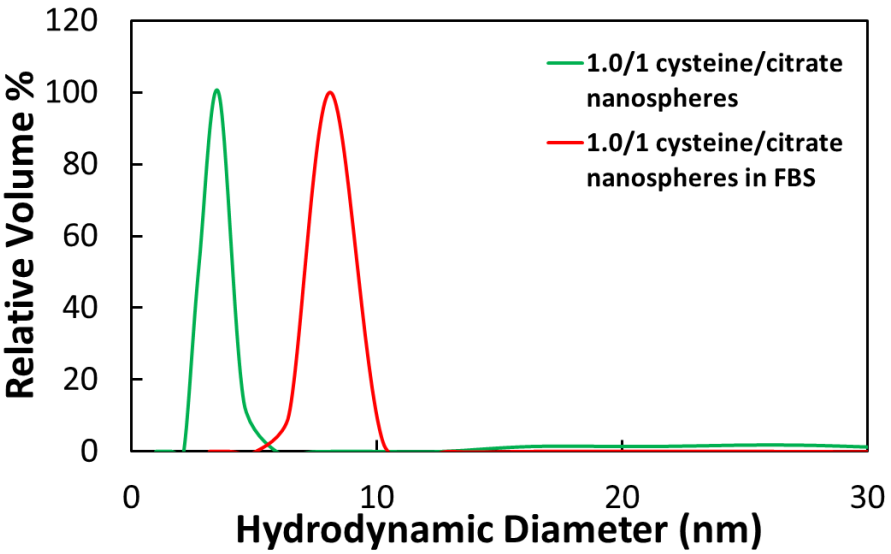

Figure B.6 DLS size distributions before and after incubation in 100% FBS for (a) 0.5/1 lysine/citrate nanospheres and (b) 1.0/1 cysteine/citrate nanospheres

Table B.1 Correlation of XPS and zeta potential results for nanospheres capped with mixed-charge monolayers.

Ligand (s)	**XPS Ligand Ratio**	**Number of Charges from XPS**	**% of Charge Retained from XPS**	**Zeta Potential (mV)**	**% of Charge Retained from Zeta Potential**
Citrate	n/a	588	100%	-58.4 ± 5.3	100%
Lysine/Citrate	0.5	327	56%	-28.9 ± 3.9	49%
Lysine/Citrate	1.4	131	22%	-16.1 ± 2.9	28%
Cysteine/Citrate	1.0	290	49%	-28.8 ± 3.2	49%
Cysteine/Citrate	1.6	228	39%	-21.6 ± 1.7	37%

Table B.2 Centrifugation yields for mixed-monolayer capped nanospheres after incubation in 100% FBS for 4 h at 37 °C.

Ligands	**XPS Ligand Ratio**	**D_h in FBS (nm)**	**Au mass yield in pellet (%)**
Lysine/Citrate in FBS	0.5	7.7 ± 3.8	53.9 ± 13.1
Lysine/Citrate in FBS	1.4	3.9 ± 2.1	26.3 ± 5.8
Cysteine/Citrate in FBS	1.0	8.8 ± 5.8	39.2 ± 13.0
Cysteine/Citrate in FBS	1.6	3.4 ± 2.7	21.3 ± 13.1

Table B.3 Centrifugation yields for mixed-monolayer capped nanospheres in water

Ligands	**XPS Ligand Ratio**	**Au mass yield in pellet (%)**
Lysine/Citrate in FBS	0.5	22.7
Cysteine/Citrate in FBS	1.0	24.1

Table B.4 Reproducibility of 0.5/1 lysine/citrate nanospheres

Sample	Zeta Potential (mV)	DLS (nm)
1	-28.8 ± 5.0	4.7 ± 1.1
2	-26.4 ± 0.4	5.4 ± 1.3
3	-31.6 ± 6.3	4.8 ± 1.2

Table B.5 Reproducibility of 1.4/1 lysine/citrate nanospheres

Sample	Zeta Potential (mV)	DLS (nm)
1	-16.0 ± 6.6	4.6 ± 1.0
2	-15.3 ± 1.2	4.4 ± 1.1
3	-17.0 ± 0.9	4.7 ± 1.2

Table B.6 Reproducibility of 1.0/1 cysteine/citrate nanospheres

Sample	Zeta Potential (mV)	DLS (nm)
1	-29.9 ± 4.3	4.5 ± 3.4
2	-27.6 ± 2.0	5.6 ± 4.4

Table B.7 Reproducibility of 1.6/1 cysteine/citrate nanospheres

Sample	Zeta Potential (mV)	DLS (nm)
1	-22.2 ± 2.7	3.6 ± 2.2
2	-21.0 ± 0.6	3.1 ± 2.8

Table B.8 Full DLS distribution data for 1.4 lysine/citrate nanospheres in 100% FBS

Diameter (nm)	Relative Volume %	Cumulative Volume %
1	0	0
2	0	0
3	100	81
6	19	97
10	4	99
18	1	100
32	0	100
56	0	100

Table B.9 Full DLS distribution data for 1.6 cysteine/citrate nanospheres in 100% FBS

Diameter (nm)	Relative Volume %	Cumulative Volume %
1	0	0
2	32	20
3	100	85
6	19	97
10	4	99
18	1	100
32	0	100
56	0	100

B.4 REFERENCES

(1) Tam, J. M.; Murthy, A. K.; Ingram, D. R.; Nguyen, R.; Sokolov, K. V.; Johnston, K. P. *Langmuir* **2010**, *26*, 8988.

(2) Tam, J. M.; Tam, J. O.; Murthy, A.; Ingram, D. R.; Ma, L. L.; Travis, K.; Johnston, K. P.; Sokolov, K. V. *ACS Nano* **2010**, *4*, 2178.

(3) Murthy, A. K.; Stover, R. J.; Borwankar, A. U.; Nie, G. D.; Gourisankar, S.; Truskett, T. M.; Sokolov, K. V.; Johnston, K. P. *ACS Nano* **2013**, *7*, 239.

(4) Watts, J. F.; Wolstenholme, J. *An Introduction to Surface Analysis by XPS and AES*; John Wiley & Sons: West Sussex, England, 2003.

(5) Aaron, J.; Travis, K.; Harrison, N.; Sokolov, K. *Nano Lett.* **2009**, *9*, 3612.

(6) Kneipp, J.; Kneipp, H.; McLaughlin, M.; Brown, D.; Kneipp, K. *Nano Lett.* **2006**, *6*, 2225.

Appendix C: Equilibrium Gold Nanoclusters Quenched with Biodegradable Polymers

C.1 Synthesis of Citrate-Capped Gold Nanospheres

Citrate-coated gold nanospheres were synthesized by adapting a synthesis route which has been described previously.[1, 2] Here, 3 L of deionized water was heated to ~ 97 °C. Aqueous solutions of 1% (w/v) $HAuCl_4 \cdot H_2O$, 1% (w/v) $Na_3C_3H_5O(COO)_3 \cdot 2H_2O$, and 0.075% (w/v) $NaBH_4$ were prepared. 30 mL of each solution was added successively to the deionized water in 1 min intervals, while the solution was stirred vigorously. The resulting gold nanoparticle solution was allowed to cool to room temperature, and was then centrifuged in 250 ml centrifuge tubes at 8500 rpm for 10 min at 4 °C in an Avanti J-E centrifuge (Beckman Coulter, Brea, CA), in order to remove ~100 ml of the 3 L solution as large particles. The remaining supernatant (~0.02 mg Au/ml) was passed through a tangential flow filtration (TFF) setup (KrosFlo Research II, Spectrum Labs, Rancho Domingo, CA), using a polystyrene filter with a pore size of 10 kDa and a filter surface area of 1050 cm^2. TFF processing removed water and excess reaction reagents from the nanoparticle solution, and resulted in ~100 ml of ~1 mg Au/ml solution. 15 ml centrifugal filter devices with a 30 kDa MW cutoff (Ultracel YM-30, Millipore, Billerica, MA) were used to additionally concentrate the nanoparticle solution. After centrifugation at 6000 rpm for 5 min, the resulting gold nanoparticle solution was adjusted with DI water to a concentration of 3.0 ± 0.1 mg Au/ml. Synthesis resulted in ~30 ml of 3 mg/ml Au nanospheres.

C.2 Citrate and Citrate/Lysine Monolayer Calculations

The theoretical weight of a monolayer coverage of citrate ligands, as well as the theoretical weight of a citrate/lysine mixed monolayer, was compared to experimental data determined by TGA. In this calculation, the lysine/citrate ratio was 1.4, as determined experimentally by XPS. The saturation monolayer coverage of citrate on a gold nanoparticle surface was reported to be 4.6×10^{-10} mol/cm^2 .[3] This value correlates to a citrate footprint value of 0.36 nm^2/ligand. The number of citrate ligands comprising a monolayer on the gold nanoparticle surface is given by

$$n = \frac{4\pi\left(\frac{D}{2}\right)^2 \times 0.9}{f} \quad \text{(C.1)}$$

where *n* is the number of citrate ligands, D is the diameter of the nanoparticle, and f is the ligand footprint. Here, *D* is taken to be 5 nm and *f* is 0.36 nm^2. The factor of 0.9 in the numerator of Equation S1 arises from the approximation of ligand attachment as close-packed circles on a planar surface.[4] Here, n is determined to be 196 citrate ligands/nanoparticle, which corresponds to ~4.7% w/w on a 5 nm gold particle, in reasonable agreement with the TGA result of 4%. In order to calculate the theoretical weight of monolayer coverage after lysine exchange with citrate, the lysine/citrate ratio of 1.4 determined by XPS was used. Since the TGA ligand weight % does not increase from 4% upon the addition of lysine, we can rule out any electrostatic binding between the anionic citrate and cationic lysine, and thus assume that one lysine ligand displaces one citrate ligand, such that the effective footprint for a lysine ligand is also 0.36 nm^2/ligand. Assuming that n remains constant at 196, a lysine/citrate ratio of 1.4 indicates

that the nanoparticle surface contains 114 lysine ligands and 82 citrate ligands, which translates to 4.1% w/w of a 5 nm gold nanoparticle, in very good agreement with the TGA result of 4% w/w. Thus, a monolayer of citrate/lysine may be assumed to be present on the nanoparticles after ligand exchange.

C.3 Calculation of Extinction Coefficients

The relationship between extinction and the extinction coefficient is given by the Beer-Lambert law:

$$A(\lambda) = \varepsilon(\lambda)Cl \tag{C.2}$$

where A is the measured extinction at a given wavelength λ, ε is the extinction coefficient at that wavelength, in cm^2/mg, C is the concentration in mg/ml, and l is the path length in cm. For all measurements in this study, the path length is 1 cm. Extinction and extinction coefficient values in this study are determined for a wavelength of 800 nm.

C.4 XPS Determination of Ligand Ratio

In order to determine the ratio of lysine/citrate ligands, XPS spectra were recorded for primary gold nanospheres after ligand exchange. Integration of N 1s and O 1s peaks was conducted in order to determine the atomic percentages of N and O atoms on the surface of the gold nanospheres. Lysine contains 2 N atoms and 2 O atoms (and has been shown to have a XPS N/O intensity ratio which corresponds favorably to $1/1$[5]), whereas citrate contains 7 O atoms and no N atoms. Thus, the following system of simultaneous equations can be set up:

$$2y_L = y_N \tag{C.3}$$

$$2y_L + 7y_C = y_O \quad \text{(C.4)}$$

where y_L is the molar fraction of lysine, y_N is the molar fraction of nitrogen, y_C is the molar fraction of citrate, and y_O is the molar fraction of oxygen. We then define the N/O atomic ratio $R_{N/O}$ as y_N/y_O, and we obtain:

$$\frac{y_L}{y_C} = \frac{7R_{N/O}}{2\text{-}2R_{N/O}} \quad \text{(C.5)}$$

Equation C.4 thus provides a simple algebraic expression for the lysine/citrate ratio. From the N 1s and O 1s peak integrations, we have a N/O ratio of 0.28, and thus a lysine/citrate ratio of 1.4. We did not attempt to determine ratios of N and O to Au, as the X-ray beam in XPS did not uniformly penetrate the entire Au sphere.[6]

C.5 Charge Screening Calculation

In order to determine the percentage of charge retained in the nanoclusters, the number of negative charges in a cluster of *n* primary particles was determined from zeta potential measurements. This value was then compared to the total theoretical number of negative charges on *n* primary particles, derived from the primary particle zeta potential. In order to determine the number of negative charges in a cluster, the charge on a nanocluster was related to the zeta potential by the equation[7]:

$$Q = 4\pi\epsilon_r\epsilon_0\zeta R_C(1 + \kappa R_C) \quad \text{(C.6)}$$

Here, Q is the charge on the nanocluster (in C), ϵ_r is the dielectric constant of the medium (80 for aqueous solvents), ϵ_0 is the permittivity of free space, ζ is the zeta potential, R_c is the nanocluster radius, and κ is the inverse Debye length. For a salt concentration of 1 mM, κ is 10^8 m^{-1}. In order to calculate the number of charges in a nanocluster, Q was divided by e, the unit of elementary charge. The relationship presented in Equation C.6 can explain the increase in number of charges per cluster even when the measured zeta potential magnitude decreases, as shown in Table 4.4. Since Q is quadratically proportional to the cluster radius, but only directly proportional to the zeta potential, an increase in cluster radius can result in an increase in nanocluster charge even when the zeta potential magnitude is decreased.

The theoretical number of charges was calculated by first determining the number of primary particles in a nanocluster, using the equation:

$$n = \left(\frac{R_C}{R}\right)^3 \times 0.72 \qquad \text{(C.7)}$$

where n is the number of primary particles in a nanocluster, R_c is the nanocluster radius, R is the primary particle radius (2.5 nm in our case), and 0.72 is the packing fraction assuming closely-packed primary particles within a cluster. The charge on a primary particle is calculated by using Equation C.5, with values for zeta potential and radius for the primary particles. The percentage of charge retained was calculated by dividing the number of negative charges on a nanocluster by the theoretical number of charges for n particles, and these results are presented in Table 4.4.

C.6 EQUILIBRIUM MODEL DETAILS

In order to generate the size contours presented in Figure 4.9, gold and polymer concentrations, and thus volume fractions, were related to the equilibrium cluster size n^* through Equation 4.5. Here, the attraction magnitude a within a nanocluster was calculated from the sum of the van der Waals attractive interaction potential and the depletion interaction potential. The van der Waals interaction potential is given by[7]:

$$V_{vdw} = -\frac{A_{gwg}}{6}\left[\frac{2R^2}{H(2R+H)} + \frac{2R^2}{(2R+H)^2} + \ln\left(\frac{H(4R+H)}{(2R+H)^2}\right)\right] \quad \text{(C.8)}$$

Here, R is the primary nanoparticle radius, H is the interparticle surface-surface separation distance, and A_{gwg} is the Au-Au Hamaker constant in an aqueous medium.[8] An interparticle distance of 1 nm is assumed within a nanocluster, and thus V_{vdw} is -3.01k_bT. The interparticle distance of 1 nm is a reasonable assumption given that the sensitivity of the free energy model is relatively low for interparticle distances up to 5 nm. Here, 5 nm is the maximum assumed interparticle distance given the strong NIR extinction exhibited by the nanoclusters. When the interparticle distance is increased from 1 nm to 5 nm, the predicted size at, for example, a c_p of 20 mg/ml and a c_{Au} of 1 mg/ml decreases from 38.9 nm to 35.9 nm, and the predicted size at a c_p of 80 mg/ml and a c_{Au} of 4 mg/ml decreases from 19.2 nm to 18.4 nm. Thus, the decrease in size is ~4-8% due to the increase in assumed interparticle spacing, within the error of DLS measurements.

In order to determine the molecular weight and R_g in Equation 4.6, we use the relationship:[9]

$$R_g = 0.0215M^{0.583} \quad \text{(C.9)}$$

where $R_g = R_h/0.64$.[9]

The depletion potentials calculated for different experimental polymer concentrations are shown in Figure C.3. The depletion component of the attraction *a* in Equation 4.4 is calculated by assuming an interparticle distance of 1 nm. Thus, *a* is the sum of the depletion and van der Waals attractions.

The entropic contributions of counterion dissociation from the charges on the gold nanoparticles is accounted for using the expression:[10, 11]

$$F_E = 2n_c q\left[\ln\left(\frac{q}{q_o}\right) - 1\right] \quad \text{(C.10)}$$

where q_0 represents the charge on the gold particle where the cluster free energy is minimized for weakly-charged systems[10, 11] and can be related to the number of dissociable ion sites per gold primary particle and gold volume fraction, as described below.

Nanocluster charge q (or q_0) depends on both the number of dissociable sites σs and on the particle volume fraction ϕ_{Au}, due to the greater entropic gains upon counterion dissociation in more dilute systems.[10, 11] The relationship between q_0, σs, and ϕ_{Au} is given by:[10]

$$q_0^2 = \frac{4\pi R^3 \sigma s}{b^3 e^{\Delta\epsilon+2}\phi_{Au}} \quad \text{(C.11)}$$

In Equation C.11, R is the radius of the primary nanoparticle, b is the distance between opposite charges in an ionic bond, σ is the density of dissociable ion sites on a primary particle, equivalent to the effective charge density on a primary gold nanoparticle, s is the surface area of a primary nanoparticle, and $\Delta\epsilon$ is the dissociation energy of an ion pair, which can be expressed as $\Delta\epsilon = \lambda_b/b$, where λ_b is the Bjerrum length. At room temperature, $\lambda_b = 56/\epsilon_r$ nm, where ϵ_r is the dielectric constant.[10] The value of σs was determined to be 2.78, using Equation C.5. Equation C.11 is used to calculate the charge per particle in a cluster, which is then fed into Equation 4.4. The size contours in Figure 4.9 are subsequently generated. The parameters used to generate these contours are given in Table C.1.

C.7 REDUCED DIELECTRIC CONSTANT OF WATER IN CLUSTERS

The dielectric constant of liquid water is known to be significantly reduced when it is confined to nanometer length scales.[11-14] This should be especially true in the small channels (less than ~1nm) between the closely spaced primary particles in the Au nanoclusters. A recent simulation study[12] found that water's dielectric constant is reduced to approximately a third of water's bulk value in highly crowded systems, which is consistent with our choice of 25 for the model calculations in the present study. This has important energetic implications, *e.g.* enhancing ion pairing between the ligand charges on the gold nanoparticle surface and the counterions and hence decreasing the effective charge per particle q. With the low local dielectric constant, the Debye length is sufficiently large for long ranged repulsion to balance short ranged attraction and favor nanocluster formation, as shown in Equation 4.4.

(a)

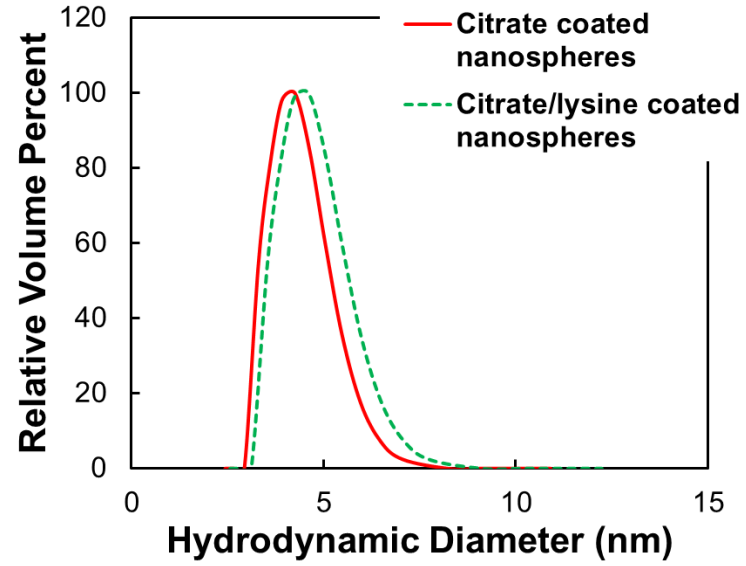

(b)

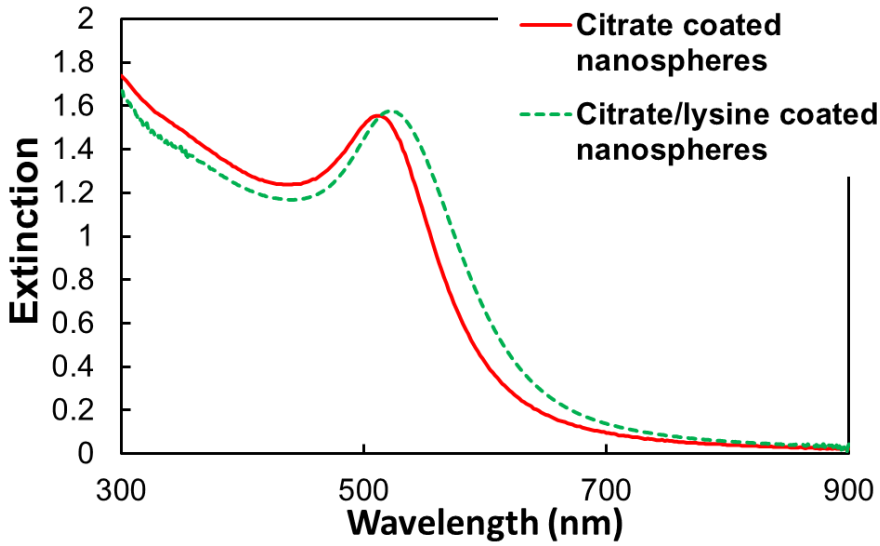

Figure C.1: (a) DLS size distributions and (b) UV-Vis-NIR extinction spectra of citrate-coated nanospheres (red, solid) and citrate/lysine coated nanospheres (green, dashed) after ligand exchange. UV-Vis-NIR spectra were taken at a gold concentration of ~90 μg/ml.

(a)

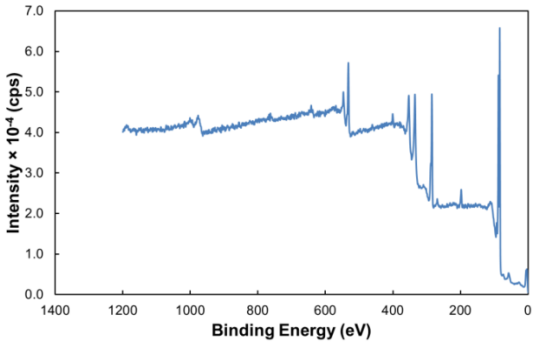

(b)

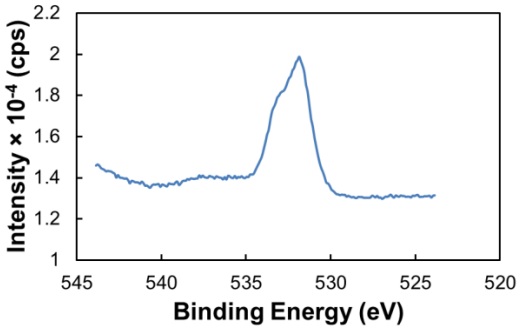

(c)

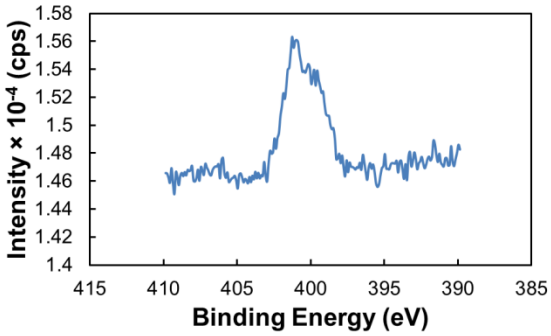

Figure C.2: (a) XPS survey scan, (b) O 1s peak and (c) N 1s peak of lysine/citrate capped Au nanospheres.

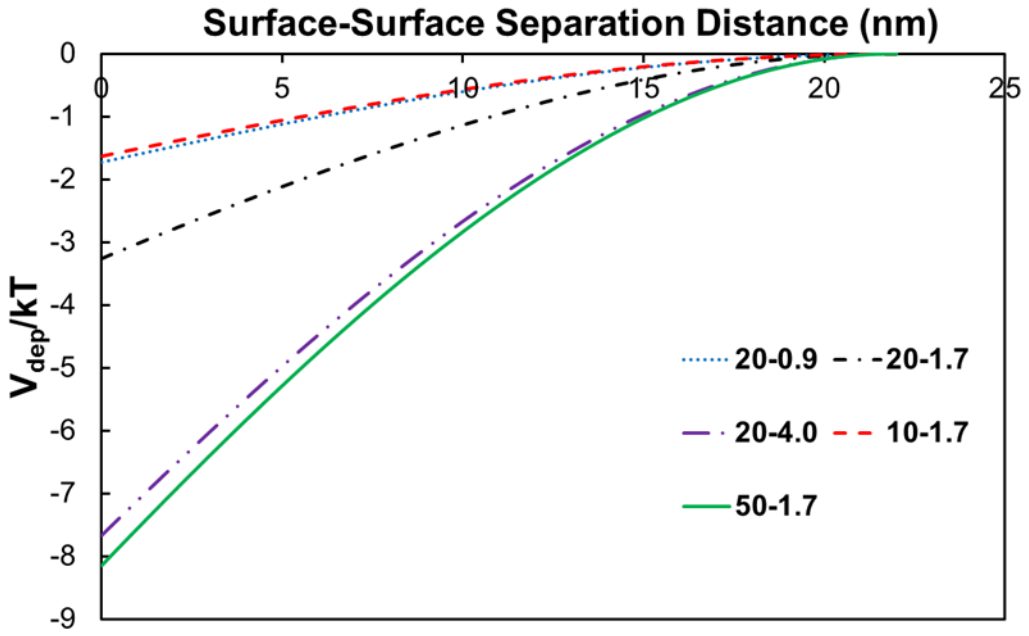

Figure C.3: Depletion potentials calculated for polymer concentrations identical to the indicated experimental samples.

(a)

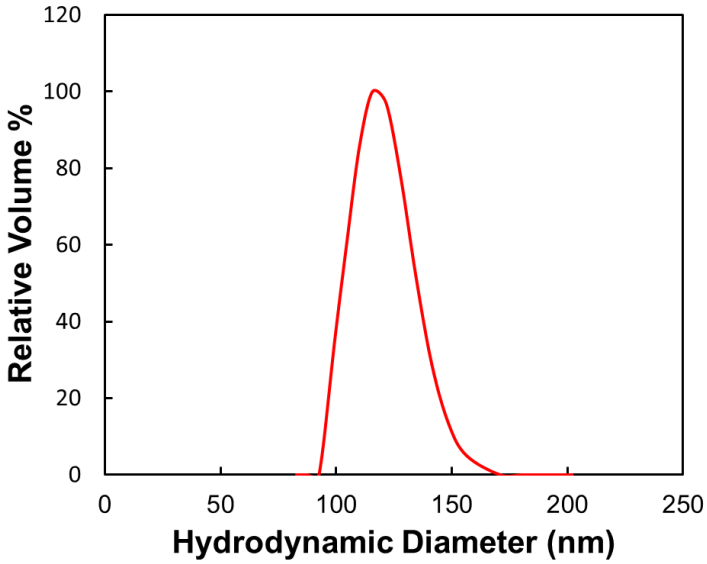

(b)

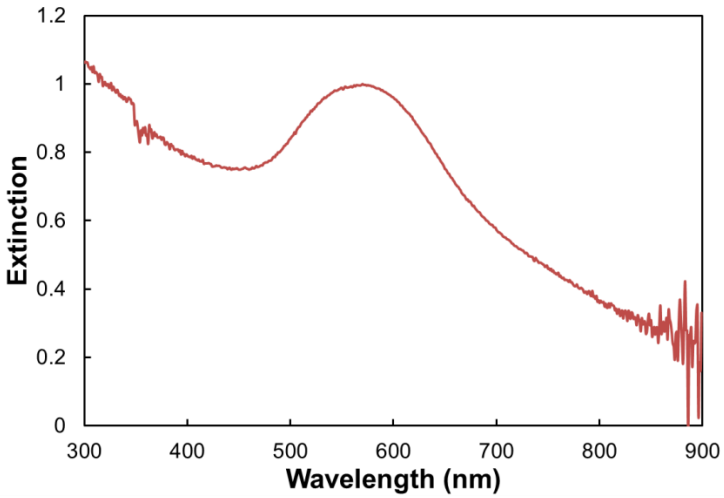

Figure C.4: (a) DLS size distribution and (b) UV-Vis-NIR extinction spectrum of nanoclusters formed with a 6 mg/ml initial Au concentration and a 16/1 polymer/Au ratio. Here, all polymer solution was added in one step instead of iteratively.

(a)

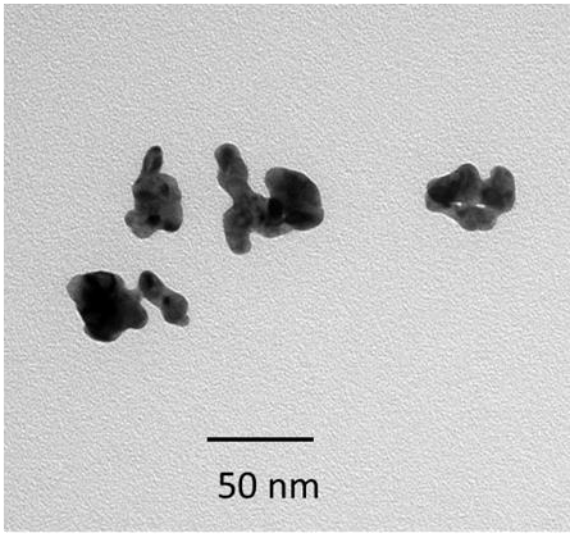

(b)

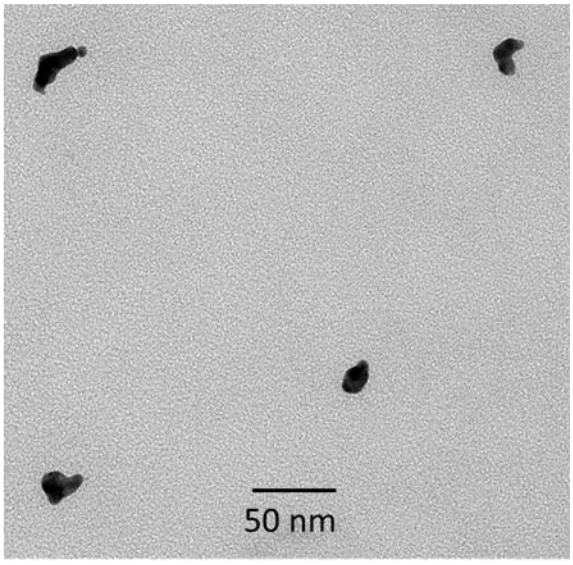

Figure C.5: TEM images showing multiple nanoclusters of (a) 20-4.0 particles and (b) 20-0.9 particles.

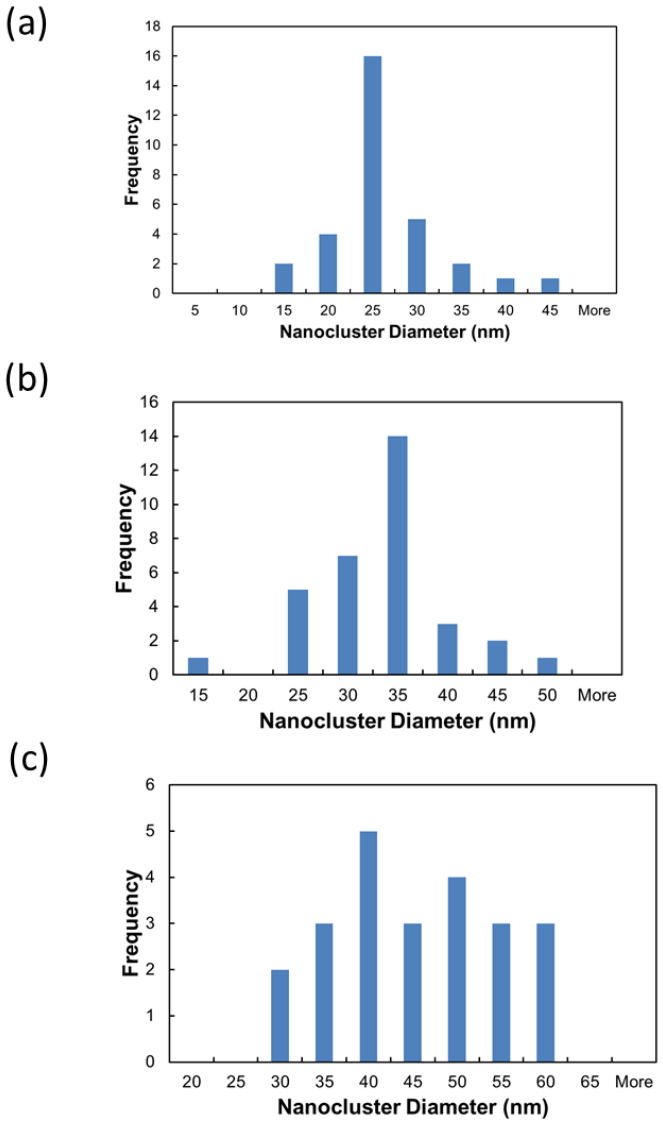

Figure C.6: Histograms of nanocluster diameters obtained from TEM image analysis of (a) 20-0.9 particles, where 31 particles were analyzed from 14 separate images from one grid (b) 20-1.7 particles, where 33 particles were analyzed from 18 separate images from one grid and (c) 20-4.0 particles, where 23 particles were analyzed from 15 separate images from one grid. TEM images were taken of clusters with discernible boundaries. Grids in all cases showed minimal unclustered particles or exceedingly large clusters (relative to the sizes shown in histograms).

(a)

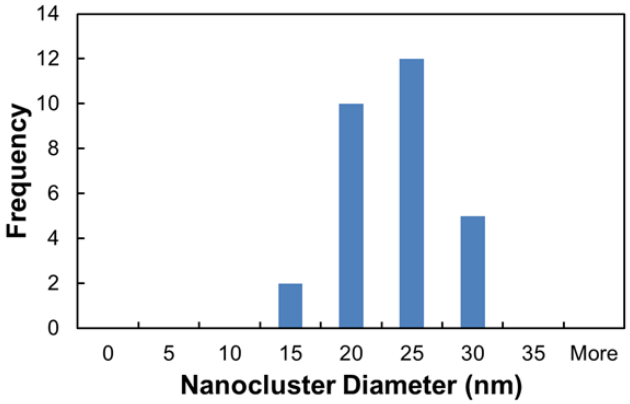

(b)

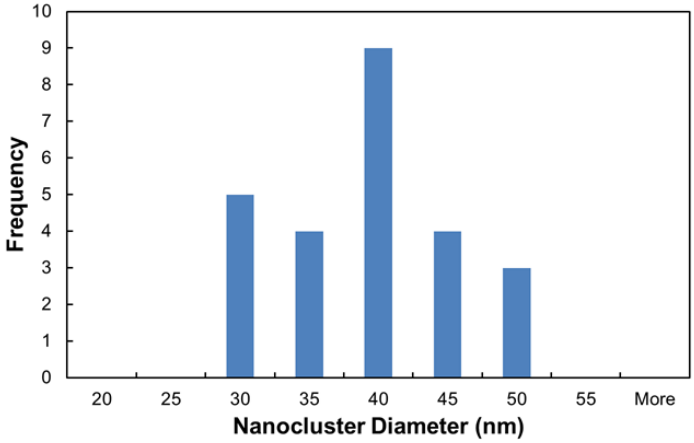

Figure C.7: Histograms obtained from TEM image analysis of (a) 10-1.7 particles, where 29 particles were analyzed from 19 separate images of one grid and (b) 50-1.7 particles, where 25 particles were analyzed from 23 separate images of one grid. TEM images were obtained in the same manner as in Figure C.6 above.

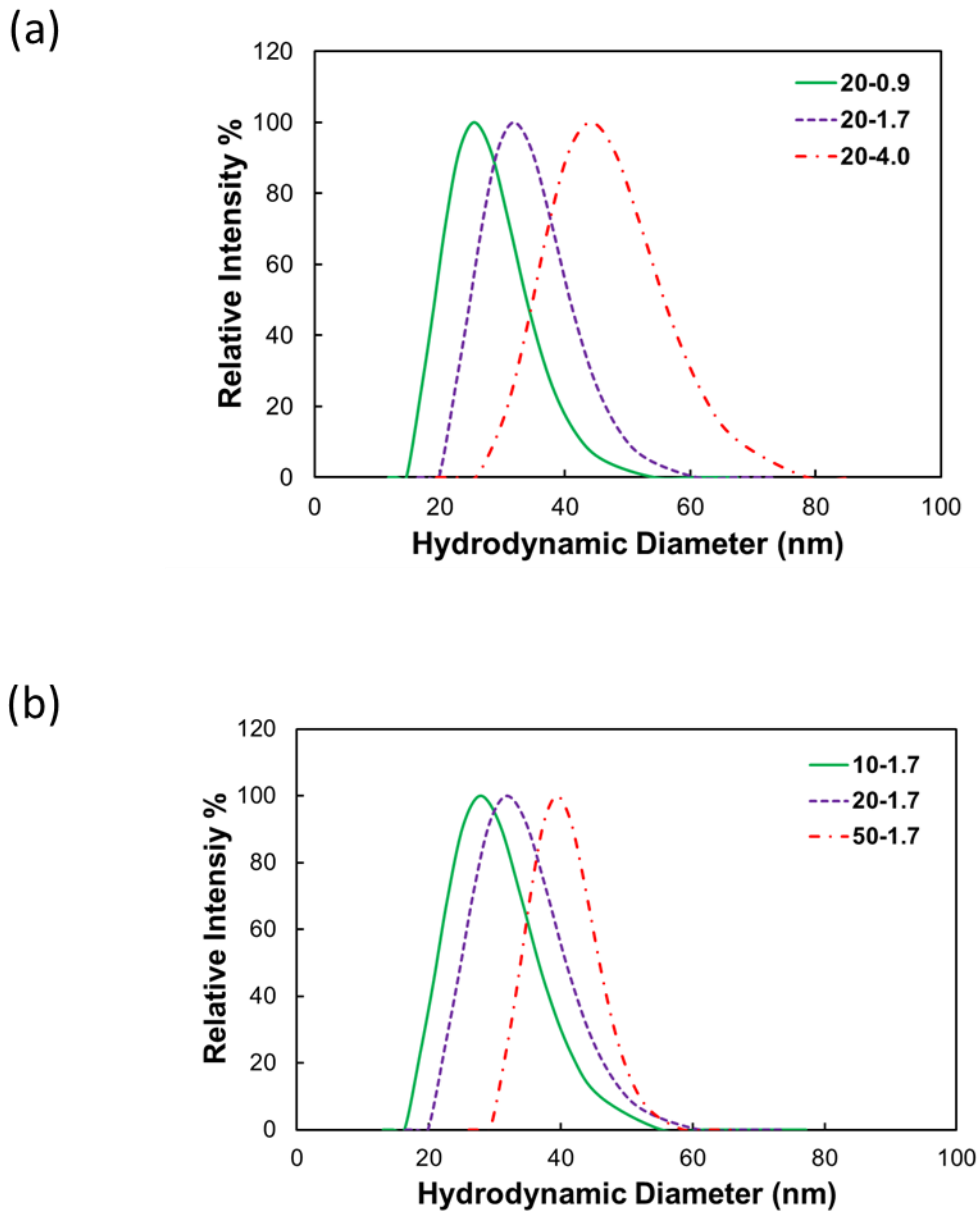

Figure C.8: Intensity-weighted DLS D_H distributions of (a) 20-0.9, 20-1.7, and 20-4.0 particles, and (b) 10-1.7, 20-1.7, and 50-1.7 particles.

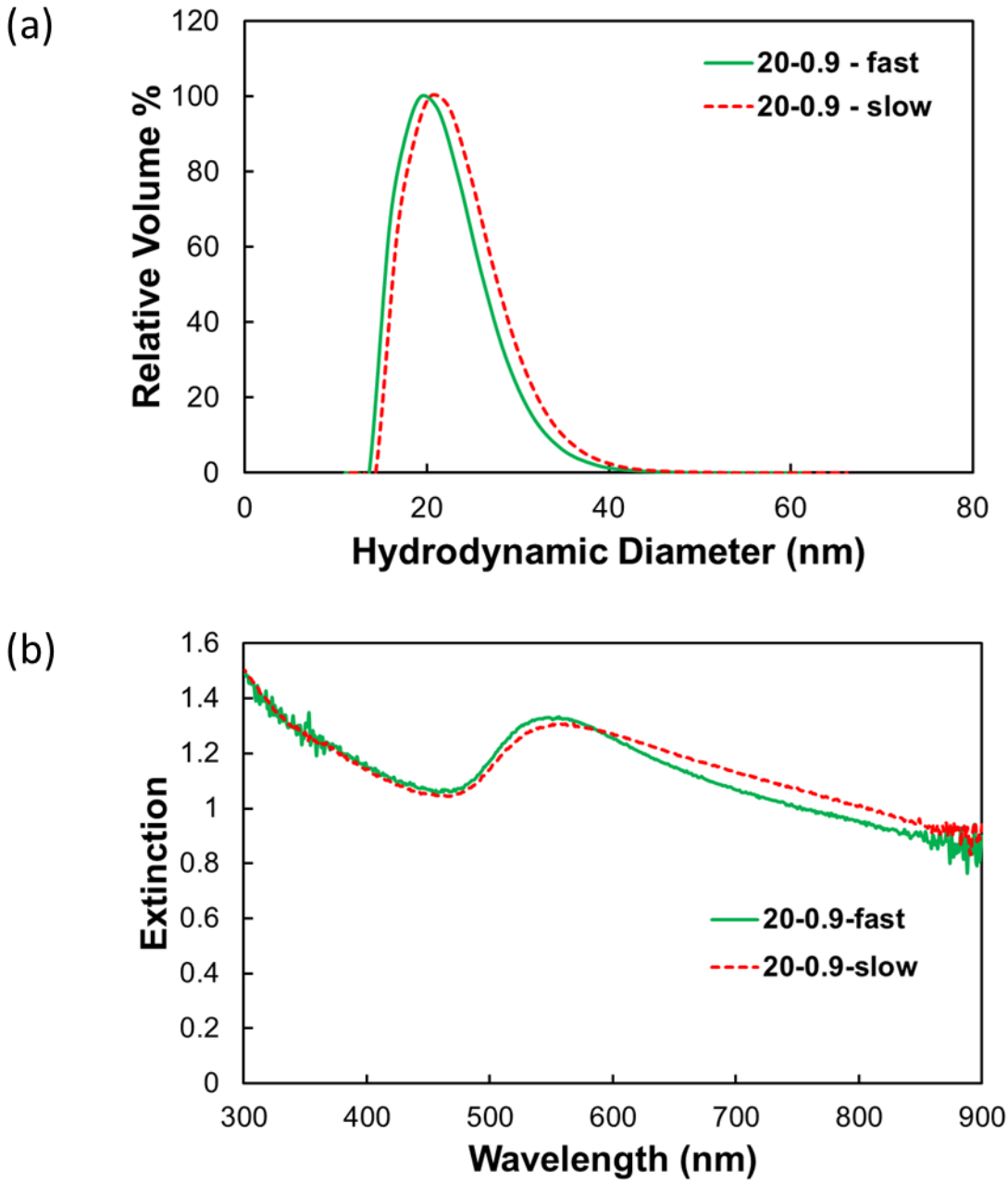

Figure C.9: (a) DLS D_H distributions and (b) UV-Vis-NIR extinction spectra for 20-0.9 particles synthesized over 40 min (fast) and 4.5 hr (slow).

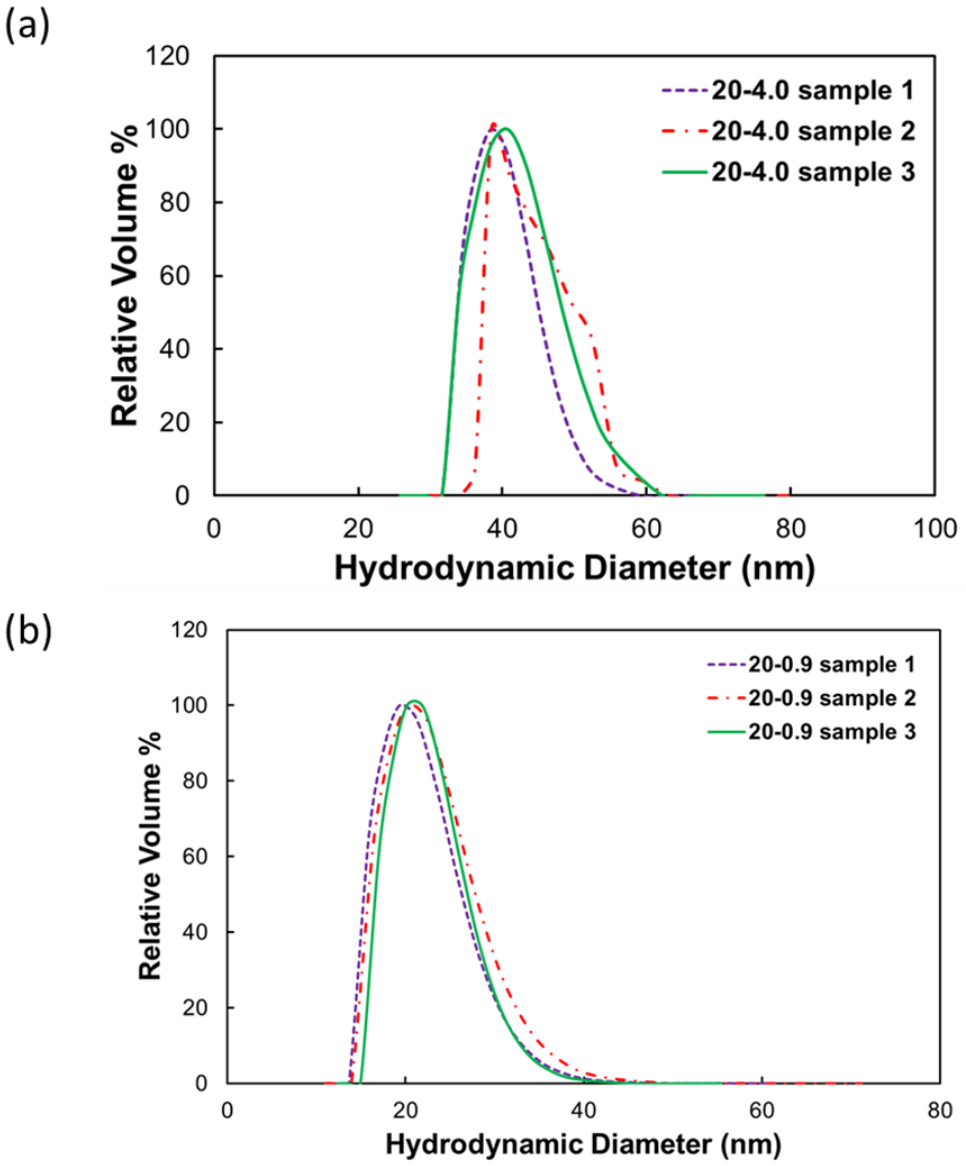

Figure C.10: Reproducibility of D_H distributions for three separate samples each of (a) 20-4.0 particles and (b) 20-0.9 particles.

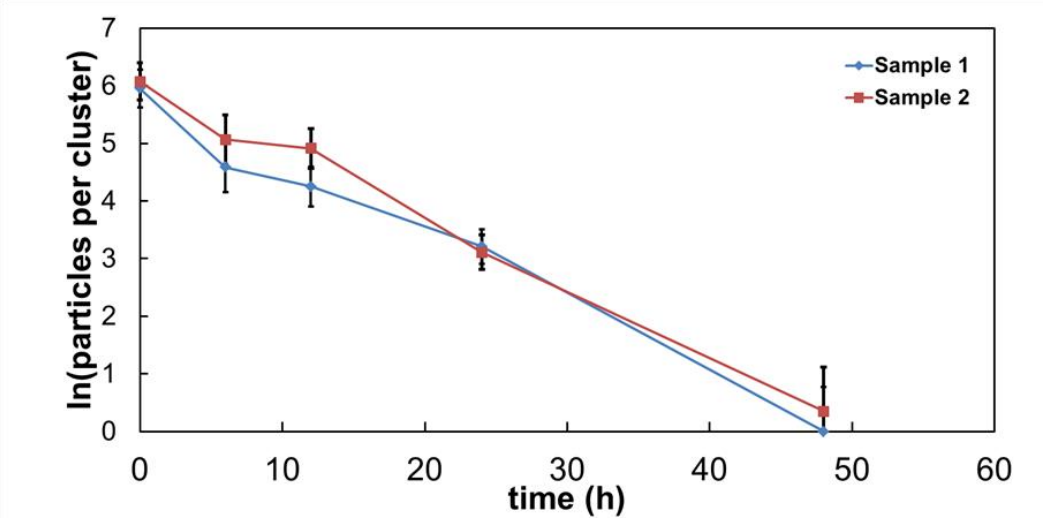

Figure C.11: Reproducibility of dissociation kinetics of 20-4.0 particles.

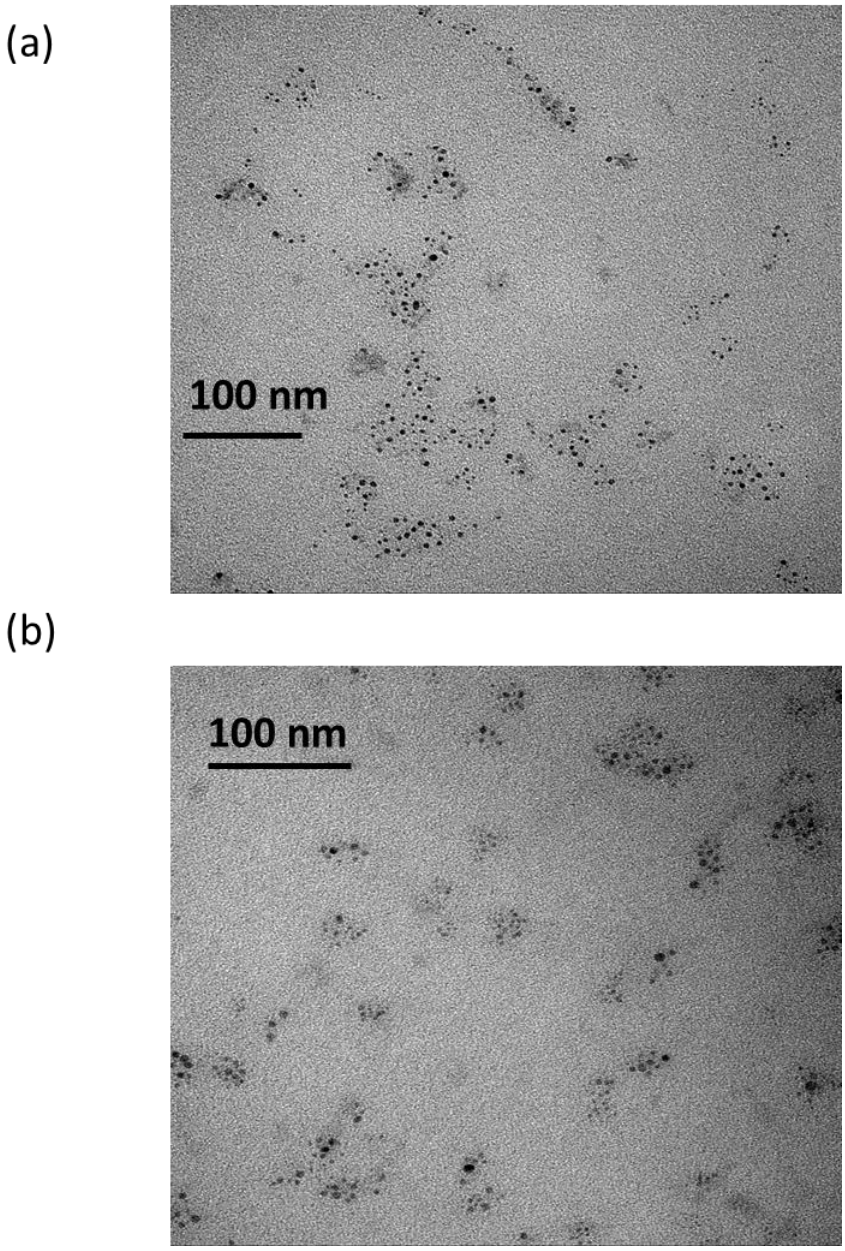

Figure C.12: TEM images of (a) Dissociated 20-4.0 particles after 48 h in pH 5 HCl and (b) dissociated 20-1.7 particles after 24 h in pH 5 HCl

Table C.1: TGA results reporting the organic mass content of 20-0.9, 20-1.7, and 20-4.0 particles, as determined from the amount of mass loss.

Sample	**Organic Mass Content (w/w)**
20-0.9	46.5%
20-1.7	50%
20-4.0	31.8%

Table C.2: Parameters used to generate theoretical size contours in Figure 4.9

Parameter	**Value**
A_{gwg} (J)	4.0×10^{-19}
Attractive VDW potential ($-a_{vdw}/k_bT$)	3.01
b (bond distance in ionic bond, nm)	0.1
σs(number of dissociable sites per particle)	2.78
R (radius of primary particle, nm)	2.0
ϵ_r (dielectric constant within nanocluster)	25

C.8 REFERENCES

1. Tam, J. M.; Tam, J. O.; Murthy, A.; Ingram, D. R.; Ma, L. L.; Travis, K.; Johnston, K. P.; Sokolov, K. V. Controlled Assembly of Biodegradable Plasmonic Nanoclusters for Near-Infrared Imaging and Therapeutic Applications. *ACS Nano* **2010**, *4*, 2178-2184.
2. Tam, J. M.; Murthy, A. K.; Ingram, D. R.; Nguyen, R.; Sokolov, K. V.; Johnston, K. P. Kinetic Assembly of Near-IR Active Gold Nanoclusters Using Weakly Adsorbing Polymers to Control the Size. *Langmuir* **2010**, *26*, 8988-8999.
3. Kunze, J.; Burgess, I.; Nichols, R.; Buess-Herman, C.; Lipkowski, J. Electrochemical Evaluation of Citrate Adsorption on Au(1 1 1) and the Stability of Citrate-Reduced Gold Colloids. *J. Electroanal. Chem.* **2007**, *599*, 147-159.
4. Bezdek, K. Circle Packings into Convex Domains of the Euclidean and Hyperbolic Plane and the Sphere. *Geometriae Dedicata* **1986**, *21*, 249-255.
5. Bozack, M. J.; Zhou, Y.; Worley, S. D. Structural Modifications in the Amino Acid Lysine Induced by Soft Xray Irradiation. *J. Chem. Phys.* **1994**, *100*, 8392-8398.
6. Watts, J. F.; Wolstenholme, J., *An Introduction to Surface Analysis by Xps and Aes*. John Wiley & Sons: West Sussex, England, 2003.
7. Hiemenz, P. C.; Rajagopalan, R., *Principles of Colloid and Surface Chemistry*. 3 ed.; Taylor & Francis: New York, 1997.
8. Israelachvili, J. N., *Intermolecular and Surface Forces*. 3 ed.; Elsevier: New York, 2011.
9. Linegar, K. L.; Adeniran, A. E.; Kostko, A. F.; Anisimov, M. A. Hydrodynamic Radius of Polyethylene Glycol in Solution Obtained by Dynamic Light Scattering. *Colloid J.* **2010**, *72*, 279-281.
10. Groenewold, J.; Kegel, W. K. Anomalously Large Equilibrium Clusters of Colloids. *J. Phys. Chem. B* **2001**, *105*, 11702-11709.
11. Johnston, K. P.; Maynard, J. A.; Truskett, T. M.; Borwankar, A. U.; Miller, M. A.; Wilson, B. K.; Dinin, A. K.; Khan, T. A.; Kaczorowski, K. J. Concentrated Dispersion of Equilibrium Protein Nanoclusters That Reversibly Dissociate into Active Monomers. *ACS Nano* **2012**, *6*, 1357-1369.
12. Harada, R.; Sugita, Y.; Feig, M. Protein Crowding Affects Hydration Structure and Dynamics. *J. Am. Chem. Soc.* **2012**, *134*, 4842-4849.
13. Despa, F.; Fernandez, A.; Berry, R. S. Dielectric Modulation of Biological Water. *Phys. Rev. Lett.* **2004**, *93*, 228104.
14. Tjong, H.; Zhou, H.-X. Prediction of Protein Solubility from Calculation of Transfer Free Energy. *Biophys. J.* **2008**, *95*, 2601-2609.

Appendix D: Quenched Assembly of NIR Active Gold Nanoclusters Capped with Strongly Bound Ligands by Tuning Particle Charge via pH and Salinity

D.1 Cysteine/Citrate Primary Nanosphere Characterization

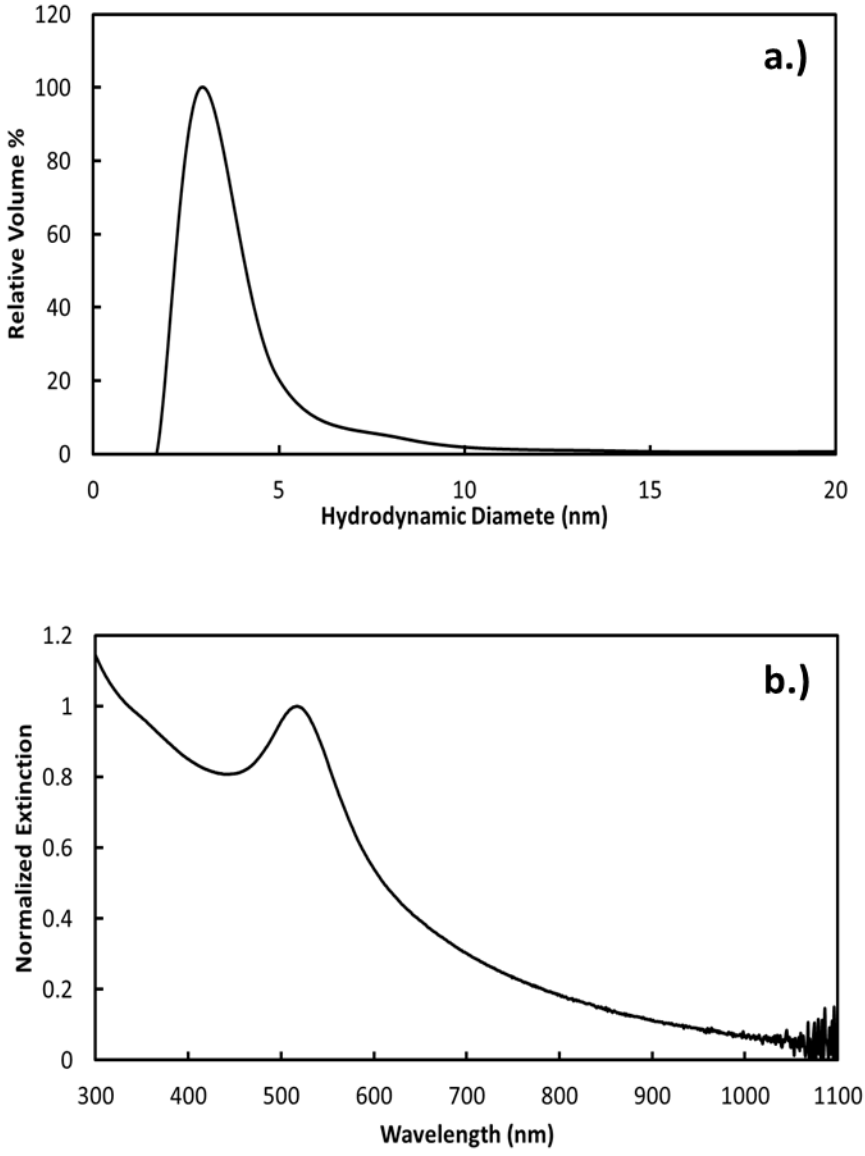

Figure D.1: (a) DLS D_h distribution and (b) UV-Vis-NIR spectrum of primary cysteine/citrate capped nanospheres used in this study.

Appendix E: Formation of Small Gold Nanoparticle Chains with High NIR-Extinction through Bridging with Calcium Ions

E.1 Figures and Tables

Table E.1: List of interaction potential parameters used to calculate $V_{electrostatic}$, V_{vdW}, $V_{bridging}$, and V_{total}.

Name	Parameter	Value
Particle Radius	a (nm)	2.5
Hamaker Constant for Water[1]	A_{water} (J)	$3.74*10^{-20}$
Hamaker Constant for Gold[2]	A_{gold} (J)	$2.50*10^{-19}$
Hamaker Constant for Gold in Water	A_{121} (J)	$9.41*10^{-19}$
Boltzmann Constant	k_B (J/K)	$1.38*10^{-23}$
Temperature	T (K)	298
Dielectric constant for vacuum	ε_0	$8.9*10^{-12}$
Relative dielectric constant of the solvent	ε_r	80
Elementary charge of electron	e (C)	$1.6*10^{-19}$
Avogadro's number	N_a (mol^{-1})	$6.02*10^{23}$
Valence of NaCl	z (NaCl)	1
Valence of CaCl2	z ($CaCl_2$)	2
Dissociation Constant for Na[3]	K_d (M) for Na	0.2
Dissociation Constant for Ca[3]	K_d (M) for Ca	0.0007
Proportionality Constant[4]	f	1.2
Ionic strength of initial Na-citrate (without added electrolyte)	I_{cit} (M)	0.025

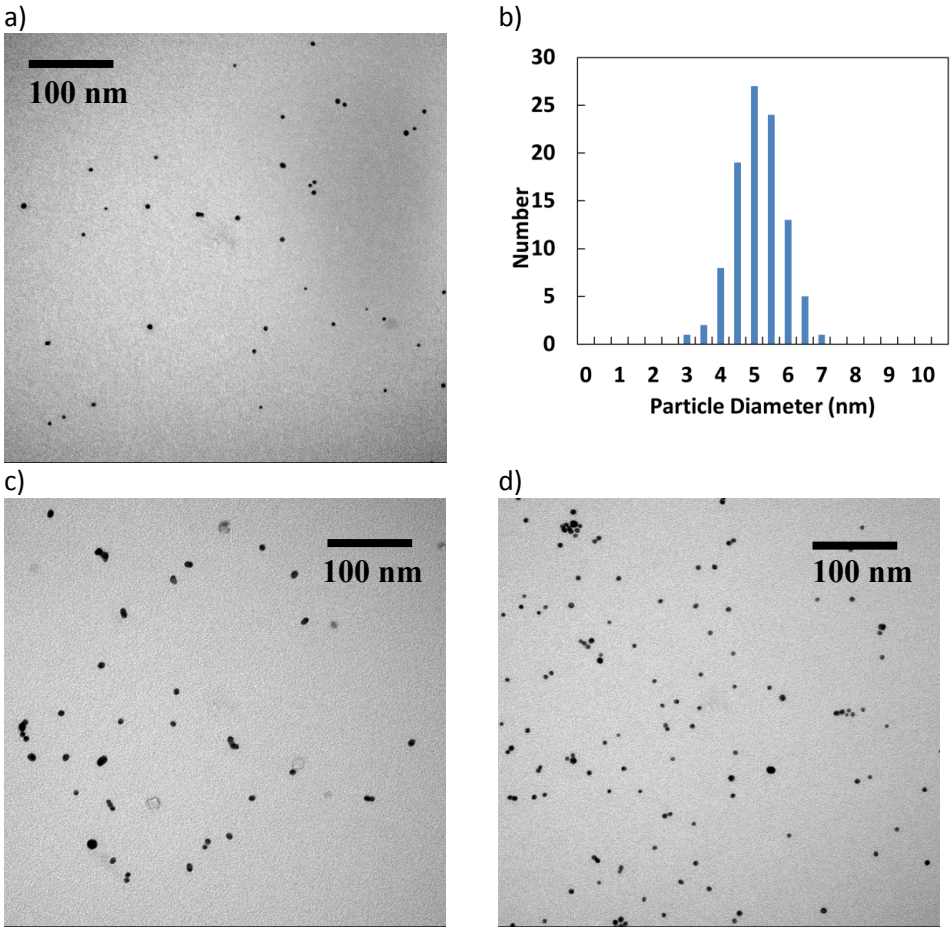

Figure E.1: TEM image of a) -45 mV, c) -34 mV, and d) -53 mV citrate-capped primary Au particles. b) TEM size distribution of -45 mV citrate-capped primary particles from a 100 particle sample size.

Table E.2: Summary of all samples detailed in this study measured immediately after being made.

Concentration (mM)	Time (s)	$A_{1000/525}$	DLS (nm)	ζ (mV)
-34 mV Citrate Particle Samples				
0.08 $CaCl_2$	30	0.023	7.2	-19.6 ± 1.1
	300	0.057	9.9	-30.7 ± 1.9
	600	0.089	14.9	
	1800	0.186	29.1	
	3600	0.257	44.03	
0.11 $CaCl_2$	1	0.023	8.7	
	300	0.213	10.4	
	600	0.301	34.7	
	1800	0.584	51.0	
	3600	0.686	57.3	
0.22 $CaCl_2$	1	0.095	4.6	
	10	0.631	18.0	
	20	0.853	21.0	
	30	1.001	22.4	-31.8 ± 1.8
	60	1.103	22.6	-26.8 ± 2.9
	120	1.180	32.7	
	180	1.154	36.7	
	600	1.040	78.2	
	1800	1.098	459.2	
	3600	0.983	615.2	
0.30 $CaCl_2$	1	0.101	19	
	300	1.094	35	
	600	1.035	55	
	1800	1.008	66	
	3600	1.004	Aggr	
25 NaCl	1	0.03	9.4	
	300	0.02	15.12	
	600	0.02	12.6	
	1800	0.04	18.1	
50 NaCl	30	0.02	16.4	-36.0 ± 3.1
	300	0.37	465.01	-46.9 ± 0.8
	600	0.32	630.87	
	1800	0.05	Aggr	

Table E.2, cont: Summary of all samples detailed in this study measured immediately after being made.

75 NaCl	1	0.44	26.7	
	2	0.52	53.4	
	3	0.62	66.7	
	4	0.64	73.9	
	5	0.97	107.8	
	10	0.94	150.2	
	20	0.92	187.4	
	30	1.00	369.4	-27.6 ± 1.8
	60	1.05	497.9	
100 NaCl	1	0.87	75.8	
-45 mV Citrate Particle Samples				
0.05 $CaCl_2$	1	0.029	6.0	
	300	0.033	7.6	
	600	0.032	5.1	
	1800	0.055	12.3	
	3600	0.146	16.0	
0.08 $CaCl_2$	30	0.028	7.7	29.0 ± 1.6
	300	0.092	15.6	-33.2 ± 1.5
	600	0.136	25.8	
	1800	0.231	31.3	
	3600	0.348	46.0	
0.22 $CaCl_2$	1	0.518	20.2	
	30	0.598	25.0	-31.8 ± 1.3
	60	0.679	33.4	
	120	0.748	37.6	
	180	0.791	41.0	
	300	0.798	53.0	-23.9 ± 4.0
	600	0.821	67.4	
	1800	0.850	57.2	
	7200	0.880	109.0	
0.22 $Ca(NO_3)_2$	1	0.66	36	
	300	1.08	51	
	600	1.03	64	
	1800	1.00	86	
	3600	Aggr	Aggr	
0.50 $CaCl_2$	1	0.792	33	
	300	0.910	229	
	600	Aggr	Aggr	

Table E.2, cont: Summary of all samples detailed in this study measured immediately after being made.

25 NaCl	1	0.01	8.3	
	300	0.03	14.3	
	600	0.01	14.9	
	1800	0.02	15.22	
50 NaCl	30	0.01	26	
	300	0.28	180.3	-40.4 ± 1.9
	600	0.22	605.1	-43.4 ± 0.6
	1800	0.02	Aggr	
75 NaCl	1	0.16	50.9	
	2	0.34	48.0	
	3	0.37	53.2	
	4	0.40	68.3	
	5	0.60	140.9	
	10	0.70	198.5	
	20	0.80	171.6	
	30	0.82	243.2	-36.0 ± 2.9
	60	0.84	679.2	
100 NaCl	1	0.49	61.5	
-53 mV Citrate Particle Samples				
0.22 $CaCl_2$	1	0.026	6.7	
	300	0.042	6.6	
	600	0.014	5.8	
	1800	0.034	12.6	
	3600	0.028	16.9	
1.50 $CaCl_2$	1	0.040	5.3	
	300	0.075	10.2	
	600	0.105	35.7	
	1800	0.145	44.1	
	3600	0.185	48.3	
2.10 $CaCl_2$	1	0.278	22.8	
	300	0.988	133.6	
	600	1.001	331.0	
	1800	1.008	875.4	
	3600	0.791	242.7	

Table E.2, cont: Summary of all samples detailed in this study measured immediately after being made.

-35 mV (6x Washed from As-Prepared) Citrate Particle Samples				
0.22 $CaCl_2$	1	0.070	9.1	
	10	0.756	17.6	
	20	0.861	18.4	
	30	1.062	18.0	
	60	1.180	21.8	
	120	1.164	28.5	
	600	1.187	46.6	

Table E.3: $A_{1000/525}$ and D_H stability of nanoclusters made at pH 7 under different $CaCl_2$ and 75 mM NaCl concentrations after 5x dilution in DI water immediately after formation and after aging at RT for 20 days.

	Initial		20 Days	
Sample	**$A_{1000/525}$**	**DLS (nm)**	**$A_{1000/525}$**	**DLS (nm)**
-34 mV_0.22 mM $CaCl_2$_120s	1.180	22.4	0.916	32.0
-34 mV_0.22 mM $CaCl_2$_300s	1.154	48.2	1.049	57.5
-34 mV _75 mM NaCl_2s	0.52	53.4	0.467	441.2
-45 mV _0.22 mM $CaCl_2$_120s	0.679	37.6	0.692	28.0
-45 mV _0.22 mM $CaCl_2$_300s	0.835	49.5	0.816	46.9
-53 mV -Cit_1.5 mM CaCl2_300s	0.054	8.0	0.114	10.2

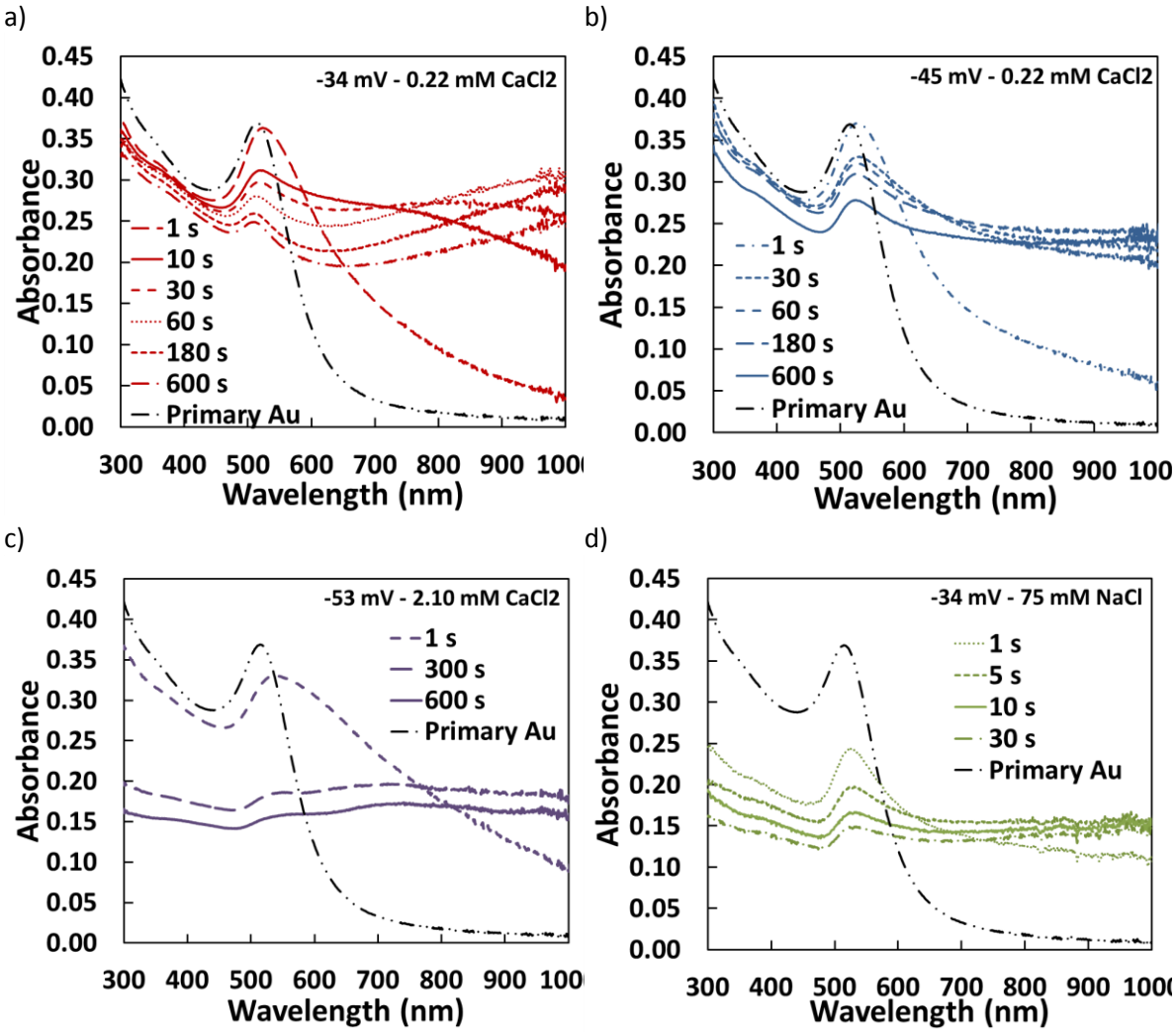

Figure E.2: Non-normalized UV-vis-NIR absorbance spectra in the presence of 0.22 mM $CaCl_2$ for a) -34 mV, and b) -45 mV, and c) -53 mV primary citrate particles, in this case with 2.1 mM $CaCl_2$. d) UV-vis-NIR spectra for -34 mV citrate made with 75 mM NaCl.

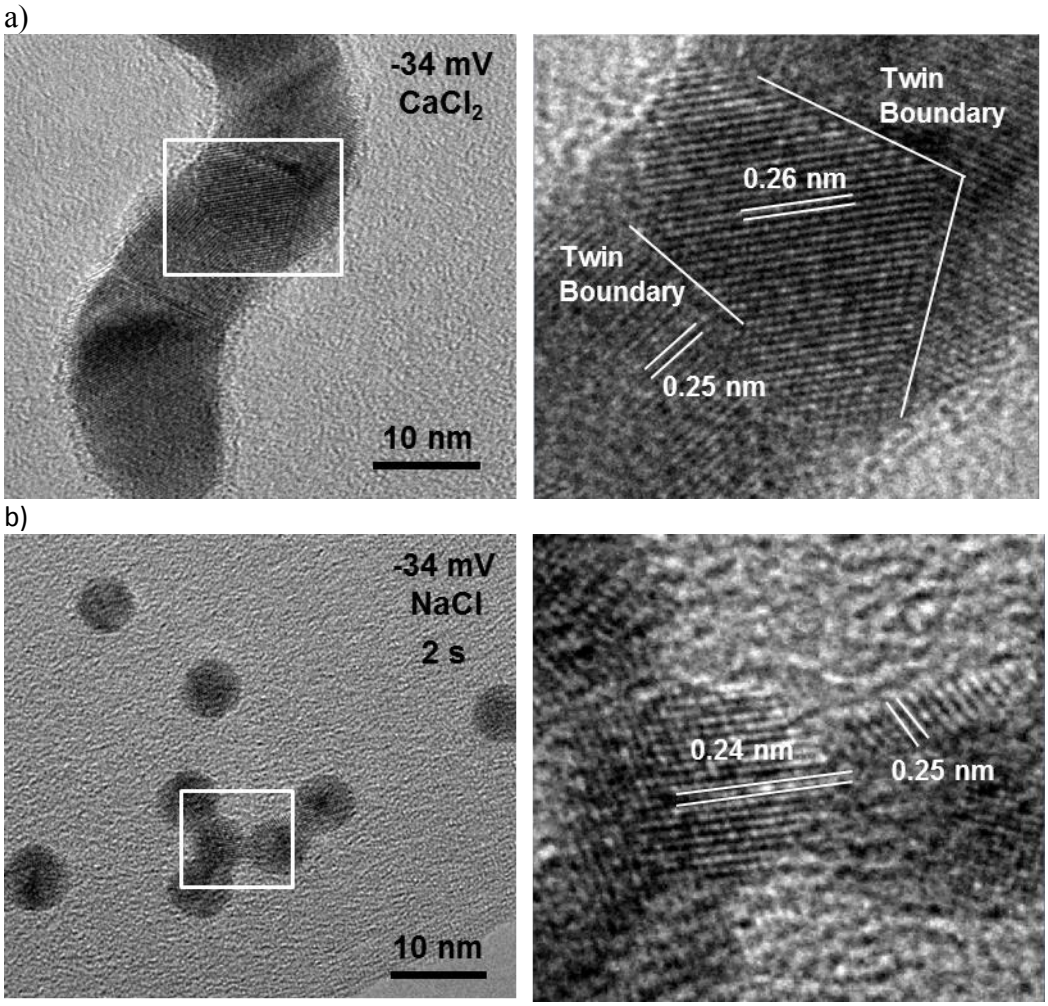

Figure E.3: High-Res TEM images of samples indicating fusion between -34 mV primary particles with a) 0.22 mM $CaCl_2$ at 2 s, (b) 75 mM NaCl at 2. Lattice spacings were measured using image J analysis of the images as shown.

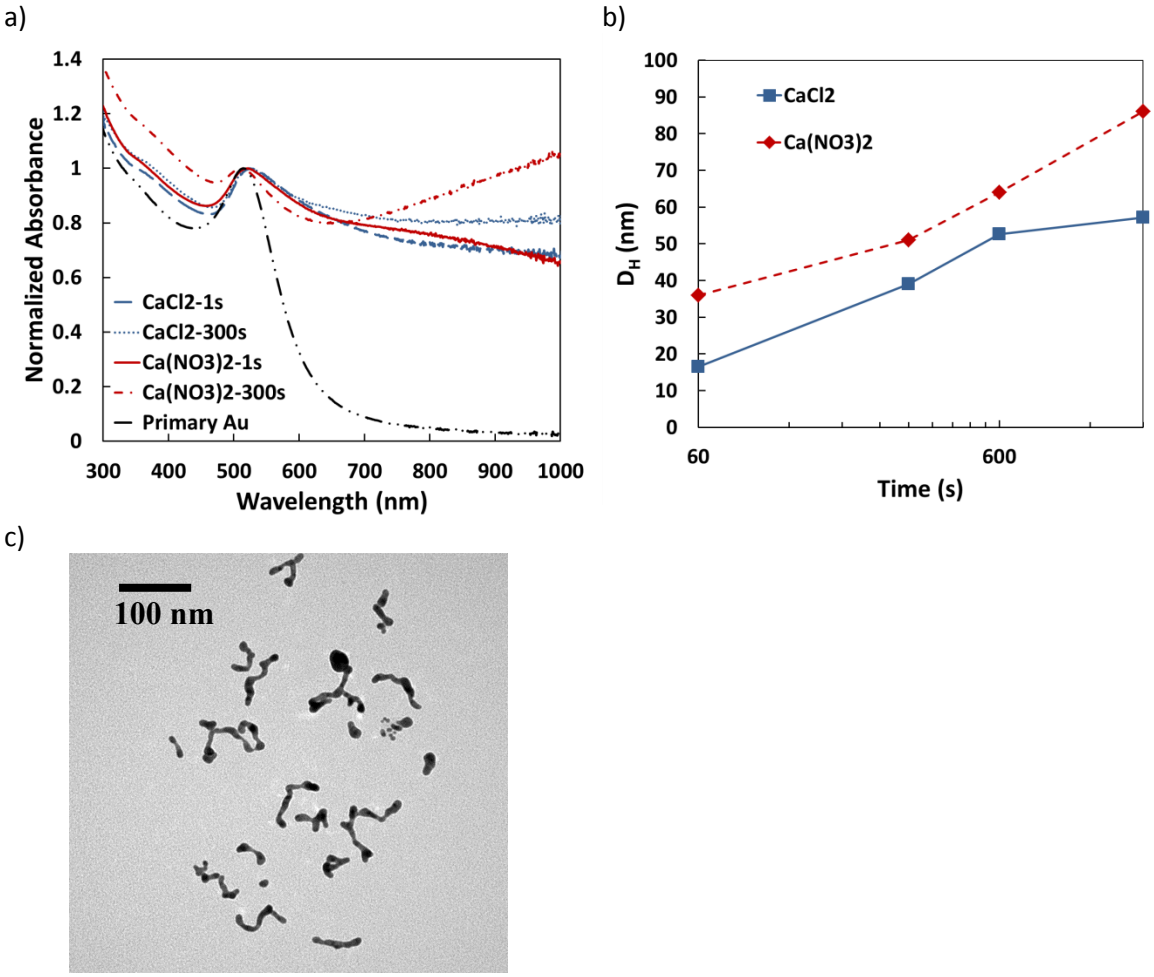

Figure E.4: a) UV-vis-NIR absorbance and b) hydrodynamic diameter of clusters made from -45 mV citrate with 0.22 mM $CaCl_2$ or $Ca(NO_3)_2$ and harvested at various time points. C) TEM image of clusters made with $Ca(NO_3)_2$ after 1800 s.

Table E.4: Images taken from videos of cluster formation from -34 mV and -45 mV Citrate-Au primary particles assembled in the presence of NaCl

Row #	NaCl Conc (mM)	-45 mV Citrate
1	50	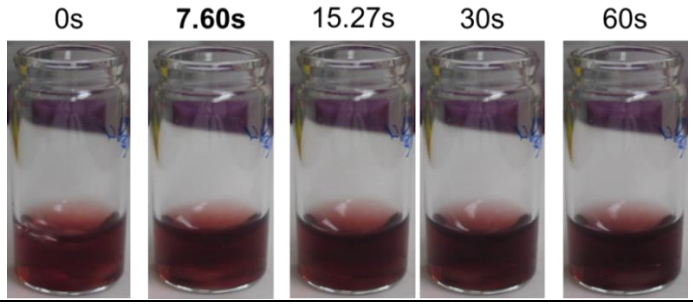
2	75	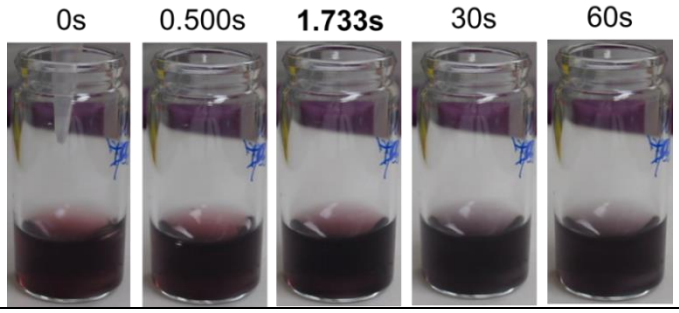
	NaCl Conc (mM)	**-34 mV Citrate**
3	50	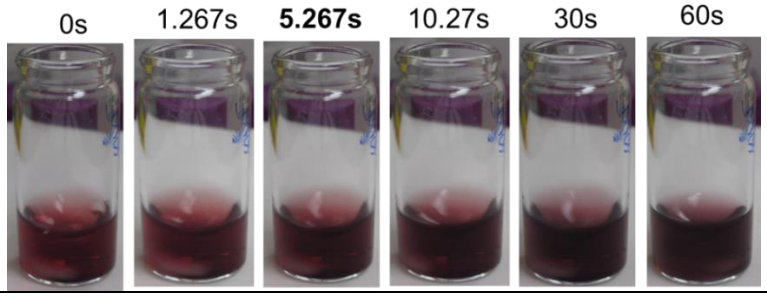
4	75	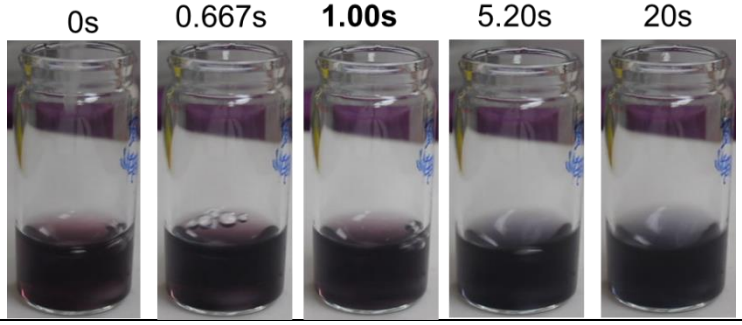

Table E.5: Images taken from videos of cluster formation from -34 mV and -45 mV Citrate-Au primary particles assembled in the presence of $CaCl_2$.

Row #	$CaCl_2$ Conc (mM)	-45 mV Citrate
1	0	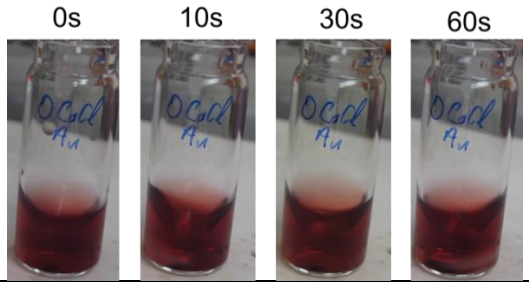
2	0.08	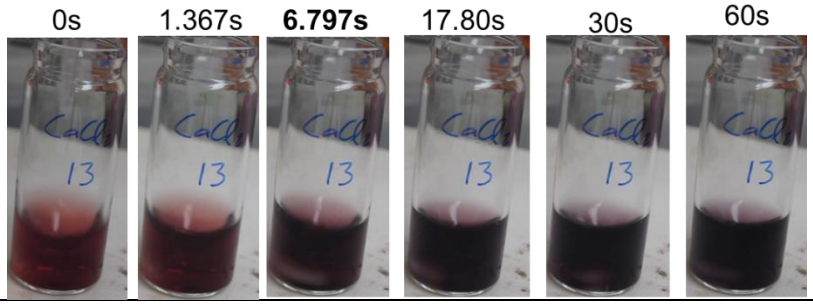
3	0.22	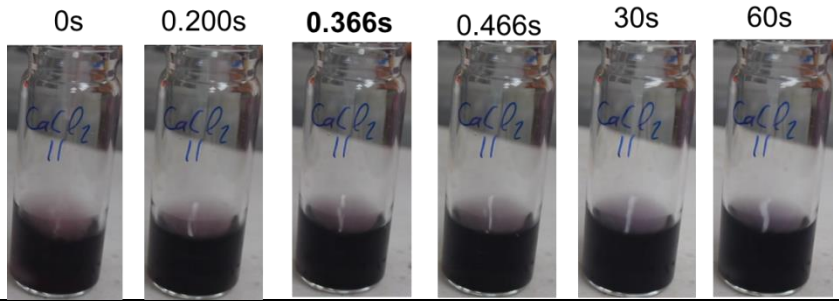
	$CaCl_2$ Conc (mM)	**-34 mV Citrate**
4	0.22	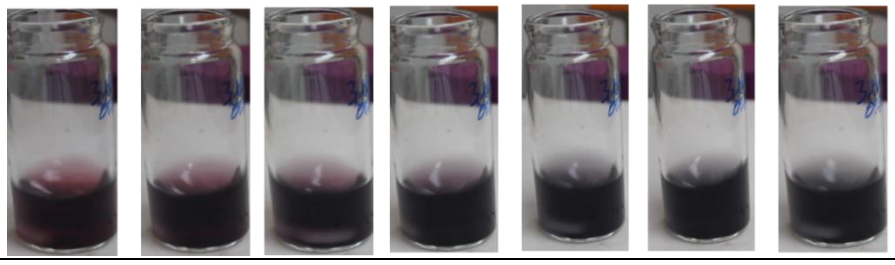

Table E.5, cont.: Images taken from videos of cluster formation from -34 mV and -45 mV Citrate-Au primary particles assembled in the presence of $CaCl_2$.

	$CaCl_2$ Conc (mM)	**-53 mV Citrate**
5	0.22	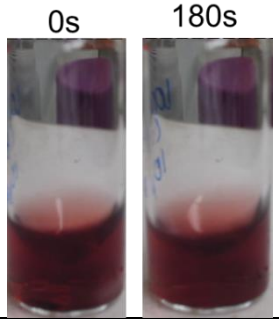
6	1.50	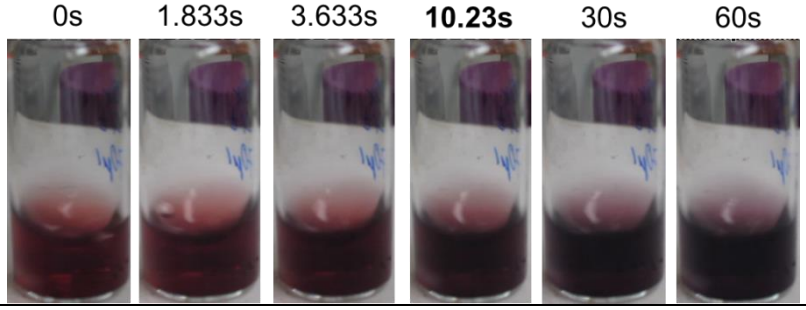
7	2.10	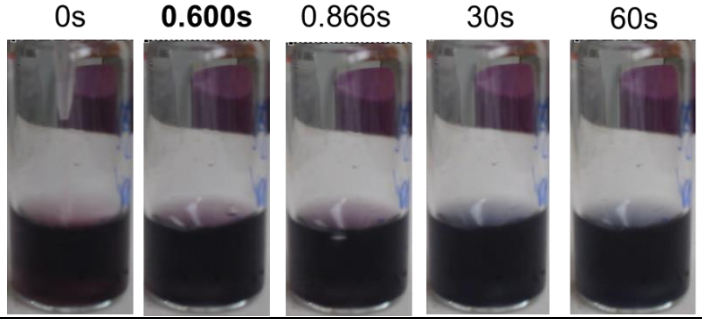

Table E.6: Representative TEM images of samples presented throughout the paper. In all cases the scale bar is 100 nm, expect where noted.

Row #	Sample	Representative TEM 1	Representative TEM 2	Representative TEM 3
1	-34 mV 0.08m M $CaCl_2$ 300 s	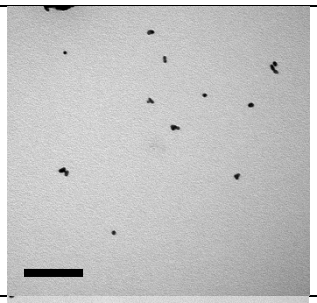	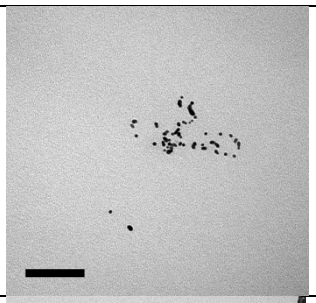	
2	-34 mV 0.08m M $CaCl_2$ 1800 s	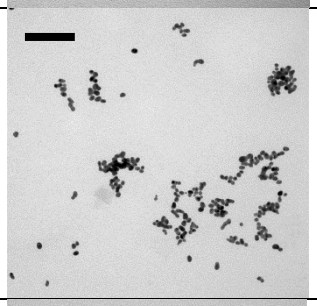	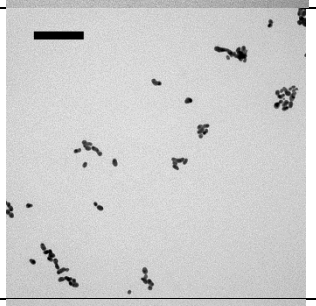	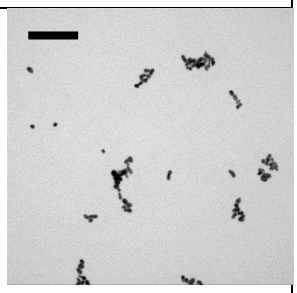
3	-34 mV 0.22m M $CaCl_2$ 10 s	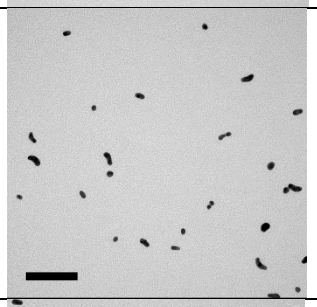	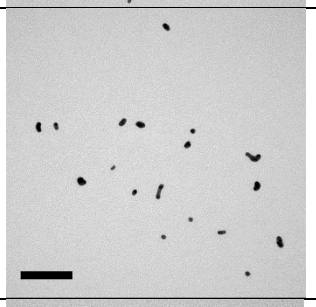	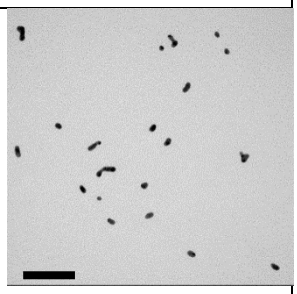
4	-34 mV 0.22m M $CaCl_2$ 30 s	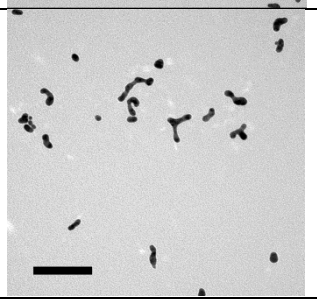	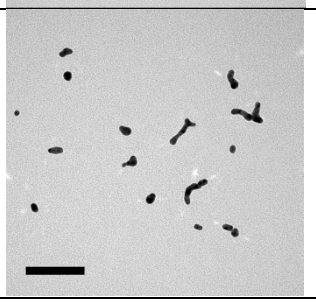	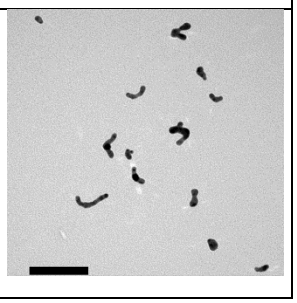

Table E.6, cont.: Representative TEM images of samples presented throughout the paper. In all cases the scale bar is 100 nm, expect where noted.

5	-34 mV 0.22mM $CaCl_2$ 60 s	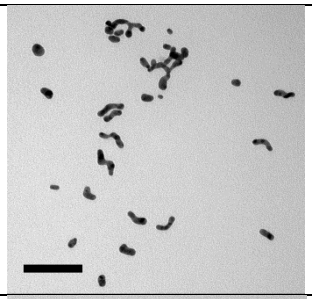	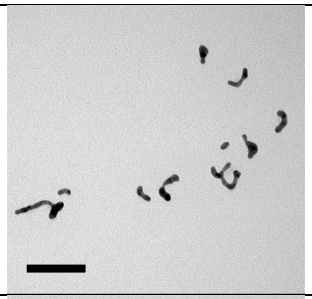	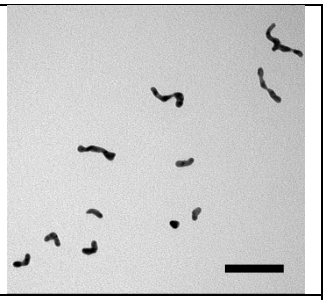
6	-34 mV 0.22mM $CaCl_2$ 120 s	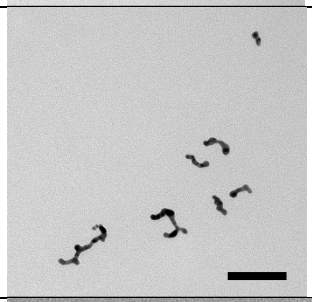	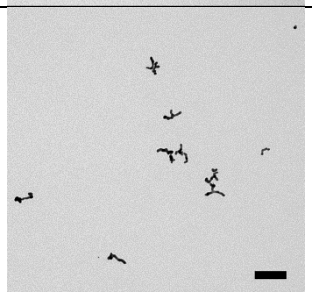	
7	High Res -34 mV 0.22mM $CaCl_2$ 120 s	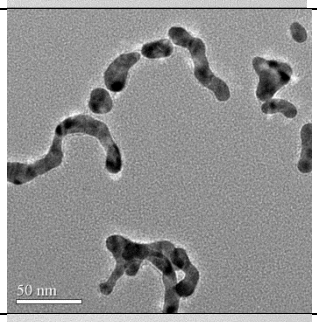	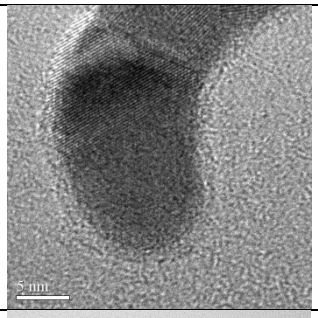	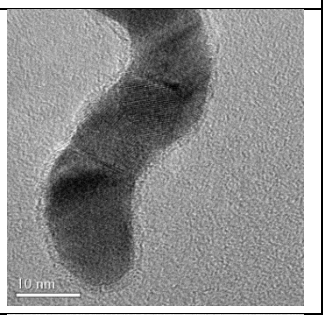
8	-34 mV 0.22mM $CaCl_2$ 1800 s	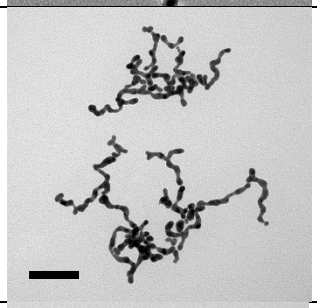	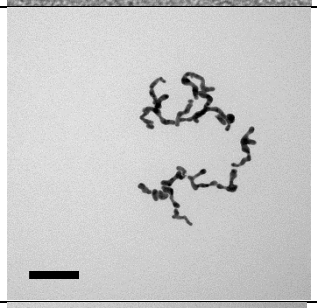	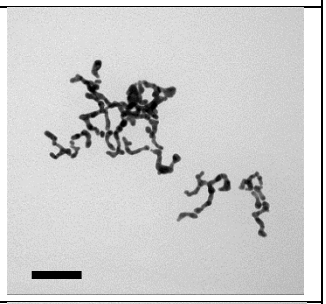
9	-45 mV 0.22mM $CaCl_2$ 120 s	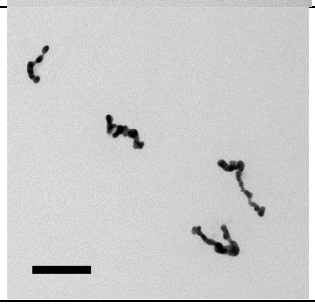	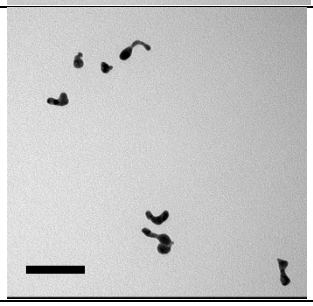	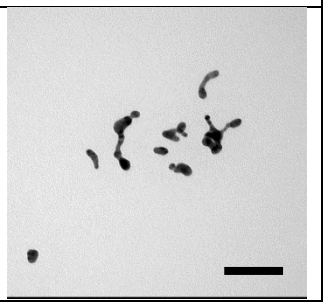

Table E.6, cont.: Representative TEM images of samples presented throughout the paper. In all cases the scale bar is 100 nm, expect where noted.

10	-53 mV 1.50 mM $CaCl_2$ 3600 s Scale Bars = 50 nm	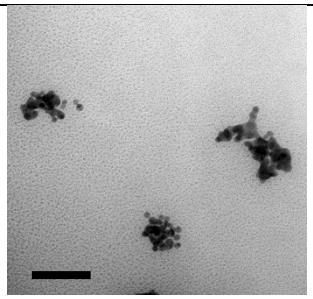	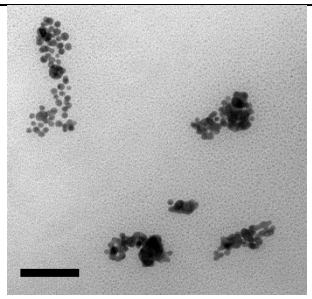	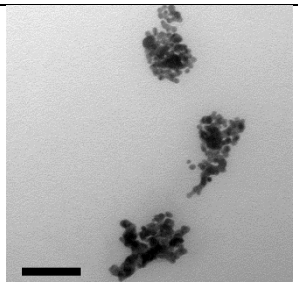
11	-34 mV 50 mM NaCl 120 s	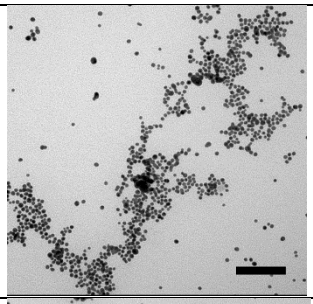	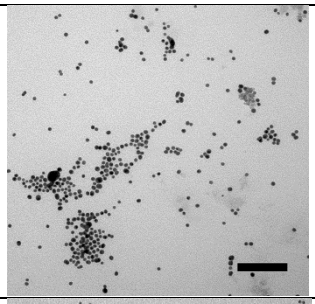	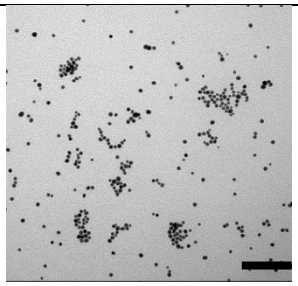
12	-34 mV 75 mM NaCl 2 s	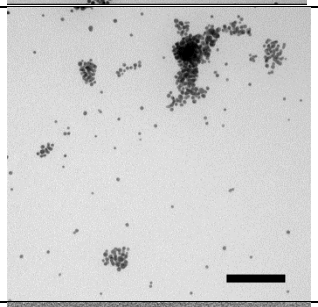	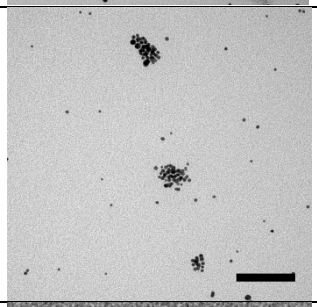	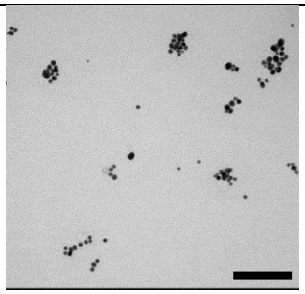
13	High Res -34 mV 75 mM NaCl 2 s	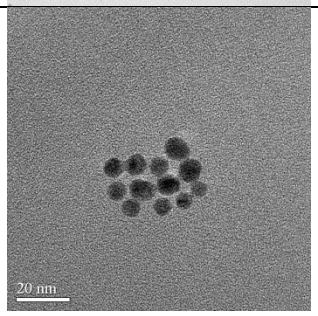	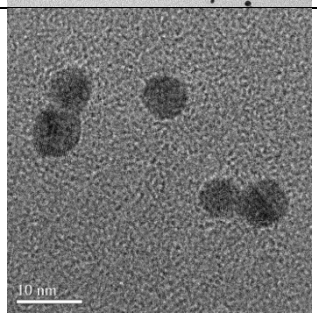	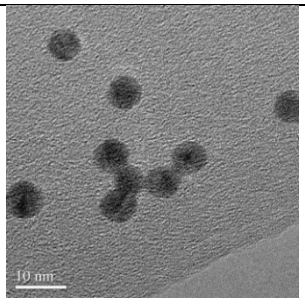

Table E.6, cont.: Representative TEM images of samples presented throughout the paper. In all cases the scale bar is 100 nm, expect where noted.

14	-34 mV 75 mM NaCl 30 s	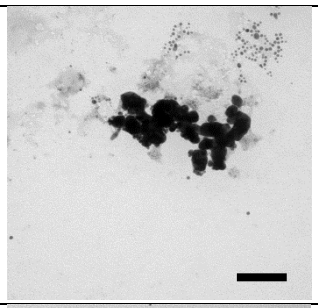	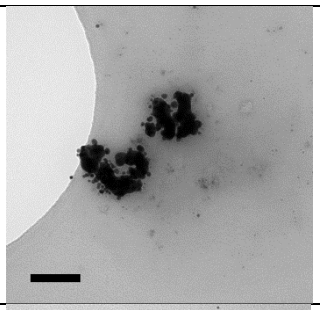	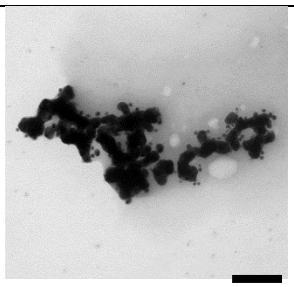
15	-45 mV 75 mM NaCl 2 s	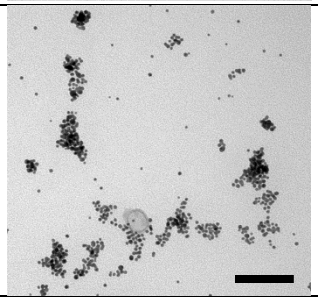	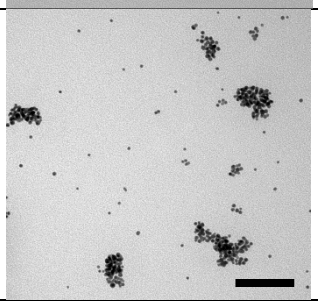	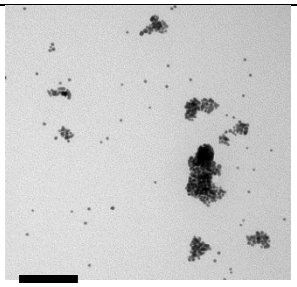

Table E.7: DLS D_H intensity-weighted distributions, TEM number average diameters from the sizing of 100 particle samples, and the resulting TEM number-weighted distribution histograms for select samples

Row #	Sample	DLS Intensity-Weighted Distr. (nm)	TEM Number Average (nm)	TEM Number-Weighted Histogram
1	-34 mV_ 0.22mM $CaCl_2$_10s	18-34 (100%)	16.2 ± 8.8	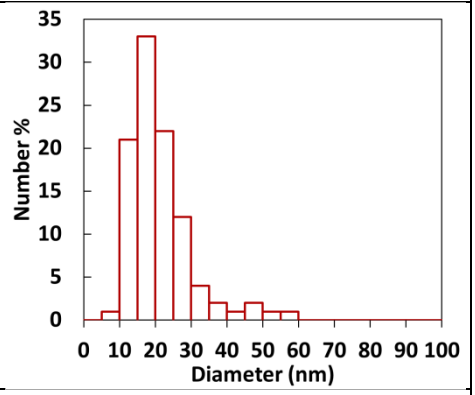
2	-34 mV_ 0.22mM $CaCl_2$_30s	22-38 (100%)	24.3 ± 14.3	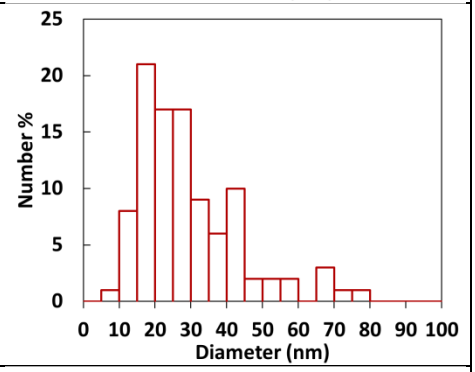
3	-34 mV_ 0.22mM $CaCl_2$_60s	23-45 (100%)	30.5 ± 17.2	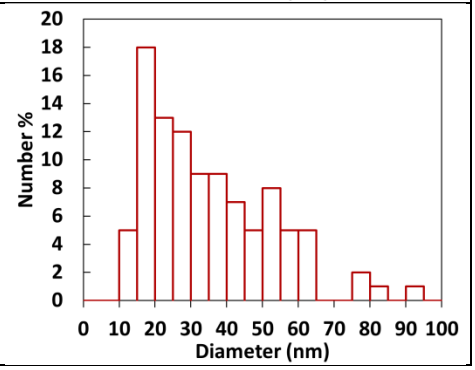

Table E.7, cont.: DLS D_H intensity-weighted distributions, TEM number average diameters from the sizing of 100 particle samples, and the resulting TEM number-weighted distribution histograms for select samples

4	-45 mV_ 0.22mM $CaCl_2$_30s	25-49 (100%)	25.9 ± 10.7	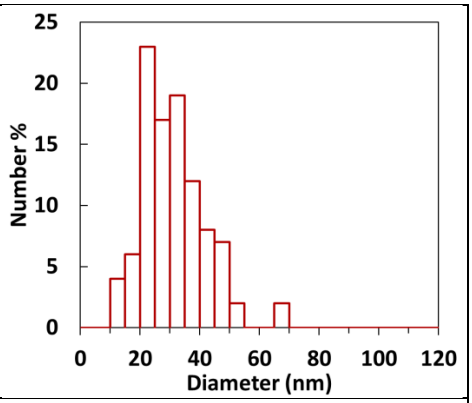
5	-45 mV_ 0.22mM $CaCl_2$_60s	4-29 (11%) 33-69 (89%)	33.8 ± 19.5	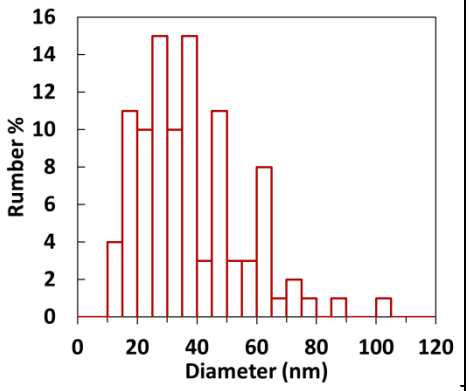
6	-45 mV_ 0.22mM $CaCl_2$_180s	4-32 (13%) 38-80 (87%)	39.5 ± 22.1	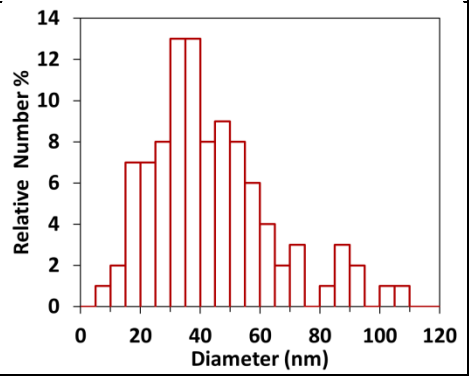

Table E.7, cont.: DLS D_H intensity-weighted distributions, TEM number average diameters from the sizing of 100 particle samples, and the resulting TEM number-weighted distribution histograms for select samples

7	-34 mV_ 75mM NaCl_2s	3-22 (20%) 27-56 (53%) 117-170 (17%)	19.9 ± 17.5	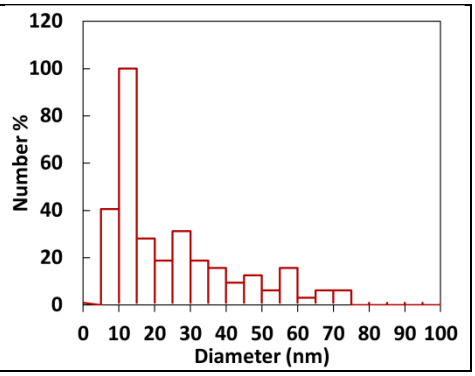

E.2 REFERENCES

1. Götzinger, M.; Peukert, W. Dispersive forces of particle–surface interactions: direct AFM measurements and modelling. Powder Technol. 2003, 130, 102-109.
2. Kim, T.; Lee, K.; Gong, M.-s.; Joo, S.-W. Control of Gold Nanoparticle Aggregates by Manipulation of Interparticle Interaction. Langmuir 2005, 21, 9524-9528.
3. Walser, M. Dissociation constants for complexes of citrate with sodium, potassium, calcium, and magnesium ions. The Journal of Physical Chemistry 1961, 65, 159-161.
4. Wang, D.; Tejerina, B.; Lagzi, I.; Kowalczyk, B.; Grzybowski, B. A. Bridging interactions and selective nanoparticle aggregation mediated by monovalent cations. ACS Nano 2010, 5, 530-536.

Appendix F: New Perspectives on Nanocluster Dissociation

F.1 Discussion

In chapter 3 of this thesis, "biodegradation" was characterized by the nearly complete loss of absorbance in the NIR region and decrease in the hydrodynamic size of nanoclusters back to primary spheres as seen in Figure 3.7. However, new results observed through the process of data collection and writing of Ch. 5 have cast some doubt regarding the accuracy of the DLS data in these tests. Firstly, these experiments were said to be run in pH 5 HCl. However, these solutions were tested with low-accuracy CardinalHealth pH indicator strips at the time which carries an uncertainty of ~ 1-2 pH units. Since then, low pH solutions were measured universally by a Mettler Toledo inLab Micro pH probe with accuracy down to the hundredth of a pH unit. This meter has revealed that previously used "pH 5" acid solutions may have actually been closer to pH 3. Additionally, lysine/citrate nanoclusters showed more full dissociation via UV-vis-NIR measurements in accurately-measured pH 3 HCl solutions than at pH 5, suggesting pH 3 was used in the experiments in Ch. 3 (Figure F.1a). These clusters were made by lowering the pH of 0.3 mg/mL 9/1 lysine/citrate Au particles to pH 3 and quenching back to pH 7 with 5:1 poly:Au within 1 second before lowering the pH of the solutions once again with HCl for dissociation testing. Hydrodynamic diameter measurements however did not support dissociation as the intensity-weighted DLS sizes were similar in both pH 5 and pH 3 solutions after 24 hrs (Figure F.1b). Furthermore, in light of the findings in chapter 5, where direct evidence of particle fusion upon clustering occurs resulting in high-NIR, doubt now exists as to if citrate-capped nanoclusters can fully dissociate– consistent with the DLS results in Figure F.1a. If high-NIR extinction is indeed the result of fusion between nanoparticles, then reversibility of these clusters should not be possible.

While definitive high-resolution TEM (HR-TEM) evidence is not available to prove the nanoclusters in Ch. 3 were indeed fused, low-res TEM images of the clusters

made from evaporation closely resemble the fused structures made from CaCl2 addition (Figure F.2a,b). Additionally, both clusters have similar NIR-extinction which could further suggest fusion, as is detailed in Ch. 5. Thus, if the clusters assembled in Ch. 3 were fused, then the dissociation behavior observed could be due to a number of misinterpretations. Firstly, the nearly complete reversibility of the UV-vis-NIR extinction back to that of primary nanospheres for the clusters incubated in pH 3 HCl could be due to changes in cluster morphology instead of dissociation. Studies on gold nanostars have demonstrated that halide ions can cause structural reorganization toward spheres.1 Similarly, TEM analysis of the 20-1.7 nanoclusters from Ch. 3 after 48 hr exposure to low pH HCl reveals populations of particles which are significantly more spherical than their original clustered state (Figure F.3a). This change in morphology to more symmetrical 30-50 nm nanospheres could result in a drop in NIR extinction to resemble that of the primary 5 nm spherical primary nanospheres. A complication of this theory arises due to the hundreds of ~3-5 nm primary particles which are also observable on these same TEM images (Figure F.3b). This indicates either true nanocluster dissociation or a complex renucleation phenomenon which could result from residual gold nuclei in solution undergoing reduction from excess citrate or NaBH4 and causing re-nucleation.

An additional error in these tests could be due to inaccurate DLS analysis of the dissociating nanoclusters. Asymmetry in gold nanoparticles can lead to "phantom" DLS peaks at small sizes due to the software's inability to decipher between rotational and translational diffusion.2 In the Brookhaven software used for testing, only models for spherical objects were available. As a result of this complication, NNLS DLS peaks at ~ 5 nm sizes were present in nearly every sample of our asymmetric clusters (Figure F.4a). Therefore, as these sizes seemed unreasonable given the high-NIR extinction of the clusters being measured, non-traditional methods for fitting DLS ACF curves were applied to attempt to give more reasonable sizing values (Figure F.4b). In this method, the "baseline" of the ACF was fit at differing points along the ACF decay such that the low part of the curve was fit well, while disregarding the long decay times (Figure F.4c). As this method appeared to allow more reasonable volume-weighted size distributions for

high-NIR absorbing clusters, these methods were applied throughout Ch. 2-3; including the cluster dissociation. This method likely led to inaccurate results in hydrodynamic sizes over time. This led to our inaccurate belief that we had full dissociation of our clusters via DLS analysis. Accurate fitting methods involve using the "auto-fit" function available on the DLS software for fitting the NNLS, intensity-weighted distributions. This methodology was used for all of Ch. 4-5, as well as in Appendix A. Recently, these same data were re-fit using an accurate fitting technique and the results are shown in Table F.1, which shows no size decrease with time – indicating the clusters may not have undergone full dissociation.

The identification of these errors has led to the conclusion that nanoclusters made with citrate as a primary ligand may not be capable of dissociation; or at least full dissociation. Work currently underway by Ehsan Moaseri suggests more complete dissociation has been observed using accurate methodologies for clusters made from particles fully capped with strongly-bound thiolated molecules. These ligands prevent interparticle fusion and therefore are reversible. Future studies into whether these clusters can achieve high-NIR at biologically relevant sizes and continue onto full dissociation are underway and are required to determine the true efficacy of the concepts detailed in this thesis.

a)

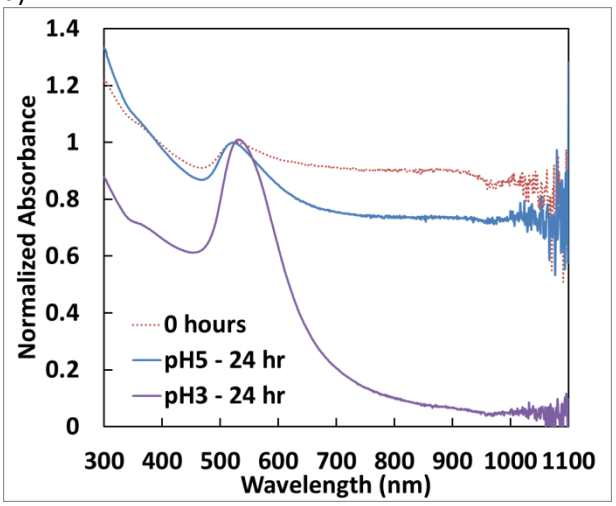

b)

	DLS Intensity-Weighted (nm)	
Sample	**Peak 1**	**Peak 2**
0 Hr	9.9	45.8
pH 5 – 24 hr	7.1	70.4
pH 3 – 24 hr	5.7	51.4

Figure F.1: A) UV-vis-NIR extinction showing the lack of dissociation of nanoclusters made from 9/1 lysine/citrate nanoparticles in pH 5 HCl (blue line), compared to pH 3 (purple). B) DLS intensity-weighted hydrodynamic sizes for samples shown in a).

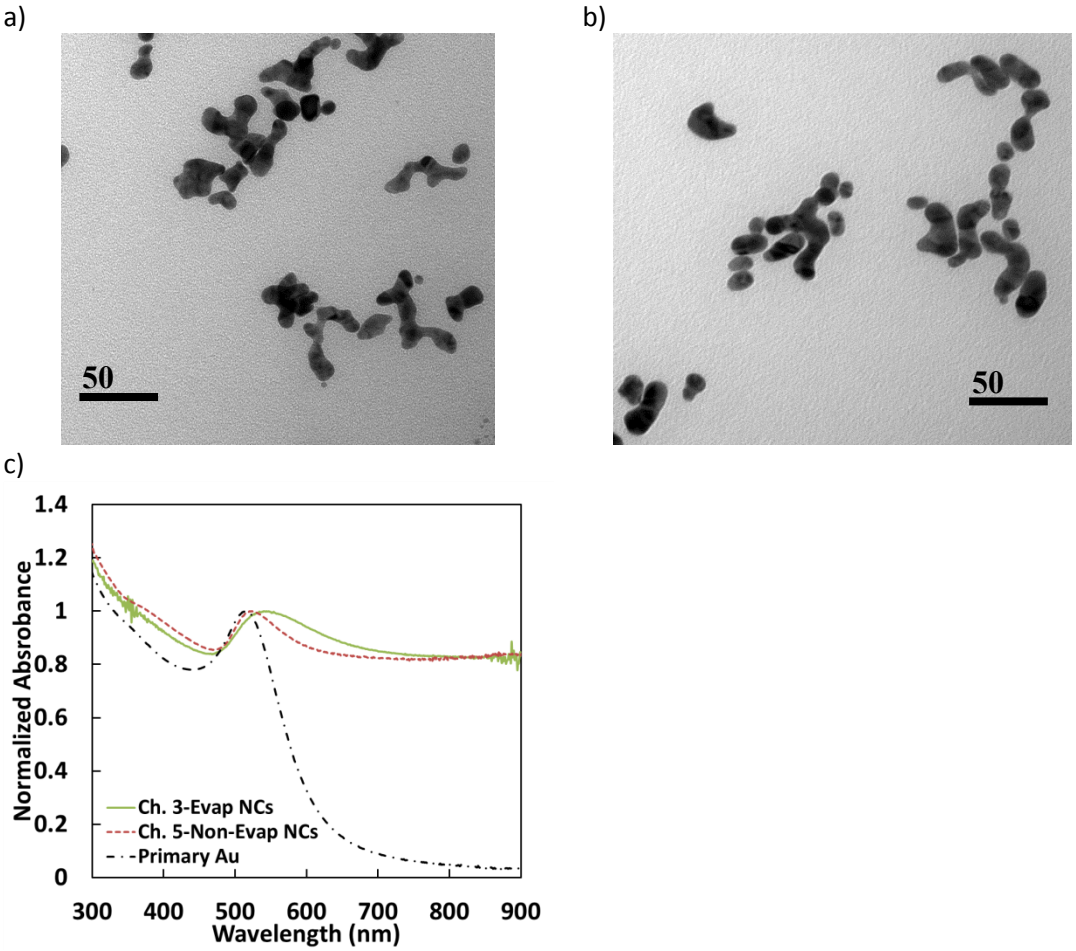

Figure F.2: TEM images of clusters showing apparent fusion. Clusters were made using the a) evaporation method and 9/1 lysine/citrate particles from Ch. 3 (sample 20-1.7) or b) $CaCl_2$ at pH 7 after 180 s of reaction time from Ch. 5. C) UV-vis-NIR absorbance spectra of samples shown in a) and b).

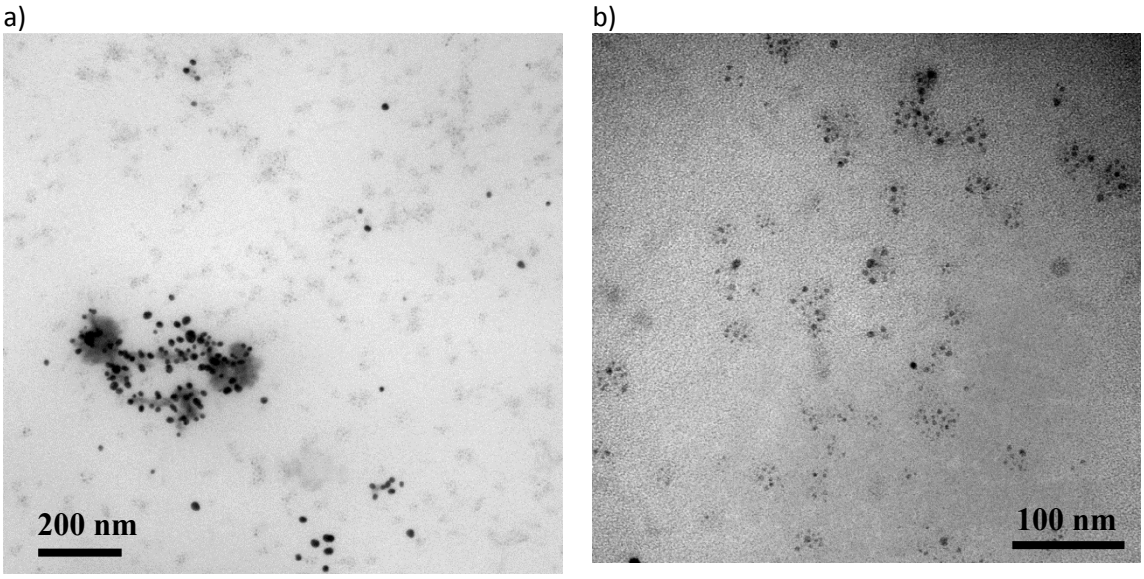

Figure F.3: TEM of dissociated nanoclusters at two magnifications showing a) large spherical particles and b) smaller 3-5 nm particle populations on grid.

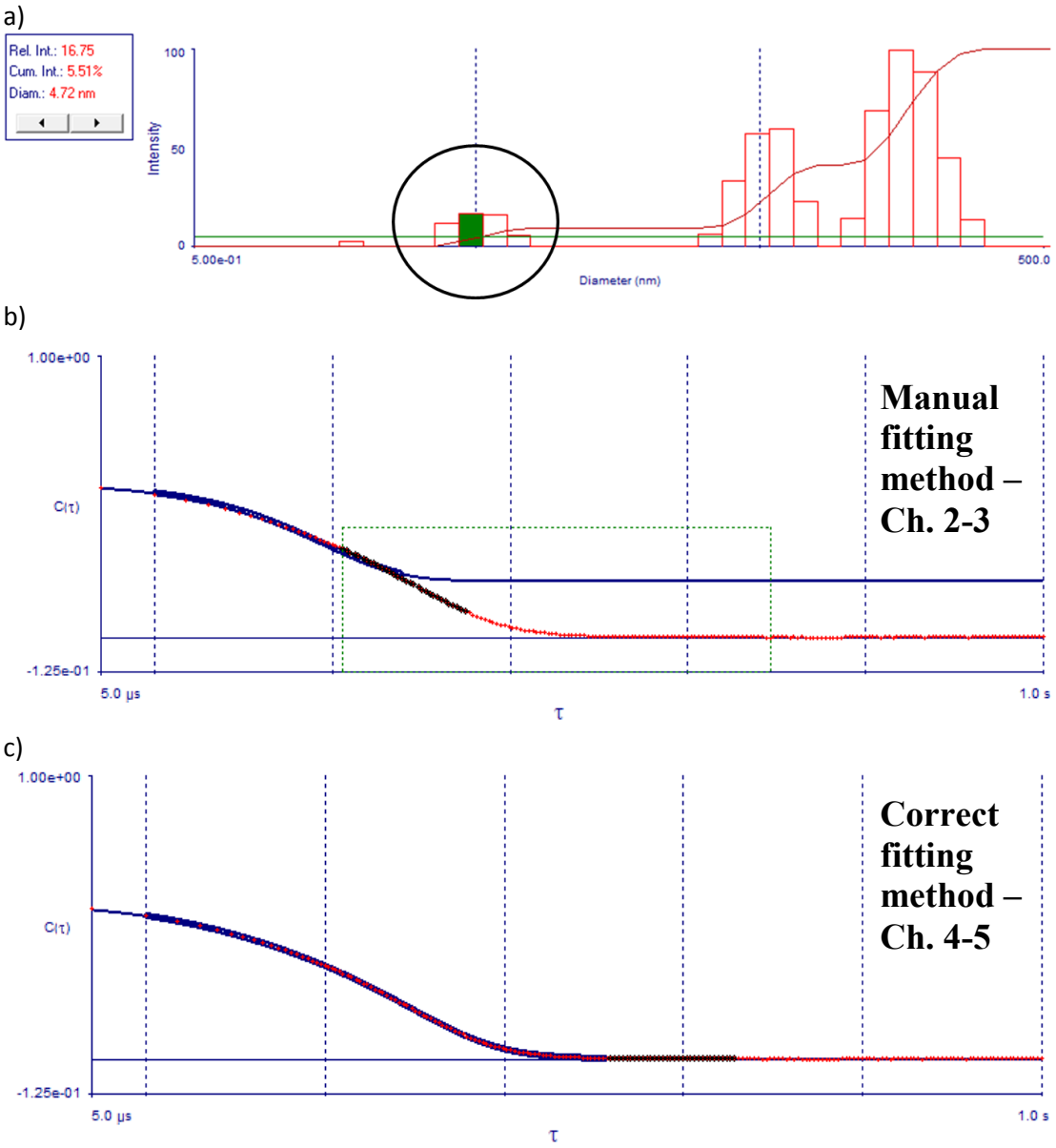

Figure F.4: Screenshots from the Brookhaven dynamic light scattering software showing a) characteristic phantom peak (black circle) present in many nanocluster samples, b) non-traditional manual fitting of an auto-correlation function (ACF) used in Ch. 2-3, and c) a correct auto-fitting of the same ACF used in chapters 4-5.

Table F.1: Data from Ch. 3 "20-1.7" dissociation sample using our old and new DLS fitting methods showing little size change throughout dissociation for newly fit DLS curves. For entries with two rows, the first row is the size by volume and the second by intensity.

Time point (hr)	A(800/525)	Original Fit (CONTIN)-Volume	New Fit (CONTIN)-Volume Intensity	New Fit (NNLS)-Volume Intensity	DLS Eff. Diam (nm)
0	0.86	26.5	4.93 82.6	3.35 98.9	60.4
2	0.28	17.6	4.05 74.5	4.17 94.9	47.1
4	0.11	12.8	5.70 95.4	6.26 105.3	53.4
6	0.09	4.9	3.13 92.51	2.19 87.26	58.1
72	0.06	4.8	25.01 123.5	4.65 102.9	66.1

F.2 Supplemental References

1. Kedia, A.; Kumar, P. S. Halide ion induced tuning and self-organization of gold nanostars. Rsc Advances 2014, 4, 4782-4790.
2. Khlebtsov, B. N.; Khlebtsov, N. G. On the measurement of gold nanoparticle sizes by the dynamic light scattering method. Colloid J. 2011, 73, 118-127.

Bibliography

Aaron, J.; Nitin, N.; Travis, K.; Kumar, S.; Collier, T.; Park, S. Y.; José-Yacamán, M.; Coghlan, L.; Follen, M.; Richards-Kortum, R., et al., Plasmon resonance coupling of metal nanoparticles for molecular imaging of carcinogenesis in vivo. Journal of Biomedical Optics 2007, 12, 034007-034007-034011.

Aaron, J.; Travis, K.; Harrison, N.; Sokolov, K., Dynamic Imaging of Molecular Assemblies in Live Cells Based on Nanoparticle Plasmon Resonance Coupling. Nano Letters 2009, 9, 3612-3618.

Agarwal, A.; Huang, S. W.; O'Donnell, M.; Day, K. C.; Day, M.; Ashkenazi, S., Targeted gold nanorod contrast agent for prostate cancer detection by photoacoustic imaging. Journal of Applied Physics 2007, 102, 0647011-0647014.

Ah, C. S.; Kim, W.-J.; Yun, W. S.; Joo, S.-W., Colorimetric quantitative sensing of alkali metal ions based on reversible assembly and disassembly of gold nanoparticles. Current Applied Physics 2013, 13, 1889-1893.

Alexandridis, P.; Holzwarth, J. F., Differential Scanning Calorimetry Investigation of the Effect of Salts on Aqueous Solution Properties of an Amphiphilic Block Copolymer (Poloxamer). Langmuir 1997, 13, 6074-6082.

Arnold, M. D.; Blaber, M. G.; Ford, M. J.; Harris, N., Universal scaling of local plasmons in chains of metal spheres. Optics Express 2010, 18, 7528-7542.

Asakura, S.; Oosawa, F., Interaction Between Particles Suspended In Solutions of Macromolecules. Journal of Polymer Science 1958, 33, 183-192.

Asakura, S.; Oosawa, F., On Interaction Between 2 Bodies Immersed in a Solution of Macromolecules. J. Chem. Phys. 1954, 22, 1255-1256.

Baalousha, M.; Nur, Y.; Römer, I.; Tejamaya, M.; Lead, J. R., Effect of monovalent and divalent cations, anions and fulvic acid on aggregation of citrate-coated silver nanoparticles. Science of the Total Environment 2013, 454–455, 119-131.

Balasubramanian, S. K.; Jittiwat, J.; Manikandan, J.; Ong, C.-N.; Liya, E. Y.; Ong, W.-Y., Biodistribution of gold nanoparticles and gene expression changes in the liver and spleen after intravenous administration in rats. Biomaterials 2010, 31, 2034-2042.

Barbosa, S.; Agrawal, A.; Rodríguez-Lorenzo, L.; Pastoriza-Santos, I.; Alvarez-Puebla, R. n. A.; Kornowski, A.; Weller, H.; Liz-Marzán, L. M., Tuning Size and Sensing Properties in Colloidal Gold Nanostars. Langmuir 2010, 26, 14943-14950.

Berchmans, S.; Thomas, P. J.; Rao, C., Novel effects of metal ion chelation on the properties of lipoic acid-capped Ag and Au nanoparticles. The Journal of Physical Chemistry B 2002, 106, 4647-4651.

Berret, J.-F., Stoichiometry of Electrostatic Complexes Determined by Light Scattering. Macromolecules 2007, 40, 4260-4266.

Beurer, E.; Venkataraman, N. V.; Sommer, M.; Spencer, N. D., Protein and Nanoparticle Adsorption on Orthogonal, Charge-Density-Versus-Net-Charge Surface-Chemical Gradients. Langmuir 2012, 28, 3159-3166.

Bezdek, K., Circle packings into convex domains of the Euclidean and hyperbolic plane and the sphere. Geometriae Dedicata 1986, 21, 249-255.

Boal, A. K.; Ilhan, F.; DeRouchey, J. E.; Thurn-Albrecht, T.; Russell, T. P.; Rotello, V. M., Self-assembly of nanoparticles into structured spherical and network aggregates. Nature 2000, 404, 746-748.

Bohren, C. F.; Huffman, D. R., Absorption and scattering of light by small particles. John Wiley & Sons: 2008.

Bozack, M. J.; Zhou, Y.; Worley, S. D., Structural modifications in the amino acid lysine induced by soft xray irradiation. Journal of Chemical Physics 1994, 100, 8392-8398.

Brewer, S. H.; Glomm, W. R.; Johnson, M. C.; Knag, M. K.; Franzen, S., Probing BSA Binding to Citrate-Coated Gold Nanoparticles and Surfaces. Langmuir 2005, 21, 9303-9307.

Buitenhuis, J.; Dhont, J. K. G.; Lekkerkerker, H. N. W., Static and Dynamic Light Scattering by Concentrated Colloidal Suspensions of Polydisperse Sterically Stabilized Boehmite Rods. Macromolecules 1994, 27, 7267-7277.

Burns, C.; Spendel, W.; Puckett, S.; Pacey, G., Solution ionic strength effect on gold nanoparticle solution color transition. Talanta 2006, 69, 873-876.

Casals, E.; Pfaller, T.; Duschl, A.; Oostingh, G. J.; Puntes, V., Time Evolution of the Nanoparticle Protein Corona. ACS Nano 2010, 4, 3623-3632.

Cedervall, T.; Lynch, I.; Lindman, S.; Berggard, T.; Thulin, E.; Nilsson, H.; Dawson, K. A.; Linse, S., Understanding the nanoparticle-protein corona using methods to quantify exchange rates and affinities of proteins for nanoparticles. Proceedings of the National Academy of Sciences 2006, 104, 2050-2055.

Chen, J.; Saeki, F.; Wiley, B. J.; Cang, H.; Cobb, M. J.; Li, Z. Y.; Au, L.; Zhang, H.; Kimmey, M. B.; Li, X., et al., Gold Nanocages: Bioconjugation and Their Potential Use as Optical Imaging Contrast Agents. Nano Letters 2005, 5, 473-477.

Chen, S.; Cao, Z.; Jiang, S., Ultra-low fouling peptide surfaces derived from natural amino acids. Biomaterials 2009, 30, 5893-5896.

Chen, S.; Li, L.; Zhao, C.; Zheng, J., Surface hydration: Principles and applications toward low-fouling/nonfouling biomaterials. Polymer 2010, 51, 5283-5293.

Chen, S.; Yu, F.; Yu, Q.; He, Y.; Jiang, S., Strong Resistance of a Thin Crystalline Layer of Balanced Charged Groups to Protein Adsorption. Langmuir 2006, 22, 8186-8191.

Chen, S.; Zhen, J.; Li, L.; Jiang, S., Strong Resistance of Phosphorylcholine Self-Assembled Monolayers to Protein Adsorption: Insights into Nonfouling Properties of Zwitterionic Materials. Journal of the American Chemical Society 2005, 127, 14473-14478.

Chen, Y.; Mao, C., pH- Induced Reversible Expansion/Contraction of Gold Nanoparticle Aggregates. Small 2008, 4, 2191-2194.

Cheng, C.; Wen, Y.; Xu, X.; Gu, H., Tunable synthesis of carboxyl-functionalized magnetite nanocrystal clusters with uniform size. Journal of Materials Chemistry 2009, 19, 8782-8788.

Chithrani, B. D.; Ghazani, A. A.; Chan, W. C. W., Determining the Size and Shape Dependence of Gold Nanoparticle Uptake into Mammalian Cells. Nano Letters 2006, 6, 662-668.

Chithrani, B. D.; Stewart, J.; Allen, C.; Jaffray, D. A., Intracellular uptake, transport, and processing of nanostructures in cancer cells. Nanomedicine: Nanotechnology, Biology and Medicine 2009, 5, 118-127.

Choi, H. S.; Liu, W.; Misra, P.; Tanaka, E.; Zimmer, J. P.; Ipe, B. I.; Bawendi, M. G.; Frangioni, J. V., Renal clearance of quantum dots. Nature Biotechnology 2007, 25, 1165-1170.

Chompoosor, A.; Han, G.; Rotello, V. M., Charge Dependent of Ligand Release and Monolayer Stability of Gold Nanoparticles by Biogenic Thiols. Bioconjugate Chemistry 2008, 19, 1342-1345.

Copland, J. A.; Eghtedari, M.; Popov, V. L.; Kotov, N.; Mamedova, N.; Motamedi, M.; Oraevsky, A. A., Bioconjugated gold nanoparticles as a molecular based contrast agent: implications for imaging of deep tumors using optoacoustic tomography. Molecular Imaging & Biology 2004, 6, 341-349.

De Paoli Lacerda, S. H.; Park, J. J.; Meuse, C.; Pristinski, D.; Becker, M. L.; Karim, A.; Douglas, J. F., Interaction of Gold Nanoparticles with Common Human Blood Proteins. ACS Nano 2010, 4, 365-379.

Despa, F.; Fernandez, A.; Berry, R. S., Dielectric Modulation of Biological Water. Physical Review Letters 2004, 93, 228104.

Dobrovolskaia, M. A.; Patri, A. K.; Zheng, J.; Clogston, J. D.; Ayub, N.; Aggarwal, P.; Neun, B. W.; Hall, J. B.; McNeil, S. E., Interaction of colloidal gold nanoparticles with human blood: effects on particle size and analysis of plasma protein binding profiles. Nanomedicine 2009, 5, 106-117.

Dominguez-Medina, S.; McDonough, S.; Swanglap, P.; Landes, C. F.; Link, S., In Situ Measurement of Bovine Serum Albumin Interaction with Gold Nanospheres. Langmuir 2012, 28, 9131-9139.

Dreaden, E. C.; Alkilany, A. M.; Huang, X.; Murphy, C. J.; El-Sayed, M. A., The golden age: gold nanoparticles for biomedicine. Chemical Society Reviews 2012, 41, 2740-2779.

Duncan, B.; Kim, C.; Rotello, V. M., Gold nanoparticle platforms as drug and biomacromolecule delivery systems. Journal of Controlled Release 2010, 148, 122-127.

Dutta, A.; Das, S.; Paul, A.; Chattopadhyay, A., Kinetics of reaction of gold nanoparticles following partial removal of stabilizers. Journal of Nanoparticle Research 2015, 17, 1-13.

Edwards, T. D.; Bevan, M. A., Polymer Mediated Depletion Attraction and Interfacial Colloidal Phase Behavior. Macromolecules 2012, 45, 585-594.

Elimelech, M.; Gregory, J.; Jia, X., Particle deposition and aggregation: measurement, modelling and simulation. Butterworth-Heinemann: 2013.
Enustun, B. V.; Turkevich, J., Coagulation of Colloidal Gold. Journal of the American Chemical Society 1963, 85, 3317-3328.
Esteban, R.; Taylor, R. W.; Baumberg, J. J.; Aizpurua, J., How chain plasmons govern the optical response in strongly interacting self-assembled metallic clusters of nanoparticles. Langmuir 2012, 28, 8881-8890.
Estephan, Z. G.; Jaber, J. A.; Schlenoff, J. B., Zwitterion-Stabilized Silica Nanoparticles: Toward Nonstick Nano. Langmuir 2010, 26, 16884-16889.
Fang, Y.; Chang, W.-S.; Willingham, B.; Swanglap, P.; Dominguez-Medina, S.; Link, S., Plasmon emission quantum yield of single gold nanorods as a function of aspect ratio. ACS Nano 2012, 6, 7177-7184.
Fernandes, R.; Li, M.; Dujardin, E.; Mann, S.; Kanaras, A. G., Ligand-mediated self-assembly of polymer-enveloped gold nanoparticle chains and networks. Chemical Communications 2010, 46, 7602-7604.
Folkers, J. P.; Laibinis, P. E.; Whitesides, G. M., Self-assembled monolayers of alkanethiols on gold: comparisons of monolayers containing mixtures of short- and long-chain constituents with methyl and hydroxymethyl terminal groups. Langmuir 1992, 8, 1330-1341.
Frankamp, B. L.; Boal, A. K.; Rotello, V. M., Controlled Interparticle Spacing through Self-Assembly of Au Nanoparticles and Poly(amidoamine) Dendrimers. Journal of the American Chemical Society 2002, 124, 15146-15147.
Fresnais, J.; Lavelle, C.; Berret, J.-F., Nanoparticle Aggregation Controlled by Desalting Kinetics. Journal of Physical Chemistry C 2009, 113, 16371-16379.
Fu, R.; Li, J.; Yang, W., Aggregation of glutathione-functionalized Au nanoparticles induced by Ni2+ ions. Journal of Nanoparticle Research 2012, 14, 1-8.
Gavrilenko, V. I., Optics of Nanomaterials. Pan Stanford Publishing: Singapore, 2011; p 63-66.
Ge, J.; Hu, Y.; Biasini, M.; Beyermann, W. P.; Yin, Y., Superparamagnetic Magnetite Colloidal Nanocrystal Clusters. Angewandte Chemie International Edition 2007, 46, 4342-4345.
Ghosh, S. K.; Pal, T., Interparticle Coupling Effect on the Surface Plasmon Resonance of Gold Nanoparticles: From Theory to Applications. Chemical Reviews 2007, 107, 4797-4862.
Gobin, A. M.; Lee, M. H.; Halas, N. J.; James, W. D.; Drezek, R. A.; West, J. L., Near-Infrared Resonant Nanoshells for Combined Optical Imaging and Photothermal Cancer Therapy. Nano Letters 2007, 7, 1929-1934.
Götzinger, M.; Peukert, W., Dispersive forces of particle–surface interactions: direct AFM measurements and modelling. Powder Technology 2003, 130, 102-109.
Gourisankar, S. Structure and Assembly of Gold Nanoclusters for Biomedical Imaging Applications. University of Texas at Austin, Austin, TX, 2015.
Grabar, K. C.; Allison, K. J.; Baker, B. E.; Bright, R. M.; Brown, K. R.; Freeman, R. G.; Fox, A. P.; Keating, C. D.; Musick, M. D.; Natan, M. J., Two-Dimensional Arrays

of Colloidal Gold Particles: A Flexible Approach to Macroscopic Metal Surfaces. Langmuir 1996, 12, 2353-2361.
Grabar, K. C.; Freeman, R. G.; Hommer, M. B.; Natan, M. J., Preparation and Characterization of Au Colloid Monolayers. Analytical Chemistry 1995, 67, 735-743.
Groenewold, J.; Kegel, W. K., Anomalously Large Equilibrium Clusters of Colloids. Journal of Physical Chemistry B 2001, 105, 11702-11709.
Groenewold, J.; Kegel, W. K., Colloidal cluster phases, gelation and nuclear matter. J. Phys.-Condes. Matter 2004, 16, S4877-S4886.
Grzelczak, M.; Vermant, J.; Furst, E. M.; Liz-Marzán, L. M., Directed Self-Assembly of Nanoparticles. ACS Nano 2010, 4, 3591-3605.
Guarise, C.; Pasquato, L.; Scrimin, P., Reversible Aggregation/Deaggregation of Gold Nanoparticles Induced by a Cleavable Dithiol Linker. Langmuir 2005, 21, 5537-5541.
Guerrini, L.; McKenzie, F.; Wark, A. W.; Faulds, K.; Graham, D., Tuning the interparticle distance in nanoparticle assemblies in suspension via DNA-triplex formation: correlation between plasmonic and surface-enhanced Raman scattering responses. Chemical Science 2012, 3, 2262-2269.
Guo, Y. M., Y.; Xu, L.; Li, J.; Yang, W., Conformational Change Induced Reversible Assembly/Disassembly of Poly-L-lysine-Functionalized Gold Nanoparticles. Journal of PHysical Chemistry C 2007, 111, 9172-9176.
Halas, N. J.; Lal, S.; Chang, W.-S.; Link, S.; Nordlander, P., Plasmons in Strongly Coupled Metallic Nanostructures. Chemical Reviews 2011, 111, 3913-3961.
Han, X.; Goebl, J.; Lu, Z.; Yin, Y., Role of Salt in the Spontaneous Assembly of Charged Gold Nanoparticles in Ethanol. Langmuir 2011, 27, 5282-5289.
Harada, R.; Sugita, Y.; Feig, M., Protein Crowding Affects Hydration Structure and Dynamics. Journal of the American Chemical Society 2012, 134, 4842-4849.
Hashmi, A. S. K., Gold-catalyzed organic reactions. Chemical Reviews 2007, 107, 3180-3211.
Hassan, S. S.; Rechnitz, G., Determination of glutathione and glutathione reductase with a silver sulfide membrane electrode. Analytical Chemistry 1982, 54, 1972-1976.
Herrmann, L.; Valev, V.; Aizpurua, J.; Baumberg, J. J., Self-sifting of chain plasmons: the complex optics of Au nanoparticle clusters. Optics Express 2013, 21, 32377-32385.
Hiemenz, P. C.; Rajagopalan, R., Principles of Colloid and Surface Chemistry, revised and expanded. CRC press: 1997; Vol. 14.
Hill, H. D.; Millstone, J. E.; Banholzer, M. J.; Mirkin, C. A., The role radius of curvature plays in thiolated oligonucleotide loading on gold nanoparticles. ACS Nano 2009, 3, 418-424.
Hill, L. J.; Pinna, N.; Char, K.; Pyun, J., Colloidal polymers from inorganic nanoparticle monomers. Progress in Polymer Science 2015, 40, 85-120.
Hirsch, L. R.; Stafford, R. J.; Bankson, J. A.; Sershen, S. R.; Rivera, B.; Price, R. E.; Hazle, J. D.; Halas, N. J.; West, J. L., Nanoshell-mediated near-infrared thermal

therapy of tumors under magnetic resonance guidance. Proceedings of the National Academy of Sciences 2003, 100, 13549-13554.
Holmlin, R. E.; Chen, X.; Chapman, R. G.; Takayama, S.; Whitesides, G. M., Zwitterionic SAMs that Resist Nonspecific Adsorption of Protein from Aqueous Buffer. Langmuir 2001, 17, 2841-2850.
Hong, R.; Han, G.; Fernandez, J. M.; Kim, B.; Forbes, N. S.; Rotello, V. M., Gluathione-Mediated Delivery and Release Using Monolayer Protected Nanoparticle Carriers. Journal of the American Chemical Society 2006, 128, 1078-1079.
Hopp, T. P.; Woods, W. R., Prediction of protein antigenic determinants from amino acid sequences. Proceedings of the National Academy of Sciences 1981, 78, 3824-3828.
Horovitz, O.; Mocanu, A.; Tomoaia, G.; Bobos, L.; Dubert, D.; Daian, I.; Yusanis, T.; Tomoaia-Cotisel, M., Lysine Mediated Assembly of Gold Nanoparticles. Studia Universitatis Babes-Bolyai Chemia 2007, 52.
Horvath, H., Gustav Mie and the scattering and absorption of light by particles: Historic developments and basics. Journal of Quantitative Spectroscopy and Radiative Transfer 2009, 110, 787-799.
Hsu, J.-P.; Kuo, Y.-C., The critical coagulation concentration of counterions: Spherical particles in asymmetric electrolyte solutions. J. Colloid Interface Sci. 1997, 185, 530-537.
Huang, D.; Liao, F.; Molesa, S.; Redinger, D.; Subramanian, V., Plastic-compatible low resistance printable gold nanoparticle conductors for flexible electronics. Journal of the Electrochemical Society 2003, 150, G412-G417.
Huang, X.; El-Sayed, I. H.; Qian, W.; El-Sayed, M. A., Cancer Cell Imaging and Photothermal Therapy in the Near-Infrared Region by Using Gold Nanorods. Journal of the American Chemical Society 2006, 128, 2115-2120.
Huang, X.; Jain, P. K.; El-Sayed, I. H.; El-Sayed, M. A., Gold nanoparticles: interesting optical properties and recent applications in cancer diagnostics and therapy. 2007.
Huynh, K. A.; Chen, K. L., Aggregation kinetics of citrate and polyvinylpyrrolidone coated silver nanoparticles in monovalent and divalent electrolyte solutions. Environmental Science & Technology 2011, 45, 5564-5571.
Israelachvili, J. N., Intermolecular and Surface Forces. 3 ed.; Elsevier: New York, 2011.
Ivanova, T.; Panaiotov, I.; Proust, J. E.; Benoit, J. P.; Verger, R., Hydrolysis kinetics of poly(D,L-lactide) monolayers spread on basic or acidic aqueous subphases. Colloids and Surfaces B: Biointerfaces 1997, 8, 217-225.
Jackson, A. M.; Myerson, J. W.; Stellacci, F., Spontaneous assembly of subnanometre-ordered domains in the ligand shell of monolayer-protected nanoparticles. Nature Materials 2004, 3, 330-336.
Jain, P. K.; Lee, K. S.; El-Sayed, I. H.; El-Sayed, M. A., Calculated Absorption and Scattering Properties of Gold Nanoparticles of Different Size, Shape, and Composition: Applications in Biological Imaging and Biomedicine. The Journal of Physical Chemistry B 2006, 110, 7238-7248.

Jia, G.; Cao, Z.; Xue, H.; Xu, Y.; Jiang, S., Novel Zwitterionic-Polymer-Coated Silica Nanoparticles. Langmuir 2009, 25, 3196-3199.
Johnston, K. P.; Maynard, J. A.; Truskett, T. M.; Borwankar, A. U.; Miller, M. A.; Wilson, B. K.; Dinin, A. K.; Khan, T. A.; Kaczorowski, K. J., Concentrated Dispersion of Equilibrium Protein Nanoclusters That Reversibly Dissociate Into Active Monomers. ACS Nano 2012, 6, 1357-1369.
Joshi, H.; Shirude, P. S.; Bansal, V.; Ganesh, K. N.; Sastry, M., Isothermal Titration Calorimetry Studies on the Binding of Amino Acids to Gold Nanoparticles. Journal of Physical Chemistry B 2004, 108, 11535-11540.
Joshi, P. Near-IR Plasmonic Contrast Agents for Molecular Imaging, Cells Tracking and Clinical Translation. University of Texas at Austin, Austin, TX, 2014.
Karplus, M., CHARMM: A program for macromolecular energy, minimization, and dynamics calculations. J Comput Chem 1983, 4, 187217.
Kaufman, E. D.; Belyea, J.; Johnson, M. C.; Nicholson, Z. M.; Ricks, J. L.; Shah, P. K.; Bayless, M.; Pettersson, T.; Feldoto, Z.; Blomberg, E., et al., Probing Protein Adsorption onto Mercaptoundecanoic Acid Stabilized Gold Nanoparticles and Surfaces by Quartz Crystal Microbalance and Z-Potential Measurements. Langmuir 2007, 23, 6053-6062.
Kedia, A.; Kumar, P. S., Halide ion induced tuning and self-organization of gold nanostars. Rsc Advances 2014, 4, 4782-4790.
Kennedy, L. C.; Bickford, L. R.; Lewinski, N. A.; Coughlin, A. J.; Hu, Y.; Day, E. S.; West, J. L.; Drezek, R. A., A New Era for Cancer Treatment: Gold-Nanoparticle-Mediated Thermal Therapies. Small 2011, 7, 169-183.
Khlebtsov, B.; Zharov, V.; Melnikov, A.; Tuchin, V.; Khlebtsov, N., Optical amplification of photothermal therapy with gold nanoparticles and nanoclusters. Nanotechnology 2006, 5167-5179.
Khlebtsov, B. N.; Khanadeyev, V. A.; Ye, J.; Mackowski, D. W.; Borghs, G.; Khlebtsov, N. G., Coupled plasmon resonances in monolayers of metal nanoparticles and nanoshells. Physical Review B 2008, 77, 035440.
Khlebtsov, B. N.; Khlebtsov, N. G., On the measurement of gold nanoparticle sizes by the dynamic light scattering method. Colloid Journal 2011, 73, 118-127.
Khlebtsov, N.; Dykman, L., Biodistribution and toxicity of engineered gold nanoparticles: a review of in vitro and in vivo studies. Chemical Society Reviews 2011, 40, 1647-1671.
Khlebtsov, N.; Dykman, L.; Krasnov, Y. M.; Mel'nikov, A., Light absorption by the clusters of colloidal gold and silver particles formed during slow and fast aggregation. Colloid Journal 2000, 62, 765-779.
Khlebtsov, N. G., T-matrix method in plasmonics: An overview. Journal of Quantitative Spectroscopy and Radiative Transfer 2013, 123, 184-217.
Kim, T.; Lee, K.; Gong, M.-s.; Joo, S.-W., Control of Gold Nanoparticle Aggregates by Manipulation of Interparticle Interaction. Langmuir 2005, 21, 9524-9528.

Kitching, H.; Shiers, M. J.; Kenyon, A. J.; Parkin, I. P., Self-assembly of metallic nanoparticles into one dimensional arrays. Journal of Materials Chemistry A 2013, 1, 6985-6999.

Klinkova, A.; Choueiri, R. M.; Kumacheva, E., Self-assembled plasmonic nanostructures. Chemical Society Reviews 2014, 43, 3976-3991.

Kneipp, J.; Kneipp, H.; McLaughlin, M.; Brown, D.; Kneipp, K., In Vivo Molecular Probing of Cellular Compartments with Gold Nanoparticles and Nanoaggregates. Nano Letters 2006, 6, 2225-2231.

Kondoh, H.; Kodama, C.; Sumida, H.; Nozoye, H., Molecular processes of adsorption and desorption of alkanethiol monolayers on Au(1 1 1). J. Chem. Phys. 1999, 111, 1175-1184.

Kooi, M. E.; Cappendijk, V. C.; Cleutjens, K. B. J. M.; Kessels, A. G. H.; Kitslaar, P. J. E. H. M.; Borgers, M.; Frederik, P. M.; Daemen, M. J. A. P.; van Engelshoven, J. M. A., Accumulation of Ultrasmall Superparamagnetic Particles of Iron Oxide in Human Atherosclerotic Plaques Can Be Detected by In Vivo Magnetic Resonance Imaging. Circulation 2003, 107, 2453-2458.

Korgel, B. A.; Fitzmaurice, D., Self- assembly of silver nanocrystals into two-dimensional nanowire arrays. Advanced Materials 1998, 10, 661-665.

Kulkarni, A. M.; Chatterjee, A. P.; Schweizer, K. S.; Zukoski, C. F., Depletion Interactions in the Protein Limit: Effects of Polymer Density Fluctuations. Physical Review Letters 1999, 83, 4554-4557.

Kunze, J.; Burgess, I.; Nichols, R.; Buess-Herman, C.; Lipkowski, J., Electrochemical evaluation of citrate adsorption on Au(1 1 1) and the stability of citrate-reduced gold colloids. Journal of Electroanalytical Chemistry 2007, 599, 147-159.

Ladd, J.; Zhang, Z.; Chen, S.; Hower, J. C.; Jiang, S., Zwitterionic Polymers Exhibiting High Resistance to Nonspecific Protein Adsorption from Human Serum and Plasma. Biomacromolecules 2008, 9, 1357-1361.

Larin, K. V.; Larina, I. V.; Esenaliev, R. O., Monitoring of tissue coagulation during thermotherapy using optoacoustic technique. Journal of Physics D: Applied Physics 2005, 38, 2645.

Larson-Smith, K.; Pozzo, D. C., Competitive Adsorption of Thiolated Poly(ethylene glycol) and Alkane-Thiols on Gold Nanoparticles and Its Effect on Cluster Formation. Langmuir 2012, 28, 13157-13165.

Larson-Smith, K.; Pozzo, D. C., Scalable synthesis of self-assembling nanoparticle clusters based on controlled steric interactions. Soft Matter 2011, 7, 5339-5347.

Larson, T. A.; Bankson, J.; Aaron, J.; Sokolov, K., Hybrid plasmonic magnetic nanoparticles as molecular specific agents for MRI/optical imaging and photothermal therapy of cancer cells. Nanotechnology 2007, 18.

Larson, T. A.; Joshi, P. P.; Sokolov, K., Preventing Protein Adsorption and Macrophage Uptake of Gold Nanoparticles via a Hydrophobic Shield. ACS Nano 2012, 6, 9182-9190.

Lassiter, J. B.; Aizpurua, J.; Hernandez, L. I.; Brandl, D. W.; Romero, I.; Lal, S.; Hafner, J. H.; Nordlander, P.; Halas, N. J., Close encounters between two nanoshells. Nano Letters 2008, 8, 1212-1218.

Lazarides, A. A.; Schatz, G. C., DNA-Linked Metal Nanosphere Materials: Structural Basis for the Optical Properties. Journal of Physical Chemistry B 2000, 104, 460-467.

Lee, J.; Zhou, H.; Lee, J., Small molecule induced self-assembly of Au nanoparticles. Journal of Materials Chemistry 2011, 21, 16935-16942.

Lee, Y.-J.; Schade, N. B.; Sun, L.; Fan, J. A.; Bae, D. R.; Mariscal, M. M.; Lee, G.; Capasso, F.; Sacanna, S.; Manoharan, V. N., Ultrasmooth, highly spherical monocrystalline gold particles for precision plasmonics. ACS Nano 2013, 7, 11064-11070.

Lekkerkerker, H. N. W.; Tuinier, R., Colloids and the Depletion Interaction. Springer: New York, 2011; Vol. 833, p 12-15.

Li, L.; Chen, S.; Zheng, J.; Ratner, B. D.; Jiang, S., Protein Adsorption on Oligo(ethylene glycol)-Terminated Alkanethiolate Self-Assembled Monolayers: The Molecular Basis for Nonfouling Behavior. Journal of Physical Chemistry B 2005, 109, 2934-2941.

Li, M.; Johnson, S.; Guo, H.; Dujardin, E.; Mann, S., A Generalized Mechanism for Ligand- Induced Dipolar Assembly of Plasmonic Gold Nanoparticle Chain Networks. Advanced Functional Materials 2011, 21, 851-859.

Li, N.; Yu, L.; Zou, J., Critical Coagulation Concentration–Based Salt Titration for Visual Quantification in Gold Nanoparticle–Based Colorimetric Biosensors. Journal of laboratory automation 2013, 2211068213498240.

Li, W.-C.; Lee, S.-W., The characteristics of lysine-mediated self-assembly of gold nanoparticles on the ITO glass. Current Applied Physics 2012, 12, 1361-1365.

Lim, I. I. S.; Ip, W.; Crew, E.; Njoki, P. N.; Mott, D.; Zhong, C.-J.; Pan, Y.; Zhou, S., Homocysteine-Mediated Reactivity and Assembly of Gold Nanoparticles. Langmuir 2007, 23, 826-833.

Lin, S.-Y.; Tsai, Y.-T.; Chen, C.-C.; Lin, C.-M.; Chen, C.-h., Two-step functionalization of neutral and positively charged thiols onto citrate-stabilized Au nanoparticles. The Journal of Physical Chemistry B 2004, 108, 2134-2139.

Lin, S.; Li, M.; Dujardin, E.; Girard, C.; Mann, S., One- Dimensional Plasmon Coupling by Facile Self- Assembly of Gold Nanoparticles into Branched Chain Networks. Advanced Materials 2005, 17, 2553-2559.

Lindman, S.; Lynch, I.; Thulin, E.; Nilsson, H.; Dawson, K. A.; Linse, S., Systematic investigation of the thermodynamics of HSA adsorption to N-iso-propylacrylamide/N-tert-butylacrylamide copolymer nanoparticles. Effects of particle size and hydrophobicity. Nano Letters 2007, 7, 914-920.

Linegar, K. L.; Adeniran, A. E.; Kostko, A. F.; Anisimov, M. A., Hydrodynamic Radius of Polyethylene Glycol in Solution Obtained by Dynamic Light Scattering. Colloid Journal 2010, 72, 279-281.

Link, S.; Mohamed, M. B.; El-Sayed, M. A., Simulation of the Optical Absorption Spectra of Gold Nanorods as a Function of Their Aspect Ratio and the Effect of the Medium Dielectric Constant. Journal of Physical Chemistry B 1999, 103, 3073-3077.

Liu, J.; Yu, M.; Ning, X.; Zhou, C.; Yang, S.; Zheng, J., PEGylation and Zwitterionization: Pros and Cons in the Renal Clearance and Tumor Targeting of Near- IR- Emitting Gold Nanoparticles. Angewandte Chemie 2013, 125, 12804-12808.

Liu, W.; Choi, H. S.; Zimmer, J. P.; Tanaka, E.; Frangioni, J. V.; Bawendi, M., Compact Cysteine-Coated CdSe(ZnCdS) Quantum Dots for in Vivo Applications. Journal of the American Chemical Society 2007, 129, 14530-14531.

Liu, X. S.; Huang, H. Y.; Jin, Q.; Ji, J., Mixed Charged Zwitterionic Self-Assembled Monolayers as a Facile Way to Stabilize Large Gold Nanoparticles. Langmuir 2011, 27, 5242-5251.

Liu, Y.; Han, X.; He, L.; Yin, Y., Thermoresponsive assembly of charged gold nanoparticles and their reversible tuning of plasmon coupling. Angewandte Chemie International Edition 2012, 51, 6373-6377.

Liz-Marzán, L. M., Tailoring surface plasmons through the morphology and assembly of metal nanoparticles. Langmuir 2006, 22, 32-41.

Loo, C.; Lowery, A.; Halas, N.; West, J.; Drezek, R., Immunotargeted Nanoshells for Integrated Cancer Imaging and Therapy. Nano Letters 2005, 5, 709-711.

Lu, P. J.; Zaccarelli, E.; Ciulla, F.; Scholfield, A. B.; Sciortino, F.; Weitz, D. A., Gelation of particles with short-range attraction. Nature 2008, 453, 499-504.

Lu, Z.; Yin, Y., Colloidal nanoparticle clusters: functional materials by design. Chemical Society Reviews 2012, 41, 6874-6887.

Lubitz, I.; Kotlyar, A., G4-DNA-Coated Gold Nanoparticles: Synthesis and Assembly. Bioconjugate Chemistry 2011, 22, 2043-2047.

Luke, G.; Yeager, D.; Emelianov, S., Biomedical Applications of Photoacoustic Imaging with Exogenous Contrast Agents. Ann Biomed Eng 2012, 40, 422-437.

Lundqvist, M.; Stigler, J.; Elia, G.; Lynch, I.; Cedervall, T.; Dawson, K. A., Nanoparticle size and surface properties determine the protein corona with possible implications for biological impacts. Proceedings of the National Academy of Sciences 2008, 105, 14265-14270.

Ma, L. L.; Borwankar, A. U.; Willsey, B. W.; Yoon, K. Y.; Tam, J. O.; Sokolov, K. V.; Feldman, M. D.; Milner, T. E.; Johnston, K. P., Growth of textured thin Au coatings on iron oxide nanoparticles with near infrared absorbance. Nanotechnology 2013, 24, 025606.

Ma, L. L.; Feldman, M. D.; Tam, J. M.; Paranjape, A. S.; Cheruki, K. K.; Larson, T. A.; Tam, J. O.; Ingram, D. R.; Paramita, V.; Villard, J. W., et al., Small Multifunctional Nanoclusters (Nanoroses) for Targeted Cellular Imaging and Therapy. ACS Nano 2009, 3, 2686-2696.

Ma, L. L.; Tam, J. O.; Willsey, B. W.; Rigdon, D.; Ramesh, R.; Sokolov, K.; Johnston, K. P., Selective Targeting of Antibody Conjugated Multifunctional Nanoclusters

(Nanoroses) to Epidermal Growth Factor Receptors in Cancer Cells. Langmuir 2011, 27, 7681-7690.
Mahmoudi, M.; Lynch, I.; Ejtehadi, M. R.; Monopoli, M. P.; Bombelli, F. B.; Laurent, S., Protein-Nanoparticle Interactions: Opportunities and Challenges. Chemical Reviews 2011, 111, 5610-5637.
Mallidi, S.; Larson, T.; Aaron, J.; Sokolov, K.; Emelianov, S., Molecular specific optoacoustic imaging with plasmonic nanoparticles. Optics Express 2007, 15, 6583-6588.
Mallidi, S.; Larson, T.; Tam, J.; Joshi, P. P.; Karplouk, A.; Sokolov, K.; Emelianov, S., Multiwavelength Photoacoustic Imaging and Plasmon Resonance Coupling of Gold Nanoparticles for Selective Detection of Cancer. Nano Letters 2009, 9, 2825-2831.
Mallidi, S.; Luke, G. P.; Emelianov, S., Photoacoustic imaging in cancer detection, diagnosis, and treatment guidance. Trends in Biotechnology 2011, 29, 213-221.
Mandal, S.; Gole, A.; Lala, N.; Gonnade, R.; Ganvir, V.; Sastry, M., Studies on the reversible aggregation of cysteine-capped colloidal silver particles interconnected via hydrogen bonds. Langmuir 2001, 17, 6262-6268.
Markarucha, A. J.; Todorova, N.; Yarovsky, I., Nanomaterials in biological environment: a review of computer modelling studies. European Biophysics Journal 2011, 40, 103-115.
Martin, J. E.; Hurd, A., Scattering from fractals. Journal of applied Crystallography 1987, 20, 61-78.
Meyer, M.; Le Ru, E. C.; Etchegoin, P. G., Self-Limiting Aggregation Leads to Long-Lived Metastable Clusters in Colloidal Solutions. The Journal of Physical Chemistry B 2006, 110, 6040-6047.
Moiraghi, R.; Douglas-Gallardo, O.; Coronado, E.; Macagno, V.; Pérez, M., Gold nucleation inhibition by halide ions: a basis for a seed-mediated approach. Rsc Advances 2015, 5, 19329-19336.
Moyano, D. F.; Ray, M.; Rotello, V. M., Nanoparticle–protein interactions: Water is the key. MRS Bulletin 2014, 39, 1069-1073.
Moyano, D. F.; Saha, K.; Prakash, G.; Yan, B.; Kong, H.; Yazdani, M.; Rotello, V. M., Fabrication of corona-free nanoparticles with tunable hydrophobicity. ACS Nano 2014, 8, 6748-6755.
Murphy, C. J. S., T.K; Gole, A.M; Orendorff, C.J; Gao, J.; Gou, L.; Hunyadi, S.E; Li, T., Anisotropic Metal Nanoparticles: Synthesis, Assembly, and Optical Applications. Journal of Physical Chemistry B 2005, 109, 13857-13870.
Murthy, A. K. Surface design and controlled assembly of gold nanoparticles into biodegradable nanoclusters for biomedical imaging applications. University of Texas at Austin, Austin, TX, 2013.
Murthy, A. K.; Stover, R. J.; Borwankar, A. U.; Nie, G. D.; Gourisankar, S.; Truskett, T. M.; Sokolov, K. V.; Johnston, K. P., Equilibrium Gold Nanoclusters Quenched with Biodegradable Polymers. ACS Nano 2013, 7, 239-251.

Murthy, A. K.; Stover, R. J.; Hardin, W. G.; Schramm, R.; Nie, G. D.; Gourisankar, S.; Truskett, T. M.; Sokolov, K. V.; Johnston, K. P., Charged Gold Nanoparticles with Essentially Zero Serum Protein Adsorption in Undiluted Fetal Bovine Serum. Journal of the American Chemical Society 2013, 135, 7799-7802.

Murugadoss, A.; Chattopadhyay, A., Surface area controlled differential catalytic activities of one-dimensional chain-like arrays of gold nanoparticles. The Journal of Physical Chemistry C 2008, 112, 11265-11271.

Nabika, H.; Oikawa, T.; Iwasaki, K.; Murakoshi, K.; Unoura, K., Dynamics of gold nanoparticle assembly and disassembly induced by pH oscillations. The Journal of Physical Chemistry C 2012, 116, 6153-6158.

Nehl, C. L.; Liao, H.; Hafner, J. H., Optical Properties of Star-Shaped Gold Nanoparticles. Nano Letters 2006, 6, 683-688.

Norman, T.; Grant, C.; Zhang, J., Optical and dynamic properties of gold metal nanomaterials: From isolated nanoparticles to assemblies. Nanoparticle Assemblies and Superstructures. Boca Raton, FL: CRC Press/Taylor & Francis 2006, 193-206.

Ofir, Y.; Samanta, B.; Rotello, V. M., Polymer and biopolymer mediated self-assembly of gold nanoparticles. Chemical Society Reviews 2008, 37, 1814-1825.

Ofir, Y. S., B.; Rotello, V.M, Polymer and biopolymer mediated self-assembly of gold nanoparticles. Chemical Society Reviews 2008, 37, 1814-1825.

Ostuni, E.; Chapman, R. G.; Holmlin, R. E.; Takayama, S.; Whitesides, G. M., A Survey of Structure-Property Relationships of Surfaces that Resist the Adsorption of Protein. Langmuir 2001, 17, 5605-5620.

Park, J.-W.; Shumaker-Parry, J. S., Strong Resistance of Citrate Anions on Metal Nanoparticles to Desorption under Thiol Functionalization. ACS Nano 2015, 9, 1665-1682.

Park, J.-W.; Shumaker-Parry, J. S., Structural study of citrate layers on gold nanoparticles: role of intermolecular interactions in stabilizing nanoparticles. Journal of the American Chemical Society 2014, 136, 1907-1921.

Pérez-Juste, J.; Pastoriza-Santos, I.; Liz-Marzán, L. M.; Mulvaney, P., Gold nanorods: synthesis, characterization and applications. Coordination Chemistry Reviews 2005, 249, 1870-1901.

Petri-Fink, A.; Steitz, B.; Finka, A.; Salaklang, J.; Hofmann, H., Effect of cell media on polymer coated superparamagnetic iron oxide nanoparticles (SPIONs): Colloidal stability, cytotoxicity, and cellular uptake studies. European Journal of Pharmaceutics and Biopharmaceutics 2008, 68, 129-137.

Piech, M.; Walz, J. Y., Direct measurement of depletion and structural forces in polydisperse, charged systems. J. Colloid Interface Sci. 2002, 253, 117-129.

Polavarapu, L.; Perez-Juste, J.; Xu, Q.-H.; Liz-Marzan, L. M., Optical sensing of biological, chemical and ionic species through aggregation of plasmonic nanoparticles. Journal of Materials Chemistry C 2014, 2, 7460-7476.

Polavarapu, L.; Xu, Q.-H., A single-step synthesis of gold nanochains using an amino acid as a capping agent and characterization of their optical properties. Nanotechnology 2008, 19, 075601.

Porcar, L.; Falus, P.; Chen, W.-R.; Faraone, A.; Fratini, E.; Hong, K.; Baglioni, P.; Liu, Y., Formation of the Dynamic Clusters in Concentrated Lysozyme Protein Solutions. Journal of Physical Chemistry Letters 2010, 1, 126-129.

Pruneanu, S.; Olenic, L.; Farha Al-Said, S.; Borodi, G.; Houlton, A.; Horrocks, B., Template and template-free preparation of one-dimensional metallic nanostructures. J Mater Sci 2010, 45, 3151-3159.

Rechberger, W.; Hohenau, A.; Leitner, A.; Krenn, J. R.; Lamprecht, B.; Aussenegg, F. R., Optical properties of two interacting gold nanoparticles. Optics Communications 2003, 220, 137-141.

Röcker, C.; Pötzl, M.; Zhang, F.; Parak, W. J.; Nienhaus, G. U., A quantitative fluorescence study of protein monolayer formation on colloidal nanoparticles. Nature Nanotechnology 2009, 4, 577-580.

Romo-Herrera, J. M.; Alvarez-Puebla, R. A.; Liz-Marzan, L. M., Controlled assembly of plasmonic colloidal nanoparticle clusters. Nanoscale 2011, 3, 1304-1315.

Ryoo, W.; Webber, S. E.; Johnston, K. P., Water-in-Carbon Dioxide Microemulsions with Methylated Branched Hydrocarbon Surfactants. Industrial and Engineering Chemistry Research 2003, 42, 6348-6358.

Sakai, T.; Alexandridis, P., Mechanism of Gold Metal Ion Reduction, Nanoparticle Growth and Size Control in Aqueous Amphiphilic Block Copolymer Solutions at Ambient Conditions. Journal of Physical Chemistry B 2005, 109, 7766-7777.

Sedgwick, H.; Egelhaaf, S. U.; Poon, W. C. K., Clusters and gels in systems of sticky particles. J. Phys.-Condes. Matter 2004, 16, S4913-S4922.

Semyonov, S. A., A study of electrolytic coagulation of gold sols by the method of localized surface plasmon resonance spectroscopy. Colloid Journal 2013, 75, 421-426.

Senapati, D.; Singh, A. K.; Khan, S. A.; Senapati, T.; Ray, P. C., Probing real time gold nanostar formation process using two-photon scattering spectroscopy. Chemical Physics Letters 2011, 504, 46-51.

Shenhar, R.; Norsten, T. B.; Rotello, V. M., Polymer-Mediated Nanoparticle Assembly: Structural Control and Applications. Advanced Materials 2005, 17, 657-669.

Si, S.; Mandal, T. K., pH-controlled reversible assembly of peptide-functionalized gold nanoparticles. Langmuir 2007, 23, 190-195.

Sinyagin, A. Y.; Belov, A.; Tang, Z.; Kotov, N. A., Monte Carlo computer simulation of chain formation from nanoparticles. The Journal of Physical Chemistry B 2006, 110, 7500-7507.

Sistach, S.; Rahme, K.; Pérignon, N.; Marty, J.-D.; Viguerie, N. L.-d.; Gauffre, F.; Mingotaud, C., Bolaamphiphile surfactants as nanoparticle stabilizers: application to reversible aggregation of gold nanoparticles. Chemistry of Materials 2008, 20, 1221-1223.

Sokolov, K.; Follen, M.; Aaron, J.; Pavlova, I.; Malpica, A.; Lotan, R.; Richards-Kortum, R., Real-time vital optical imaging of precancer using anti-epidermal growth factor receptor antibodies conjugated to gold nanoparticles. Cancer Research 2003, 63, 1999-2004.

Sokolov, K.; Stover, R.; Joshi, P.; Yoon, S. J.; Murthy, A.; Emelianov, S.; Johnston, K. In Biodegradable Plasmonic Nanoparticles: Overcoming Clinical Translation Barriers, Optical Molecular Probes, Imaging and Drug Delivery, Optical Society of America: 2015; p OM3D. 4.

Song, K. H.; Kim, C.; Cobley, C. M.; Xia, Y.; Wang, L. V., Near-Infrared Gold Nanocages as a New Class of Tracers for Photoacoustic Sentinel Lymph Node Mapping on a Rat Model. Nano Letters 2009, 9, 183-188.

Spirou, G. M.; Vitkin, I. A.; Wilson, B.; Whelan, W. M.; Henrichs, P. M.; Mehta, K.; Miller, T.; Yee, A.; Meador, J.; Oraevsky, A. A. In Development and testing of an optoacoustic imaging system for monitoring and guiding prostate cancer therapies, Biomedical Optics 2004, International Society for Optics and Photonics: 2004; pp 44-56.

Srivastava, S.; Frankamp, B. L.; Rotello, V. M., Controlled Plasmon Resonance of Gold Nanoparticles Self-Assembled with PAMAM Dendrimers. Chemistry of Materials 2005, 17, 487-490.

Stover, R. J.; Murthy, A. K.; Nie, G. D.; Gourisankar, S.; Dear, B. J.; Truskett, T. M.; Sokolov, K. V.; Johnston, K. P., Quenched Assembly of NIR-Active Gold Nanoclusters Capped with Strongly Bound Ligands by Tuning Particle Charge via pH and Salinity. The Journal of Physical Chemistry C 2014, 118, 14291-14298.

Stradner, A.; Sedgwick, H.; Cardinaux, F.; Poon, W. C. K.; Egelhaaf, S. U.; Schurtenberger, P., Equilibrium cluster formation in concentrated protein solutions and colloids. Nature 2004, 432, 492-495.

Striemer, C. C.; Gaborski, T. R.; McGrath, J. L.; Fauchet, P. M., Charge- and size-based separation of macromolecules using ultrathin silicon membranes. Nature 2007, 445, 749-753.

Su, Y.-L.; Wei, X.-F.; Liu, H.-Z., Effect of sodium chloride on association behavior of poly(ethylene oxide)-poly(propylene oxide)-poly(ethylene oxide) block copolymer in aqueous solutions. J. Colloid Interface Sci. 2003, 264, 526-531.

Sun, M., Hoffman, D., Sundaresan, G., Yang, L., Lamichhane, N., Zweit, J., Synthesis and characterization of intrinsically radiolabeled quantum dots for bimodal detection. American Journal of Nuclear Medicine and Molecular Imaging 2012, 2, 122-135.

Tadros, T. F.; Vincent, B., Influence of Temperature and Electrolytes on the Adsorption of Poly(ethylene oxide)-Poly(propylene oxide) Block Copolymer on Polystyrene Latex and on the Stability of the Polymer-Coated Particles. Journal of Physical Chemistry 1980, 84, 1575-1580.

Tam, J. M.; Murthy, A. K.; Ingram, D. R.; Nguyen, R.; Sokolov, K. V.; Johnston, K. P., Kinetic Assembly of Near-IR Active Gold Nanoclusters Using Weakly Adsorbing Polymers to Control the Size. Langmuir 2010, 26, 8988-8999.

Tam, J. M.; Tam, J. O.; Murthy, A.; Ingram, D. R.; Ma, L. L.; Travis, K.; Johnston, K. P.; Sokolov, K. V., Controlled Assembly of Biodegradable Plasmonic Nanoclusters for Near-Infrared Imaging and Therapeutic Applications. ACS Nano 2010, 4, 2178-2184.

Tam, J. O. Interactions of composite gold nanoparticles with cells and tissue: implications in clinical translation for cancer imaging and therapy. University of Texas at Austin, 2012.

Tan, J.; Liu, R.; Wang, W.; Liu, W.; Tian, Y.; Wu, M.; Huang, Y., Controllable aggregation and reversible pH sensitivity of AuNPs regulated by carboxymethyl cellulose. Langmuir 2009, 26, 2093-2098.

Tang, Z.; Kotov, N. A.; Giersig, M., Spontaneous organization of single CdTe nanoparticles into luminescent nanowires. Science 2002, 297, 237-240.

Templeton, A. C.; Wuelfing, W. P.; Murray, R. W., Monolayer-protected cluster molecules. Accounts of Chemical Research 2000, 33, 27-36.

Tirumalai, R. S.; Chan, K. C.; Prieto, D. A.; Issaq, H. J.; Conrads, T. P.; Veenstra, T. D., Characterization of the Low Molecular Weight Human Serum Proteome. Molecular & Cellular Proteomics 2003, 2, 1096-1103.

Tjong, H.; Zhou, H.-X., Prediction of Protein Solubility from Calculation of Transfer Free Energy. Biophysical Journal 2008, 95, 2601-2609.

Trigari, S.; Rindi, A.; Margheri, G.; Sottini, S.; Dellepiane, G.; Giorgetti, E., Synthesis and modelling of gold nanostars with tunable morphology and extinction spectrum. Journal of Materials Chemistry 2011, 21, 6531-6540.

Verma, A.; Uzun, O.; Hu, Y.; Hu, Y.; Han, H.-S.; Watson, N.; Chen, S.; Irvine, D. J.; Stellacci, F., Surface-structure-regulated cell-membrane penetration by monolayer-protected nanoparticles. Nature Materials 2008, 7, 588-595.

Vinluan III, R. D.; Liu, J.; Zhou, C.; Yu, M.; Yang, S.; Kumar, A.; Sun, S.; Dean, A.; Sun, X.; Zheng, J., Glutathione-coated luminescent gold nanoparticles: a surface ligand for minimizing serum protein adsorption. Acs Applied Materials & Interfaces 2014, 6, 11829-11833.

von Maltzahn, G.; Park, J.-H.; Agrawal, A.; Bandaru, N. K.; Das, S. K.; Sailor, M. J.; Bhatia, S. N., Computationally Guided Photothermal Tumor Therapy Using Long-Circulating Gold Nanorod Antennas. Cancer Research 2009, 69, 3892-3900.

Walkey, C. D.; Olsen, J. B.; Guo, H.; Emili, A.; Chan, W. C. W., Nanoparticle Size and Surface Chemistry Determine Serum Protein Adsorption and Macrophage Uptake. Journal of the American Chemical Society 2012, 134, 2139-2147.

Walser, M., Dissociation constants for complexes of citrate with sodium, potassium, calcium, and magnesium ions. The Journal of Physical Chemistry 1961, 65, 159-161.

Wang, D.; Tejerina, B.; Lagzi, I.; Kowalczyk, B.; Grzybowski, B. A., Bridging interactions and selective nanoparticle aggregation mediated by monovalent cations. ACS Nano 2010, 5, 530-536.

Wang, M.-H.; Li, Y.-J.; Xie, Z.-X.; Liu, C.; Yeung, E. S., Fabrication of large-scale one-dimensional Au nanochain and nanowire networks by interfacial self-assembly. Materials Chemistry and Physics 2010, 119, 153-157.
Wang, S.; Chen, K. J.; Wu, T. H.; Wang, H.; Lin, W. Y.; Ohashi, M.; Chiou, P. Y.; Tseng, H. R., Photothermal effects of supramolecularly assembled gold nanoparticles for the targeted treatment of cancer cells. Angewandte Chemie International Edition 2010, 49, 3777-3781.
Wang, T.; LaMontagne, D.; Lynch, J.; Zhuang, J.; Cao, Y. C., Colloidal superparticles from nanoparticle assembly. Chemical Society Reviews 2013, 42, 2804-2823.
Wang, W.; Yang, X.; Cui, H., Growth Mechanism of Flowerlike Gold Nanostructures: Surface Plasmon Resonance (SPR) and Resonance Rayleigh Scattering (RRS) Approaches to Growth Monitoring. Journal of Physical Chemistry C 2008, 112, 16348-16353.
Wang, X.; Li, G.; Chen, T.; Yang, M.; Zhang, Z.; Wu, T.; Chen, H., Polymer-Encapsulated Gold-Nanoparticle Dimers: Facile Preparation and Catalytical Application in Guided Growth of Dimeric ZnO-Nanowires. Nano Letters 2008, 8, 2643-2647.
Wang, Y.; Liang, W.; Geng, C., Coalescence behavior of gold nanoparticles. Nanoscale research letters 2009, 4, 684-688.
Wang, Z.; Zhang, J.; Ekman, J. M.; Kenis, P. J. A.; Lu, Y., DNA-Mediated Control of Metal Nanoparticle Shape: One-Pot Synthesis and Cellular Uptake of Highly Stable and Functional Gold Nanoflowers. Nano Letters 2010, 10, 1886-1891.
Watts, J. F.; Wolstenholme, J., An Introduction to Surface Analysis by XPS and AES. John Wiley & Sons: West Sussex, England, 2003.
Wei, H.; Insin, N.; Lee, J.; Han, H.-S.; Cordero, J. M.; Liu, W.; Bawendi, M. G., Compatct Zwitterion-Coated Iron Oxide Nanoparticles for Biological Applications. Nano Letters 2011, 12, 22-25.
Weissleder, R., A clearer vision for in vivo imaging. Nature Biotechnology 2001, 19, 316-317.
Weitz, D. A.; Huang, J. S.; Lin, M. Y.; Sung, J., Limits of the Fractal Dimension for Irreversible Kinetic Aggregation of Gold Colloids. Physical Review Letters 1985, 54, 1416-1419.
Wilcoxon, J. P.; Martin, J. E.; Schaefer, D. W., Aggregation in colloidal gold. Physical Review A 1989, 39, 2675-2688.
Willets, K. A.; Van Duyne, R. P., Localized surface plasmon resonance spectroscopy and sensing. Annu. Rev. Phys. Chem. 2007, 58, 267-297.
Wozniak, M.; Onofri, F.; Barbosa, S.; Yon, J.; Mroczka, J., Comparison of methods to derive morphological parameters of multi-fractal samples of particle aggregates from TEM images. Journal of Aerosol Science 2012, 47, 12-26.
Xi, C.; Marina, P. F.; Xia, H.; Wang, D., Directed self-assembly of gold nanoparticles into plasmonic chains. Soft Matter 2015, 11, 4562-4571.

Xia, H.; Su, G.; Wang, D., Size- Dependent Electrostatic Chain Growth of pH- Sensitive Hairy Nanoparticles. Angewandte Chemie International Edition 2013, 52, 3726-3730.

Xia, Y. S.; Nguyen, T. D.; Yang, M.; Lee, B.; Santos, A.; Podsiadlo, P.; Tang, Z. Y.; Glotzer, S. C.; Kotov, N. A., Self-assembly of self-limiting monodisperse supraparticles from polydisperse nanoparticles. Nature Nanotechnology 2011, 6, 580-587.

Xu, L.; Guo, Y.; Xie, R.; Zhuang, J.; Yang, W.; Li, T., Three-dimensional assembly of Au nanoparticles using dipeptides. Nanotechnology 2002, 13, 725-728.

Yang, M.; Chen, G.; Zhao, Y.; Silber, G.; Wang, Y.; Xing, S.; Han, Y.; Chen, H., Mechanistic investigation into the spontaneous linear assembly of gold nanospheres. Physical Chemistry Chemical Physics 2010, 12, 11850-11860.

Yang, W.; Xue, H.; Li, W.; Zhang, J.; Jiang, S., Pursuing "Zero" Protein Adsorption of Poly(carboxybetaine) from Undiluted Blood Serum and Plasma. Langmuir 2009, 25, 11911-11916.

Yang, W.; Zhang, L.; Wang, S.; White, A. D.; Jiang, S., Functionalizable and ultra stable nanoparticles coated with zwitterionic poly(carboxybetaine) in undiluted blood serum. Biomaterials 2009, 30, 5617-5621.

Yao, Q.; Luo, Z.; Yuan, X.; Yu, Y.; Zhang, C.; Xie, J.; Lee, J. Y., Assembly of nanoions via electrostatic interactions: ion-like behavior of charged noble metal nanoclusters. Scientific Reports 2014, 4.

Yoon, S. J. Photoacoustic Imaging using Nanoclsuters. University of Texas at Austin, Austin, TX, 2014.

Yoon, S. J.; Mallidi, S.; Tam, J. M.; Tam, J. O.; Murthy, A.; Johnston, K. P.; Sokolov, K. V.; Emelianov, S. Y., Utility of biodegradable plasmonic nanoclusters in photoacoustic imaging. Optics Letters 2010, 35, 3751-3753.

You, C.-C.; De, M.; Han, G.; Rotello, V. M., Tunable Inhibition and Denaturation of a-Chymotrypsin with Amino Acid-Functionalized Gold Nanoparticles. Journal of the American Chemical Society 2005, 127, 12873-12881.

Yu, M.; Zheng, J., Clearance Pathways and Tumor Targeting of Imaging Nanoparticles. ACS Nano 2015.

Yu, M.; Zhou, C.; Liu, J.; Hankins, J. D.; Zheng, J., Luminescent Gold Nanoparticles with pH-Dependent Membrane Adsorption. Journal of the American Chemical Society 2011, 133, 11014-11017.

Zaccarelli, E., Colloidal gels: equilibrium and non-equilibrium routes. J. Phys.-Condes. Matter 2007, 19, 1-50.

Zakaria, H. M.; Shah, A.; Konieczny, M.; Hoffmann, J. A.; Nijdam, A. J.; Reeves, M., Small molecule-and amino acid-induced aggregation of gold nanoparticles. Langmuir 2013, 29, 7661-7673.

Zhan, N.; Palui, G.; Safi, M.; Ji, X.; Mattoussi, H., Multidentate Zwitterionic Ligands Provide Compact and Highly Biocompatible Quantum Dots. Journal of the American Chemical Society 2013, 135, 13786-13795.

Zhang, C.; Pansare, V. J.; Prud'homme, R. K.; Priestley, R. D., Flash nanoprecipitation of polystyrene nanoparticles. Soft Matter 2012, 8, 86-93.
Zhang, H.; Fung, K.-H.; Hartmann, J. r.; Chan, C.; Wang, D., Controlled chainlike agglomeration of charged gold nanoparticles via a deliberate interaction balance. The Journal of Physical Chemistry C 2008, 112, 16830-16839.
Zhang, H.; Wang, D., Controlling the Growth of Charged-Nanoparticle Chains through Interparticle Electrostatic Repulsion. Angewandte Chemie 2008, 120, 4048-4051.
Zhang, H. F.; Maslov, K.; Stoica, G.; Wang, L. V., Functional photoacoustic microscopy for high-resolution and noninvasive in vivo imaging. Nature Biotechnology 2006, 24, 848-851.
Zhang, X.-D.; Luo, Z.; Chen, J.; Song, S.; Yuan, X.; Shen, X.; Wang, H.; Sun, Y.; Gao, K.; Zhang, L., et al., Ultrasmall Glutathione-Protected Gold Nanoclusters as Next Generation Radiotherapy Sensitizers with High Tumor Uptake and High Renal Clearance. Scientific Reports 2015, 5, 8669.
Zhang, X.; Servos, M. R.; Liu, J., Ultrahigh Nanoparticle Stability against Salt, pH, and Solvent with Retained Surface Accessibility via Depletion Stabilization. Journal of the American Chemical Society 2012, 134, 9910-9913.
Zhao, Y.; Xu, L.; Liz-Marzán, L. M.; Kuang, H.; Ma, W.; Asenjo-García, A.; García de Abajo, F. J.; Kotov, N. A.; Wang, L.; Xu, C., Alternating plasmonic nanoparticle heterochains made by polymerase chain reaction and their optical properties. The Journal of Physical Chemistry Letters 2013, 4, 641-647.
Zhou, C.; Long, M.; Qin, Y.; Sun, X.; Zheng, J., Luminescent Gold Nanoparticles with Efficient Renal Clearance. Angewandte Chemie International Edition 2011, 50, 3168-3172.
Zhuang, J.; Wu, H.; Yang, Y.; Cao, Y. C., Controlling Colloidal Superparticle Growth Through Solvophobic Interactions. Angewandte Chemie International Edition 2008, 47, 2208-2212.

Vita

Robert John Stover was born in Boulder, CO and grew up along the Rocky Mountain Front Range in Longmont, CO. After graduating from Longmont High School, he moved to the Sonoran desert to attend the University of Arizona – Bear Down! In Tucson, he received a Bachelor of Science in Materials Science and Engineering where he worked as an undergradauate researcher in Dr. Doug Loy's lab studying synthesis and surface modifications of aerogel nanocomposites for insulation applications. It was here that he met his graduate student mentor, Dr. Dylan Boday who encouraged him to pursue a doctorate degree. That decision led him to the University of Texas at Austin where he began his Ph.D. work with Dr. Keith Johnston in the fall of 2010. In addition to his undergraduate research background, he also brought to Austin, TX his experience from his two summer research internships at Ball Aerospace in Boulder, CO where he worked on testing the properties of particle resistant surfaces.

As a graduate student, Stover stayed active outside of the lab as well; road racing with the UT cycling club team, winning two intramural softball championships, graduating from Coldtowne Theater Conservatory for improvised comedy, and touring the Austin open-mic scene with his violin.

Permanent Email: rjstover487@gmail.com

This dissertation was typed by the author.